

PROCESS MAPPING, FRACTURE AND FATIGUE BEHAVIOR OF Ti-6Al-4V PRODUCED BY EBM ADDITIVE MANUFACTURING

Mohsen Seifi¹, Daniel Christiansen², Jack Beuth², Ola Harrysson³, and John J. Lewandowski¹

¹: Department of Materials Science and Engineering, Case Western Reserve University, Cleveland, OH

²: Department of Mechanical Engineering, Carnegie Mellon University, Pittsburgh, PA

³: Department of Industrial and Systems Engineering, North Carolina State University, Raleigh, NC

Abstract

The present work was conducted as part of a larger America Makes funded project to begin to examine the effects of changes in process variables on the resulting microstructure and fracture and fatigue behavior of as-deposited Ti-6Al-4V. In addition to presenting initial results on process mapping of the electron beam powder bed process, the present work also documents the location-dependent properties of the as-deposited materials with respect to the build direction. In the fatigue crack growth tests, the fatigue threshold, Paris law slope, and overload toughness were determined at load ratio, $R=0.1$, while fatigue precracked samples were tested to determine the fracture toughness. Fracture surface examination revealed the presence of unmelted powders, disbonded regions and isolated porosity, however, the resulting mechanical properties were in the range of those reported for cast and wrought Ti-6Al-4V.

Keywords: Process Mapping, Electron-Beam Melting, Additive Manufacturing, Ti-6Al-4V, Fracture Toughness, Fatigue Crack Growth, Fractography, Defects

Introduction

Recent work [1] has documented orientation-dependent fracture and fatigue properties of as-deposited Ti-6Al-4V prepared by electron beam melting, in addition to providing a modified ASTM nomenclature to begin the discussion of possible orientations to consider for mechanical characterization. A proposed work item has been registered with ASTM to develop a guideline based on the previous work [2]. While it was also shown that fracture toughness and fatigue crack growth behavior of the as-deposited Ti-6Al-4V were in the range of those reported for cast and wrought material [1], the presence of unmelted particles, porosity, and other defects likely reduced the properties somewhat. Although these will be detrimental to the mechanical properties, it has been shown that HIPing can be used to remove some porosity defects depending on their origin [3], [4]. Other recent works have also investigated the effects of build direction on fracture and fatigue behavior of these alloys [5]–[8]. Edwards et al. [5] showed higher fracture toughness on laser-processed Ti-6Al-4V in orientations where crack propagation occurred perpendicular to the build direction, while Cain et al. [6] reported much lower fracture toughness values than Edwards [5] as well as that reported presently. In both studies [5], [6], some toughness improvement was obtained after heat treatment and HIPing.

Although preliminary work is examining the orientation dependence of AM properties on bulk samples at a number of institutions [1-3], there is also a critical need to understand the processing-structure-property envelope that is possible with all AM processes [9], [10]. Beuth et al. have developed a process mapping strategy to begin to predict and control microstructure

[10], [11] that is being used across all AM processes. The present work captures this approach for the electron beam powder bed system for Ti-6Al-4V in addition to providing additional characterization of the location-dependent properties on bulk samples that can arise in such processes.

Materials and Methods

The process modeling approach [9]–[11] utilizes ABAQUS finite element simulations (initially developed by Soylemez et al. [12]) that were modified to examine the thermal profile resulting from the exposure of a substrate to a heat source at different combinations of power (P) and velocity (V). The details of the simulation include a distributed heat flux on a semi-infinite substrate with increased mesh resolution around the path of the melt pool, with temperature dependent properties and latent heat included (cf. Fig. 1). The maximum melt pool width, W , was determined for 12 power (P) and velocity (V) combinations.

Experimental verification of the modeling was conducted on an ARCAM™ model A2 EBM machine at NCSU, using ARCAM pedigree Ti-6Al-4V ELI spherical powders with an average particle size of 40–105 μm . The same combinations of P and V described above were utilized on both bare plate as well as with one layer of powder in a high vacuum chamber maintained at 1.5×10^{-3} Torr and 7.1×10^{-6} Torr in the electron gun, while the base preheat temperature was maintained around 750°C. Microstructure examinations conducted on cross-sections enabled the correlation of melt pool width to regions of P-V that produced constant beta grain width, as shown in Fig. 6 for single bead Ti-6Al-4V Arcam EBM deposits in earlier work by Gockel et al. [9].

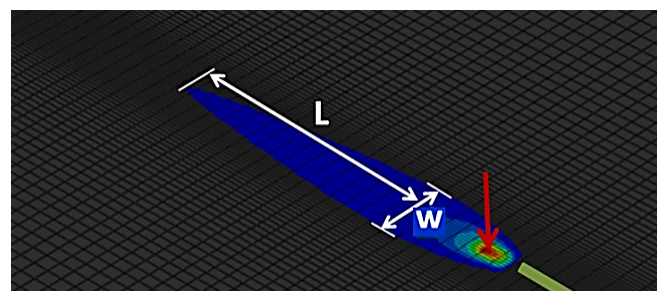


Figure 1: Abaqus FEA model of heat source and single bead on a semi-infinite substrate.

While the single bead results provide critical information on the possibility of microstructure control of such processes, continuing work by the authors is investigating such approaches using multi-layer powder deposits at standard Arcam preheat temperatures. That work has examined beta grain size/growth through several layers and reveals that the beta grain size continues to scale with the melt pool width although the exact

scaling shown in Fig. 6 will likely not continue in multi-layered prints. Recent work has also shown that the beta grain widths increase with build height as the columnar grains combine and extend through several layers [13]. Despite this complication, it is clear that there is a correlation between melt pool size and beta grain size, with the expectation that parts produced with larger melt pools will exhibit larger average beta grain widths than those produced using smaller melt pools.

In addition to the bead on plate tests, multi-layer pads were prepared using the same powders on the same ARCAM™ model A2 EBM machine at NCSU to produce bend bar samples with final dimensions of $10\text{ mm} \times 20\text{ mm} \times 100\text{ mm}$. Default ARCAM process parameters were used to construct the bend bar samples in a high vacuum chamber maintained at $1.5 \times 10^{-3}\text{ Torr}$ and $7.1 \times 10^{-6}\text{ Torr}$ in the electron gun, while the base preheat temperature was maintained around 750°C . The present work solely evaluated as-deposited material in the absence of any post processing (e.g. Heat treatment, Hot Isotactic Pressing, etc.) in order to develop baseline properties while documenting the orientation dependence of the microstructure and properties present in as-deposited material.

The as-deposited surfaces were analyzed with Scanning Electron Microscopy (SEM) on a FEI™ Quanta 200 3D microscope operated at 20 keV. Scanning Laser Confocal Microscopy was also conducted on Olympus BX62 to evaluate surface roughness at the end of the build.

Fracture toughness was determined on the as-deposited bend bars in three point bending using single edge notch (SEN) specimens on a Model 810 MTS servo-hydraulic machine in general accordance with ASTM E399 [14]. In this study, location-specific fracture properties throughout the build were determined in the SL orientation, defined previously [1], at three different locations with respect to the build, e.g. middle, near start of the build, and near end of the build. The as-deposited bend bar samples were first notched using a slow speed diamond wire saw to introduce a notch root radius of about $75\text{-}100\text{ }\mu\text{m}$ followed by fatigue precracking to a crack depth/sample width (i.e. a/w) of 0.45 to 0.55, in accordance with ASTM E399 [14]. The Direct Current Potential Drop (DCPD) technique, based on procedure on ASTM E647 [15], was used to monitor the ΔK rate in order to adhere to ASTM E399. The fracture toughness experiments were conducted to failure at a displacement rate of 0.05 mm/min. Fracture Technology Associates (FTA™) software was used to continuously monitor crack growth in both the fatigue and fracture toughness tests in order to also comply with existing ASTM requirements. In all cases 1-1.5 amp current input was used with voltage drop amplified by 10K gain.

Fatigue crack growth tests were performed at 20 Hz in room temperature air with relative humidity of 40% in accordance with ASTM E647 [15] on various orientations, e.g. LS-END, LS-START and LT-BOTH as defined previously [1]. The DCPD technique was again used to monitor and control crack growth. Fatigue crack growth tests were first started at an intermediate ΔK using R values of 0.1, followed by load-shedding in order to establish the true fatigue threshold, ΔK_{th} , as required by ASTM E647. The fatigue test was then stopped and restarted at a ΔK that was 5% lower than the ΔK that was used initially (i.e. to obtain enough data overlap) and the test was run under rising ΔK conditions until catastrophic fracture. The Paris Law slope and fatigue overload K_c was calculated for multiple tests conducted in this manner. In the fatigue study the specimen orientation was varied in order to determine the presence of any anisotropy.

Scanning Electron Microscopy (SEM) of fractured samples was conducted on a FEI Quanta 200 3D microscope utilizing secondary electron imaging (SE) operated at 20 keV.

Results and Discussion

Fig. 2 shows an SEM image of the end of the build on the as-deposited Ti-6Al-4V sample, with surface roughness measurements on the order of the powder size (e.g. $40\text{-}105\text{ }\mu\text{m}$).

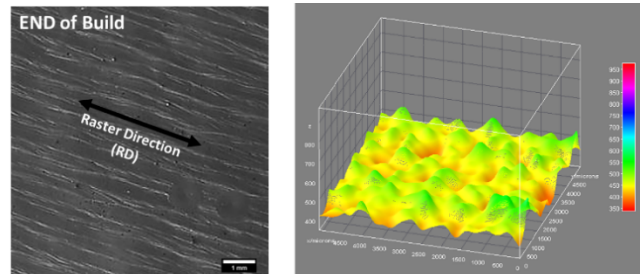


Figure 2: SEM image of END of build and Laser Confocal Microscopy image showing surface roughness.

Fracture toughness results for the SL orientations tested are provided in Table 1. The sample thickness requirement (i.e. 11-16 mm) for valid K_{IC} measurements was nearly met presently, requiring the present fatigue-precracked fracture toughness data to be reported as K_q . Much higher toughness values were obtained near the END of the build. The 2nd highest toughness was obtained for the specimen tested near the START of the build, with the lowest toughness measured at the middle location. Earlier work has shown [1] that a coarser microstructure exists near the START of the build with refinement near the END of the build. Although these results are consistent with previous work on Ti-6Al-4V [16], [17] where finer microstructures produced much higher fracture toughness/strength, another source of the location-dependent SL toughness properties relates to the presence and distribution of defects at different locations of the build. These have been quantified using X-ray Computerized Tomography (XCT) and will be reported separately.

Specimen Orientation	Thickness s, B (mm)	Span, S (mm)	Fracture Toughness K_q (MPa $\sqrt{\text{m}}$)
SL- Near START	10	40	79
SL- MIDDLE	10	80	65
SL- Near END	10	40	100

Table 1: Summary of Toughness Results

Fig. 3 is provided to demonstrate the presence and distribution of defects in the SL sample along with the location of the notches with respect to the build direction. The location of defects was obtained by polishing the outer surface of this sample to a metallographic finish and then imaging the defects using a copying machine. Fig. 3 shows that the porosity distribution in the middle of this as-deposited sample is much higher than that present at the START or END of the build, also in rough agreement with the ranking of toughness shown in Table 1. Defect density was also confirmed with XCT. Consistent with this ranking, Fig. 3(b) and 3(c) reveals that a very small plastic zone size is present on the surface of the lower toughness sample taken

from the middle of the build, while a much larger plastic zone size accompanied the higher toughness sample taken from the END of the build.

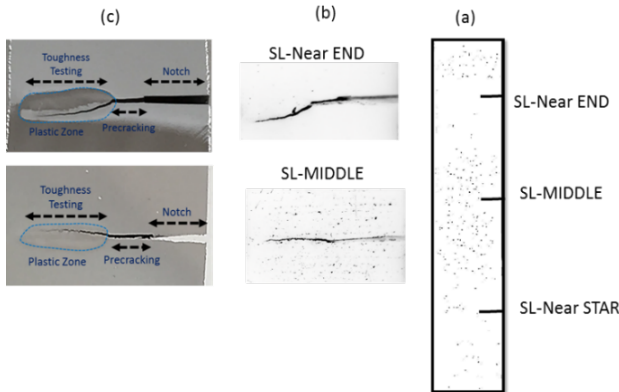


Figure 3: (a) Schematic of fracture toughness test location with respect to build direction in SL specimen. Porosity distribution is also evident, (b) Crack path of fractured sample. Also evident is porosity level, (c) Optical images of the fractured sample showing various stages of crack advancement along with the plastic zone size.

Fig. 4 provides some representative fatigue crack growth curves at load ratio of 0.1 provided in Table 2. Fatigue overload values, K_c , reported in Table 2 were all obtained at very high a/W (e.g. 0.7-0.8) and are presented only for completeness. Planar crack fronts were exhibited for all toughness and fatigue samples, suggesting minimal residual stress in the as-deposited builds. Toughness is denoted as K_q due to inadequate thickness.

Table 2: Summary of Fatigue Crack Growth Results.

Specimen Orientation	R, (Load Ratio)	K_c , Fatigue Overload (MPa \sqrt{m})	m, (Paris Slope)	ΔK_{th} , Threshold (MPa \sqrt{m})
LS-START	0.1	96	4.1	5.7
LS-END	0.1	53	3.5	4.2
LT-BOTH	0.1	91	2.9	3.8

The fatigue crack growth tests summarized in Table 2 also reveal some level of anisotropy. The AM specimens tested in fatigue in three different LS-END, LS-START and LT-BOTH orientations at $R=0.1$ displayed different behavior, with the highest Paris slope (e.g. 4.1) and higher fatigue overload K_c (e.g. 96 MPa \sqrt{m}) exhibited for LS-START, with lower values exhibited for LT-BOTH. The LS-START also exhibited a higher Paris Law slope and higher fatigue overload K_c in comparison to LS-END that exhibited lower Paris slope (e.g. 3.5) and lowest fatigue overload K_c . The highest ΔK_{th} was obtained for LS-START (e.g. 5.7 MPa \sqrt{m}) while the lowest was obtained for LT-BOTH (e.g. 3.8 MPa \sqrt{m}).

Similar fatigue threshold (e.g. 5.7 MPa \sqrt{m}) results at $R = 0.1$ have been reported for Ti-6Al-4V containing a lamellar microstructure by Nalla et al. [18], although much higher fatigue thresholds have been reported for as-cast TiAl [19]. Differences in ΔK_{th} along the build can be attributed in part to the grain size variation throughout the build. For example, for the LS-START specimen, the original notch length of $a/W = 0.25$ was placed in

the coarser grain size region while the fatigue threshold was measured in regions with much finer grain size. In contrast, the notch in the LS-END specimen required the fatigue crack to initiate and grow in the much finer grain size region with the fatigue threshold occurring in the coarser grain size region. The variation in ΔK_{th} is the subject of ongoing work.

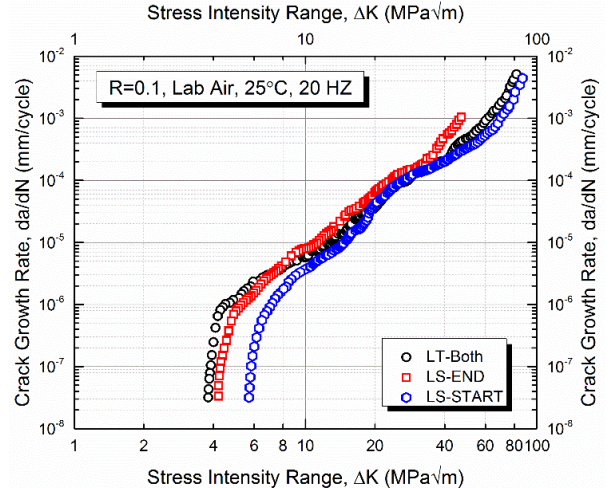


Figure 4: Fatigue Crack Growth Curve.

SEM examination of fractured samples revealed various defects, as shown in Fig. 5(a) for the LT-Both specimen. Metallographic cross sections taken behind the fracture surface are provided in Fig. 5 (b & c) and reveal the presence of similar features, indicating that these defects are as result of EBM processing and not fatigue testing. The larger defects are always perpendicular to the build direction, while the size of isolated porosity is on the order of the powder size.

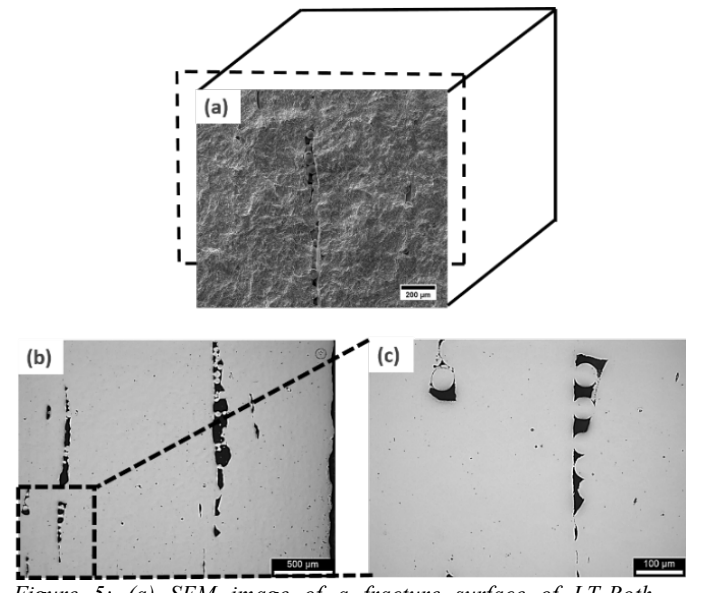


Figure 5: (a) SEM image of a fracture surface of LT-Both specimen fractured in fatigue, (b) low magnification of metallographic cross section taken behind the fracture surface of boxed region shown in (a), (c) higher magnification of boxed region shown in (b).

The source(s) of the defects shown in Fig. 5 are not completely clear at this point since both the FEM calculations and

single bead experiments reveal the size scale of the melt pool to exist on the order of the defect size. Much additional work is needed to determine the regimes and source(s) of such defects, with a view toward their elimination. In the meantime, the process mapping approach shown in Fig. 6 is useful in defining effects of variations in P and V on melt pool geometry and resulting microstructure. The single bead tests summarized in Fig. 6 were conducted on an Arcam A2 at NCSU with a single 70 μm layer of powder on a Ti-6Al-4V plate. The P-V map clearly shows that the high velocity, low power combinations shown in yellow exhibited beading up, undermelting, and surface tension effects which can lead to porosity in final deposited parts. On the other side of process space, low velocity, high power combinations shown in red produced irregular “dips” that can also lead to porosity from a different source. Although it was not investigated in these experiments, low velocity, high power combinations can also exhibit key holing, where material is locally vaporized by the electron beam, causing spherical pores in the final part. At this point, the highest quality regions obtained in the single bead P-V plot are outlined in green in Fig. 6. Much additional process modeling work and experimentation is required on multiple bead samples in order to define regimes of defect generation as well as microstructure.

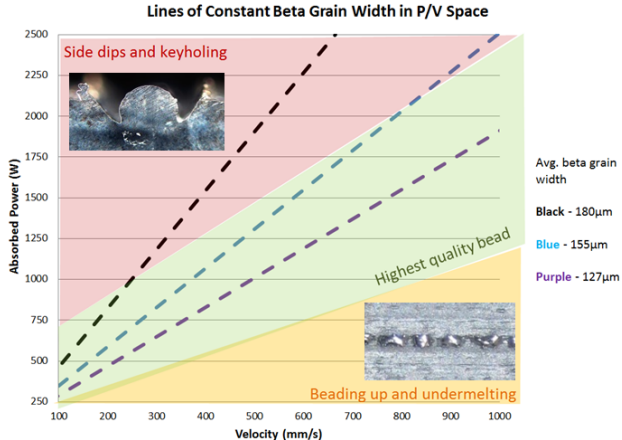


Figure 6: P/V process map showing lines of constant beta grain width and bead quality in Arcam processing space.

Conclusions

Preliminary work has been conducted to both model the melt pool and experimentally examine the effects of variations in process conditions on the melt pool size and resulting microstructure in single bead-on-plate experiments (with and without powder) for EBM Ti-6Al-4V. The single bead experiments and model showed that the melt pool size was significantly affected by the combinations of P and V utilized, while regions of constant melt pool size were both predicted and experimentally validated. Changes in melt pool size also controlled the size of the beta grains, with larger melt pool sizes producing correspondingly larger beta grain sizes. Preliminary work on the single bead experiments also revealed regimes of defect generation and both the nature and type of defect were different in different regimes of P and V.

Multi-layer bend bar samples were also created, enabling documentation of the fracture toughness and fatigue crack growth behavior of as-deposited Ti-6Al-4V. While the as-deposited properties were in the range of those reported for cast

and wrought Ti-6Al-4V, the properties were location-dependent within one build and orientation-dependent between different build orientations. In addition to microstructure inhomogeneity both within and between builds, various defects were present in the as-deposited materials. These consisted of isolated porosity, disbonded regions, and unmelted regions. The effects of such regions on the properties should be examined in future work where post-processing treatments (e.g. heat treatment, HIP, etc) could be used to reduce/eliminate these defects. Optimization of the initial processing conditions (e.g. control of the melt pool size) may also eliminate such features. This will enable a closer examination of microstructure-dependent properties.

Acknowledgements

This work was supported by America Makes, the National Additive Manufacturing Innovation Institute, through contract No. FA8650-12-2-7230 and is highly appreciated. Additional support was provided by an ASTM Scholarship (M. Seifi) and the Armington Professorship (J.J. Lewandowski). Various discussions with academic team members as well as industrial partners and government labs during monthly webinars are appreciated. These include four other university partners (NCSU, CMU, UofL and WSU), five industrial partners (Lockheed Martin, Pratt & Whitney, GE, Kennametal and Bayer) and two government labs (Oak Ridge National Lab and NIST). Various discussions with ASTM F42 and E08 committee members as well as Ulf Ackelid of Arcam AB are also appreciated as is access to equipment in the Advanced Manufacturing and Mechanical Reliability Center (AMMRC) at CWRU. Part of optical microscopy performed at Struers with the special help of Judy Arner and is appreciated.

References

- [1] M. Seifi, M. Dahir, R. Aman, O. Harrysson, J. Beuth, and J. J. Lewandowski, “Evaluation of Orientation Dependence of Fracture Toughness and Fatigue Crack Propagation Behavior of As-Deposited ARCAM EBM Ti-6Al-4V,” *JOM*, vol. 67, no. 3, pp. 597–607, 2015.
- [2] ASTM WK49229, “New Guide for Anisotropy Effects in Mechanical Properties of AM Parts.” ASTM International, West Conshohocken, PA, 2015.
- [3] M. Svensson, U. Ackelid, and A. Ab, “Titanium Alloys Manufactured with Electron Beam Melting Mechanical and Chemical Properties,” in *Proceedings of Materials & Processes for Medical Devices Conference*, 2010, p. p 189–194.
- [4] U. Ackelid and M. Svensson, “Additive Manufacturing of Dense Metal Parts by Electron Beam Melting,” in *Proceedings of Materials Science and Technology Conference (MS&T)*, 2009, pp. 2711–2719.
- [5] P. Edwards and M. Ramulu, “Effect of build direction on the fracture toughness and fatigue crack growth in selective laser melted Ti-6Al-4 V,” *Fatigue Fract. Eng. Mater. Struct.*, p. n/a-n/a, 2015.

- [6] V. Cain, L. Thijs, J. Van Humbeeck, B. Van Hooreweder, and R. Knutsen, “Crack propagation and fracture toughness of Ti6Al4V alloy produced by selective laser melting,” *Addit. Manuf.*, pp. 54–55, 2015.
- [7] P. Edwards and M. Ramulu, “Fatigue performance evaluation of selective laser melted Ti–6Al–4V,” *Mater. Sci. Eng. A*, vol. 598, pp. 327–337, Mar. 2014.
- [8] P. Edwards, A. O’Conner, and M. Ramulu, “Electron Beam Additive Manufacturing of Titanium Components: Properties and Performance,” *J. Manuf. Sci. Eng.*, vol. 135, no. 6, p. 61016, 2013.
- [9] J. Gockel, J. Fox, J. Beuth, and R. Hafley, “Integrated melt pool and microstructure control for Ti–6Al–4V thin wall additive manufacturing,” *Mater. Sci. Technol.*, vol. 31, no. 8, pp. 912–916, 2015.
- [10] J. Beuth, J. Fox, J. Gockel, C. Montgomery, R. Yang, H. Qiao, P. Reesewatt, A. Anvari, S. Narra, and N. Klingbeil, “Process Mapping for Qualification Across Multiple Direct Metal Additive Manufacturing Processes,” in *Solid Freeform Fabrication Proceedings*, 2013, pp. 655–665.
- [11] J. Gockel and J. Beuth, “Understanding Ti-6Al-4V Microstructure Control in Additive Manufacturing via Process Maps,” in *Solid Freeform Fabrication Proceedings*, 2013, pp. 666–674.
- [12] E. Soylemez, J. L. Beuth, and K. Taminger, “Controlling Melt Pool Dimensions over a Wide Range of Material Deposition Rates in Electron Beam Additive Manufacturing,” *Proc. 2010 Solid Free. Fabr. Symp.*, no. August, pp. 571–582, 2010.
- [13] R. Ding, Z. X. Guo, and A. Wilson, “Microstructural evolution of a Ti–6Al–4V alloy during thermomechanical processing,” *Mater. Sci. Eng. A*, vol. 327, no. 2, pp. 233–245, Apr. 2002.
- [14] ASTM Standard E399, “Standard Test Method for Linear-Elastic Plane-Strain Fracture Toughness KIC of Metallic Materials,” in *ASTM Book of Standards*, West Conshohocken, PA: ASTM International, 2012.
- [15] ASTM Standard E647, “Standard Test Method for Measurement of Fatigue Crack Growth Rates,” in *ASTM Book of Standards*, West Conshohocken, PA: ASTM International, 2013.
- [16] C. A. Stubbington and A. W. Bowen, “Improvements in the fatigue strength of Ti-6Al-4V through microstructure control,” *J. Mater. Sci.*, vol. 9, pp. 941–947, 1974.
- [17] M. Peters, A. Gysler, and G. Lotjering, “Influence of Texture on Fatigue Properties of Ti-6Al-4V,” vol. 15A, no. August, pp. 1597–1605, 1984.
- [18] R. K. Nalla, B. L. Boyce, J. P. Campbell, J. O. Peters, and R. O. Ritchie, “Influence of Microstructure on High-Cycle Fatigue of Ti-6Al-4V : Bimodal vs . Lamellar Structures,” *Metall. Mater. Trans. A*, vol. 33A, no. March, 2002.
- [19] M. S. Dahar, S. M. Seifi, B. P. Bewlay, and J. J. Lewandowski, “Effects of test orientation on fracture and fatigue crack growth behavior of third generation as-cast Ti–48Al–2Nb–2Cr,” *Intermetallics*, vol. 57, pp. 73–82, Feb. 2015.



**PROCEEDINGS OF THE 13TH
WORLD CONFERENCE ON TITANIUM**

**Additive and Near Net Shape
Manufacturing I**

MICROSTRUCTURE AND MECHANICAL PROPERTIES OF Ti-48Al-2Cr-2Nb MANUFACTURED VIA ELECTRON BEAM MELTING

Mohsen Seifi¹, Iman Ghamarian², Peyman Samimi², Ulf Ackelid³, Peter Collins² and John Lewandowski¹

¹ Department of Materials Science and Engineering Case Western Reserve University, Cleveland, OH 44106, USA

² Department of Materials Science and Engineering, University of North Texas, Denton, TX 76203, USA

³ Arcam AB, Molndal; SE-431 37, Sweden

Abstract

Titanium aluminide (TiAl) alloys have been studied for many years with the intent to replace heavier Ni-based superalloys currently used in aerospace structural parts. Various additive manufacturing techniques are being explored to produce near net shape components of TiAl and other materials. Due to the multiple cycles of heating and cooling at different rates, a complex microstructure evolution and resulting mechanical response is expected for materials made by these techniques. In this work, the microstructure of as-deposited Ti-48Al-2Cr-2Nb was documented at different length scales in addition to evaluating the fracture toughness and fatigue crack growth behavior.

Keywords: Additive Manufacturing, Gamma Titanium aluminide alloy, Ti-48Al-2Cr-2Nb, Electron beam melting, microstructure evolution, fracture toughness, fatigue crack growth

Introduction

Gamma titanium aluminides (γ -TiAl) have been recognized as suitable materials for aerospace and automotive applications due to their low density and high strength at elevated temperatures, particularly in the context of replacing the heavier, nickel-based superalloys [1]–[6]. A recent example includes cast Ti-48Al-2Cr-2Nb blades which have been certified and implemented recently in GE commercial turbofan engines [7]–[9]. However, the casting of γ -TiAl alloys has some processing complications in addition to machining difficulties that arise from the low ductility inherent with many intermetallic phases. The limited number of slip systems in γ -TiAl can also produce relatively low fracture toughness [10].

TiAl alloys considered for structural applications typically contain two main phases, γ -TiAl as the base and α_2 -Ti₃Al distributed in different ways depending on the type of processing/heat treatment. A number of different freeform fabrication techniques have been recently used to produce TiAl structures to near net shape. One such approach involves using laser-based techniques to melt pre-alloyed powders to produce TiAl components [10] while more recent approaches use electron beam melting (EBM) via techniques developed by Arcam AB [11]–[13]. EBM allows the production of complex shaped metallic components from a precursor powder [12] and the deposition rate is higher in comparison to laser-based techniques. However, EBM requires processing with a high vacuum environment that can produce preferential vaporization of certain alloying elements. Despite these complications, EBM is being explored to produce complex, near net shape γ -TiAl parts with short lead times for various applications [11], [14]–[19]. EBM is also being used for other Titanium alloys (e.g. Ti-6Al-4V) and

previous work has documented location- and orientation-dependent microstructure/property combinations [20]–[23].

The EBM technology uses a computer-aided design (CAD) file as a tool path for layer-by-layer fabrication of the 3D components. Due to the nature of the process and rapid directional solidification of the localized melt pool, the microstructure and resulting mechanical properties may differ substantially from those obtained with conventional processing techniques.

To date, relatively few works have investigated the fracture and fatigue behavior of EBM γ -TiAl alloys. Patriarca [24] suggested that one advantage of EBM processing of γ -TiAl relates to the potential of avoiding/minimizing defects typically present in cast or powder metallurgy (PM) techniques, resulting in higher fatigue threshold and fatigue strength in comparison to competing technologies. Due to its limited ductility/toughness, Patriarca [24] utilized compression fatigue pre-cracking at constant amplitude in order to obtain fatigue crack growth data on EBM-processed materials.

In the present work, the microstructure of a EBM TiAl both in as-deposited and HIPed condition was characterized, followed by the determination of fracture toughness, hardness and fatigue crack growth behavior.

Materials and Methods

An Arcam™ EBM machine, model A2X, was used to produce 15 mm diameter \times 75 mm length multi-layer circular rods using ARCAM pedigree gas-atomized (from the pre-alloyed melt) Ti-48Al-2Cr-2Nb spherical powders with an average particle size of 45–150 μm . A standard Arcam™ EBM raster strategy operated at 1050 °C process temperature was used to deposit the bars. The as-deposited specimens and the subsequently machined samples with 10 mm \times 10 mm cross-section are shown in Fig. 1(a) and Fig. 1(b), respectively. All mechanical tests were conducted on the as-deposited material while post processing effects (e.g. heat treatment, HIP, etc.) are reported elsewhere [13].

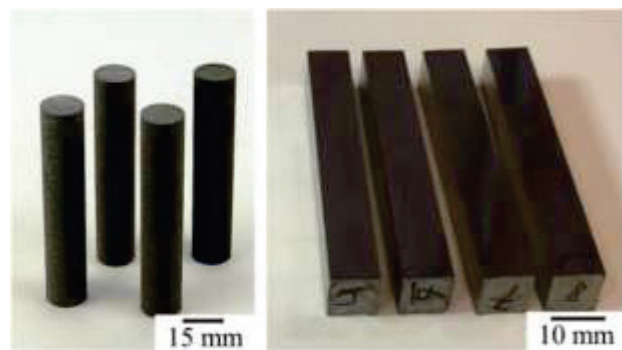


Figure 1. a) The as-built specimens and b) the machined specimens.

Detailed microstructure characterization was conducted midway from the start to the end of the build on one of the as-deposited rods shown in Figure 1, initially using Robo-Met.3D to prepare a sample for optical microscopy. The sample was polished and then etched with concentrated Kroll's reagent that contained 2 vol.% HF, 6 vol.% HNO₃ and 92 vol.% distilled water. Multiple optical micrographs were stitched together using Photoshop software in order to create a montage.

The metallographic sample was subsequently polished using MultiPrep™ system (Allied, CA) to remove the previously etched material in order to prepare a well-polished sample for further scanning electron microscopy (SEM) analyses. SEM studies were conducted on an FEI Nova 230 NanoSEM field emission gun equipped with electron-backscattered detector operate at 15 keV. One thin foil was prepared using dual-beam focused ion beam (FIB) on an FEI Nova Nanolab 200 system for subsequent transmission electron microscopy (TEM) studies. TEM examination was conducted on an FEI Tecnai G2 F20 S-Twin field emission gun scanning/transmission electron microscope operated at 200 kV in order to characterize the phases present in the as-deposited material. Fracture toughness testing was performed in three-point bending using 10 mm x 10 mm x 75 mm single edge notch (SEN) specimens, Figure 1b, machined from the as-deposited cylinders in Figure 1a. Tests were conducted on a Model 810 MTS servo-hydraulic machine in general accordance with ASTM E399 [25]. An attempt was also made to obtain fatigue crack growth data according to ASTM E647 [26]. In both cases, the specimens were first notched using a slow speed diamond wire saw to introduce a notch with root radius of about 100 µm. Fatigue crack growth was monitored using DCPD technique following crack initiation at low ΔK using constant cyclic loading with incremental elevation in cyclic load until crack growth was initiated. Paris slope, ΔK_{th} , and K_{max} at failure were recorded and compared with data in the literature.

Results and Discussion

The as-deposited material contained a limited number of micro-cracks as shown by the arrows in the optical micrograph shown in Fig. 2. Although these will be detrimental to the mechanical properties, it has been shown that HIPping can be used to remove such defects [11], [16]. Equally important for the resulting properties of the as-deposited material relates to the scale of the microstructure. Previous studies [27] have shown that the typical grain size for as-cast γ -TiAl is on the order of 1 mm. In contrast, the EBM as-deposited material presented in Fig. 2 exhibits an average grain size of only 25 µm. This significant microstructure refinement is partly responsible for the elevated hardness/strength reported in such materials [11], [16]. SEM examination of as-polished samples similarly revealed the presence of isolated micro-cracks, Fig. 3. The micro-cracks were often, but not always, present at grain boundaries in the as-deposited material. In order to obtain a broader view of the microstructure, twenty-five high-resolution optical images were additionally captured using Robo-Met.3D. These images were stitched together to form a montage and are presented in Fig. 4. Interestingly, the scale of the microstructure is spatially inhomogeneous. For example, in some areas (i.e. those surrounded by green color in Fig. 4) the microstructure is relatively coarse compared to adjacent areas (e.g. areas surrounded by red lines).

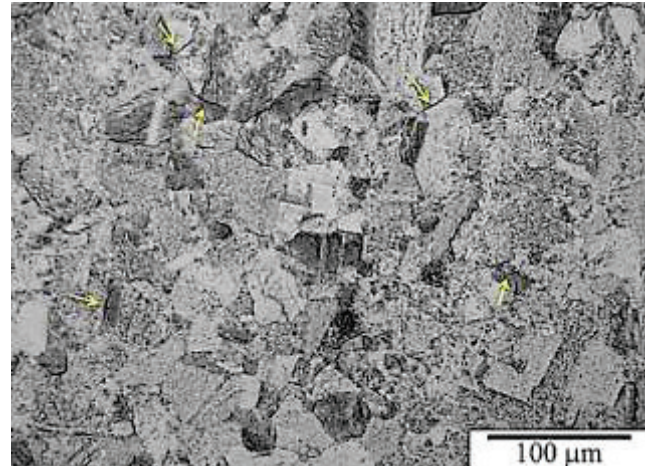


Figure 2. Optical micrograph taken at the center of the cross section of the as-deposited material reveals refined grain size and some isolated micro-cracks (arrowed). Kroll's etch.

This inhomogeneity likely results from the complex temperature profile experienced during multi-layer deposition that produces different and locally varying cooling rates. This variation in the microstructure feature size will also produce spatially varying mechanical properties.

The fine grain size exhibited in the as-deposited EBM material is unique and much finer than that obtained via other commercial manufacturing techniques. Cast materials can exhibit grain sizes in the range 1000 ± 140 µm [27] while wrought materials have been reported to exhibit grain sizes around 300 µm [28]. The as-deposited EBM material in this study exhibits a grain size range of about 10-40 µm for the coarsest part of the microstructure shown in Figure 2, with far smaller grain sizes in other regions (e.g. 10 µm). Other work conducted on HIP'ped material revealed an average grain size of around 11 µm for fine grained regions and average grain size of around 50 µm for larger grained regions [16].

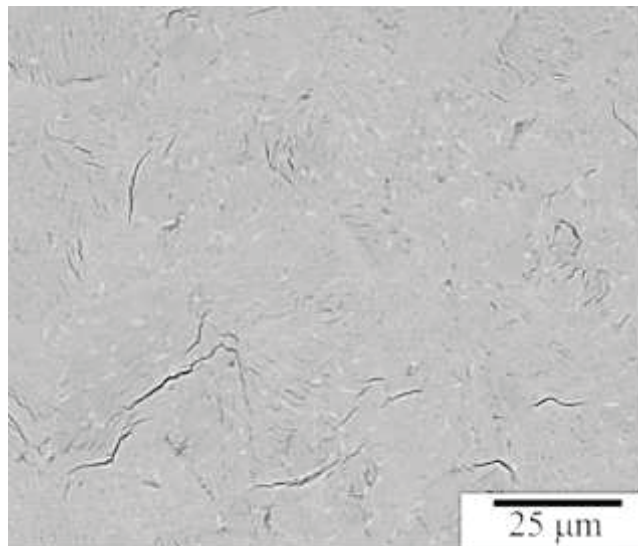


Figure 3. SEM image of as-deposited material illustrating many isolated micro-cracks. Unetched.

In order to further investigate the microstructure in the as-deposited material, a TEM foil was prepared from an area in which the microstructure was very fine. The STEM image in Fig. 5(a) reveals a lamellar microstructure within a few micrometer-sized large grains. Electron dispersive spectroscopy (EDS) was used to identify the phases present. The first EDS line profile scan was conducted along the vector labeled ‘b’ in Fig. 5(a). The composition profile of this scan is plotted in Fig. 5(b). Based on the chemistry of the phases, it appears that α_2 laths (Ti₃Al) formed within the γ matrix (TiAl). It is important to note that the slight deviation of the composition profile from the stoichiometric composition can be attributed to the accuracy of the measurement. It seems that α_2 phase can form either from the grain boundary or inside a grain.

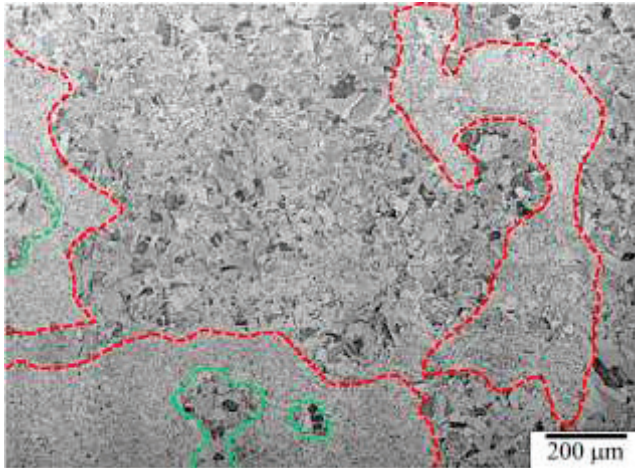


Figure 4. High-resolution optical image of a wide area located at the center of the as-deposited rod. The microstructure is very inhomogeneous with local variations in feature sizes. Kroll's etch.

The likely formation of α_2 phase from the grain boundary was confirmed by doing an EDS scan along the vector labeled c in Fig. 5(a). The composition profile of this line (Fig. 5(c)) reveals that the phase corresponding to the white feature is α_2 . Similar analyses revealed that the white feature that is surrounded by the green circle in Fig. 5(a) is α_2 .

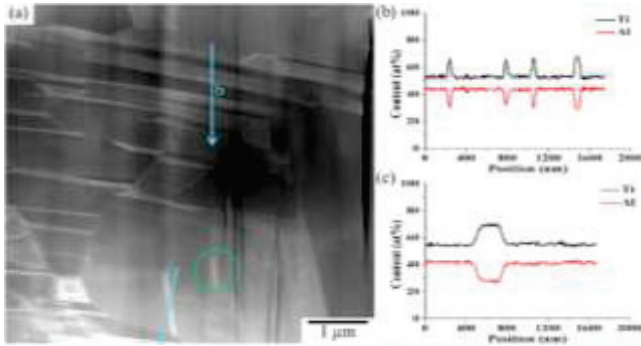


Figure 5. (a) STEM image (b) composition profile along vector ‘b’ and (c) composition profile along vector ‘c’.

While the detailed effects of HIPping have been reported elsewhere [13], HIPping at 1200°C for 4 hours at 100 MPa somewhat reduced the microstructure inhomogeneity in addition to producing slight grain growth, Fig. 6.

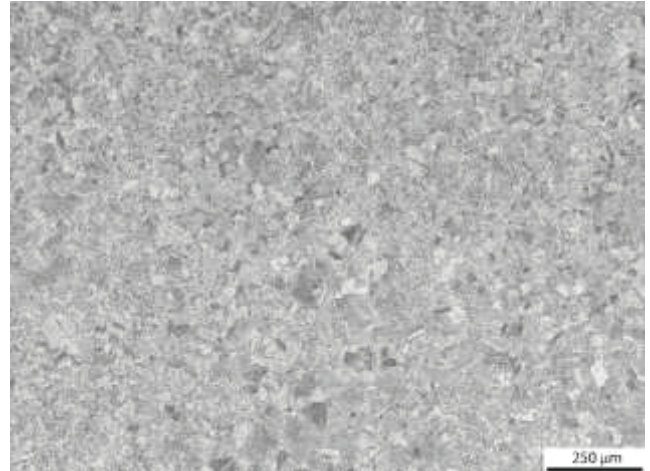


Figure 6. High-resolution optical image of a wide area located at the center of the HIPped rod. Much lower inhomogeneity observed.

Notched toughness results and the compressive strength values for the present alloy are summarized in Table 1. The notched toughness values are in the range of 26 to 28 MPa/m and are comparable with as-cast notched toughness properties reported previously [27]. Rockwell C hardness values are around 30 and slightly higher than the as-cast hardness, which was Rockwell C 24, consistent with the microstructure refinement in the as-deposited EBM material. The current work has only evaluated the notched toughness at the midpoint of the build (i.e. midway between the start and end of the build). Other work [13] reports the variation in toughness with respect to the build location (e.g. near the start of the build vs. near the end of the build).

Table 1: Summary of fracture toughness/hardness results

Specimen Condition	Notch Root Radius (μm)	Thickness, B (mm)	Notched Toughness K_q (MPa/m)	Rockwell C	Strength (MPa)
As-built	100	10	26,27,29	30±1	750
As Cast (LT) [27]	100	7.5	25	24±2	NA
As Cast (TL) [27]	100	9.5	24	NA	NA

Representative SEM fracture surface images of the as-deposited materials are provided in Fig. 7. In general, a faceted appearance is evident with isolated regions of local plasticity in some regions (Fig. 7 (a), (b)). Also evident are regions of porosity that are in the range of the powder size. Some of this porosity can be healed during HIPping as shown in other works [11], [13], [16].

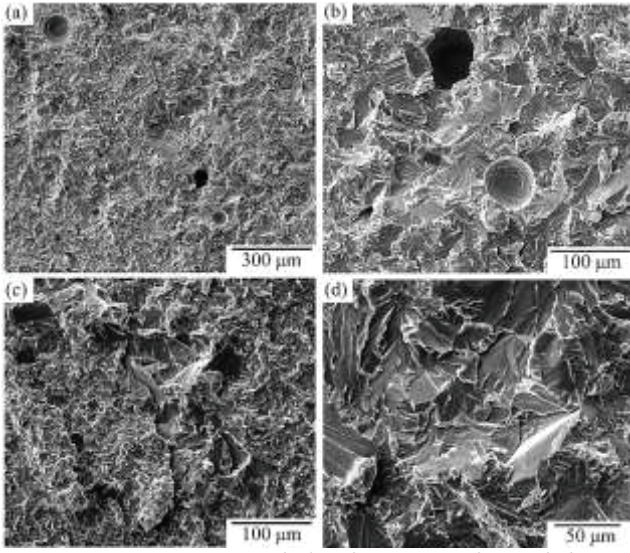


Figure 7. SEM images of the fracture surface of fracture toughness sample.

Scanning laser confocal microscopy was also conducted on the fracture surfaces in order to determine the level of fracture surface roughness. Fig. 8 provides a topographic map of a 1.2 mm by 1.2 mm region of the fracture surface and reveals a relatively flat fracture surface with limited tortuosity, likely a result of fracture through the very fine grains. The resulting scale of the fracture surface roughness is on the order of 50 μm and much less than that of the as-cast material [27] where surface roughness in excess of 1 mm was measured using a similar technique.

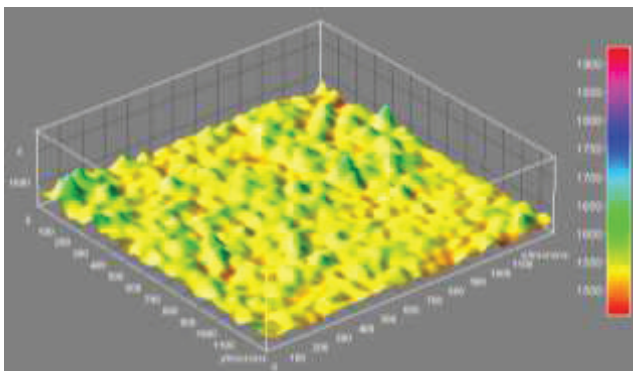


Figure 8. Scanning Laser Confocal Microscopy of a random 1.2 mm x 1.2 mm region on the fracture surface showing minimal surface roughness.

Representative fatigue crack growth data (da/dN vs. ΔK) is shown in Fig. 9. The lack of ductility and limited crack path tortuosity in the as-deposited condition produced rapid fatigue crack growth once the crack started to grow, producing a very high Paris slope and catastrophic fracture soon after crack initiation. Very similar observations were reported by Patriarca [24] on a similar alloy system, but after pre-oxidation at 650 °C for 20 hours. Those results [24] along with the current results are listed in Table 2. In the present work, separate fatigue crack growth measurements were made in regions close to the ‘start’ and ‘end’ of the build. While high ΔK threshold values were obtained in the as-deposited material, the very rapid crack growth

produced catastrophic fracture soon after crack initiation. The K_{\max} at failure was 13.2–13.9 MPa $\sqrt{\text{m}}$, somewhat lower than the notched toughness values, as expected.

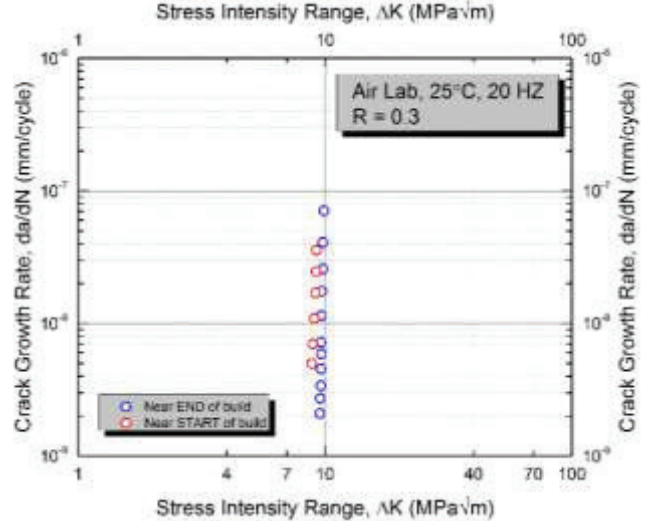


Figure 9. Fatigue Crack Growth curve showing very steep Paris slope.

Table 2. Summary of Fatigue Crack Growth Data

Specimen Condition	Load Ratio, R	Threshold, ΔK_{th} (MPa $\sqrt{\text{m}}$)	Paris Slope, m	K_{\max} , (MPa $\sqrt{\text{m}}$)
As-deposited (Near START of build)	0.3	8	42	13.2
As-deposited (Near END of build)	0.3	9	105	13.9
Pre-oxidized [24]	0.05	6	15	10.8
Pre-oxidized [24]	0.6	3	40	11.5
As-Cast (LT) [27]	0.3	8	23	18.3
As-Cast (TL) [27]	0.3	9	34	20.4

Conclusions

Electron Beam Melting is an additive manufacturing technique capable of producing complex metal parts from metal powders. EBM processing of γ -TiAl may overcome some processing issues inherent in conventional techniques.

Microstructure characterization, fracture toughness testing, and fatigue crack growth behavior of the as-deposited EBM γ -TiAl were conducted in the present work. The following was found on the as-deposited material:

1. The as-deposited material exhibited numerous isolated micro-cracks at various regions throughout the build. Fracture surface examinations of the failed samples also revealed regions of isolated porosity.
2. The as-deposited material exhibited a very fine grain size and microstructure inhomogeneity.
3. The fracture surfaces showed limited plasticity and roughness along with isolated porosity. Fracture

- toughness values were in the range of those reported for as-cast material.
4. The fatigue crack growth behavior revealed relatively high fatigue threshold. However, rapid crack growth produced very high values for Paris slope and catastrophic fracture soon after fracture initiation.
- More work is needed to investigate the effects of post-processing on these alloys (e.g. heat treatment, hot isostatic pressing, etc.) as well as location-specific fracture properties (e.g. near START, near END of build) as well as their orientation dependence.
- Acknowledgments**
- This work was partially supported by the Arthur P Armington Professorship (JYL) and conducted in the Advanced Manufacturing and Mechanical Reliability Center (AMMRC) at CWRU. The authors also gratefully acknowledge the University of North Texas; the Center for Advanced Non-Ferrous Structural Alloys, which is a joint industry-university center between the Colorado School of Mines and the University of North Texas (NSF award no. 1134873) and the Center for Advanced Research and Testing at the University of North Texas.
- ### References
- [1] X. Wu, "Review of alloy and process development of TiAl alloys," *Intermetallics*, vol. 14, no. 10–11, pp. 1114–1122, Oct. 2006.
 - [2] Y.-W. Kim, "Intermetallic alloys based on gamma titanium aluminide," *JOM*, vol. 41, no. 7, pp. 24–30, 1989.
 - [3] P. Bartolotta, J. Barrett, T. Kelly, and R. Smashey, "The use of cast Ti–48Al–2Cr–2Nb in jet engines," *JOM*, vol. 49, no. 5, pp. 48–50, 1997.
 - [4] S. C. Huang and M. F. X. Gigliotti, "Chromium-Modified Titanium Aluminum Alloys and Method of Preparation." US Patent, 1989.
 - [5] F. Appel, J. D. H. Paul, and M. Oehring, *Gamma Titanium Aluminide Alloys Science and Technology*. Wiley-VCH Verlag, 2011.
 - [6] Y. W. Kim, W. Smarsly, J. Lin, D. M. Dimiduk, and F. Appel, Eds., *Gamma Titanium Aluminide Alloys*. Wiley, 2014.
 - [7] M. Thomas, "Processing and Characterization of TiAl-based Alloys : Towards an Industrial Scale," *J. Aerosp. Lab*, no. 3, pp. 1–11, 2011.
 - [8] M. J. Weimer and T. J. Kelly, "TiAl Alloy 48Al-2Nb-2Cr Material database and application status," in *3rd International Workshop on γ - TiAl technologies*, 2006, pp. 1–15.
 - [9] B. P. Bewlay, M. Weimer, T. Kelley, A. Suzuki, and P. R. Subramanian, "The science, technology, and implementation of TiAl alloys in commercial aircraft engines," in *MRS Symp. Intermetallic-Based Alloys-Science, Technology and Applications*, 2013, vol. 1516, pp. 49–58.
 - [10] D. Srivastava, "Microstructural characterization of the γ -TiAl alloy samples fabricated by direct laser fabrication rapid prototype technique," *Bull. Mater. Sci.*, vol. 25, no. 7, pp. 619–633, 2002.
 - [11] S. Sabbadini, O. Tassa, P. Gennaro, and U. Ackelid, "Additive Manufacturing of Gamma Titanium Aluminide Parts By Electron Beam Melting," in *TMS Proceedings (The Minerals, Metals & Materials Society)*, 2010, pp. 267–274.
 - [12] S. Biamino, A. Penna, U. Ackelid, S. Sabbadini, O. Tassa, P. Fino, M. Pavese, P. Gennaro, and C. Badini, "Electron beam melting of Ti–48Al–2Cr–2Nb alloy: Microstructure and mechanical properties investigation," *Intermetallics*, vol. 19, no. 6, pp. 776–781, Jun. 2011.
 - [13] M. Seifi, A. Salem, D. Satko, U. Ackelid, and J. J. Lewandowski, "Microstructural Inhomogeneity and Post Processing Effects on Mechanical Properties of Ti-48Al-2Cr-2Nb Manufactured by EBM Additive Manufacturing," *Intermetallics*, 2016.
 - [14] S. Biamino, B. Kloden, T. Weibgarber, B. Kieback, and U. Ackelid, "Titanium aluminides for automotive applications processed by electron beam melting," in *MPIF*, 2014, pp. 96–103.
 - [15] D. Cormier, O. Harrysson, T. Mahale, and H. West, "Freeform Fabrication of Titanium Aluminide via Electron Beam Melting Using Prealloyed and Blended Powders," *Res. Lett. Mater. Sci.*, vol. 2007, pp. 1–4, 2007.
 - [16] S. F. Franzen, J. Karlsson, R. Dehoff, U. Ackelid, O. Rios, C. Parish, and W. Peters, "Microstructural Properties of Gamma Titanium Aluminide Manufactured by Electron Beam Melting," in *TMS Proceedings (The Minerals, Metals & Materials Society)*, 2011, pp. 455–462.
 - [17] M. Filippini, S. Beretta, L. Patriarca, and S. Sabbadini, "Effect of the Microstructure on the Deformation and Fatigue Damage in a Gamma TiAl Produced by Additive Manufacturing," in *TMS Proceedings (The Minerals, Metals & Materials Society)*, 2014, pp. 189–193.
 - [18] M. Filippini, S. Beretta, C. Içöz, and L. Patriarca, "Effect of the Microstructure on the Fatigue Strength of a TiAl Intermetallic Alloy Produced by Additive Manufacturing," in *Mater. Res. Soc. Symp. Proc.*, 2015, vol. 1, pp. 3–8.
 - [19] J. Porter, J. Wooten, O. Harrysson, and K. Knowlson, "Digital manufacturing of gamma-TiAl by electron beam melting," *Mater. Sci. Technol. Conf.*, pp. 1434–1441, 2011.
 - [20] M. Seifi, M. Dahar, R. Aman, O. Harrysson, J. Beuth, and J. J. Lewandowski, "Evaluation of Orientation Dependence of Fracture Toughness and Fatigue Crack Propagation Behavior of As-Deposited ARCAM EBM Ti-6Al-4V," *JOM*, vol. 67, no. 3, pp. 597–607, 2015.
 - [21] M. Seifi, A. Salem, J. Beuth, O. Harrysson, and J. J. Lewandowski, "Overview of Materials Qualification Needs for Metal Additive Manufacturing," *JOM*, vol. 68, no. 3, pp. 747–764, 2016.

- [22] J. J. Lewandowski and M. Seifi, "Metal Additive Manufacturing: A Review of Mechanical Properties," *Annu. Rev. Mater. Res.*, vol. 46, 2016.
- [23] M. Seifi, D. Christiansen, J. L. Beuth, O. Harrysson, and J. J. Lewandowski, "Process Mapping, Fracture and Fatigue Behavior of Ti-6Al-4V Produced by EBM Additive Manufacturing," in *Ti-2015: The 13th World Conference on Titanium*, 2016.
- [24] L. Patriarca, "Fatigue crack growth of a gamma titanium aluminide alloy," in *9th Youth Symposium on Experimental Solid Mechanics*, 2010, pp. 36–39.
- [25] ASTM Standard E399, "Standard Test Method for Linear-Elastic Plane-Strain Fracture Toughness KIC of Metallic Materials," in *ASTM Book of Standards*, West Conshohocken, PA: ASTM International, 2012.
- [26] ASTM Standard E647, "Standard Test Method for Measurement of Fatigue Crack Growth Rates," in *ASTM Book of Standards*, West Conshohocken, PA: ASTM International, 2013.
- [27] M. S. Dahar, S. M. Seifi, B. P. Bewlay, and J. J. Lewandowski, "Effects of test orientation on fracture and fatigue crack growth behavior of third generation as-cast Ti-48Al-2Nb-2Cr," *Intermetallics*, vol. 57, no. 2, pp. 73–82, 2015.
- [28] J. H. Westbrook and R. L. Fleischer, *Intermetallic Compounds Principles and Practice*. John Wiley & Sons, Ltd, 1995.

Microstructures and Mechanical Properties of Ti6Al4V Parts Fabricated by Selective Laser Melting and Electron Beam Melting

H.K. Rafi, N.V. Karthik, Haijun Gong, Thomas L. Starr, and Brent E. Stucker

(Submitted March 1, 2013; in revised form May 23, 2013; published online August 6, 2013)

This work compares two metal additive manufacturing processes, selective laser melting (SLM) and electron beam melting (EBM), based on microstructural and mechanical property evaluation of Ti6Al4V parts produced by these two processes. Tensile and fatigue bars conforming to ASTM standards were fabricated using Ti6Al4V ELI grade material. Microstructural evolution was studied using optical and scanning electron microscopy. Tensile and fatigue tests were carried out to understand mechanical properties and to correlate them with the corresponding microstructure. The results show differences in microstructural evolution between SLM and EBM processed Ti6Al4V and their influence on mechanical properties. The microstructure of SLM processed parts were composed of an α' martensitic phase, whereas the EBM processed parts contain primarily α and a small amount of β phase. Consequently, there are differences in tensile and fatigue properties between SLM- and EBM-produced Ti6Al4V parts. The differences are related to the cooling rates experienced as a consequence of the processing conditions associated with SLM and EBM processes.

Keywords EBM, fatigue testing, microstructure, SLM, tensile testing

1. Introduction

Selective laser melting (SLM) and electron beam melting (EBM) are two powder-bed fusion-based additive manufacturing processes used to fabricate metallic parts (Ref 1, 2). These processes are of interest due to several advantages over conventional manufacturing methods. Freedom to fabricate intricate geometries, optimum material usage, elimination of expensive tooling etc. are some of the notable advantages of additive manufacturing processes. In these processes the CAD model of the part is fed to the machine where pre-processing software slices the model into layers of finite thickness. A powder layer is deposited on to a base plate above the build platform. A focused laser/electron beam scans the powder-bed-based on the sliced CAD data. The scanning results in localized melting and solidification of the powder to form a layer of the part. Subsequent layers are built one over the other by lowering the build platform equivalent to the layer thickness until the part is completed.

Selective laser melting utilizes a fiber laser heat source. The four main parameters in SLM are laser power, scan speed, hatch spacing, and layer thickness. Generally, the process is

characterized by high scanning speeds and high thermal gradients, leading to high cooling rates. High cooling rates result in non-equilibrium microstructures which may require heat treatment for certain applications. The SLM build chamber is continuously flushed with inert gas to reduce oxygen level. Typical layer thickness lies in the range of 20–100 μm . SLM is capable of processing standard materials like Ti6Al4V, 316L, 17-4PH, 15-5PH, hot work steels, cobalt-based and nickel-based alloys (Ref 3) and more. A description of SLM processes has been detailed elsewhere (Ref 4).

Arcam EBM technology uses an electron beam to melt powder layer. Electron beam-powder interactions are substantially different than laser-powder interactions. The penetration depth of an electron beam into the irradiated material is multiple times greater than it is with a laser beam (Ref 5). When the high speed electron beam interacts with the powder layer, kinetic energy is converted into thermal energy, causing the powder to melt. The build chamber is kept at an elevated temperature (approx. 700 °C) in a vacuum environment. Elevated temperatures help minimize thermally induced residual stresses and the formation of non-equilibrium microstructures. The high intensity electron beam first preheats the powder at a very high scan speed, large focal spot, and low beam current. Preheating of the powder can help lower moisture content and thus reduce the possibility of oxygen pickup. More importantly preheating can reduce residual stress buildup by bringing down the temperature-gradient between successive layers during processing. The preheating stage is followed by a melting stage where the electron beam scans the powder at a lower scan speed, smaller spot size, and higher beam current. Once the build is completed the part is allowed to cool slowly from 700 °C to room temperature. Due to the higher beam intensities and scan available with electron beams, the EBM process is much faster than the SLM process. A description of EBM processes has been detailed elsewhere (Ref 6).

H.K. Rafi, N.V. Karthik, Haijun Gong, Thomas L. Starr, and Brent E. Stucker, Department of Industrial Engineering, JB Speed School of Engineering, University of Louisville, Louisville, KY 40292. Contact e-mails: khalidrafi@gmail.com and brent.stucker@louisville.edu.

Previous studies carried out by different researchers showed typical microstructures and related properties for SLM- and EBM-produced materials. Thijss et al. (Ref 7) studied the influence of process parameters and the scanning strategy on the microstructural evolution during SLM processing of Ti64. They observed the resulting microstructure as acicular martensite as a consequence of very high cooling rates. The microstructure was significantly affected by factors such as high localized heat inputs, very short interaction times, local heat transfer conditions, and processing conditions like scanning velocity, hatch spacing (the distance between two adjacent scan vectors), and scanning strategy. Facchini et al. also found SLM-produced Ti64 microstructures to be as completely martensitic. Song et al. (Ref 8) studied the effect of process parameters in terms of microstructure, densification, surface roughness, and microhardness for Ti64. They suggested a laser power of 110 W and scan speed of 0.4 m/s in a continuous melting mode to obtain a Ti64 part with maximum density. Other than the microstructural aspects, previous studies performed by Yadroitsev et al. (Ref 9), Morgan et al. (Ref 10), and Yasa et al. (Ref 11) have provided the details on the influence of substrate, energy input, laser pulsing, and laser irradiation parameters on process stability and dimensional accuracy of the final product.

Murr et al. (Ref 6) carried out characterization and comparison of Ti64 produced by EBM processing with wrought products. Microstructural characterization revealed acicular α and associated β microstructure. Prior β grains form

epitaxially and extend through many layers which is a direct consequence of the thermal gradient in the build direction (Ref 12). Facchini et al. (Ref 13) also showed a very fine and acicular morphology when Ti64 parts were produced using EBM.

Although the microstructural aspects of SLM-produced and EBM-produced samples have been studied, little attention has been paid to a comparison and contrast between these processes with respect to a given material. Therefore, this work is aimed at comparing SLM and EBM processes in terms of microstructure, tensile properties, and fatigue properties of Ti64.

2. Experimental Methods

Ti64 parts were produced using an EOS M270 SLM machine and an Arcam S400 EBM machine. Ti64 powder was procured from each respective machine manufacturer. Powder particle size was measured using a "Microtarc 3000" particle analyzer. The average particle size of the powder supplied by EOS was 36 μm and the powder supplied by Arcam was 60 μm . The particle size distribution and corresponding SEM-SE images of Arcam Ti64 powder and EOS Ti64 powder are shown in Fig. 1. Cylindrical specimens and specimens conforming to ASTM standards (ASTM: E8) for tensile testing and for fatigue testing (ASTM: E466) were fabricated. The as-built cylindrical specimens were analyzed for surface finish and

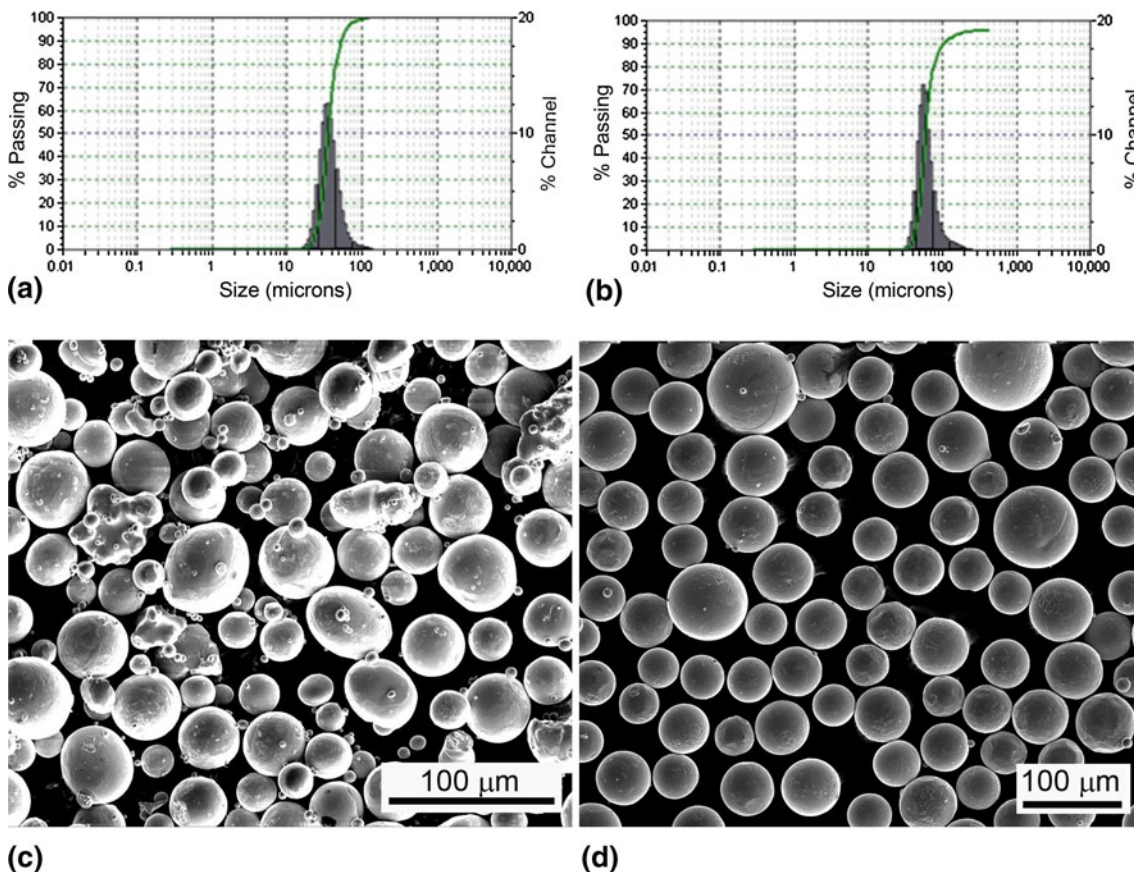


Fig. 1 (a) Powder size distribution of EOS supplied Ti64 powder (avg. particle size: 36 μm). (b) Powder size distribution of Arcam supplied Ti64 powder (avg. particle size: 60 μm). (c) SEM-SE image of EOS supplied Ti64 powder. (d) SEM-SE image of Arcam supplied Ti64 powder

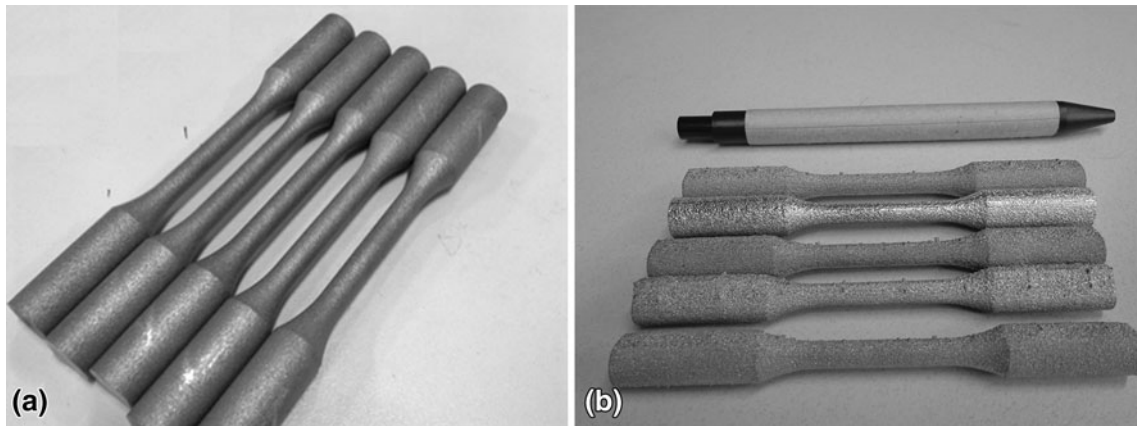


Fig. 2 (a) As-built tensile samples produced in SLM. (b) As-built tensile samples produced in EBM

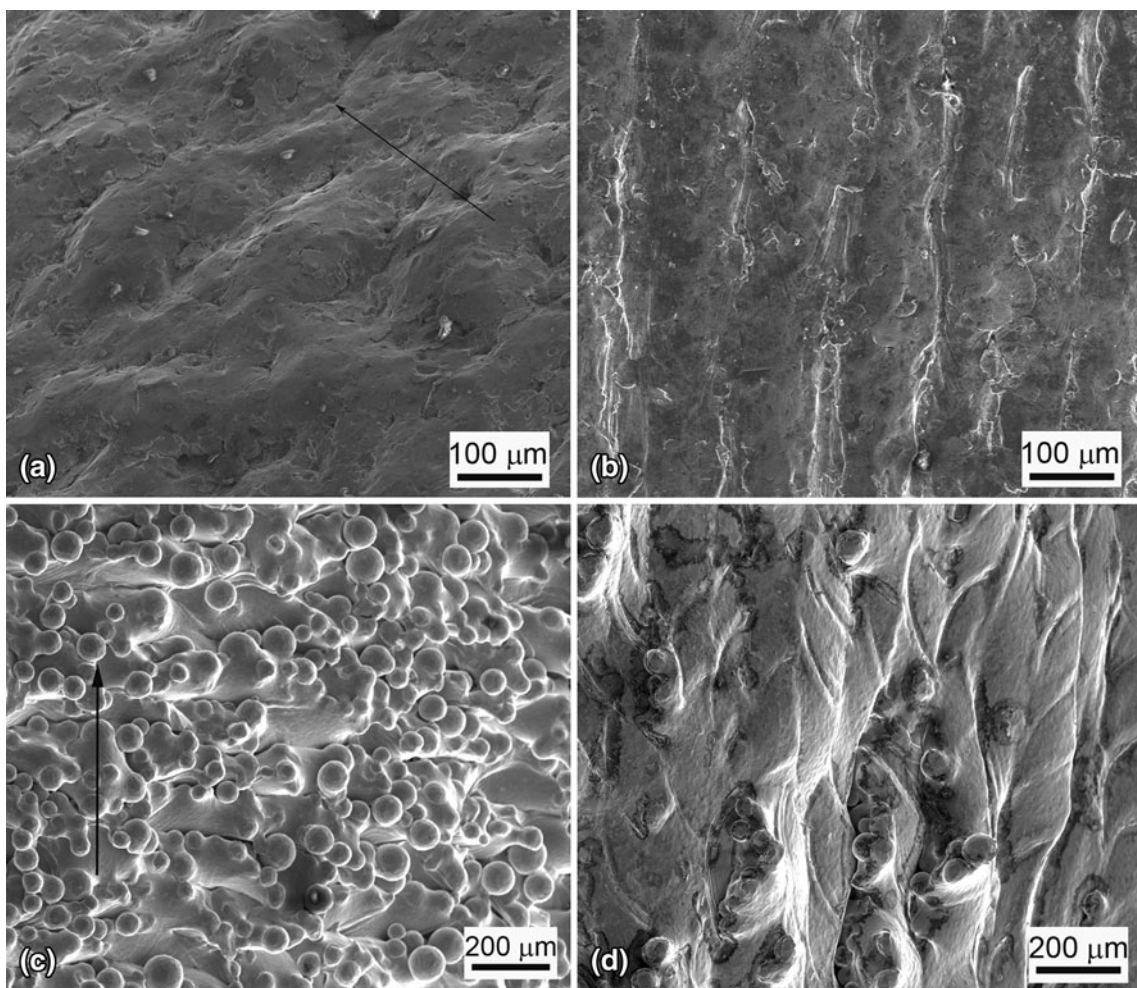


Fig. 3 (a) External surface of a vertically built SLM sample (arrow shows the build direction). (b) External surface of a horizontally built SLM sample (build direction is perpendicular to the image plane). (c) External surface of a vertically built EBM sample (arrow shows the build direction). (d) External surface of a horizontally built EBM sample (build direction is perpendicular to the image plane)

sectioned for metallographic characterization. Metallographic specimens were prepared following standard specimen preparation methods. Optical microscopy (OM) and scanning electron microscopy (SEM) were used for microstructural characterization. SEM-EDS (energy dispersive spectroscopy)

was carried out to compare any compositional differences which may have occurred due to differences in processes characteristics. OM was carried out on an Olympus optical microscope and SEM was carried out in FEI FEG-SEM. X-ray diffraction (XRD) was carried out to analyze the differences in

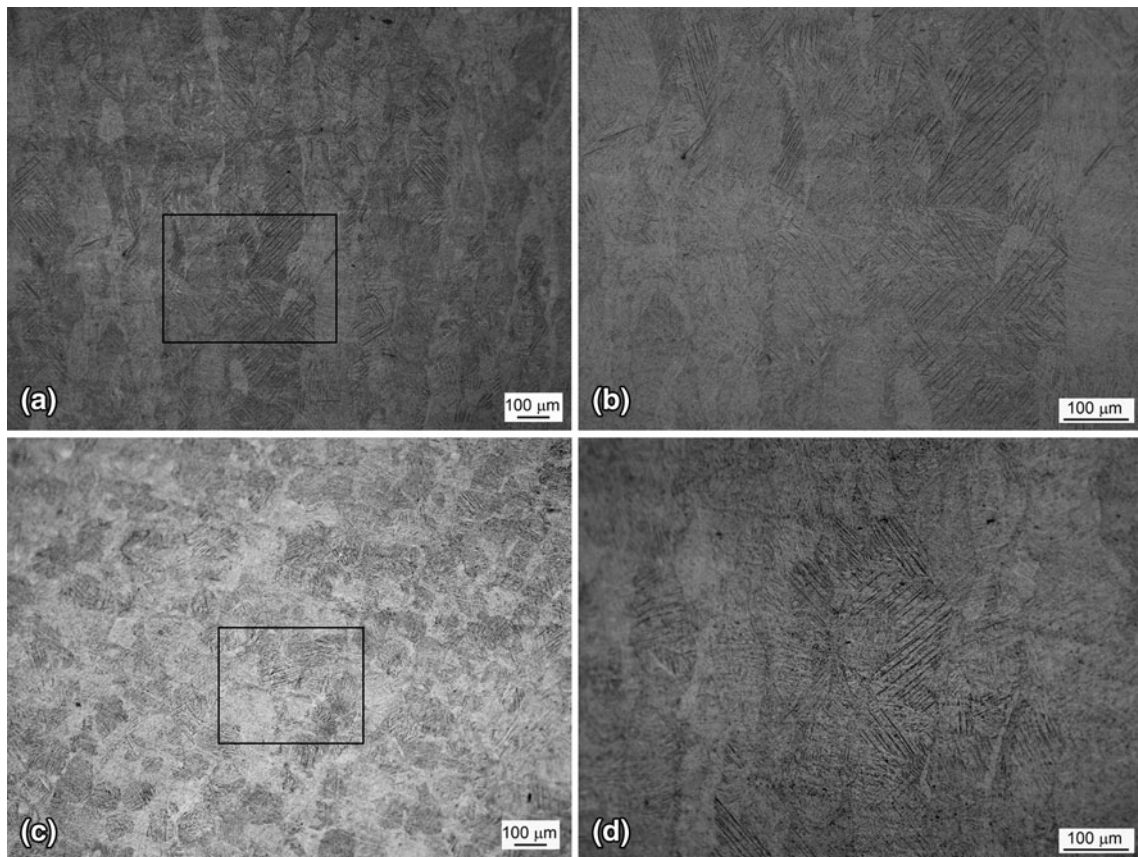


Fig. 4 Optical micrographs of SLM-produced Ti64 samples. (a) Longitudinal cross-section showing columnar grains. (b) High magnification longitudinal cross-section image showing fine α martensitic laths (from the boxed region in 'a'). (c) Transverse cross-section showing bundles of columnar grains. (d) High magnification transverse cross-section image showing fine α martensitic laths in a columnar grain (from the boxed region in 'c')

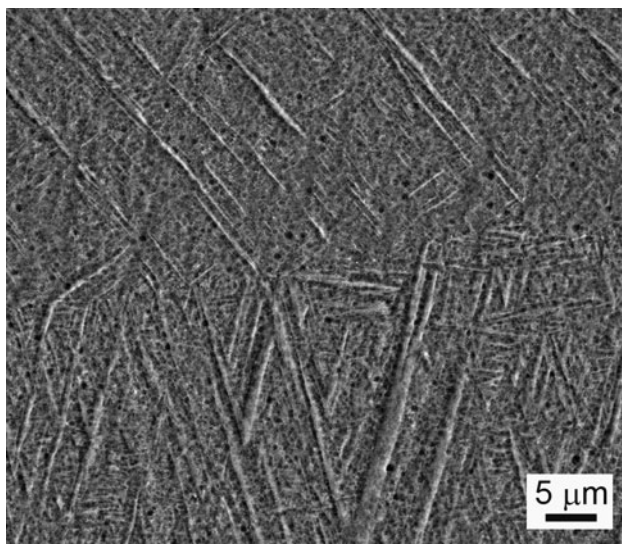


Fig. 5 SEM-SE image of SLM-produced Ti64 sample

phase composition. Tensile tests at room temperature were performed for samples built in both vertical and horizontal orientations using an Instron 50 kN tensile testing machine. Rockwell hardness testing was carried out using a Wilson Rockwell Hardness 3JR tester. High cycle fatigue tests at room temperature were performed on a 10 kN Instron Electropulse

10000 fatigue testing machine. Fatigue tests were performed at a stress ratio of $R = 0.1$ and a sinusoidal frequency of 50 Hz. Fatigue tests were stopped when specimens broke or the fatigue cycles reached 10^7 cycles.

3. Results and Discussions

3.1 Surface Characteristics

The external surfaces of the parts fabricated by SLM and EBM processes have different surface roughness because of the difference in scan speed, powder particle size, and layer thickness. Figure 2(a) and (b) shows as-built tensile samples produced by SLM and EBM, respectively. From the external appearance it is clear that there is a difference in the surface condition. Figure 2 shows magnified SEM images of the external surfaces of solid cylindrical specimens fabricated by SLM and EBM. The surfaces of parts fabricated by SLM are relatively smooth when compared to EBM fabricated parts. Figure 3(a) and (b) shows the external surfaces of vertical and horizontal SLM samples, respectively. The surfaces of vertically built samples are characterized by a wavy appearance without any discontinuity. For horizontally built cylindrical samples the curved surfaces are formed by consecutive steps. Figure 3(c) and (d) shows the external surface of EBM-produced samples in vertical and horizontal orientations,

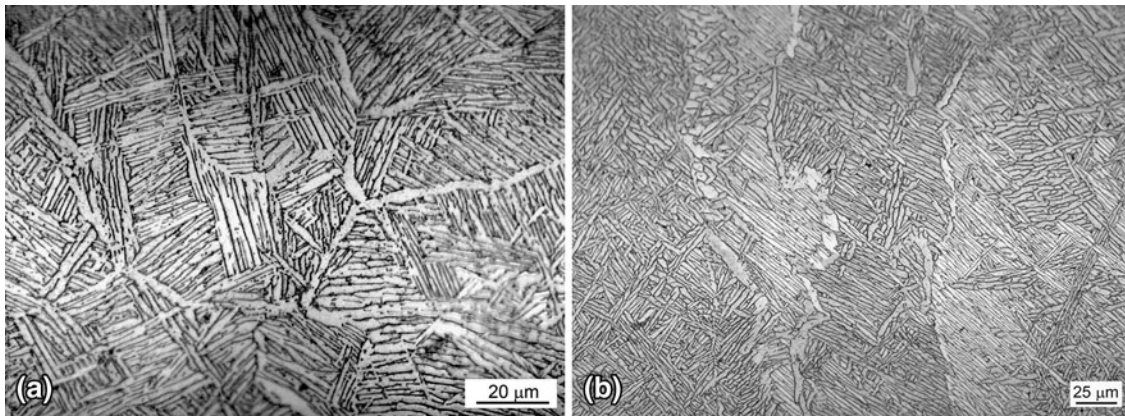


Fig. 6 Optical micrograph of EBM-produced Ti64 samples. (a) Transverse cross-section. (b) Longitudinal cross-section

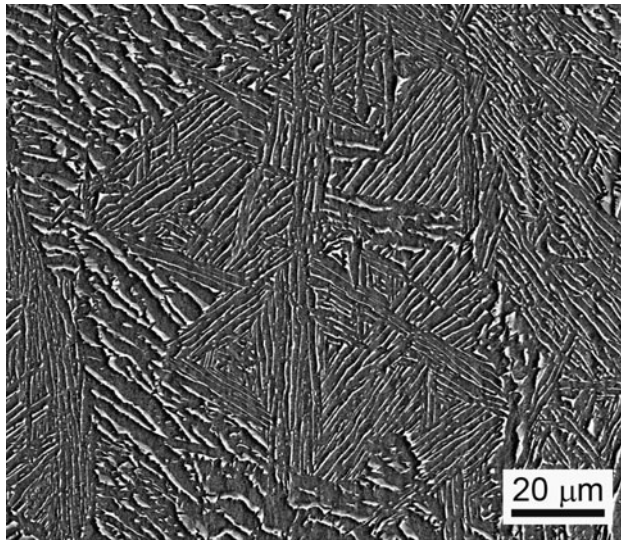


Fig. 7 SEM-SE image showing Widmanstatten structure in EBM-produced Ti64 sample

respectively. Partly melted powders sticking to the surface and gaps showing distinct layers are visible at the external surface of vertically built samples. Similar to SLM samples, the horizontally built EBM sample surfaces also showed overlapping layers forming steps on the curved external surface.

The smooth surfaces for SLM fabricated parts are present due to the thinner layers, slower scan speeds, and finer powder particle sizes. The scan speed in EBM is an order of magnitude higher when compared to the scan speed in SLM. This makes the EBM process faster at the expense of poor surface finish. Formation of relatively thicker layers (70 μm as compared to 30 μm in SLM process) in the EBM process cause a more pronounced “stairstep effect” which results in a greater surface roughness. Surface conditions can have a significant effect on mechanical properties, particularly for fatigue. For many applications the parts must be subjected to machining to obtain a desired surface finish.

3.2 Microstructure

Microstructural evolution is primarily a function of cooling rate. The materials processed in SLM and EBM undergo very

high cooling rates. Figure 4 shows the optical microstructure of SLM processed Ti64. SLM processing of Ti64 resulted in a complete martensitic (α) microstructure as expected (Ref 7). Martensitic laths originated from the prior β grain boundaries and fill the columnar grains. The morphology of lath martensite can be observed from the SEM-SE image shown in Fig. 5. The martensitic lath width is about 1-2 μm and the length is close to the width of the columnar grains.

The optical micrographs of EBM-produced Ti64 given in Fig. 6 show a completely different microstructure. The microstructure is mainly composed of an α phase and a small amount of β within the prior β columnar grains oriented along the build direction. The α phase posses a lamellar morphology with β surrounding the α lamellae boundary. The α lamellae are arranged in a Widmanstatten/basket weave structure with different sizes and orientations, and forms alpha platelet colonies within the columnar grains as can be seen in Fig. 7. This means that the SLM and EBM processes produce different microstructures at least for Ti64. However, in both cases prior β columnar grain boundaries are clearly visible. This implies that the primary mode of solidification still remains β , which is characteristic of Ti64 alloys irrespective of the process. Therefore the difference in microstructure is because of the differences in cooling rate when the β transforms to α as it cools through the transus temperature. Since the SLM process has cooling rates on the order of 10^6 K/s , this results in the transformation of α to α .

For EBM the build chamber is maintained at a temperature of 650-700 °C which is well above the M_s temperature for Ti64. Therefore, even though the cooling rates are higher at elevated temperatures, the material cools down to an isothermal temperature of 650-700 °C. This does not allow the transformation of α to α . After completion of the build, the slow cooling rates from 700 °C to room temperature within the build chamber result in the formation of α platelets. This means that there would be a corresponding difference in mechanical properties between SLM-processed and EBM-processed samples.

The microstructures of SLM- and EBM-produced Ti64 also differ from the microstructure of conventional wrought materials as shown in Fig. 8. The wrought Ti64 microstructure is composed of both α and β grains oriented in the rolling direction. The suitability of the microstructure obtained from SLM and EBM processes for different applications are still a matter of debate. Since Ti64 and many other alloys respond

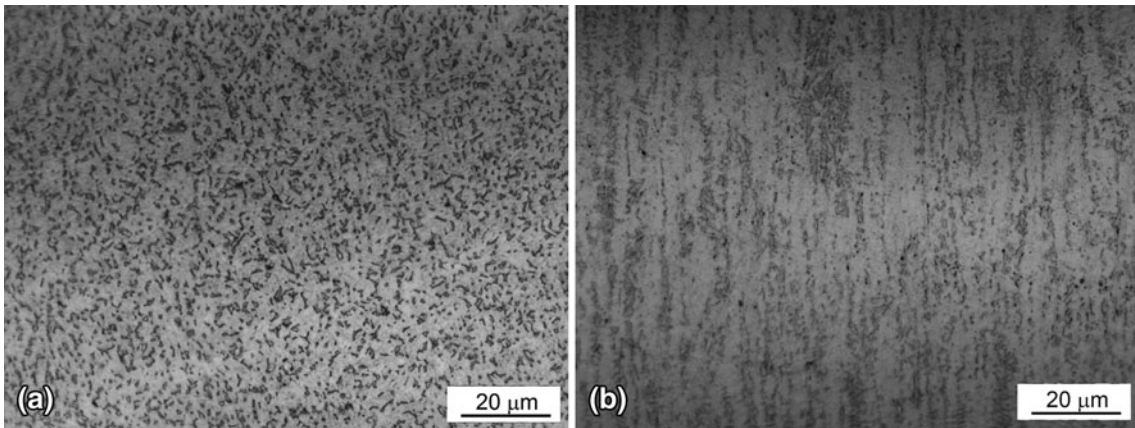


Fig. 8 Optical micrograph of wrought Ti64 (annealed and rolled). (a) Transverse cross-section. (b) Longitudinal cross-section

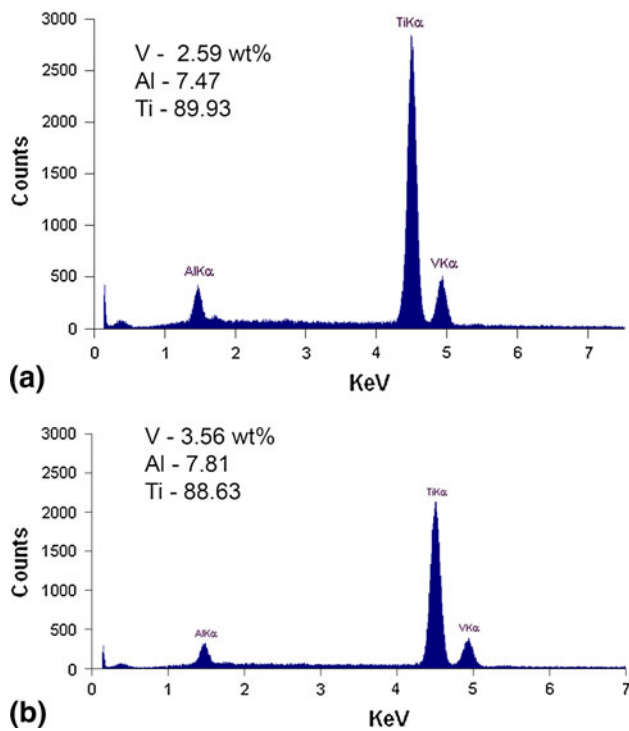


Fig. 9 EDS spectrum and the composition in wt% of Ti64 samples produced by (a) SLM and (b) EBM

well to different heat treatments, selecting an appropriate post-heat treatment method can likely give the desired properties (Ref 14).

3.3 Composition and Phase Analysis

The chemical composition of SLM- and EBM-produced samples was compared using SEM-EDS. Though SEM-EDS is a semi quantitative method which lacks accuracy for obtaining the exact chemical composition, it is quite good for comparative purpose. Figure 9(a) and (b) shows the EDS spectrum and the composition in wt.% for SLM Ti64 and EBM Ti64, respectively. No significant difference is observed in the chemical composition, indicating that the formation of martensite in SLM Ti64 is not influenced by a variation in alloying element composition.

Figure 10(a) and (b) shows the XRD spectrum of SLM-processed Ti64 and EBM-processed Ti64, respectively. Analysis of XRD patterns from the SLM- and EBM-processed Ti64 show similar diffraction patterns. All the peaks can be identified as α/α' . As α and α' have the same crystal structure, hcp, it is difficult to differentiate the peaks though they are two different phases. However, the peak intensities in SLM-processed Ti64 are slightly lower compared to the spectra of EBM-processed Ti64. This is because of the finer structure in SLM-processed Ti64.

3.4 Tensile Properties

Tensile results of EBM- and SLM-produced Ti64 samples are summarized in Table 1. Corresponding stress-strain curves are shown in Fig. 11. The results are the mean values based on five duplicate tests. The yield strength, ultimate tensile strength, and percentage strain were obtained as direct output from the tensile testing machine. The percentage strain-to-failure was measured using a clip-on extensometer that was attached to the gage section of the test specimen. Substantial difference in tensile properties can be seen between the EBM-produced Ti64 and the SLM-produced Ti64 samples. However, the tensile strength values are comparable with or even better than the standard Ti64 material data given in the ASM Handbook (Ref 15). The tensile results are due to the differences observed in the microstructures. The higher tensile strength observed in SLM-produced Ti64 can be attributed to the martensitic microstructure as compared to the α lamellar structure in EBM-produced Ti64 samples. Vilaro et al. (Ref 16) and Facchini et al. (Ref 17) also reported higher yield and ultimate strengths for as-fabricated SLM Ti64 specimens. Though the yield strength and tensile strength of EBM-produced Ti64 samples are low when compared to the SLM-produced Ti64 samples, the strain at break is higher indicating good ductility. The tensile strength values reported by Facchini et al. (Ref 13), Al-Bermani (Ref 12), and Chahine et al. (Ref 18) for EBM-produced Ti64 samples are similar to the results obtained in the current study. However, the tensile strength values reported by Murr et al. are slightly higher than the values reported in this study (Ref 6). The ultimate tensile strengths for both SLM- and EBM-produced Ti64 samples are only marginally higher than their yield strengths indicating the work hardening rate beyond the yield point is low.

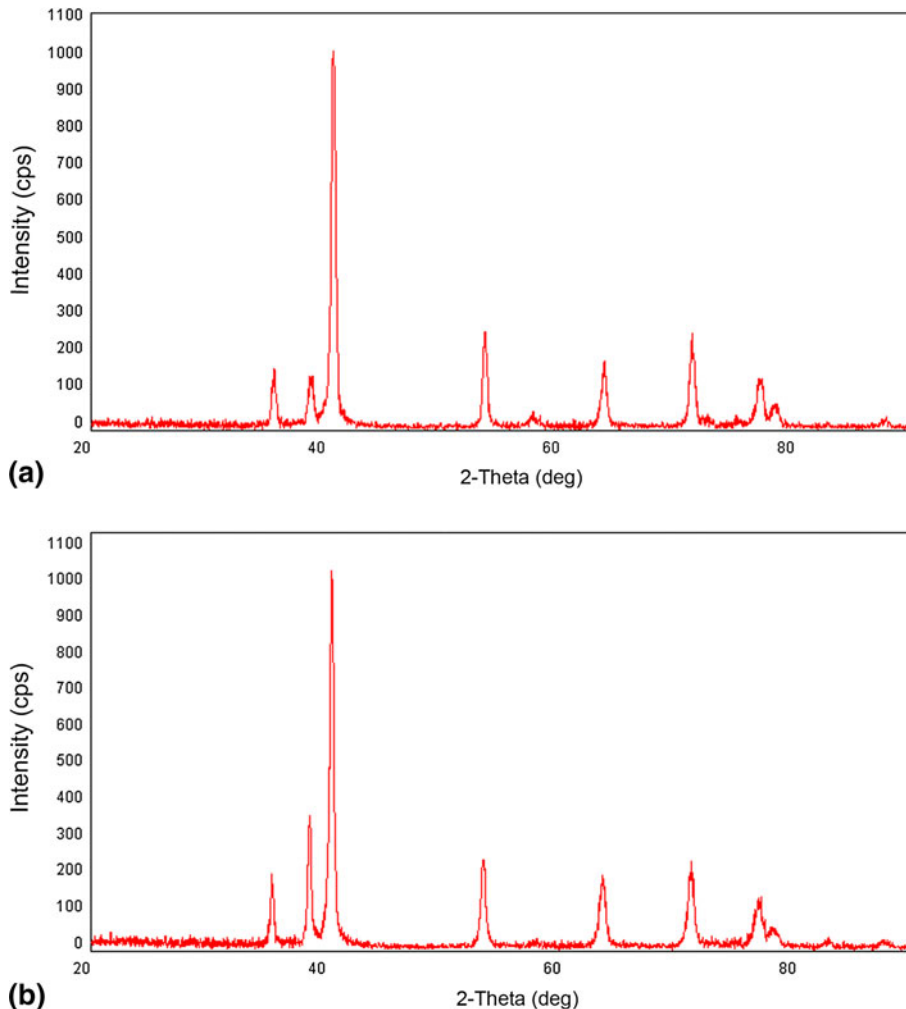


Fig. 10 XRD spectrum of Ti64 samples produced by (a) SLM and (b) EBM

Table 1 Tensile results for SLM-produced and EBM-produced Ti64 alloy samples

	Stress at yield (Offset 0.2%), MPa	Ultimate tensile stress, MPa	Strain at break, %
EBM (vertically built and Machined)	869 (SD: 7.2)	928 (SD: 9.8)	9.9 (SD: 1.7)
SLM (vertically built and Machined)	1143 (SD: 30)	1219 (SD: 20)	4.89 (SD: 0.6)
% Increase	31	31	-50
EBM (horizontally built and Machined)	899 (SD: 4.7)	978 (SD: 3.2)	9.5 (SD: 1.2)
SLM (horizontally built and Machined)	1195 (SD: 19)	1269 (SD: 9)	5 (SD: 0.5)
% increase	33	30	-47
ASM Handbook (Ref 15) (cast and annealed)	885	930	

SD: standard deviation

The tensile test results are in conformation with the bulk hardness tests. The Rockwell hardness test resulted in higher hardness for SLM-processed Ti64 (HRC: 41) compared to the hardness of EBM-processed Ti64 (HRC: 33).

Martensitic microstructure in Ti64 results in high strength and low ductility. Because of the low ductility, the SLM Ti64 samples failed at lower strain values. Ductility of SLM-produced Ti64 samples can be improved by proper post-heat treatment which decomposes the harder martensitic phase to

softer α phase (Ref 14). The tensile properties of EBM-produced Ti64 sample are greatly influenced by the alpha lath width and alpha colony size in the microstructure. Coarsened α phase and larger α colony size results in the reduction of tensile strength (Ref 12). In EBM processes the morphology of the α phase is primarily determined by the temperature maintained in the build chamber. A slight increase in build chamber temperature can cause coarsening of the α phase and thereby causes a reduction in tensile strength. Another factor which

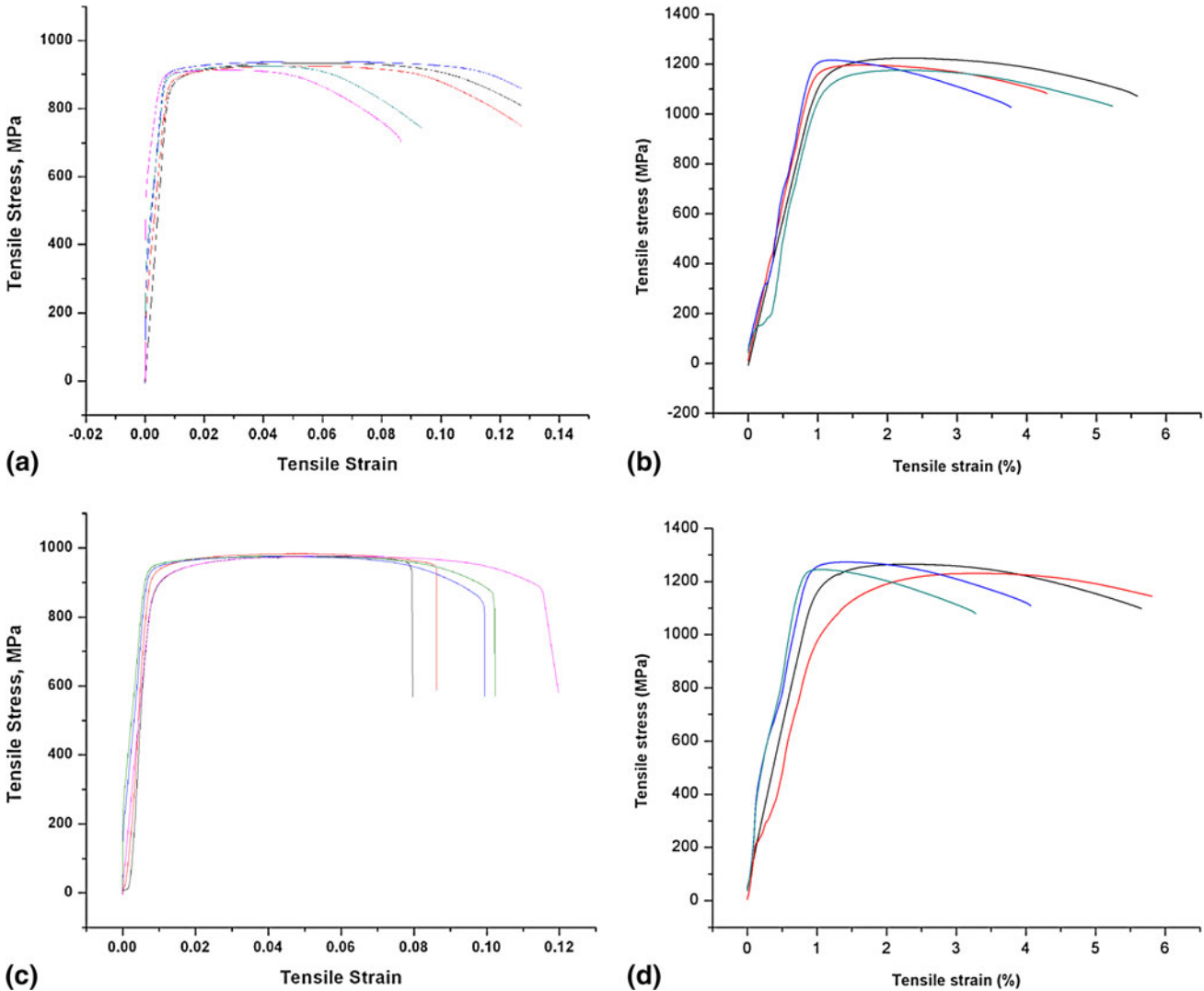


Fig. 11 Stress-Strain plots of Ti64 samples (a) EBM specimen built in vertical orientation, (b) SLM specimen built in vertical orientation, (c) EBM specimen built in horizontal orientation and (d) SLM specimen built in horizontal orientation

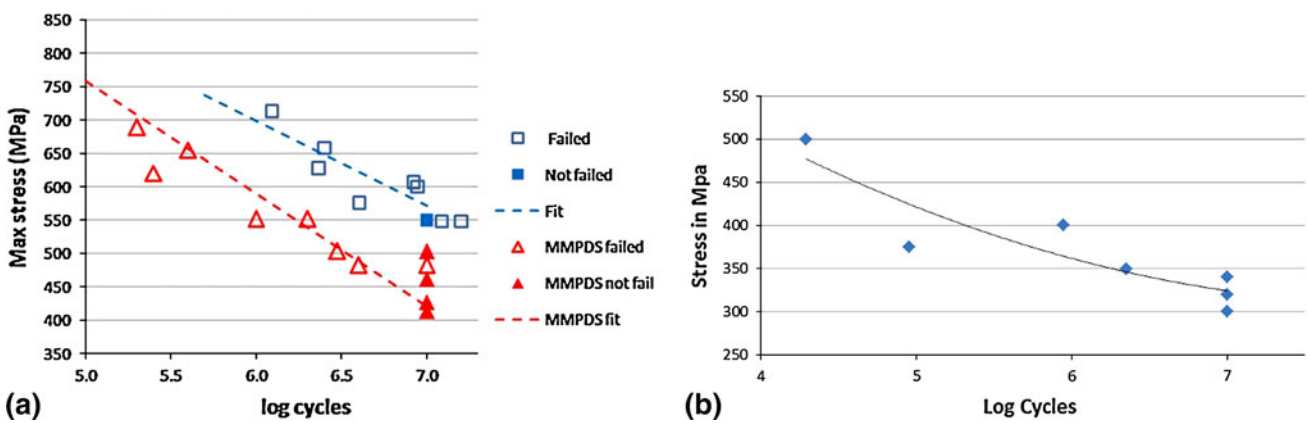


Fig. 12 S-N curve showing fatigue behavior of Ti64 samples (a) SLM and (b) EBM

affects the tensile properties is a chemical difference. This becomes a major concern when the Ti64 powder is recycled many times. Though there would not be any change in the

composition of major alloying elements like V and Al, over time the Ti64 powder picks up oxygen due to the high affinity of Ti for oxygen (Ref 12).

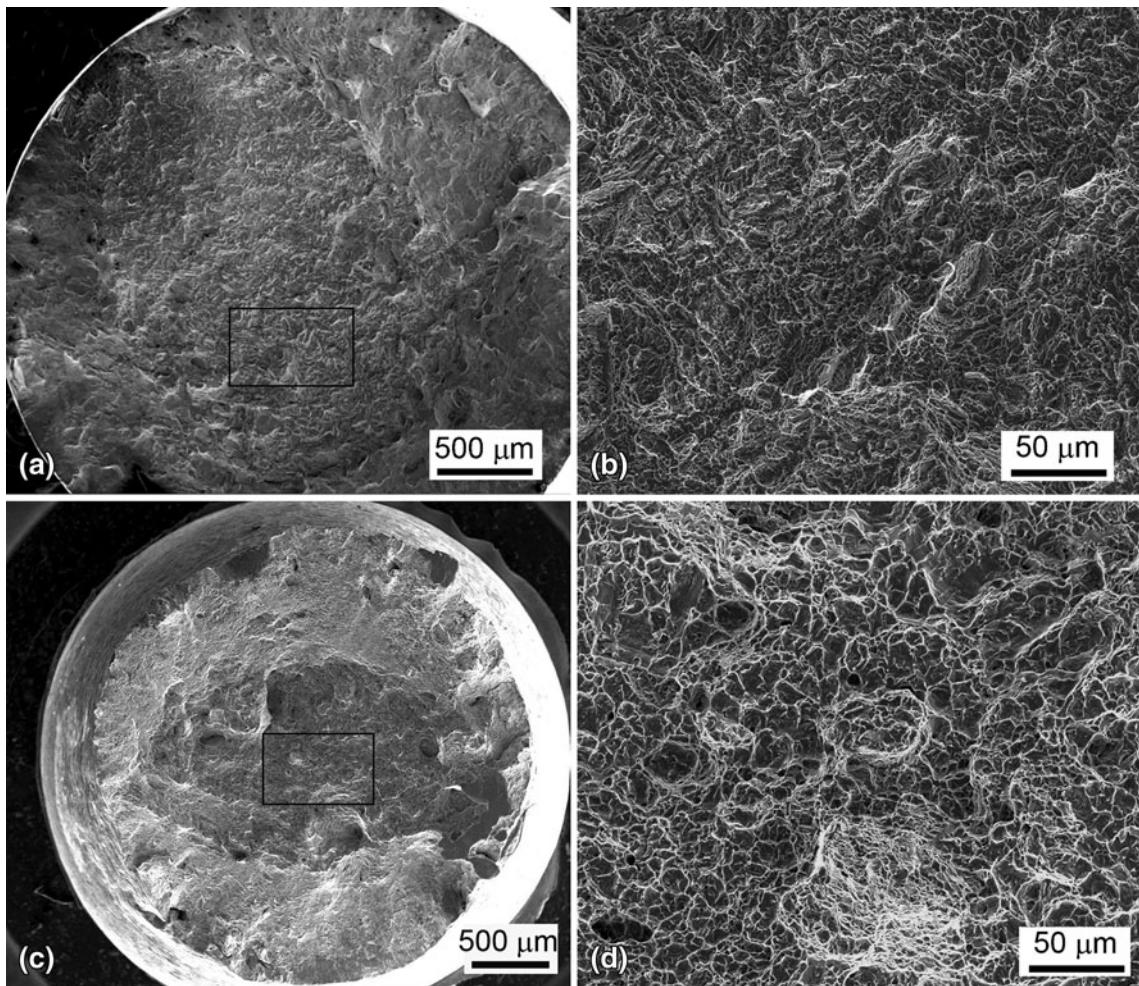


Fig. 13 SEM-SE images of tensile fracture surfaces. (a) Overall view of SLM-produced Ti64 tensile fracture surface. (b) Enlarged view from the boxed region in “a.” (c) Overall view of EBM-produced Ti64 tensile fracture surface. (d) Enlarged view from the boxed region in “c”

3.5 Fatigue Properties

S-N curves illustrating the fatigue behavior of SLM-produced Ti64 and EBM-produced Ti64 are shown in Fig. 12. For SLM-produced Ti64 samples a fatigue limit of 550 MPa was observed (Fig. 12a). A comparison with MMPDS (Metallic Materials Properties Development and Standardization Handbook, Battelle Memorial Institute, Columbus, Ohio, April 2010) fatigue data shows better fatigue performance for Ti64 specimens built using SLM compared to Ti64 that is cast and annealed (430 MPa). However, the fatigue performance of EBM-produced Ti64 samples was inferior (Fig. 12b, fatigue limit: 340 MPa) as compared to the SLM-produced Ti64 and the MMPDS data. The better fatigue strength properties of SLM-produced Ti64 can be attributed to the martensitic phase. Martensite impedes dislocation motion and thus leads to a strengthening effect. Because of this strengthening effect, the total strain amplitude introduced during fatigue testing causes smaller plastic strain.

3.6 Fracture Behavior

3.6.1 Tensile Fracture. Representative fractographs of the tensile fracture surface of SLM- and EBM-produced Ti64 samples are shown in Fig. 13. SLM-produced Ti64 sample

fracture surfaces exhibited a mixed mode of brittle and ductile fracture (Fig. 13a, b) showing predominantly cleavage facets. Cleavage fracture is a low energy brittle fracture which propagates along low index crystallographic planes (Ref 19). This fracture is characterized by flat, cleavage facets. River markings separating the facets result from the propagation of the crack on a number of planes of different levels (Ref 20). The fracture surface of EBM-produced Ti64 sample is characterized by transgranular ductile dimple tearing resulting from the coalescence of microvoids (Fig. 13c, d). A healthy population of fine dimples at the tensile fracture surface indicates the extent of plastic deformation.

3.6.2 Fatigue Fracture. Figure 14 shows the fatigue fracture surfaces of SLM-produced Ti64 and EBM-produced Ti64. In SLM-produced Ti64 samples (Fig. 14a, b) the crack initiated from an internal defect and propagated radially outwards. Three distinct regions show crack initiation, steady crack growth, and overload regions typical for fatigue fracture. The crack propagation looks more tortuous as it propagated through multiple crystallographic planes. The fracture surface of EBM-produced Ti64 samples appear normal, with a characteristic fatigue fracture surface (Fig. 14c). The crack initiation site is characterized by microscopically smooth facets away from the surface as evident from Fig. 14(d). It can also be

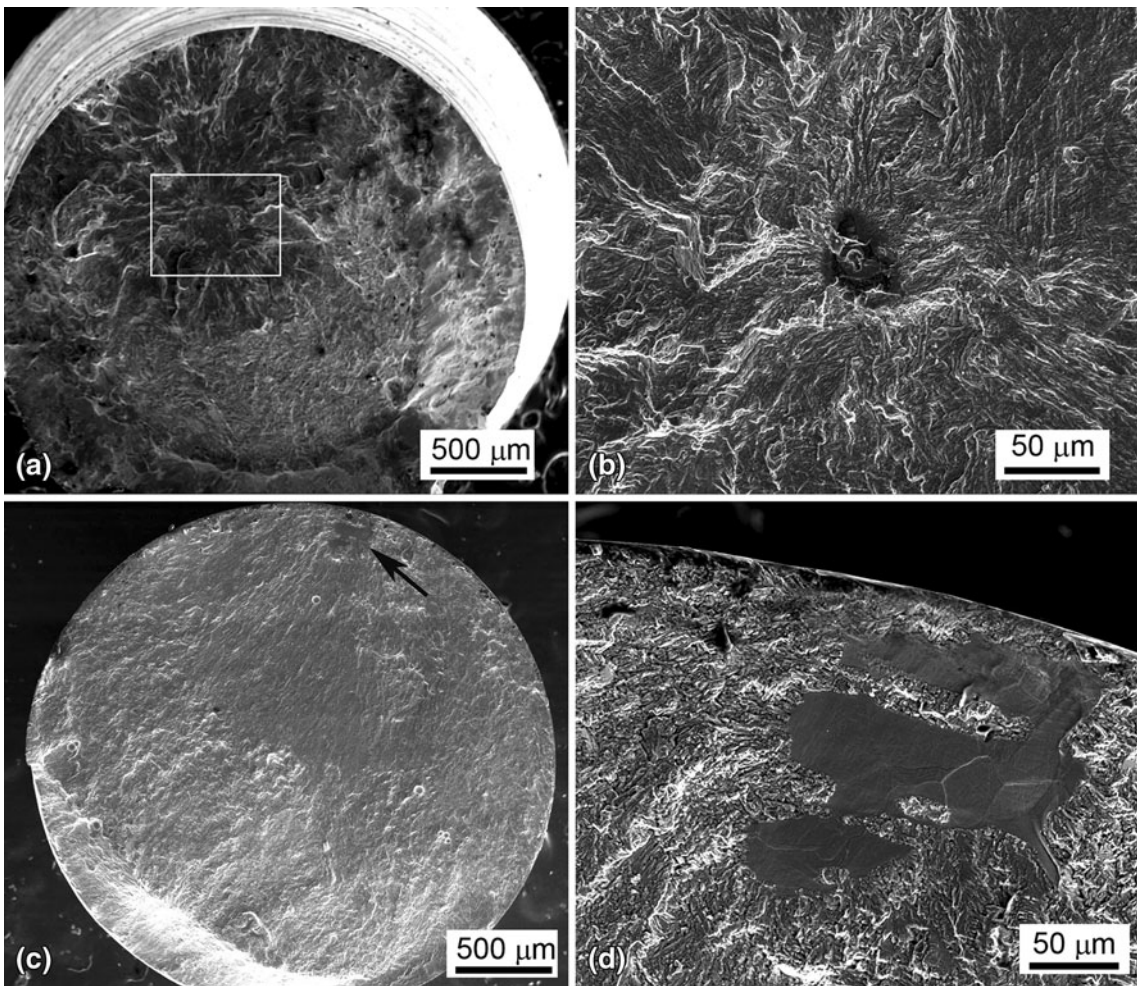


Fig. 14 SEM-SE images of fatigue fracture surfaces. (a) Overall view of SLM-produced Ti64 fracture surface. (b) Enlarged view from the boxed region in “a.” (c) Overall view of EBM-produced Ti64 fracture surface. (d) Enlarged view from the arrow pointed region in “c”

noted that the crack initiation site has multiple facets which could possibly be due to crack initiation occurring at the α colony boundaries and shear across neighboring α colonies. This indicates that crack initiation is not caused by the classical slip-band intrusion/extrusion mechanism. Therefore, one common feature that can be seen between the fatigue fracture surfaces of SLM- and EBM-produced Ti64 samples is that the crack initiation occurred from the interior or the sub surface and not from the external surface. In general, for metallic materials fatigue crack initiation occurs at the surface if the sample is free from large internal defects. Previous studies show that this may not be true in the case of Ti64 with dual phase microstructures. In α/β titanium alloys, cracks tend to initiate either at the surface or at the subsurface or at the impingement of slip bands within the alpha lamellae of a fully lamellar microstructure. They can also initiate at the boundaries separating the α and β phase (Ref 21).

Fatigue behavior of Ti64 is greatly influenced by its microstructure. Depending on the process conditions the morphology and volume fraction of α and β constituents in Ti64 changes. The microstructure of Ti64 can exist in forms such as bi-modal, equiaxed, lamellar α and β , and martensitic α' structures. All these microstructures can result in different fatigue properties. As observed earlier, Ti64 processed by SLM resulted in martensitic α' and EBM resulted in lamellar α with

smaller amount of β . Ivanova et al. observed that in the high cycle fatigue regime the preferred crack initiation sites are within the alpha grains in an equiaxed grain structure. The crack nucleates along the slip bands within the alpha grain and results in cleavage fracture (Ref 22). For a bimodal microstructure the crack initiates by the cracking of suitably oriented α grains and subsequent growth along the planar slip bands within interconnected α grains. Crack initiation occurs by cross-colony slip-band fracture for the lamellar microstructure (Ref 23). Oh et al. showed that fatigue crack initiation occurs mainly at the prior β grain boundary for an electron beam welded and then annealed Ti64 sample. They also observed that the large micropores present in the weld act as fatigue crack initiation sites. However, the micropores did not have any effect on crack propagation (Ref 24). In titanium alloys, an increase in oxygen content can also lead to the embrittlement of the alpha phase. Among the different characteristic microstructures exhibited by Ti64, lamellar structures are more prone to crack initiation as compared to equiaxed or bi-modal structures. But for crack propagation, lamellar structures offer greater resistance to crack growth than equiaxed structures. In high cycle fatigue, crack initiation forms the major part of the fatigue life. To increase the resistance to fatigue crack nucleation, the maximum dislocation slip length in the microstructure should be reduced. Generally, a fatigue crack nucleates due to

irreversible slip bands within the longest crystallographic planes available in the microstructure. Consequently, coarse lamellar microstructures with colonies of aligned α and extended planar-slips running across these colonies often have less resistance to crack nucleation when compared to fine-grained equiaxed and acicular martensitic microstructures (Ref 23). Therefore, the inferior fatigue strength of EBM samples could be attributed to its lamellar microstructure rather than due to the presence of micropores or voids.

4. Summary

In this study an attempt was made to highlight the differences between SLM and EBM processes concerning Ti64. A clear difference in surface conditions, microstructure, tensile properties, and fatigue properties are evident. The primary difference between the processes boils down to the cooling rate. The same material processed using SLM and EBM can have different properties. Irrespective of the processes, what matters is the suitability of a final part for a specific application. Ti64 is considered for very wide range of applications from biomedical to aerospace. The property requirements for a part produced for biomedical applications may differ from a part produced for aerospace applications. As discussed earlier, processing of Ti64 with SLM and EBM results in microstructures containing α , β , and γ phases. With respect to the volume fraction of these phases and their morphology the resulting properties will vary to a certain extent. For instance, the higher hardness possessed by α phases may be beneficial for certain applications and on the other hand it may be detrimental for some other applications. Therefore, selection of a particular process, whether SLM or EBM, primarily depends on the requirements for end-use. For that, one should have a proper understanding of the structure-property relationship of the material chosen.

5. Conclusions

This comparative study on SLM and EBM processes when using Ti64 as the build material has resulted in the following conclusions:

1. The surface finish of SLM-produced samples is better than EBM-processed samples. Relatively thick layers in EBM cause more pronounced “stairstep effects” and larger particle size powders adhering to the surface result in rougher surfaces.
2. The SLM-produced and EBM-produced samples resulted in two different microstructures for Ti64. SLM-produced Ti64 resulted in martensitic α microstructures and EBM-produced Ti64 resulted in an α phase with β separating the α lamellae.
3. SLM-produced Ti64 samples have higher tensile strength than EBM-produced samples. But EBM-produced samples have higher ductility. Higher tensile strength of SLM samples is attributed to the martensitic α microstructure and the higher ductility in EBM-produced samples is attributed to the lamellar α phase.
4. The SLM-produced samples showed a fatigue limit of 550 MPa, whereas EBM-produced samples showed

a fatigue limit of 340 MPa. The inferior fatigue limit observed for EBM is because of the lamellar phase microstructure.

5. Selecting between SLM and EBM for fabrication of a specific Ti64 part depends on the application requirements as both result in mechanical properties suitable for many applications.

Acknowledgments

The authors acknowledge the Office of Naval Research (ONR), USA for support through grant #'s N00014-09-1-0147, N00014-10-1-0800, and N00014-11-1-0689.

References

1. F. Abe, K. Osakada, M. Shiomii, K. Uematsu, and M. Matsumoto, The Manufacturing of Hard Tools from Metallic Powders by Selective Laser Melting, *J. Mater. Process. Technol.*, 2001, **111**, p 210–213
2. S.M. Gaytan, L.E. Murr, E. Martinez, J.L. Martinez, B.I. Machado, D.A. Ramirez, F. Medina, S. Collins, and R.B. Wicker, Comparison of Microstructures and Mechanical Properties for Solid and Mesh Cobalt-Based Alloy Prototypes Fabricated by Electron Beam Melting, *Metall. Mater. Trans. A*, 2010, **41A**, p 3216–3227
3. E. Brinksmeier, G. Levy, D. Meyer, and A.B. Spierings, Surface Integrity of Selective-Laser-Melted Components, *CIRP Ann. Manuf. Technol.*, 2010, **59**(1), p 601–606
4. J.P. Kruth, G. Levy, F. Klocke, and T.H.C. Childs, Consolidation Phenomena in Laser and Powder-Bed Based Layered Manufacturing, *CIRP Ann. Manuf. Technol.*, 2007, **56**, p 730–759
5. M.F. Zah and S. Lutzmann, Modelling and Simulation of Electron Beam Melting, *Prod. Eng. Res. Dev.*, 2010, **4**, p 15–23
6. L.E. Murr, E.V. Esquivel, S.A. Quinones, S.M. Gaytan, M.I. Lopez, E.Y. Martinez, F. Medina, D.H. Hernandez, E. Martinez, J.L. Martinez, S.W. Stafford, D.K. Brown, T. Hoppe, W. Meyers, U. Lindhe, and R.B. Wicker, Microstructures and Mechanical Properties of Electron Beam-Rapid Manufactured Ti-6Al-4V Biomedical Prototypes Compared to Wrought Ti-6Al-4V, *Mater. Charact.*, 2009, **60**, p 96–109
7. L. Thijis, F. Verhaeghe, T. Craeghs, J.V. Humbeeck, and J.P. Kruth, A Study of the Microstructural Evolution During Selective Laser Melting of Ti-6Al-4V, *Acta Mater.*, 2010, **58**, p 3303–3312
8. B. Song, S. Dong, B. Zhang, H. Liao, and C. Coddet, Effects of Processing Parameters on Microstructure and Mechanical Property of Selective Laser Melted Ti6Al4V, *Mater. Des.*, 2012, **35**, p 120–125
9. I. Yadroitsev, P. Bertrand, and I. Smurov, Parametric Analysis of the Laser Melting Process, *Appl. Surf. Sci.*, 2007, **253**(19), p 8064–8069
10. R. Morgan, C.J. Sutcliffe, and W. O'Neill, Density Analysis of Direct Metal Laser Remelted 316L Stainless Steel Cubic Primitives, *J. Mater. Sci.*, 2004, **39**(4), p 1195–1205
11. E. Yasa, J. Deckers, and J.P. Kruth, The Investigation of the Influence of Laser Re-Melting on Density, Surface Quality and Microstructure of Selective Laser Melting Parts, *Rapid Prototyp. J.*, 2011, **17**(5), p 312–327
12. S.S. Al-Bermani, M.L. Blackmore, W. Zhang, and I. Todd, The Origin of Microstructural Diversity, Texture, and Mechanical Properties in Electron Beam Melted Ti-6Al-4V, *Metall. Mater. Trans. A*, 2010, **41A**, p 3422–3432
13. L. Facchini, E. Magalini, P. Robotti, and A. Molinari, Microstructure and Mechanical Properties of Ti-6Al-4V Produced by Electron Beam Melting of Pre-Alloyed Powders, *Rapid Prototyp. J.*, 2009, **15**(3), p 171–178
14. B. Vrancken, L. Thijis, J.P. Kruth, and J.V. Humbeeck, Heat Treatment of Ti6Al4V Produced by Selective Laser Melting—Microstructure and Mechanical Properties, *J. Alloy Compd.*, 2012, **541**, p 177–185
15. ASM Handbook, Vol. 1, ASM International, Materials Park, OH, 1993, p 2071

16. T. Vilaro, C. Colin, and J.D. Bartout, As-Fabricated and Heat Treated Microstructures of the Ti-6Al-4V Alloy Processed by Selective Laser Melting, *Metall. Mater. Trans. A.*, 2011, **42**, p 3190
17. L. Faccini, E. Magalini, P. Robotti, A. Molinari, S. Hogess, and K. Wissenbach, Ductility of Ti-6Al-4V Alloy Produced by Selective Laser Melting of Pre-Alloyed Powders, *Rapid Prototyp. J.*, 2010, **16**(6), p 450–459
18. G. Chahine, M. Koike, T. Okabe, P. Smith, and R. Kovacevic, The Design and Production of Ti-6Al-4V ELI, Customized Dental Implants, *JOM*, 2008, **60**(11), p 50–55
19. G.E. Dieter, *Mechanical Metallurgy*, McGraw Hill, New York, 1986
20. M. Erdogan and S. Tekeli, The Effect of Martensitic Particle Size on Tensile Fracture of Surface-Carburized AISI, 8620 Steel with Dual Phase Core Microstructure, *Mater. Des.*, 2002, **23**, p 597–604
21. T.S. Srivatsana, M. Kuruvilla, and L. Park, A Study at Understanding the Mechanisms Governing the High Cycle Fatigue and Final Fracture Behavior of the Titanium Alloy: Ti-4Al-2.5V, *Mater. Sci. Eng. A.*, 2010, **527**, p 435–448
22. S.G. Ivanova, R.R. Biederman, and R.D. Sisson, Jr., Investigation of Fatigue Crack Initiation in Ti-6Al-4V During Tensile-Tensile Fatigue, *J. Mater. Eng. Perform.*, 2002, **11**(2), p 226–231
23. R.K. Nalla, B.L. Boyce, J.P. Campbell, J.O. Peters, and R.O. Ritchie, Influence of Microstructure on High-Cycle Fatigue of Ti-6Al-4V: Bimodal vs. Lamellar Structures, *Metall. Mater. Trans. A.*, 2002, **33A**, p 899–918
24. J. Oh, N.J. Kim, S. Lee, and W. Lee, Correlation of Fatigue Properties and Microstructure in Investment Cast Ti-6Al-4V, *Mater. Sci. Eng. A.*, 2003, **340**, p 232–242



Heat treatment of Ti6Al4V produced by Selective Laser Melting: Microstructure and mechanical properties

Bey Vrancken ^{a,*}, Lore Thijs ^a, Jean-Pierre Kruth ^b, Jan Van Humbeeck ^a

^a Katholieke Universiteit Leuven, Department of Metallurgy and Materials Engineering, Leuven, Belgium

^b Katholieke Universiteit Leuven, Department of Mechanical Engineering, Leuven, Belgium

ARTICLE INFO

Article history:

Received 15 June 2012

Received in revised form 29 June 2012

Accepted 2 July 2012

Available online 14 July 2012

Keywords:

Metals and alloys

Powder metallurgy

Rapid solidification

Mechanical properties

Microstructure

ABSTRACT

The present work shows that optimization of mechanical properties via heat treatment of parts produced by Selective Laser Melting (SLM) is profoundly different compared to conventionally processed Ti6Al4V. In order to obtain optimal mechanical properties, specific treatments are necessary due to the specific microstructure resulting from the SLM process. SLM is an additive manufacturing technique through which components are built by selectively melting powder layers with a focused laser beam. The process is characterized by short laser-powder interaction times and localized high heat input, which leads to steep thermal gradients, rapid solidification and fast cooling. In this research, the effect of several heat treatments on the microstructure and mechanical properties of Ti6Al4V processed by SLM is studied. A comparison is made with the effect of these treatments on hot forged and subsequently mill annealed Ti6Al4V with an original equiaxed microstructure. For SLM produced parts, the original martensite α' phase is converted to a lamellar mixture of α and β for heat treating temperatures below the β -transus (995°C), but features of the original microstructure are maintained. Treated above the β -transus, extensive grain growth occurs and large β grains are formed which transform to lamellar $\alpha + \beta$ upon cooling. Post treating at 850°C for 2 h, followed by furnace cooling increased the ductility of SLM parts to $12.84 \pm 1.36\%$, compared to $7.36 \pm 1.32\%$ for as-built parts.

© 2012 Elsevier B.V. All rights reserved.

1. Introduction

The Selective Laser Melting (SLM) process is one of recently developed additive manufacturing techniques that emerged in the late 1980s and early 1990s [1–3]. The process has been described in detail elsewhere and the reader is referred to Ref. [3] for more detail.

SLM offers several advantages compared to conventional production techniques, such as reduction of production steps, a high level of flexibility, a high material use efficiency and a near net shape production. Furthermore, hard materials or materials with a high melting point can be processed with SLM. Most important, because of the layer-wise building, SLM enables the production of parts with a high geometrical complexity. However, the unique conditions during the SLM process give rise to some problems. Because of the short interaction times and accompanying highly localized heat input, large thermal gradients exist during the process. These lead to the build-up of thermal stresses, while the rapid solidification leads to segregation phenomena and the development of non-equilibrium phases. Moreover, non-optimal scan

parameters may cause melt pool instabilities during the process, which leads to an increased porosity and a higher surface roughness.

To ensure optimal building conditions, the influence of the different process parameters, such as layer thickness, scan spacing, scan strategy, laser power and scan speed on the microstructure and mechanical properties [4–8] and other properties such as the density and surface quality [9–12] have been investigated. Other research has focused on optimization and control of the process [13–15] and simulation of the melt pool behavior [16].

On the other hand, heat treatments of Ti6Al4V have been investigated extensively. Amongst others, attempts have been made to model the kinetics [17–19] and phase morphology [20–22], to measure the alpha fraction at high temperature [23] and to create a CCT diagram [24,25]. However, the starting material is always in the mill annealed condition (i.e. with equiaxed alpha grains) or has been subjected to some degree of previous deformation. Mill annealing is performed on heavily deformed Ti6Al4V, in which the breakup of the α plates leads to a recrystallization of the α phase. This results in an equiaxed microstructure and a small, general improvement of the mechanical properties.

As is shown in previous studies [4,7], the microstructure of Ti6Al4V processed by SLM consists of a fine acicular martensite called the α' phase. Mechanical properties of these SLM parts are

* Corresponding author.

E-mail address: bey.vrancken@mtm.kuleuven.be (B. Vrancken).

a high yield stress (about 1 GPa), a high ultimate tensile strength but a relatively low ductility (less than 10%). To improve the ductility of Ti6Al4V products manufactured by SLM, and to achieve a variety of desired mechanical properties for particular applications, suitable post-production heat treatments must be elaborated. Furthermore, these treatments allow the reduction of thermal stresses that have been built up during the process. Only limited research has been performed on this topic [5,26,27], and has mainly been observational. In this paper, the different response of SLM parts on generally applied titanium heat treatments is studied and the influence of time, temperature and cooling rate is distinguished. It appears that standard treatments for bulk alloys are not optimal for SLM produced parts and have to be adapted for optimal mechanical properties.

2. Materials and methods

Extra-low interstitial Ti6Al4V (Grade 23) powder was used as a base material for the SLM process. The powder is produced via the plasma-atomization process by Raymor Industries. The equiaxed Ti6Al4V (Grade 5) was hot forged and mill annealed. This material will further be addressed as the reference material.

All SLM parts were produced on the in-house developed LM-Q SLM machine of the PMA Division of the Department of Mechanical Engineering, KU Leuven. This machine is equipped with an IPG YLR-300 SMYb:YAG fiber laser, with a wavelength of 1070 nm, a maximum power of 300 W in continuous laser mode and a spot size of 52 μm . For more details, the reader is referred to Ref. [13].

Samples were produced with a scanning speed v of 1600 mm/s, a laser power P of 250 W, 60 μm hatch spacing h (the distance between two adjacent scan vectors) and a 30 μm layer thickness t . Layers were scanned using a continuous laser mode according to a zigzag pattern, which was rotated 90° between each layer. This parameter set was determined to obtain fully dense, good quality Ti6Al4V products.

Before heat treating, samples were enclosed in a vacuum quartz tube, with vacuum better than 10⁻⁶ mbar. Heat treatments were executed in a vertical tube furnace, with a heating rate of approximately 10 °C/min. Three different cooling regimes were applied. Furnace cooling was attained by turning the heating off, taking approximately 2 h to cool from 800 °C to 500 °C, which corresponds to an average cooling rate of 0.04 °C/s, and air cooling by cooling the quartz tube in a room temperature environment, leading to an approximate cooling rate of 7 °C/s [22,25]. To water quench, the tube was dropped and broken in a water reservoir, cooling the samples to room temperature in a matter of seconds. Some heat treatments were performed purely for microstructural examination.

Four tensile test samples of the SLM material were tested for each treatment to determine the mechanical properties. These samples were built as rectangular beams from which the final shape was cut by wire EDM. Tensile tests were performed according to ASTM E 8M at a strain rate of 1 mm/min. Displacements were measured using an extensometer with a 25 mm gauge length. Yield stress and Young's modulus were determined according to ASTM E 111. Samples were tested perpendicular to the build direction.

Examination of the microstructure occurred after grinding with SiC grinding paper up to a fine 4000 grit size, and polished with SiO₂ suspension. To reveal the microstructure, samples were etched with a 50 ml H₂O, 25 ml HNO₃ and 5 ml HF solution. Because of the anisotropic build process, two cross-sections are always considered. One is a side view parallel to the build direction, and the other is a top view, perpendicular to the build direction. Micrographs were taken using an Axioskop 40 Pol/40 A Pol microscope. A Philips SEM XL30 FEG was used for the examination of fracture surfaces and higher resolution micrographs. Texture and crystallographic orientation were examined by X-ray diffraction (XRD) and electron backscattered diffraction (EBSD). EBSD uses inelastic scattering of electrons to generate Kikuchi patterns which can be compared to Kikuchi patterns of known crystal orientations.

Dimensions of microstructural features are measured using the line intercept method described in ASTM E112. Circles are used instead of straight lines when measuring the size of elongated features such as needles and lamellae. Lamella size is reported as the true thickness, which is taken as half of the measured thickness, according to Ref. [28]. All measurements of these properties are given with a 95% confidence interval.

3. Results

3.1. Microstructure

Fig. 1a and b shows respectively a top and side view of non-heat treated Ti6Al4V, produced by SLM. The top view indicates that a fully acicular α' martensitic microstructure is developed during

the SLM process. XRD measurements did not indicate the presence of β phase. Due to the alternating scan pattern and the 90° shift between subsequent layers, a chessboard pattern appears. The squares are about 60 μm wide, corresponding to the hatch spacing of 60 μm used to build the part. At a smaller magnification, the side view reveals long, columnar grains which are oriented more or less in the building direction. These are identified as prior β grains which grow epitaxially during the process, up to several millimeters in length. The average width of the β grains is 55.5 ± 5 μm , which is close to the hatch spacing. A more comprehensive overview of the microstructure obtained by SLM is given by Ref. [7].

The reference material, shown in **Fig. 1c**, consists of equiaxed α grains with 10.7 ± 0.9% β phase at the grain boundaries, as determined by pixel count of SEM images. A slight anisotropy exists in the reference material, with the α grains measuring 16.2 ± 2.6 μm in one direction and only 11.6 ± 1.7 μm in the perpendicular direction. This is attributed to the hot forging this material has been subjected to.

3.1.1. Influence of temperature

Microstructures of the SLM material after heat treating at different temperatures are shown in **Fig. 2**. After 2 h at 780 °C, the fine martensitic structure has been transformed to a mixture of α and β , in which the α phase is present as fine needles (**Fig. 2a**). The long, columnar grains remain visible in the side view of the material.

At 850 °C, the β -fraction at high temperature is larger, reducing the equilibrium α -fraction from approximately 87% at 780 °C to 73% at 850 °C and 23% at 950 °C [20,23]. From comparison of **Fig. 2a** with **Fig. 2b**, it is clear that the α plates are significantly coarser for higher temperatures. This observation corresponds to the FE calculations performed by Katzarov et al. [20], where the α - β morphology was predicted to be coarser for higher holding temperatures beneath the β transus. The effect of temperature for subtransus treatments is further discussed in Section 4.

When heating above the β transus of 995 °C, a fully homogenous, 100% β phase microstructure exists at high temperature. During furnace cooling, a lamellar α + β mixture is formed, as shown in **Fig. 2c**.

Fig. 3a shows the side view of SLM material after a heat treatment at 940 °C, below the β transus. After heat treatment below the β transus and at sufficiently low cooling rates, the prior β grains are now even more visible due to the formation of a layer of grain boundary α and the more aggressive etching of the α + β mixture as opposed to the original α' . On the other hand, **Fig. 3b** shows that the microstructure no longer contains long columnar prior β grains after treatment above the β transus, indicating extensive grain growth of the SLM material when heated above the β transus, up to the point of semi-equiaxed β grains. The length of the prior β grains seems unchanged but the width has increased and is now roughly 620 μm wide after 2 h at 1015 °C. A comparison of the microstructure of SLM material after sub- and super-transus treatments by Sercombe et al. [26] led to similar results, as did work by Vilaro et al. [27].

As the equilibrium fraction of β phase rises at high temperatures, the intergranular β phase in the *reference material* grows into equiaxed grains. Upon cooling, these β grains transform to lamellar α + β , leading to a duplex microstructure, seen in **Fig. 4**. This microstructure consists of equiaxed α grains and lamellar transformed β grains. At higher heat treatment temperatures, the equilibrium volume fraction of β phase is higher, which ultimately leads to a higher fraction of lamellar α + β at room temperature. When heated above the β transus, grain growth of the β phase can take place, leading to large grains.

Reference material samples treated at 1015 °C still showed a duplex microstructure whereas a 100% transformed β structure

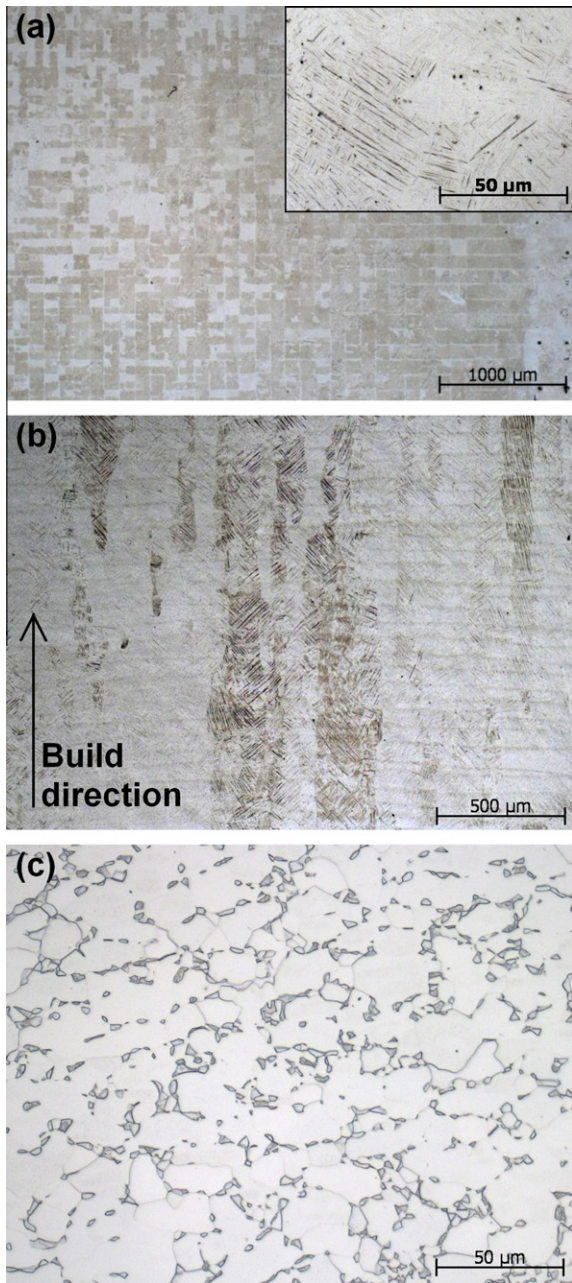


Fig. 1. Top (a) and side (b) view of untreated Ti6Al4V produced by SLM. (c) Original microstructure of the reference material. The microstructure in (a) and (b) is fully martensitic. In (c), the α phase is lighter and the β phase darker.

was expected. This is cause to believe that the β transus of the reference material is higher than 1015 °C. When treated at 1040 °C, the microstructure fully consists of transformed β grains with varying degrees of grain boundary α , depending on the cooling rate.

3.1.2. Influence of the residence time

The residence time at high temperature affects grain growth, with longer residence times leading to larger grains. An analogous remark can be made about the heating rate. The time at high temperature and the heating rate are however of minor importance compared to the temperature for Ti6Al4V SLM parts when treated below the β transus. Both the α and the β phase will tend to coarsen but will hinder each other, hereby limiting grain growth. This effect diminishes as the temperature rises closer to the β transus.

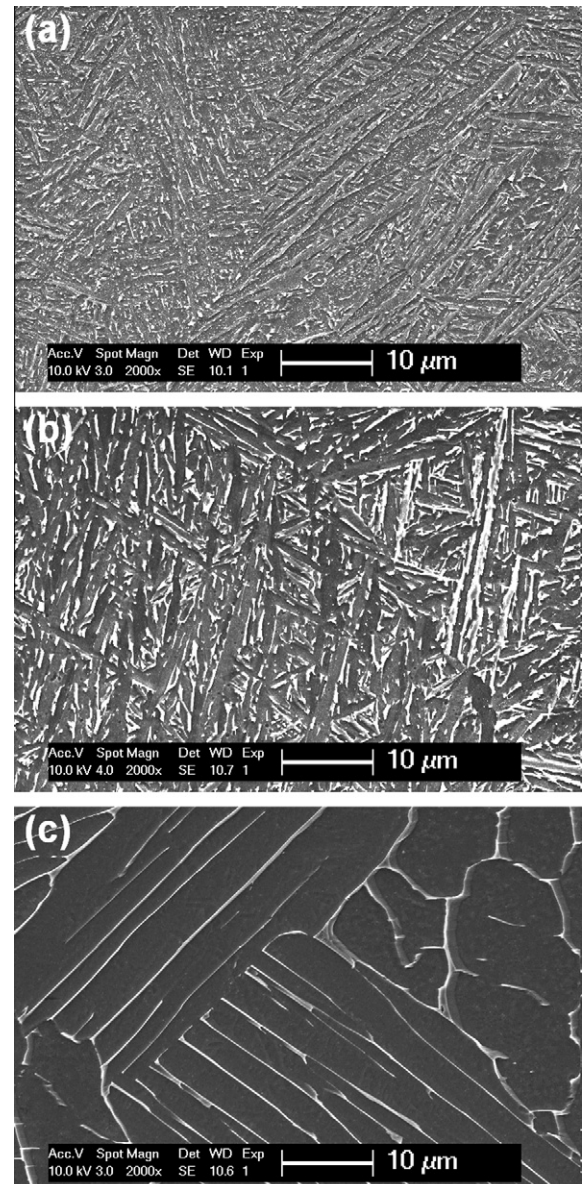


Fig. 2. Microstructure of Ti6Al4V produced by SLM after heat treating at different temperatures for 2 h, followed by FC. (a) 780 °C and (b) 843 °C below the β transus, (c) 1015 °C above the β transus. Lighter zones are β phase, the dark phase is the α phase.

and the α fraction decreases. The influence of the residence time will thus increase for higher temperatures in the $\alpha + \beta$ range.

Further evidence is provided in Fig. 5, where the microstructure of SLM material is compared after 2 and 20 h at 940 °C, below the β transus. The α phase has started to globularize at some locations as indicated by the arrows in Fig. 5b, whereas the majority of the section is similar to that after 2 h. The α plates are 2.23 ± 0.12 μm wide after 2 h and have coarsened to an average width of 2.80 ± 0.16 μm after 20 h.

Previous research suggests that to achieve 50% globularization of the α phase at 955 °C, a residence time of approximately 8 h is necessary [17]. However, the starting material was originally equiaxed and deformed to local strains of 0.49, with a microstructure resembling elongated α grains rather than a lamellar structure. For finer, lamellar or platelike structures, it is expected that the time for globularization is drastically increased.

The residence time is more important when heat treating above the β transus. Consisting of a single phase, grain growth can now

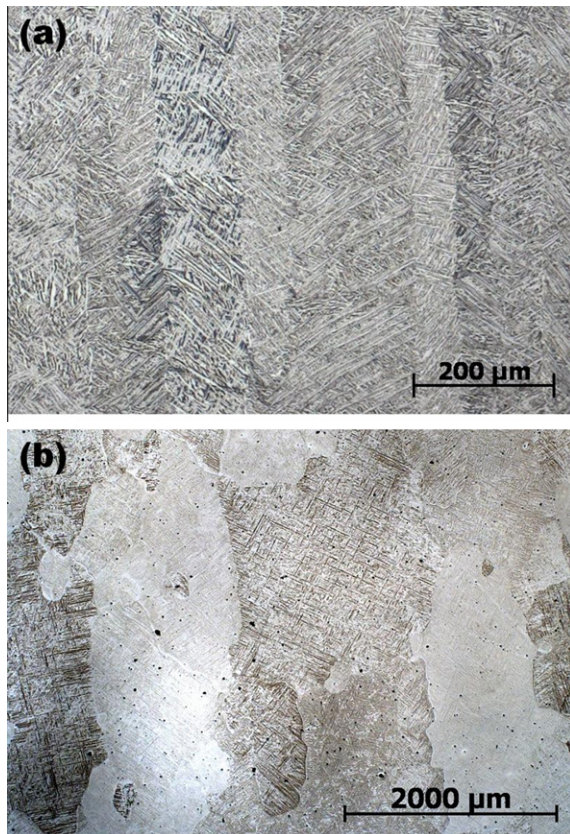


Fig. 3. Side view of SLM material (a) after 1 h at 940 °C followed by 2 h at 650 °C, illustrating the long columnar prior β grains. After heat treatment, a lamellar mixture of α and β is present inside the columnar prior β grains. (b) After 1015 °C, 2 h, WQ, indicating the extensive growth of the columnar grains. Due to the water quench, the microstructure is fully martensitic. Notice the different scales.

take place unhindered and fast, considering the high temperatures. As the size of α colonies is limited to the β grain size, larger colonies are possible for longer residence times. From Fig. 6, it is clear that the α colonies are larger after prolonged residence times. Lütjering [29] showed that the α colony size is a determining factor for the mechanical properties. As such, the residence time is an important parameter during β annealing.

3.1.3. Influence of the cooling rate

In Fig. 7, the microstructure of SLM produced parts after 2 h at 850 °C is compared for different cooling rates. These structures all look alike, and the α needle width is similar for all three, measuring $1.27 \pm 0.13 \mu\text{m}$ after furnace cooling, $1.22 \pm 0.09 \mu\text{m}$ after air cooling and $1.16 \pm 0.13 \mu\text{m}$ after water quenching. Since the α fraction at 850 °C is fairly large (73%, [20,23]), the influence of the cooling rate is minimal. With rising maximum temperature, the amount of primary α that is still present at high temperature decreases and the influence of the cooling rate increases. This is apparent from needle size measurements after treatment at 950 °C with different cooling rates. At this temperature, the α phase volume fraction is reduced to 23% and single α plates can now grow to a larger extent. The effect of cooling rate is now larger, leading to needle sizes of $1.48 \pm 0.14 \mu\text{m}$ after water quenching, $1.57 \pm 0.21 \mu\text{m}$ after air cooling and $2.23 \pm 0.12 \mu\text{m}$ after furnace cooling. During both air cooling and water quenching the cooling rate is too high for significant grain growth to occur. Low cooling rates, such as during furnace cooling, allow the grains to grow during cooling.

When treated above the β transus, the cooling rate is the most important parameter that determines the final dimensions of the α

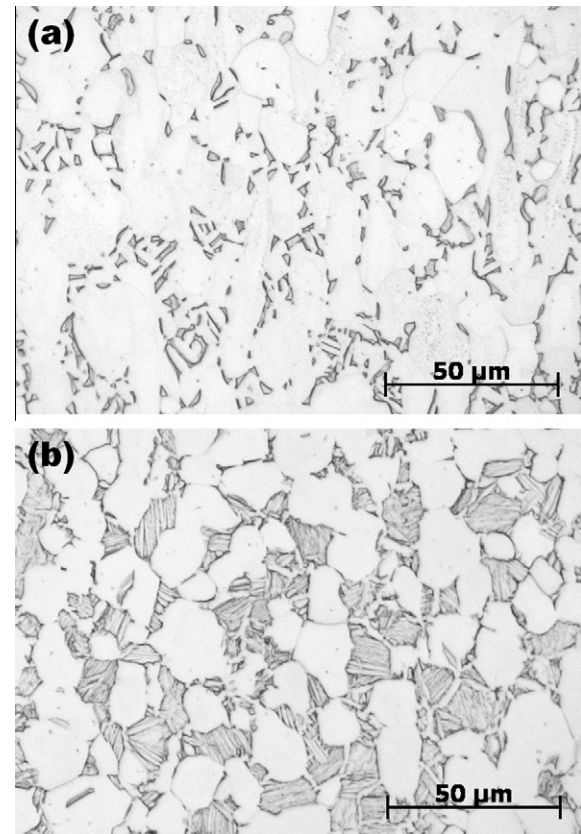


Fig. 4. Duplex microstructure of the reference material consisting of equiaxed α grains and lamellar $\alpha + \beta$. (a) 2 h at 780 °C, followed by furnace cooling and (b) 1 h at 940 °C, followed by air cooling to 650 °C. The α phase is light, the β phase is dark. Notice the increase in lamellar fraction when treated at a higher maximum temperature.

phase and even the morphology [22,29]. At high cooling rates, the large undercooling leads to the formation of many α nuclei resulting in smaller α colony size and a finer spacing between individual α plates. Furnace cooling results in lamellar $\alpha + \beta$ and air cooling results in an α -Widmanstätten microstructure or basket weave structure. The cooling rate during water quenching is higher than 410 °C/s, leading to α' martensite [24].

The microstructure of the reference material displays a predictable dependency on the cooling rate: upon cooling, the transformation of equiaxed β grains that exist at high temperatures produces lamellar $\alpha + \beta$. The lamellar spacing is dependent on the cooling rate, and decreases with increasing cooling rate. The thickness of the grain boundary α is also dependent on the cooling rate, decreasing with increasing cooling rate. When cooled from above the β transus, the cooling rate determines the size of the α colonies. The maximum size of an α colony is limited by the size of the β grain in which it originates [30].

3.2. Mechanical properties

The mechanical properties of untreated SLM and reference material are shown in Fig. 8 and are listed in Table 1. Three differences should be noted. First, the Young's modulus of the SLM material is slightly lower than that of the reference material. This is most likely caused by texture, which will be discussed in Section 4. Second, the SLM material is much stronger than the reference material. This is true for all material processed by SLM because the rapid cooling conditions always lead to a fine microstructure. Third, because of the fine lamellar structure, the fracture strain is

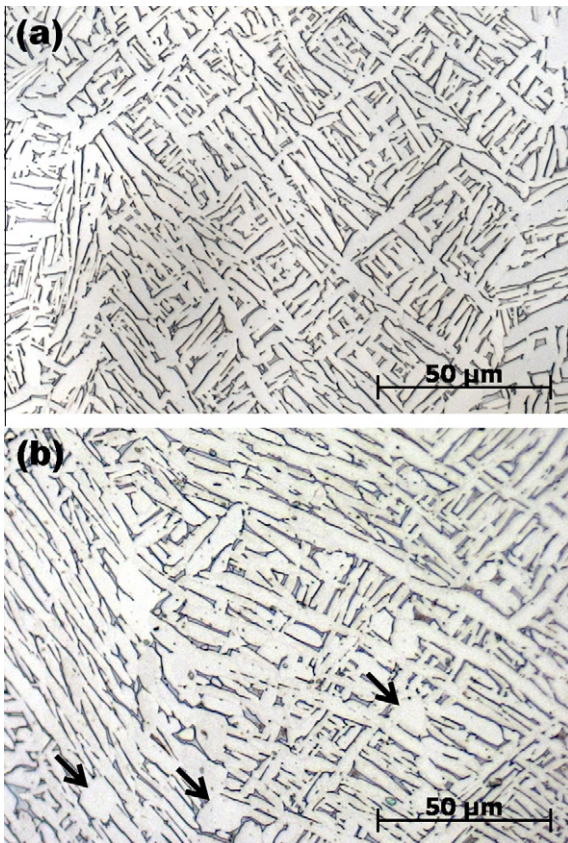


Fig. 5. Comparison of the similarity in α plate size after (a) 2 h at 940 °C and (b) 20 h at 940 °C, followed by furnace cooling. The α phase is light, β is dark. The arrows in (b) indicate globularized α grains.

much lower compared to the equiaxed reference material. Note that the yield and ultimate strength of the reference material differ by only 50 MPa, indicating low strengthening by deformation.

An overview of results after heat treatments of the SLM material is given in Table 2. From these results, treatment two (2 h at 850 °C, followed by furnace cooling) and seven (1 h at 940 °C, followed by air cooling and tempering for 2 h at 650 °C and air cooling) seem to produce the best overall results. Both of these treatments reach temperatures relatively high in the $\alpha + \beta$ zone and maintain some α at high temperature. A previous study on increasing the ductility of Ti6Al4V produced by SLM [5] produced the same mechanical properties as were obtained after treatment two, but did not state the heat treatment parameters that were used. The microstructure however differed to some extent, with some globular α being reported.

The mechanical properties differ greatly after the various heat treatments. When plotting the maximum strain and yield stress in function of the maximum heat treating temperature, as in Fig. 9, certain tendencies can be noticed, regardless of the cooling rate. First, the fracture strain of the SLM material goes up with rising maximum temperature, from 9.04 ± 2.03 after heat treatment six (max. 705 °C) to 14.06 ± 2.53 after heat treatment five (max. 1020 °C). The low fracture strain after treatment one could be due to the formation of very fine Ti_3Al precipitates, although these were not visible by SEM. These precipitates are known to occur for holding temperatures below 550 °C [29]. In contrast to the results in Refs. [5,27], where yield stress and UTS values are reported to increase, the yield stress and UTS decrease after heat treatment, as was expected due to coarsening of the microstructure compared to the original fine α' martensite. The yield stress decreases from 1026 ± 35 after heat treatment six to 760 ± 19 after heat treatment

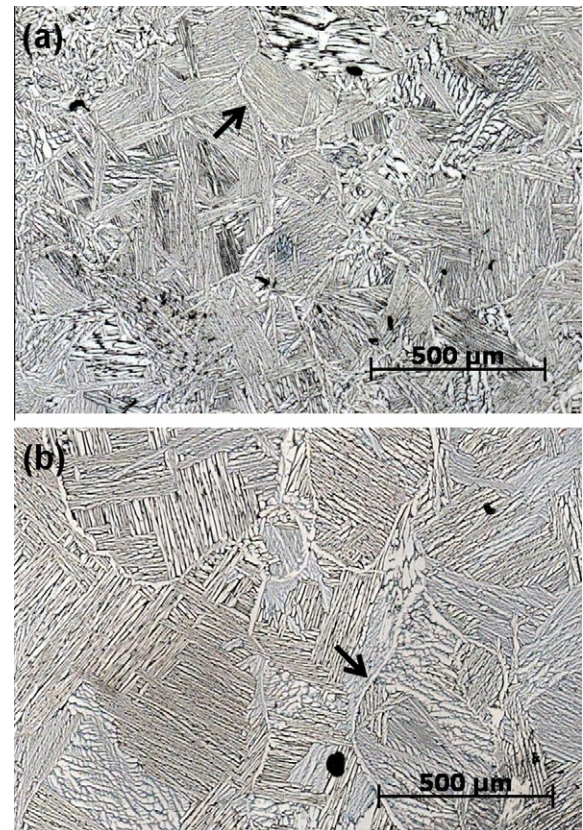


Fig. 6. Illustration of the smaller α colony size after (a) 2 h at 1020 °C compared to after (b) 20 h at 1040 °C, followed by furnace cooling. The α phase is light, β is dark. The arrows indicate grain boundary α .

five. The difference between the yield stress and the ultimate tensile strength, which is more than 200 MPa for as built SLM parts remains stable at about 60 MPa after heat treatment. This means that after heat treatment, the SLM material partially loses the ability to strengthen by deformation.

The response of the *reference material* to the heat treatments is completely different and is shown in Fig. 9a and c. It is clear that the yield stress does not change significantly after the different heat treatments. This is due to the competitive growth of both the α and β grains at high temperature, thus effectively hindering each other to grow. This leads to similar grain sizes after each treatment. Following the Hall-Petch relation, the yield stresses after the treatments do not differ largely. As illustrated in Fig. 9a, the fracture strain of the reference material decreases drastically with rising heat treatment temperature. This is attributed to the development of a duplex microstructure, as will be discussed in Section 4.

Standard heat treatments for Ti6Al4V were also performed on SLM produced parts, including the regular ‘mill anneal’ for cold deformed Ti6Al4V (treatment six, Table 2), duplex anneal (treatment seven) and a β anneal (treatment eight) [30]. β annealing normally leads to improved fracture toughness but a lower ductility.

From the results in Table 2 and Fig. 9, it can be seen that these treatments did not produce the expected results, neither for the SLM material nor for the equiaxed reference material. This is because these treatments are designed for specific purposes, starting from a specific microstructure, for example the heavily deformed structure before mill annealing. The reference material already consists of the equiaxed microstructure desired after treatment six, and the SLM material consists of a very fine, needle-like martensite rather than a heavily deformed mixture of α and β . The

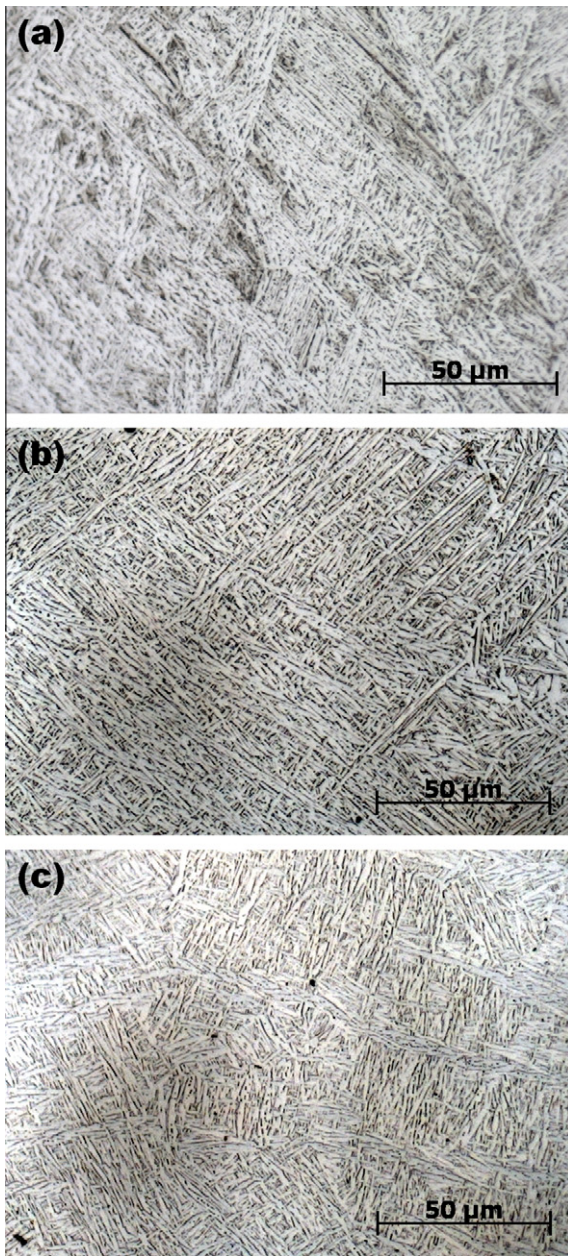


Fig. 7. Microstructure of the SLM material after 2 h at 850 °C, followed by (a) furnace cooling, (b) air cooling and (c) water quenching. The α needle size is very similar for all three microstructures, illustrating the minor effect of cooling rate when treated below the β transus.

maximum temperature of treatment six is too low to lead to any significant changes. Treatment seven however is executed at high temperature below the β transus. As debated earlier in Section 3.1, temperature is of major importance when treated below the β transus, which is why this treatment led to favorable results for SLM produced parts. Considering the β anneal, the ductility of the SLM material is increased rather than decreased. β annealing an equiaxed microstructure transforms it to a lamellar $\alpha + \beta$, Widmanstätten α or martensitic α' microstructure, depending on the cooling rate. All of these structures have a lower ductility and because of the lamellar structure, the crack path is deviated during fracture. This leads to an increased fracture toughness [31]. However, during β annealing of SLM material, the α' structure transforms into a coarser lamellar structure, increasing rather than decreasing the ductility.

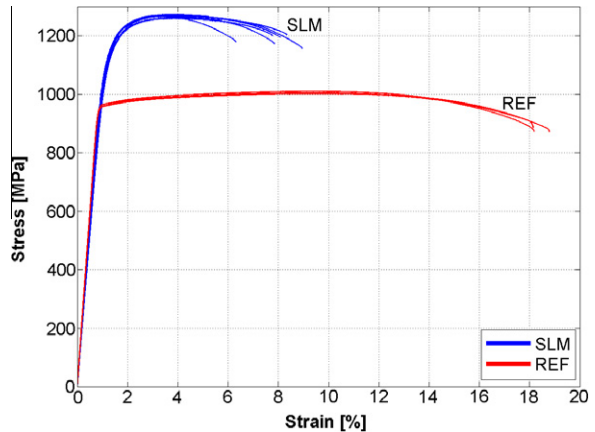


Fig. 8. Stress–strain curves for untreated SLM material and reference material.

Table 1
Mechanical properties of untreated SLM and reference material.

	E (GPa)	σ_y (MPa)	UTS (MPa)	$\varepsilon_{\text{fracture}}$ (%)
SLM	109.2 ± 3.1	1110 ± 9	1267 ± 5	7.28 ± 1.12
Reference	120.2 ± 1.9	960 ± 10	1006 ± 10	18.37 ± 0.88

4. Discussion

Comparing the ductility of the reference material and the SLM material after heat treatment as in Fig. 9, the fracture strain of the SLM material increases with rising maximum temperature, whereas the reference material loses up to 86% of its ability to deform. This is most likely caused by the formation of a duplex structure in the reference material, in which the α stabilizing alloying elements are mostly located in the primary α grains. The α phase in the lamellar section is then relatively poor in alloying elements, causing a great difference in strength between the α and β lamellae. This causes rapid formation of cracks and early failure of the material [29,32]. Because there are no equiaxed α grains, this segregation effect does not occur in the SLM material.

For the *reference material*, the maximum heat treating temperature determines only the final lamellar $\alpha + \beta$ fraction when treated below the β transus. Since the equilibrium β fraction is higher at temperatures closer to the β transus, and these equiaxed β grains transform to lamellar $\alpha + \beta$ upon cooling, a higher heat treating temperature will result in a larger lamellar fraction at room temperature. The lamellar spacing is determined by the cooling rate, with higher cooling rates resulting in a finer lamellar spacing.

The final spacing of the microstructural features in the *SLM material* is not primarily dependent on the cooling rate, but on the maximum temperature for heat treatments in the intermediate $\alpha + \beta$ range. The SLM material originally consists of fine α' needles. When heated, α phase is nucleated along the α' boundaries and vanadium atoms are expulsed, leading to the formation of β at the α phase boundaries [33]. At high temperatures, only a fraction of the original amount of nuclei is still present, since the equilibrium α fraction is lower, but still considerable (e.g. 73% at 850 °C, 23% at 950 °C [20,23]). Originating from a fine α' microstructure, these α phase nuclei are scattered at high temperature. For higher temperatures, less nuclei are present and they can coarsen to a greater extent before interaction with other plates will occur.

Thus, for intermediate temperatures in the $\alpha + \beta$ range, the size of the α needles at room temperature is mostly determined by the number of α needles at high temperature, which in turn is closely related to the temperature. At high temperatures in the $\alpha + \beta$ range,

Table 2

Mechanical properties of the SLM material after different heat treatments. WQ = water quenching, AC = air cooling, FC = furnace cooling. Treatment six to eight are well known titanium heat treatments [30]. Samples for treatment three were built in a different batch in which building errors are present, which led to premature failure of the components.

Nr.	T (°C)	t (h)	Cooling rate	E (GPa)	σ_y (MPa)	UTS (MPa)	$\varepsilon_{\text{fracture}}$ (%)
1	540	5	WQ	112.6 ± 30.2	1118 ± 39	1223 ± 52	5.36 ± 2.02
2	850	2	FC	114.7 ± 3.6	955 ± 6	1004 ± 6	12.84 ± 1.36
3	850	5	FC	112.0 ± 3.4	909 ± 24	965 ± 20	– (premature failure)
	1015	0.5	AC				
4	followed by			114.9 ± 1.5	801 ± 20	874 ± 23	13.45 ± 1.18
	843	2	FC				
5	1020	2	FC	114.7 ± 0.9	760 ± 19	840 ± 27	14.06 ± 2.53
6	705	3	AC	114.6 ± 2.2	1026 ± 35	1082 ± 34	9.04 ± 2.03
	940	1	AC				
7	followed by			115.5 ± 2.4	899 ± 27	948 ± 27	13.59 ± 0.32
	650	2	AC				
	1015	0.5	AC				
8	followed by			112.8 ± 2.9	822 ± 25	902 ± 19	12.74 ± 0.56
	730	2	AC				

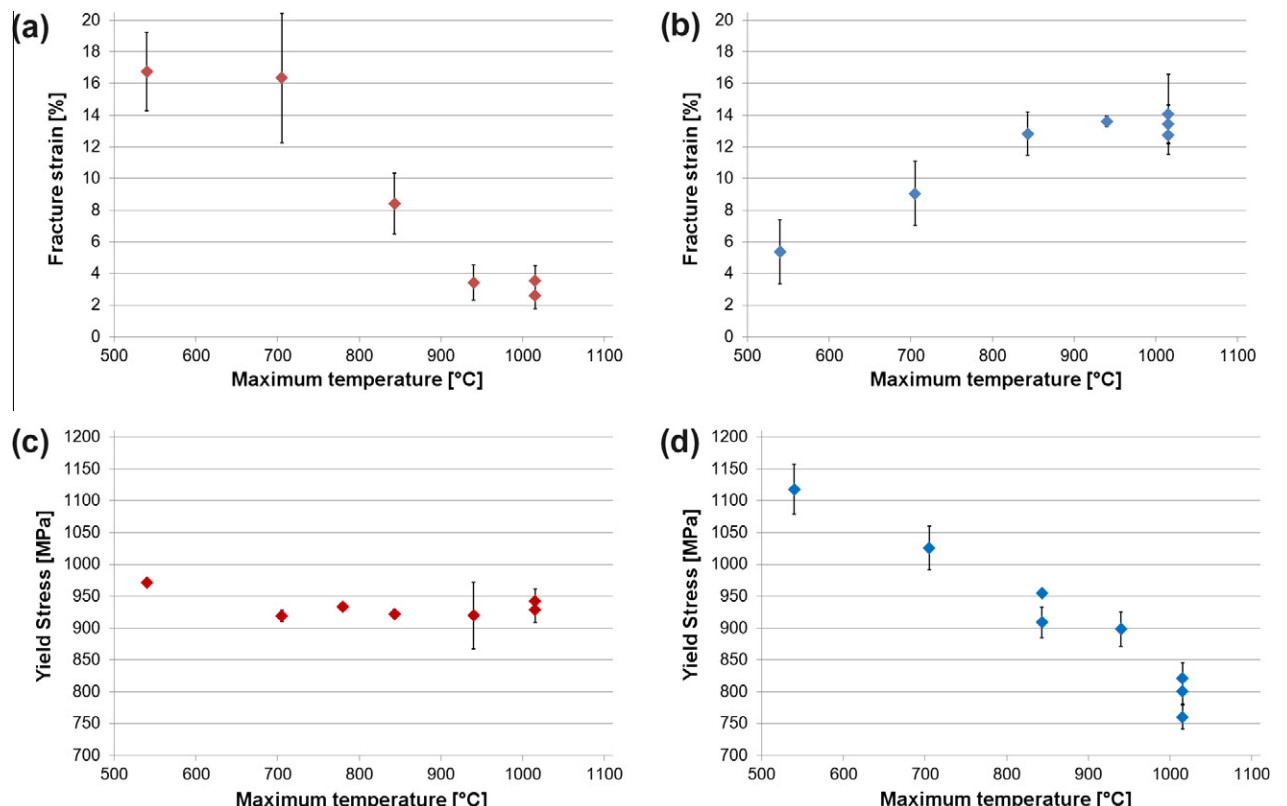


Fig. 9. Fracture strain and yield stress of the reference (a and c) and SLM material (b and d) in function of the maximum heat treating temperature. Results of all heat treatments are shown, regardless of cooling rate. All super-transus treatments used either AC or FC from the β range.

the effect of cooling rate becomes more distinct, with furnace cooling leading to a coarser microstructure.

From comparison between the microstructure of the SLM material treated below the β and above the β transus it is clear that the SLM footprint is erased for temperatures above the β transus. During heating, the SLM material gradually transforms back to the original columnar β grains. However, these columnar grains are no longer present after cooling from above the β transus. Instead, the microstructure consists of α colonies inside large, semi-equiaxed, previous β grains. Following the Burgers relation given in Equation (1) [34], a Widmanstätten structure is formed due to the preferential growth of the α phase parallel to the (110) family of crystallographic planes of the β phase [22,24] for intermediate cooling rates between air cooling and furnace cooling [30].

$$(110)_\beta \leftrightarrow (0001)_\alpha \quad (1)$$

$$\langle 1\bar{1}1 \rangle_\beta \leftrightarrow \langle 11\bar{2}0 \rangle_\alpha$$

Because growth along these planes is faster, the α phase is formed as flat plates or needles. The large difference in size and shape of the transformed β grains after treatment above 995 °C compared to the original columnar β grains present in as built SLM parts indicates extensive grain growth at temperatures above the β transus, up to the point where the columnar grains resemble a coarse equiaxed microstructure with large grains several millimeters long and approximately 620 μm wide. This is illustrated by Fig. 10, where EBSD orientation maps of the microstructure after treatments below (a) and above (b) the β transus are shown. The black lines are intensified drawings of the prior β grain boundaries.

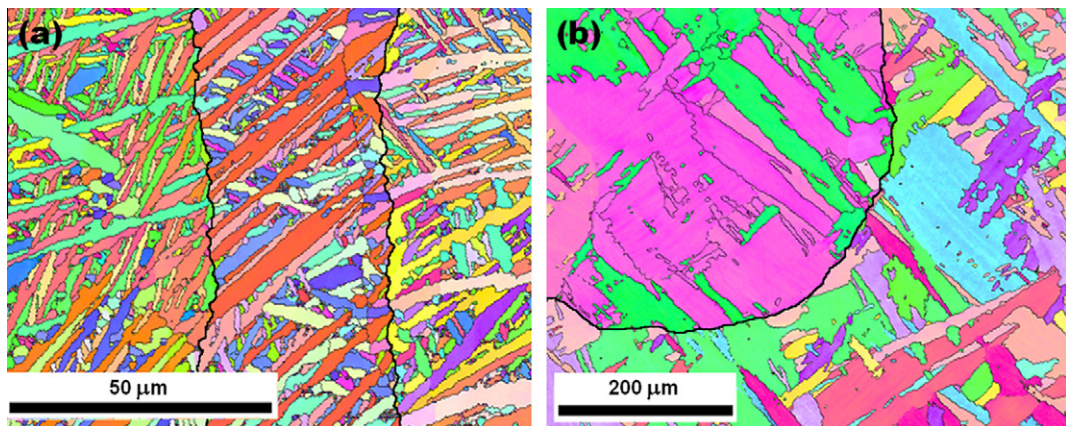


Fig. 10. EBSD orientation maps of (a) SLM material after 2 h at 850 °C, followed by furnace cooling, (b) SLM material after half an hour at 1020 °C, followed by 2 h at 730 °C and air cooling. Contrast is provided by the different orientations of the α' phase, while the β phase is present as a thin layer between the α' phase. Notice the different scale. The build direction for both images is vertical.

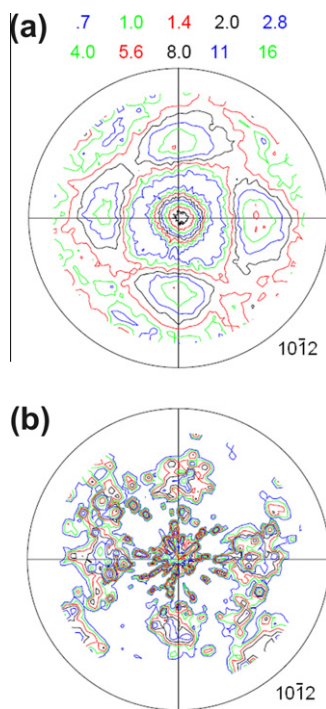


Fig. 11. HCP $\langle 1\ 0\ \bar{1}\ 2 \rangle$ pole figures of (a) the untreated SLM material and (b) the SLM material heat treated above the β transus, for 20 h at 1040 °C, followed by furnace cooling. In (a), the texture is present in the α' phase which has a similar crystal lattice as the α phase. In (b) the texture in the α phase is shown.

During solidification, the bcc β phase preferentially grows in the $\langle 100 \rangle$ direction, giving rise to the long, columnar prior β grains as described by Thijs et al. [7] and Kobryn and Semiatin [35]. The $\langle 100 \rangle$ direction of each of these columnar grains is thus oriented quasi parallel to the build direction, and the rotation of the grain around this direction is considered to be random, causing the presence of a fiber-like texture. Due to the fast cooling, the β phase then transforms to the α' phase according to the Burgers relation given by Equation (1). The texture of the parent β phase is transmitted to a texture of the α' phase, as can be seen in the $\langle 1\ 0\ \bar{1}\ 2 \rangle$ pole figure of the top view of untreated SLM material in Fig. 11a.

When treated above the β transus, the β grains in the SLM material will grow and the texture is maintained, as seen in the pole figure in Fig. 11b. The texture after homogenization in the β field is not

as distinguished because of the extremely large grain sizes after prolonged treatment above the β transus, causing large intensity peaks for one individual grain.

Due to the texture in the build direction, it is suspected that mechanical properties of SLM parts are different parallel to the build direction compared to perpendicular to the build direction. For an austenitic stainless steel, Meier and Haberland [36] reported the tensile strength and elongation to be lower for samples tested in the build direction compared to horizontally built specimens.

5. Conclusion

Several heat treatments were performed on Ti6Al4V produced by SLM with an original α' microstructure. The influence of temperature, time and cooling rate were distinguished. When heated, α' phase is precipitated at the α' boundaries. At maximum temperatures below the β transus, the mixture of α' and β phase prevents grain growth and the original, columnar prior β grains remain visible after cooling. The width of the α' plates after heat treatment is mainly dependent on the maximum temperature for sub-transus treatments, and primarily dependent on the cooling rate for super-transus treatments. The residence time and cooling rate do not have a significant influence for sub-transus treatments, although their influence increases when temperatures are closer to the β transus. When treated above the β transus, the columnar β grains grow extensively to form large, semi-equiaxed β grains. For FC, AC and WQ samples, the β grains then transform to lamellar $\alpha + \beta$, α -Widmanstätten colonies or α' martensite, respectively. The residence time influences the final dimensions of the transformed β grains.

Mechanical properties are very much dependent on the maximum heat treatment temperature. With rising maximum temperature, σ_y and UTS decline and the fracture strain rises because of the transformation of the fine α' needles to a more coarse mixture of α and β . Overall best results are obtained after 2 h at 850 °C, followed by furnace cooling, or 1 h at 940 °C, air cooling and tempering for 2 h at 650 °C followed by air cooling. The results for all properties are well above ASTM Standards for forged (ASTM F1472) and cast Ti6Al4V (ASTM F1108). The importance of the initial microstructure cannot be stressed enough. Due to the very fine martensite, the kinetics are completely different as compared to treatment of equiaxed or heavily deformed microstructures. Consequently, application of standard heat treatments shows that these treatments do not lead to the usual or expected results. Due to the specific process conditions and hence specific microstructure, SLM produced parts need to be treated differently than bulk alloy parts.

For SLM produced Ti6Al4V parts, heat treating at intermediate to high temperatures below the β transus, followed by furnace cooling proved to be optimal for an overall optimization of tensile properties, with deformability levels safely above the prescribed standards and yield stress and UTS levels close to 1 GPa.

References

- [1] G.N. Levy, Phys. Proc. 5 (2010) 65–80.
- [2] J. Kruth, CIRP Ann. – Manuf. Technol. 40 (1991) 603–614.
- [3] J.P. Kruth, G. Levy, F. Klocke, T.H.C. Childs, CIRP Ann. – Manuf. Technol. 56 (2007) 730–759.
- [4] L.E. Murr, S.A. Quinones, S.M. Gaytan, M.I. Lopez, A. Rodela, E.Y. Martinez, D.H. Hernandez, E. Martinez, F. Medina, R.B. Wicker, J. Mech. Behav. Biomed. Mater. 2 (2009) 20–32.
- [5] L. Facchini, E. Magalini, P. Robotti, A. Molinari, S. Hoges, K. Wissenbach, Rapid Prototyping J. 16 (2010) 450–459.
- [6] L. Facchini, E. Magalini, P. Robotti, A. Molinari, Rapid Prototyping J. 15 (2009) 171–178.
- [7] L. Thijss, F. Verhaeghe, T. Craeghs, J. Van Humbeeck, J.P. Kruth, Acta Mater. 58 (2010) 3303–3312.
- [8] E. Chlebus, B. Kuźnicka, T. Kurzynowski, B. Dybała, Mater. Charact. 62 (2011) 488–495.
- [9] R. Morgan, C.J. Sutcliffe, W. O'Neill, J. Mater. Sci. 39 (2004) 1195–1205.
- [10] I. Yadroitsev, I. Smurov, Surface morphology in selective laser melting of metal powders lasers, in: Manufacturing 2011 (Ed.), Proceedings of the Sixth International, Wlt Conference on Lasers in Manufacturing, vol. 12, Pt A, Amsterdam, Elsevier Science Bv., 2011, pp. 264–270.
- [11] E. Yasa, J. Deckers, J.P. Kruth, Rapid Prototyping J. 17 (2011) 312–327.
- [12] A.B. Spierings, N. Herres, G. Levy, Rapid Prototyping J. 17 (2011) 195–202.
- [13] J. Van Vaerenbergh, Process optimisation in Selective Laser Melting, Ph.D. Twente, University of Twente, 2008.
- [14] P. Mercelis, J.P. Kruth, Rapid Prototyping J. 12 (2006) 254–265.
- [15] B. Vandenbroucke, Selective Laser Melting of Biocompatible Metals for Rapid Manufacturing of Medical Parts, Ph.D. Leuven, KU Leuven, 2008.
- [16] F. Verhaeghe, T. Craeghs, J. Heulens, L. Pandelaers, Acta Mater. 57 (2009) 6006–6012.
- [17] N. Stefansson, S. Semiatin, D. Eylon, Metall. Mater. Trans. A 33 (2002) 3527–3534.
- [18] S. Semiatin, N. Stefansson, R. Doherty, Metall. Mater. Trans. A 36 (2005) 1372–1376.
- [19] S. Malinov, Z. Guo, W. Sha, A. Wilson, Metall. Mater. Trans. A – Phys. Metall. Mater. Sci. 32 (2001) 879–887.
- [20] I. Katzarov, S. Malinov, W. Sha, Metall. Mater. Trans. A – Phys. Metall. Mater. Sci. 33 (2002) 1027–1040.
- [21] S. Semiatin, S. Knisley, P. Fagin, D. Barker, F. Zhang, Metall. Mater. Trans. A 34 (2003) 2377–2386.
- [22] F.J. Gil, M.P. Ginebra, J.M. Manero, J.A. Planell, J. Alloys Compd. 329 (2001) 142–152.
- [23] R. Pederson, O. Babushkin, F. Skystedt, R. Warren, Mater. Sci. Technol. 19 (2003) 1533–1538.
- [24] T. Ahmed, H.J. Rack, Mater. Sci. Eng. A 243 (1998) 206–211.
- [25] R. Dabrowski, Arch. Metall. Mater. 56 (2011) 217–221.
- [26] T. Sercombe, N. Jones, R. Day, A. Kop, Rapid Prototyping J. 14 (2008) 300–304.
- [27] T. Vilaro, C. Colin, J.D. Bartout, Metall. Mater. Trans. A 42A (2011) 3190–3199.
- [28] E.E. Underwood, Quantitative Stereology, Addison-Wesley Educational Publishers Inc., 1970.
- [29] G. Lütjering, Mater. Sci. Eng. A 243 (1998) 32–45.
- [30] R.R. Boyer, G. Welsh, E.W. Collings, Materials Properties Handbook: Titanium Alloys, ASM International, Materials Park, Ohio, 1994.
- [31] G. Lütjering, J.C. Williams, A. Gysler, Microstructure and Mechanical Properties of Titanium Alloys, Springer Science and Business Media, Titanium, 2007.
- [32] E. Brandl, Ph.D. Thesis, Brandenburg Technical University of Cottbus, 2010.
- [33] F.X. Gil Mur, D. Rodríguez, J.A. Planell, J. Alloys Compd. 234 (1996) 287–289.
- [34] W. Burgers, Physica 1 (1934) 561.
- [35] P.A. Kobry, S.L. Semiatin, J. Mater. Process. Technol. 135 (2003) 330–339.
- [36] H. Meier, C. Haberland, Experimental studies on selective laser melting of metallic parts, Materialwiss. Werkstofftech. 39 (2008) 665–670.

Ductility of a Ti-6Al-4V alloy produced by selective laser melting of prealloyed powders

Luca Facchini

Department of Materials Engineering and Industrial Technologies, University of Trento, Trento, Italy

Emanuele Magalini and Pierfrancesco Robotti

Eurocoating s.p.a., Ciré di Pergine, Italy

Alberto Molinari

Department of Materials Engineering and Industrial Technologies, University of Trento, Trento, Italy

Simon Höges

Department of Laser Technology, University of Aachen, Aachen, Germany, and

Konrad Wissenbach

Fraunhofer Institute for Laser Technology, Aachen, Germany

Abstract

Purpose – The aim of the paper is the study of the change in the mechanical properties (and in particular in ductility), with the microstructure, of a biomedical Ti-6Al-4V alloy produced by different variants of selective laser melting (SLM).

Design/methodology/approach – Ti-6Al-4V alloy produced by different variants of SLM has been mechanically characterized through tensile testing. Its microstructure has been investigated by optical observation after etching and by X-ray diffraction analysis.

Findings – SLM applied to Ti-6Al-4V alloy produces a material with a martensitic microstructure. Some microcracks, due the effect of incomplete homologous wetting and residual stresses produced by the large solidification undercooling of the melt pool, are observable in the matrix. Owing to the microstructure, the tensile strength of the additive manufactured parts is higher than the strength of hot worked parts, whereas the ductility is lower. A pre-heating of the powder bed is effective in assisting remelting and reducing residual stresses, but ductility does not increase significantly, since the microstructure remains martensitic. A post-building heat treatment causes the transformation of the metastable martensite in a biphasic a-b matrix, with a morphology that depends on the heat treatment. This results in an increase in ductility and a reduction in strength values.

Originality/value – The study evidenced how it is possible to obtain a fully dense material and make the martensite transform in Ti-6Al-4V alloy through the variation of the SLM process. The stabilization of the microstructure also results in an improvement of the ductility.

Keywords Alloys, Mechanical properties of materials, Manufacturing systems, Powders, Ductility

Paper type Research paper

1. Introduction

Ti-6Al-4V is an α - β titanium alloy widely used in the aeronautical and medical fields because of its chemical and mechanical features along with well-documented biocompatibility (Ping Li *et al.*, 2006). It is mostly processed by hot working, but in the last few years rapid prototyping techniques, based on sintering/melting of powders, have been developed for the production of complex geometries, directly from 3D CAD-data. One of the main advantages of these

techniques is the possibility to create complex networks with open and interconnected porosity both in the core material and onto the surface (Hollander *et al.*, 2006; Ponader *et al.*, 2007).

The energy for consolidation of the powders is provided by either a laser beam (selective laser melting (SLM)) (Hollander *et al.*, 2006; Bourell *et al.*, 2002; Over *et al.*, 2003) or an electron beam (electron beam melting (EBM)) (Cormier *et al.*, 2002; Mitchell, 1999). The common feature of these technologies is the melting and rapid solidification of a powder layer; under specific process conditions, solidification results in a fully dense solid body.

The current issue and full text archive of this journal is available at
www.emeraldinsight.com/1355-2546.htm

The authors thank Dr Mirco D'Incau and Ing. Ivan Lonardelli for supplying the XRD analyses, also the Provincia Autonoma di Trento, which co-founded the project.

Received: 20 March 2009

Revised: 17 July 2009, 9 November 2009

Accepted: 12 April 2010



- The optimization of the process has the following main tasks:
- The production of a fully dense material (except for the porous surface layers, when needed), which is obtained by the optimum combination of the four main process parameters: the power of the energy source (P), the scan speed (v), the hatch distance (d) and the thickness of the single layer (l) using a fixed beam diameter (D) (Simchi and Pohl, 2003).
 - The control of the residual stresses, caused by the localization of the thermal input, which may lead to distortion of the pieces, as well as to the formation of cracks.
 - The control of the as-built microstructure, which is strongly influenced by the large solidification undercooling of the melting pool.

Residual stresses are almost unavoidable. They are influenced by the building strategy (Kruth *et al.*, 2004) and are significantly smaller in EBM than in SLM since the former process is carried out with preheating of the powder bed to an average temperature of about 600°C (Facchini *et al.*, 2009), which reduces thermal gradients.

Titanium alloys typically undergo thermomechanical processes. Their conventional microstructure can be fundamentally classified by the size and the arrangement of the two phases α (hcp) and β (bcc) (Leyens and Peters, 2003; Collings, 1984). Depending on the working temperature and the cooling rate, the resulting microstructure can be lamellar or globular, fine or coarse. The lamellar microstructure is usually preferable for fracture toughness, fatigue crack propagation and oxidation behaviour, whilst the globular microstructure is better for strength, ductility and fatigue crack initiation.

The microstructure after rapid prototyping is quite different from that typical of hot worked parts, since the large undercooling promotes the formation of an acicular/lamellar hcp phase, which is inherently less ductile than the globular microstructure formed during hot working. In EBM, the as-built microstructure of Ti-6Al-4V contains acicular α , and β -phase, and does not find a correspondence in the international standard for biomedical applications (ISO 20160). It cannot be modified by heat treatment; nevertheless, the mechanical properties of the alloy satisfy the standard requirements (Facchini *et al.*, 2009).

In SLM, the solidification rate is higher than in EBM, since no pre-heating is applied to the growing part and the working zone. This results in a finer microstructure and larger residual stresses. Pre-heating has another eminent effect: it assists, in terms of energy, the remelting of the just-consolidated substrate, allowing incomplete homologous wetting due to oxide films to be avoided (Das, 2003).

In fact, if a contamination layer of oxide is present on the just-built metallic substrate, melted metal powder cannot properly wet the substrate itself. Surface remelting of the underlying substrate is effective in the elimination of the oxide layer; as a consequence, the molten metal can spread and wet the substrate.

In this work, the fabrication of a Ti-6Al-4V alloy by SLM has been investigated. Once the process parameters had been adjusted to obtain a full dense material, attention was focused on residual stresses and microstructure. Several process variants were investigated in order to reduce thermal gradients and modify the microstructure, and their effect on mechanical properties was studied, with particular reference to ductility.

2. Technologies and experimental procedures

2.1 The SLM process

The parts were produced in an EOS EOSINT M 270 machine or in an experimental machine at Fraunhofer ILT. In the first case, a power of 195 W and a scan speed of 225 mm/s were used. The SLM process at Fraunhofer ILT was instead carried out in an experimental machine built at ILT in which an neodymium-doped yttrium aluminium garnet laser developed at ILT is used to melt the powder with a maximum laser power of 180 W and a wavelength of 1,064 nm.

Energy involved in the melting of the metal powder is directly proportional to the power of the beam and inversely to the scan speed, the hatch distance and the layer thickness (Simchi and Pohl, 2003). As stated above, the optimum combination of these four main process parameters leads to full density of the part. Investigation of the parameters was carried out following a systematic procedure, consisting in fixing three of the four parameters and varying the fourth, thus evaluating the contribution of the single parameter.

An argon gas atomized powder, with spherical morphology and particle size below 50 µm, was used. Its nominal composition is reported in Table I.

Parts were built under an Ar protective atmosphere, with a nominal beam power of 120–200 W and a beam diameter of 200–600 µm for a melt pool diameter of 200–300 µm.

2.2 Chemical and microstructural analysis

The oxygen and nitrogen contents were analyzed by gas fusion in a Leco TC400 analyzer, while carbon and hydrogen contents were analyzed by combustion and by IR spectroscopy in a Leco CS125 and Leco TCH600 analyzer, respectively.

The microstructure was investigated under an optical microscope after polishing and etching with Kroll reagent. X-Ray Diffractometry (CuK α radiation on a Rigaku 3D-Max diffractometer) was used for the quantitative analysis of the microstructural constituents.

2.3 Mechanical testing

Batches of five to six samples for tensile testing were obtained from a job of bars with a rectangular cross-section, which were built up perpendicularly to their main axis. All the batches were machined in order to obtain the specimen geometry for tensile testing, according to the ASTM E8M standard. Specimens have a rectangular section, with an overall length of 89.64 mm and a reduced section length of 31.76 mm.

Table I Nominal chemical composition of the Ti-6Al-4V pre-alloyed powder used in the process

Chemical element	SLM powder (%)	ISO 5832-3 requirements (%)
Al	5.970	5.5/6.75
V	4.010	3.5/4.5
Fe	0.056	<0.3
O	0.160	<0.2
H	0.0034	<0.015
N	0.010	<0.05
C	0.013	<0.08
Ti	Balance	Balance

Note: Standard requirements reported

Tensile tests were carried out with an Instron 8516 servo-hydraulic machine, following the ASTM E8M standard and according to the ISO 6892 standard indications. A 0.2 mm/min cross-head speed was applied. An axial extensometer was employed for the elongation measurement, with a gage length of 12.5 mm.

Elastic modulus (E), yield stress at 0.2 per cent of elongation (σ_y), ultimate tensile strength (UTS) and percent elongation at fracture (ε) were determined from stress-strain curves. The fracture surface of broken specimens was examined by an environmental scanning electron microscope using gaseous secondary electrons.

In order to obtain a good comparison with Ti-6Al-4V produced by traditional processes, ten tensile specimens were machined from a wrought and annealed bar, and then tested.

3. Results and discussion

The presence of interstitial elements (oxygen, hydrogen, nitrogen and carbon) is critical for the ductility of the alloy. In fact, these elements are α -stabilizers (and α -phase is less ductile than β). Moreover, oxygen and nitrogen distort the hcp lattice, limiting the mobility of dislocations and embrittling the material (Leyens and Peters, 2003).

The results of the chemical analysis of SLM parts are reported in Table II. Carbon and oxygen contents are in agreement with the ASTM and ISO prescriptions; the detected amounts do not greatly affect the mechanical properties.

As previously described, the microstructure of the Ti-6Al-4V alloy can be lamellar or globular. Hot working and annealing produce a typical α -globular microstructure, because of the strain involved in the process. Semiatin *et al.* (2005) found that heat treatment of an acicular microstructure in the biphasic $\alpha + \beta$ field produces some globularization of the α -phase only in the case of pre-strained material, and even in this case the kinetics are quite slow. The microstructure of the hot worked and annealed material considered in this work is shown in Figure 1, where an α -globular phase in an $\alpha + \beta$ matrix is observable. The presence of the β -phase (8 per cent) is confirmed by X-ray diffraction (XRD) analysis (Figure 2).

Figure 3 shows the tensile stress-strain curve of the wrought alloy. The material has a peculiar strain hardening behaviour, with a very low strain hardening rate. In consequence, the UTS and the yield stress are quite similar. The ductility is good, and well associated to the microstructure, as reported in Leyens and Peters (2003).

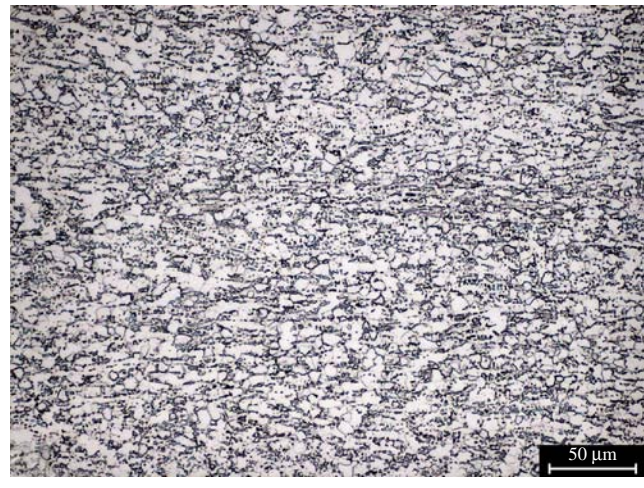
Such a microstructure is associated to the mechanical properties reported in Table III.

Table II Chemical analysis on tensile specimens: oxygen, hydrogen, nitrogen and carbon percentages

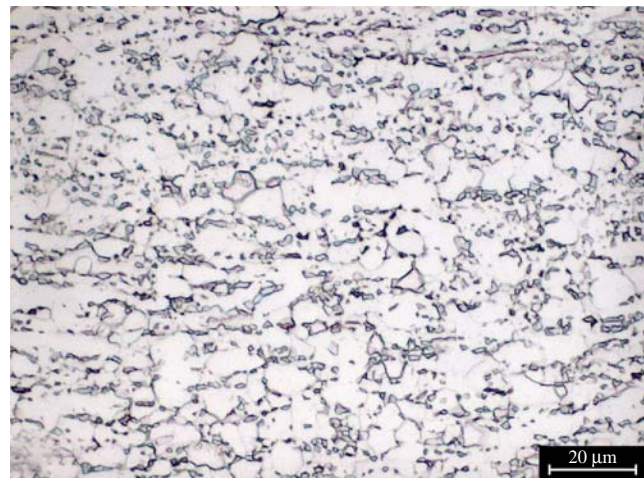
	SLM	ASTM F1472	ISO 5832-3
O	0.1900 ± 0.020	< 0.20	< 0.20
H	0.0049 ± 0.0005	< 0.015	< 0.015
N	0.0041 ± 0.0002	< 0.05	< 0.05
C	0.0280 ± 0.0031	< 0.08	< 0.08

Note: Requirements for ASTM and ISO standards are reported

Figure 1 Microstructure of the material produced by hot working and annealing



(a)



(b)

Note: Globular α -phase (light) in a biphasic $\alpha + \beta$ matrix

Figure 2 XRD pattern of the hot worked and annealed material

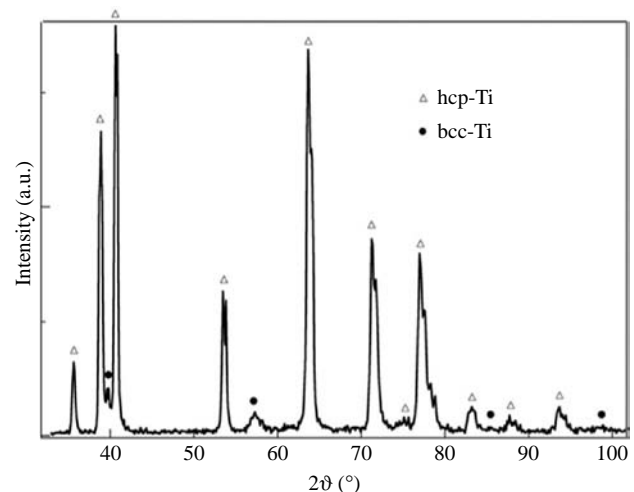


Figure 3 Stress-strain curves for the material produced by hot working and annealing

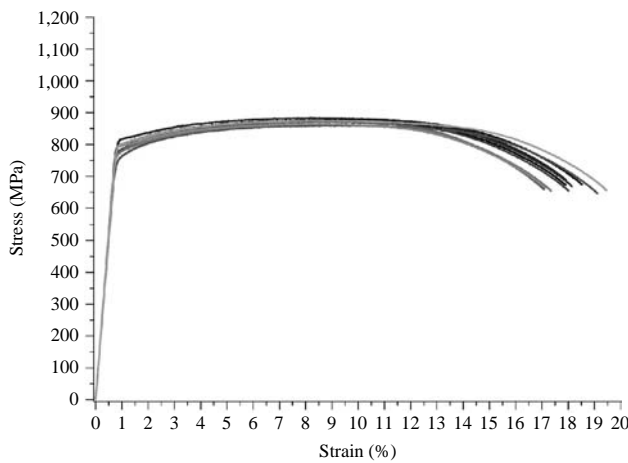


Table III Tensile properties of the material produced by SLM compared to the wrought material and to the ISO standard

	Hot worked and annealed	SLM	ISO 5832-3
E (GPa)	104 ± 2	110 ± 5	—
σ_y (MPa)	790 ± 20	990 ± 5	>780
UTS (MPa)	870 ± 10	1,095 ± 10	>860
A (%)	18.1 ± 0.8	8.1 ± 0.3	>10

The as-built microstructure of the material produced by SLM has a very fine, acicular morphology (Figure 4). The XRD analysis indicates the presence of hcp phase only (Figure 5). The hcp pattern can be attributed to both the α -phase and the α' martensite, as they have the same crystalline structure and very similar lattice parameters (Kubiak and Sieniawski, 1998; Jovanović *et al.*, 2006; Malinov *et al.*, 2002).

Because of the very large solidification undercooling, the microstructure is interpreted as martensitic, with the typical needles visible on the etched metallographic section (Figure 4). Differently from EBM, where the formerly produced martensite (with a very high solidification rate of the melt spun) is transformed into $\alpha + \beta$ mixture by soaking at the process temperature (Gil Mur *et al.*, 1996), here the metastable martensite remains the only phase present at room temperature.

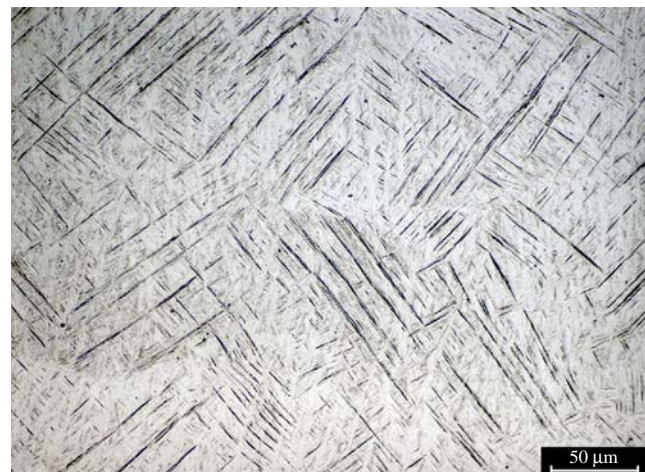
The material produced by SLM is fully dense (relative density 99.7 ± 0.1 per cent), but the metallographic observation evidenced the presence of microcracks (length 50/100 μm ; Figure 6), as a consequence of incomplete homologous wetting (Das, 2003).

Figure 7 shows the tensile stress-strain curve of the as-built material. The yield stress is higher than in wrought alloy, because of the martensitic microstructure, but the combined effect of martensite, microcracks and residual stress is responsible for low ductility, as shown in Figure 7.

Figure 8 shows the fracture surface of the as-built material. The morphology is mainly ductile, but deformation is quite poor around pre-existing cracks, because of the poor work hardenability of the alloy.

Tensile properties are summarized in Table III, including reference to those predicted by ISO 5832-3 and comparison with those of the wrought alloy. The as-built material has a higher strength but a lower ductility than those taken as a reference.

Figure 4 Microstructure of the material produced by SLM



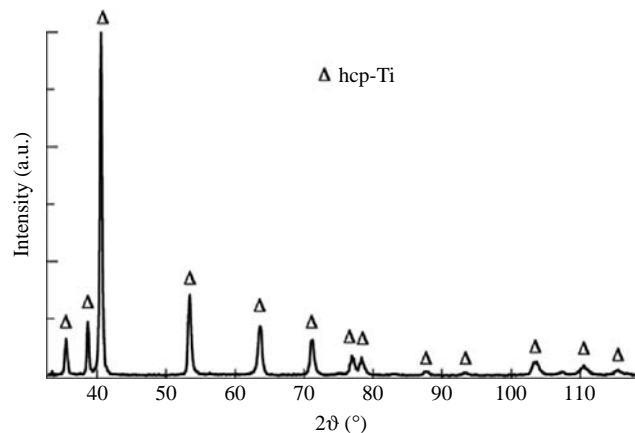
(a)



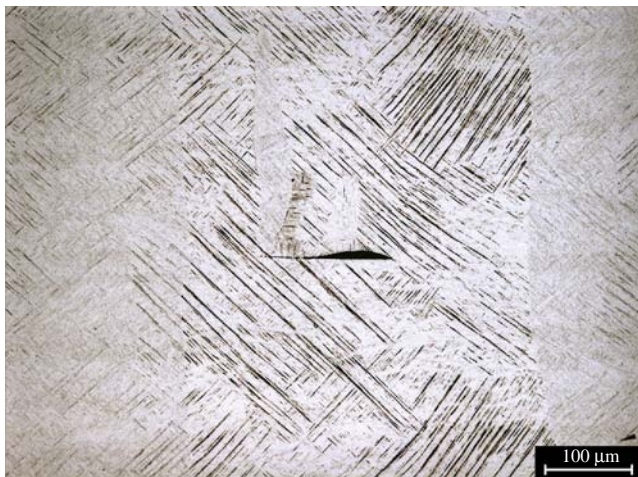
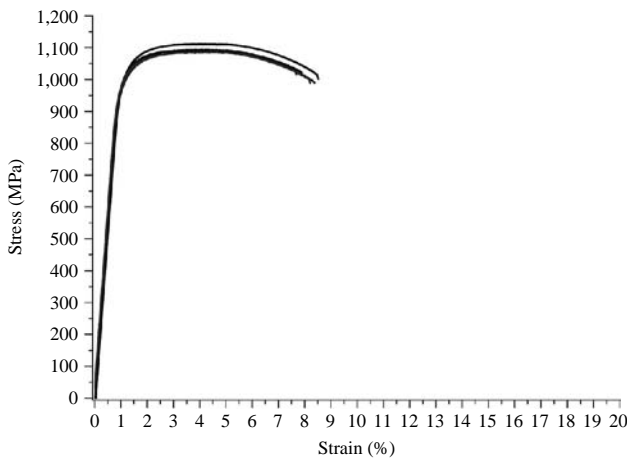
(b)

Note: Oriented martensite plates containing acicular hcp phase

Figure 5 XRD pattern of the as-built material



In order to assist the remelting of the just-consolidated material and to reduce residual stresses, the process has been suitably modified following literature references (Over, 2003). This solution actually eliminates cracks in the as-built material,

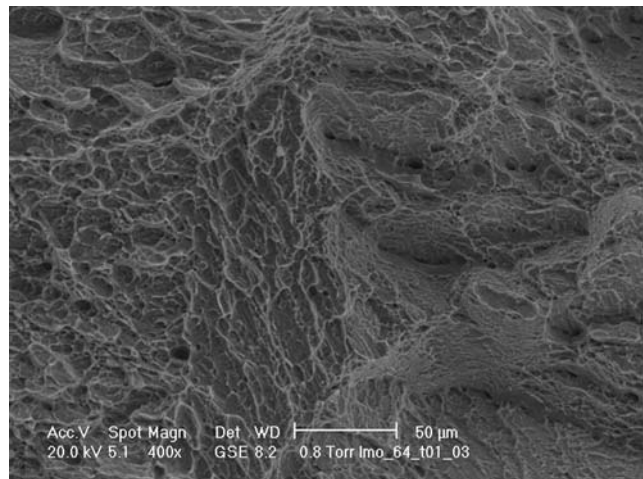
Figure 6 Microcrack in the material produced by SLM**Figure 7** Stress-strain curves for the as-built material

but the microstructure is still acicular martensitic, as shown by Figure 9 and confirmed by XRD analysis.

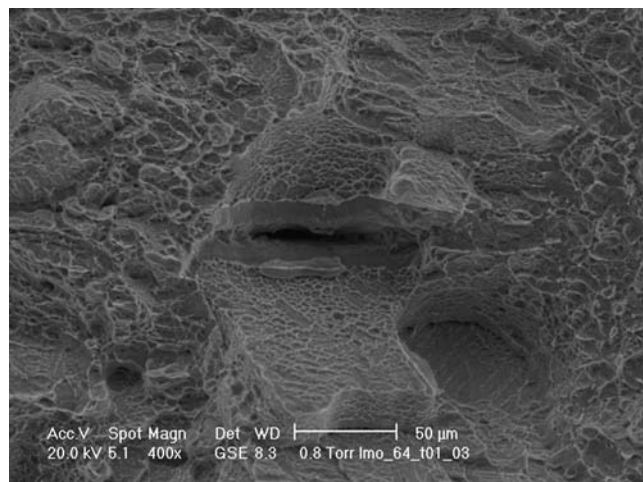
After the modified process, the tensile behaviour does not improve significantly (Figure 10), comparing them with those of Figure 7; yield stress and UTS are increased up to 1,040 and 1,140 MPa, respectively, but ductility is still low, around 8 per cent.

The presence of martensite is then responsible for the low ductility. Martensite is a metastable phase, which can be transformed by heat treatment. A post-SLM heat treatment was then carried out, obtaining the microstructure shown in Figure 11. It is biphasic, with columnar α -phase crystals formed at the boundaries of the original martensitic plates and an α - β mixture within. The amount of β -phase is 6 per cent, as shown measured by XRD (Figure 12). The microstructure is quite different from the globular microstructure of a wrought alloy, since alpha phase nucleates and grows in the interplate regions, developing a texture. There is a clear memory effect in the martensite to alpha transformation. In wrought alloy, instead, α -phase nucleates in the highly strained regions, which are homogeneously distributed in the cross-section, and grows symmetrically; this leads to the globular microstructure.

The mechanical properties are significantly improved by this process, as expected. Figure 13 shows the tensile stress-strain curves of the heat treated materials; strength is lower

Figure 8 Fracture surface of the as-built material

(a)



(b)

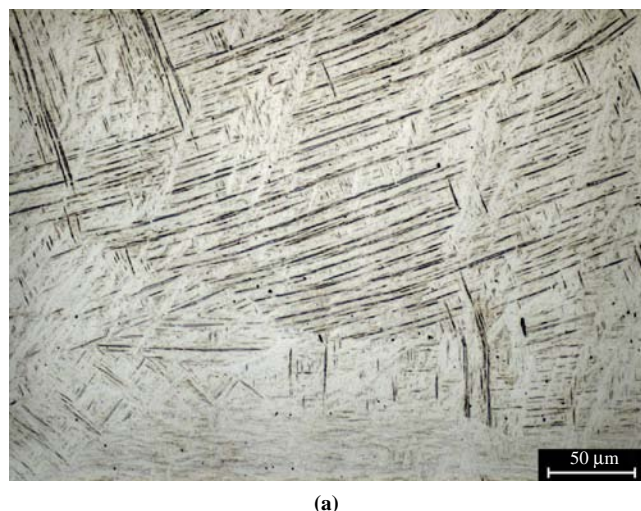
than that of the as-built alloy, but ductility is increased up to 10.6 ± 0.6 per cent.

In order to prevent the memory effect of the martensite to alpha transformation during heat treatment and obtain a biphasic microstructure, a second variant has been introduced in the process as a combination of heat treatments (Over, 2003; Hollander *et al.*, 2006). The microstructure resulting is shown in Figure 14: it consists of coarse lamellae of α -phase, with some globularization in isolated regions (Figure 14(b) and (c)). The amount of β -phase is 7 per cent, as measured by XRD analysis (Figure 15).

The stress-strain curves related to such a microstructure are shown in Figure 16. The tensile properties are very similar to those of the previous case, but ductility is slightly increased, due to the lack of texture in the alpha phase. Properties are reported in Table IV, and compared to those of the as-built material and of the references.

4. Conclusions

Ti-6Al-4V is an α - β titanium alloy widely used in orthopaedic and dental surgery because of its biocompatibility. Its mechanical properties strongly depend on its microstructure.

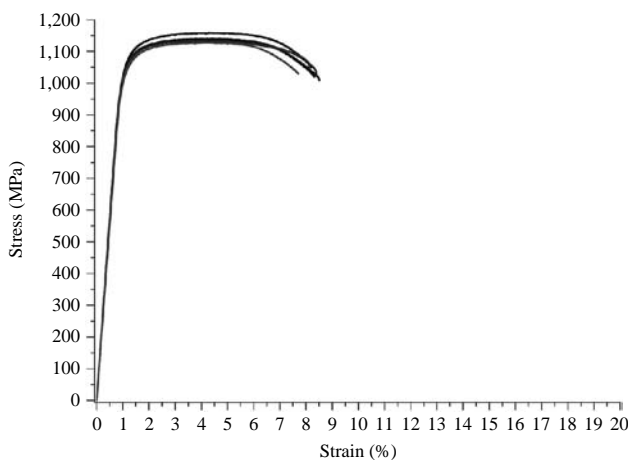
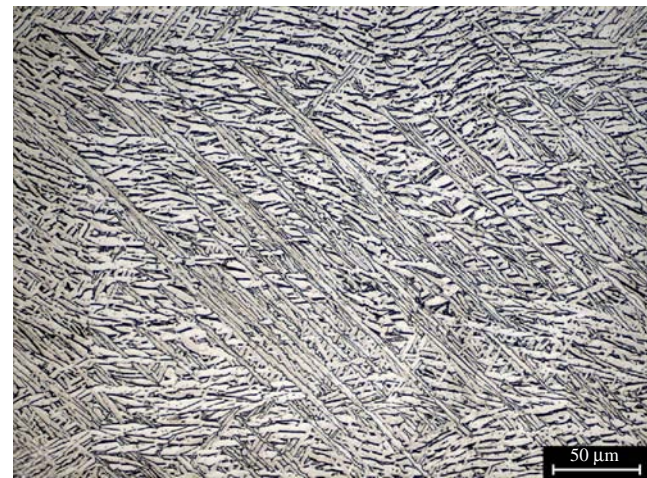
Figure 9 Microstructure of the material produced by modified SLM

(a)

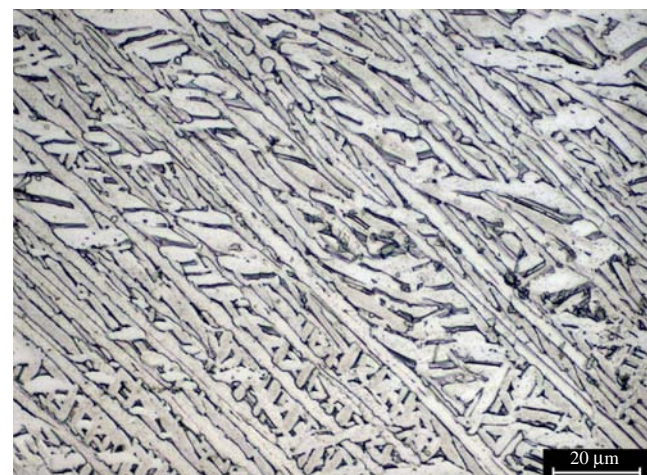


(b)

Note: Martensite plates still visible

Figure 10 Stress-strain curves for the material produced by modified SLM**Figure 11** Microstructure of the material produced by SLM and heat treated (variant 1)

(a)



(b)

Notes: A biphasic microstructure developed into the prior martensite plates; light α -phase precipitates at the former plate edges

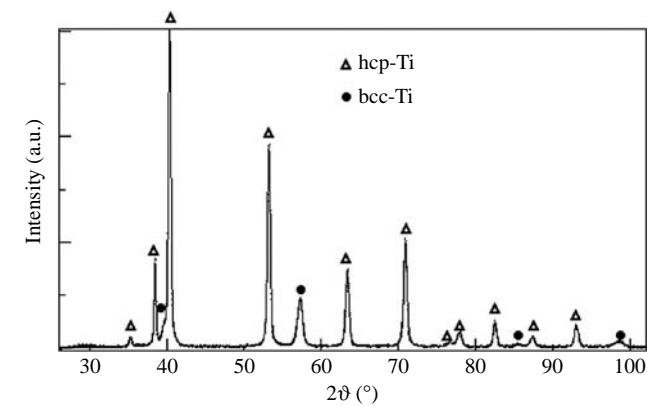
Figure 12 XRD pattern of the material produced by SLM and heat treated (variant 1)

Figure 13 Stress-strain curves for the material produced by SLM and heat treated (variant 1)

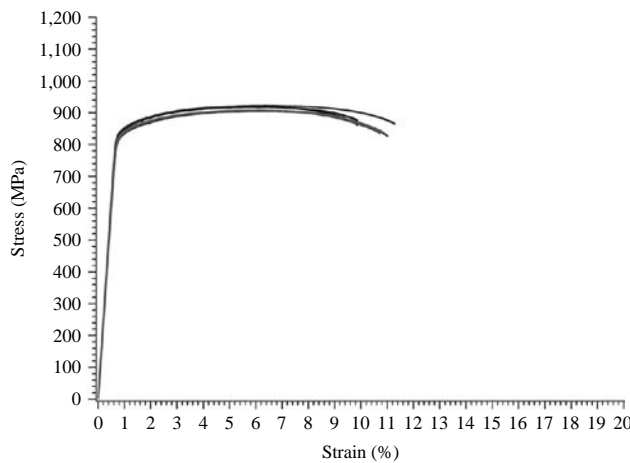
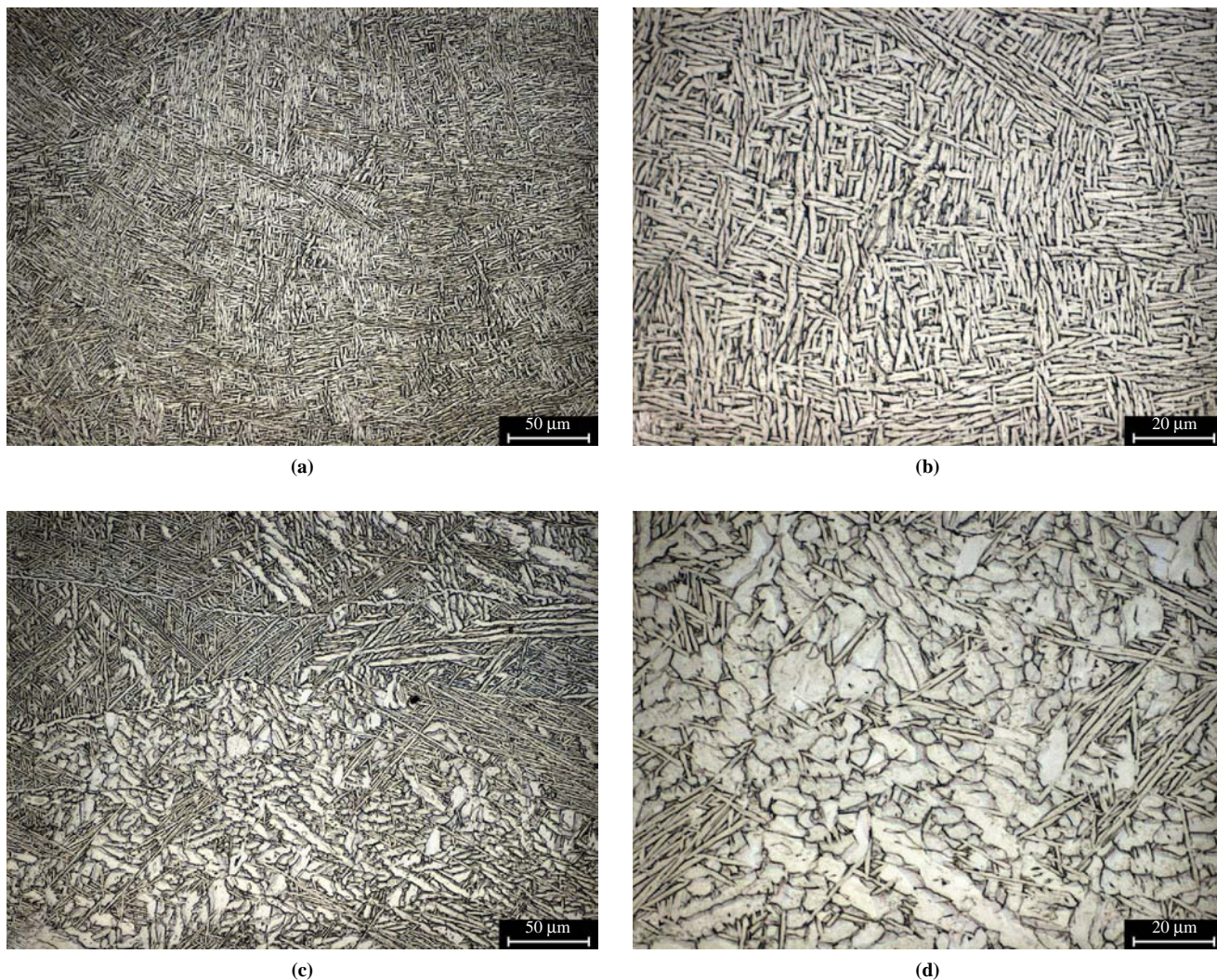


Figure 14 Microstructure of the material produced by SLM and heat treated (variant 2)



Notes: Coarse lamellae of α -phase; β -phase appeared; globalization of α -phase occurred in isolated regions

Rapid prototyping techniques are currently being developed for the production of complex prostheses, directly from 3D CAD-data. These techniques uniquely allow the functionalization of the surfaces by building up, in one single step, a porous surface layer with a tailored trabecular structure, which is able to enhance the interaction with the tissues. The mastery of the process necessitates obtaining the full density, the minimization of the residual stresses and the control of the microstructure.

The as-built material coming from the SLM process has a martensitic microstructure; the matrix is composed of acicular α -phase, while no β -phase is present. Some microcracks are also observable in the matrix; they are due to the effect of incomplete homologous wetting and residual stresses produced by the large solidification undercooling of the melt pool.

A proper modification of the standard process is effective in supporting homologous wetting during the melting of the powder and reducing residual stresses, but ductility does not increase significantly, since the microstructure remains martensitic.

Figure 15 XRD pattern of the material produced by SLM and heat treated (variant 2)

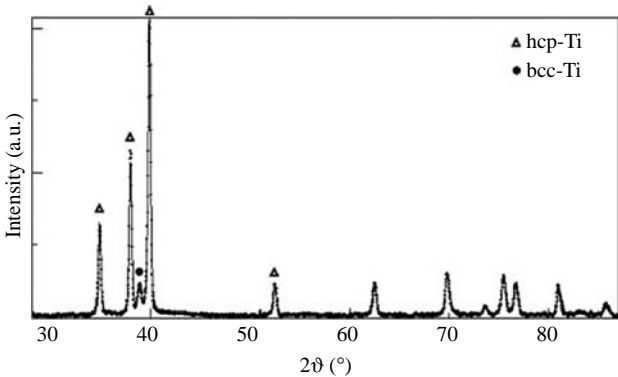


Figure 16 Stress-strain curves for the material produced by SLM and heat treated (variant 2)

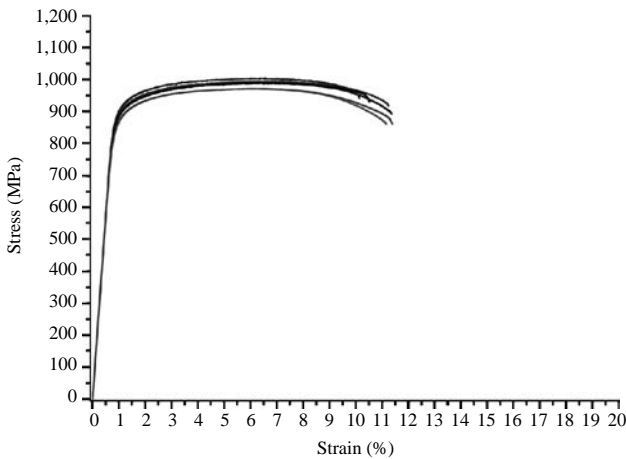


Table IV Tensile properties of the material produced by SLM and SLM heat treated (variant 2), in comparison with reference data

	Hot worked and annealed	SLM	SLM heat treated (variant 2)	ISO 5832-3
E (GPa)	104 ± 2	110 ± 5	117 ± 1	-
σ_y (MPa)	790 ± 20	990 ± 5	870 ± 15	>780
UTS (MPa)	870 ± 10	1,095 ± 10	990 ± 15	>860
A (%)	18.1 ± 0.8	8.1 ± 0.3	11.0 ± 0.5	>10

A post-building heat treatment causes the transformation of the metastable martensite into a biphasic α - β matrix, with a morphology that depends on the heat treatment. This results in an increase in the ductility and a reduction in the strength values. The properties then match the international standard prescriptions. A summary of the different states of the process comparing the microstructure and the resulting mechanical properties is shown in Table V, while a comparison between the stress-strain curves is shown in Figure 17.

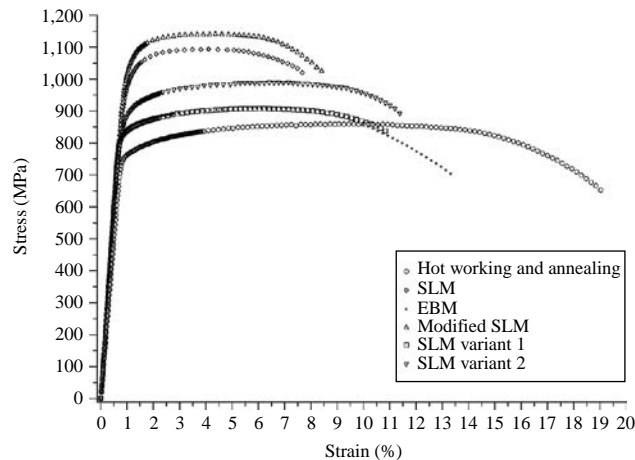
Work is in progress in order to further extend available combinations of strength and ductility.

Table V Summary of different procedures for rapid manufacturing of Ti-6Al-4V

	Microstructure	UTS	Yield stress	Breaking elongation
Hot worked	Globular α in $\alpha + \beta$ matrix	870 ± 10	790 ± 20	18.1 ± 0.8
EBM	acicular α + β	915 ± 10	830 ± 5	13.1 ± 0.4
SLM	acicular α'	1,095 ± 10	990 ± 5	8.1 ± 0.3
Modified SLM	acicular α'	1,140 ± 10	1,040 ± 10	8.2 ± 0.3
SLM variant 1	Lamellar α + β	915 ± 5	835 ± 5	10.6 ± 0.6
SLM variant 2	Lamellar α + β Globular α	990 ± 15	870 ± 15	11.0 ± 0.5

Note: Microstructure and mechanical properties

Figure 17 Stress-strain curves for the material produced by different process variants; a comparison



References

- Bourell, D., Wohlert, M., Harlan, N., Das, S. and Beaman, J. (2002), “Powder densification maps in selective laser sintering”, *Advanced Engineering Materials*, Vol. 9 No. 4, pp. 663-9.
- Collings, E.W. (1984), *The Physical Metallurgy of Titanium Alloys*, American Society for Metals, Materials Park, OH.
- Cormier, D., Harrysson, O. and West, H. (2002), “Characterization of H13 steel produced via electron beam melting”, *Rapid Prototyping Journal*, Vol. 10 No. 1, pp. 35-41.
- Das, S. (2003), “Physical aspects of process control in selective laser sintering of metals”, *Advanced Engineering Materials*, Vol. 5 No. 10, pp. 701-11.
- Facchini, L., Magalini, E., Robotti, P. and Molinari, A. (2009), “Microstructure and mechanical properties of Ti-6Al-4V produced by electron beam melting of pre-alloyed powders”, *Rapid Prototyping Journal*, Vol. 15 No. 3, pp. 171-8.

- Gil Mur, F.X., Rodríguez, D. and Planell, J.A. (1996), "Influence of tempering temperature and time on the α' -Ti-6Al-4V martensite", *Journal of Alloy and Compounds*, Vol. 234, pp. 287-9.
- Hollander, D.A., von Walter, M., Wirtz, T., Sellei, R., Schmidt-Rohlfing, B., Paar, O. and Erli, H. (2006), "Structural, mechanical and in-vitro characterization of individually structured Ti-6Al-4V produced by direct laser forming", *Biomaterials*, Vol. 27, pp. 955-63.
- Jovanović, M.T., Tadić, S., Zec, S., Mišković, Z. and Bobić, I. (2006), "The effect of annealing temperatures and cooling rate on microstructure and mechanical properties of investment cast Ti-6Al-4V alloy", *Materials and Design*, Vol. 27, pp. 192-9.
- Kruth, J.-P., Froyens, L., Van Vaerenbergh, J., Mercelis, P., Rombouts, M. and Lawers, B. (2004), "Selective laser melting of iron-based powder", *Journal of Materials Processing Technology*, Vol. 149, pp. 616-22.
- Kubiak, K. and Sieniawski, J. (1998), "Development of the microstructure and fatigue strength of two phase titanium alloys in the processes of forging and heat treatment", *Journal of Materials Processing Technology*, Vol. 78, pp. 117-21.
- Leyens, C. and Peters, M. (2003), *Titanium and Titanium Alloys*, Wiley-Vch Verlag GmbH & Co. KGaA, Weinheim.
- Malinov, S., Sha, W., Guo, Z., Tang, C.C. and Long, A.E. (2002), "Synchrotron X-ray diffraction study of the phase transformations in titanium alloys", *Materials Characterization*, Vol. 48, pp. 279-95.
- Mitchell, A. (1999), "The electron beam melting and refining of titanium alloys", *Materials Science and Engineering*, Vol. A263, pp. 217-23.
- Over, C. (2003), "Generative fertigung von bauteilen aus werkzeugstahl X38CrMoV5-1 und Ti-6Al-4V mit selective laser melting", Dissertation at Rheinisch-Westfälische Technische Hochschule Aachen, Shaker, Aachen.
- Over, C., Meiners, W., Wissenbach, K., Hutfless, J. and Lindemann, M. (2003), "Rapid manufacturing of metal parts and tools using laser melting", *Proceedings of the Second International WLT-Conference on Lasers in Manufacturing, Munich, Germany*.
- Ping Li, J., de Wijn, J.R., Van Blitterswijk, C.A. and de Groot, K. (2006), "Porous Ti₆Al₄V scaffold directly fabricating by rapid prototyping: preparation and in-vitro experiment", *Biomaterials*, Vol. 27, pp. 1223-35.
- Ponader, S., Vairaktaris, E., Heinl, P., von Wilmowsky, C., Rottmair, A., Körner, C., Singer, R.F., Holst, S., Schlegel, K.A., Neukam, F.W. and Nkenke, E. (2007), "Effect of topographical surface modifications of electron beam melted Ti-6Al-4V titanium on human fetalosteoblasts", *Journal of Biomedical Materials Research Part A*, Vol. 84A No. 4, pp. 1111-19.
- Semiatin, S.L., Stefansson, N. and Doherty, R.D. (2005), "Prediction of the kinetics of static globularization of Ti-6Al-4V", *Metallurgical and Materials Transactions A*, Vol. A36, pp. 1372-6.
- Simchi, A. and Pohl, H. (2003), "Effects of laser sintering processing parameters on the microstructure and densification of iron powder", *Materials and Engineering*, Vol. A359, pp. 119-28.

of Ultrafine Grained Materials by mechanical milling ad spark plasma sintering. He is a PhD student in the Department of Materials Engineering and Industrial Technologies of the University of Trento, Italy. He works on the characterization of biomedical alloys produced by Laser Melting and EBM. He has also worked on the sintering of hard metals. Luca Facchini is the corresponding author and can be contacted at: luca.facchini@ing.unitn.it

Emanuele Magalini received the MSc in Materials Engineering at the University of Trento, Italy, with a thesis on a review of the drying process of gypsum. He is developing some R&D projects for Eurocoating s.p.a. – Italy; these projects are focused on medical devices made with new and innovative materials including plastic, metals, ceramics and composite. In particular, he supervises the mechanical and chemical characterization of the material and the improvement of the production/manufacturing process.

Pierfrancesco Robotti received his MSc in Biomedical Engineering at Milan Polytechnic University, Italy. He has served for about ten years c/o Tecres s.p.a. – Italy, an international market leader company, manufacturer of acrylic-based bone cements world wide. He was initially a Researcher, later on Research Officer and finally he had Officer responsibility to coordinate both Research and Regulatory Affair activities. Since 2005, he is Research Officer c/o Eurocoating s.p.a. – Italy, an international market leader company, manufacturer of porous structures for bone integration world wide. Eurocoating s.p.a., among the others activities, has in place a Rapid Prototyping Department where several direct metal manufacturing technologies, based on powder metallurgy, are investigated and, when possible, exploited for commercial production of orthopaedic and dental implantable components.

Alberto Molinari is a Full Professor of Metallurgy at the University of Trento. He received his MSc in Chemical Engineering at the University of Padova, Italy and his PhD in Metallurgical Engineering at the Turin Polytechnic University, Italy. Since 2003, he has been the Head of the Department of Materials Engineering and Industrial Technologies, of the University of Trento. He is also the Head of the Metallurgy Group of the Department. His main research areas are: production and heat treatment of special steels and irons (ADI and CGI); hot and cold working of steels and non-ferrous alloys; surface engineering of steels and titanium alloys; powder metallurgy (production, heat treatment, mechanical, tribological and corrosion properties of sintered steels and non-ferrous alloys); metal injection moulding; nanomaterials by powder metallurgy (milling and consolidation of metallic powders); laser melting and EBM of metallic powders; spark plasma sintering of functionally graded materials, composite and ceramics; cryogenic treatment of steel and non-ferrous alloys. He is the author of more than 300 publications in international and national journals and conference proceedings.

Simon Höges received his Diploma in Physics at the University of Aachen, Germany with a thesis on process simulation of melt flow behaviour in small melt pools. Since then, he has been working as a Research Assistant and a PhD student at the Department of Laser Technology. He works on the process development of SLM for biomedical applications.

About the authors

Luca Facchini received the MSc in Materials Engineering at the University of Trento, Italy, with a thesis on the production

Konrad Wissenbach is a Research Assistant at the Fraunhofer ILT and Head of the Department “Surface Treatment” with the main foci in laser cleaning, laser cladding, alloying and dispersing, laser heat treatment, rapid prototyping and rapid manufacturing by SLM, laser polishing and structuring as well as functionalization of coatings by

laser radiation. He received his Diploma in Physics at the University of Darmstadt. He then worked as a Research Assistant at the Institute for Applied Physics in Darmstadt in the field of laser surface technology with the main focus in laser hardening. He received his PhD with a thesis on transformation hardening with CO₂-laser radiation.



Influence of defects on mechanical properties of Ti–6Al–4 V components produced by selective laser melting and electron beam melting

Haijun Gong ^a, Khalid Rafi ^b, Hengfeng Gu ^c, G.D. Janaki Ram ^d, Thomas Starr ^a, Brent Stucker ^{e,*}

^a J. B. Speed School of Engineering, University of Louisville, Louisville, KY, United States

^b UL International-Singapore Pte Ltd, Singapore

^c College of Engineering, North Carolina State University, Raleigh, NC, United States

^d Dept. of Metallurgical and Materials Engineering, IIT Madras, Chennai 600 036, India

^e 3DSIM LLC, Park City, UT, United States



ARTICLE INFO

Article history:

Received 20 March 2015

Received in revised form 2 July 2015

Accepted 27 July 2015

Available online 30 July 2015

Keywords:

Additive manufacturing

Selective laser melting

Electron beam melting

Ti–6Al–4 V

Defects

Mechanical properties

ABSTRACT

This study evaluates the mechanical properties of Ti–6Al–4 V samples produced by selective laser melting (SLM) and electron beam melting (EBM). Different combinations of process parameters with varying energy density levels were utilized to produce samples, which were analyzed for defects and subjected to hardness, tensile, and fatigue tests. In SLM samples, small pores in amounts up to 1 vol.% resulting from an increase in energy density beyond the optimum level were found to have no major detrimental effect on the mechanical properties. However, further increase in the energy density increased the amount of porosity to 5 vol.%, leading to considerable drop in tensile properties. Samples produced using lower-than-optimum energy density exhibited unmelted powder defects, which, even at 1 vol.% level, strongly affected both tensile and fatigue properties. In EBM, insufficient energy input was found to result in large, macroscopic voids, causing serious degradation in all mechanical properties. These findings are helpful in process optimization and standardization of SLM and EBM processes.

© 2015 Elsevier Ltd. All rights reserved.

1. Introduction

Additive manufacturing (AM) produces parts directly from three-dimensional CAD data, layer upon layer. Selective laser melting (SLM) and electron beam melting (EBM) are two commonly used AM processes based on powder bed fusion. In SLM, a metallic powder is spread into a thin layer and a finely focused laser selectively melts the powder, fusing it to the previous layer [1]. Part fabrication takes place inside a chamber filled with inert gas. Many different metal powders can be utilized for part fabrication in SLM, including stainless steel, maraging steel, cobalt–chromium and titanium alloys [2–4]. The EBM process is similar to the SLM process, but makes use of an electron beam for selectively melting the metal powder. In contrast to SLM, part fabrication in EBM takes place inside a vacuum chamber and the powder surrounding the part is maintained at an elevated temperature. At present, EBM is mainly used for producing parts in titanium alloys [1,5,6].

Because of their layered microstructure, the mechanical behavior of AM parts can be significantly different from conventionally manufactured parts. Further, AM parts can develop a variety of defects due to improper choice of process parameters or process disturbances. For example, incomplete wetting and balling effects associated with insufficient energy input lead to pores or voids in SLM parts [7,8]. Similarly, when the energy

input is not sufficient, successive scan tracks do not properly fuse together and defects appear along the scan lines [4,9]. EBM parts generally show large voids or cavities extending across several layers when the process parameters are not carefully chosen. Smaller spherical pores can also develop in EBM parts due to entrapment of gases originally present in gas-atomized metal powders [10]. While these defects can be expected to be detrimental to part mechanical properties, how different types of defects influence the mechanical properties and what type of defects can be tolerated in what amounts in AM parts is a matter of current interest and study.

A number of studies are available on the mechanical properties (mainly, hardness, tensile, and fatigue) of SLM and EBM Ti–6Al–4 V parts [11–14]. In general, porosity was found to have a strong impact on the mechanical properties of SLM and EBM parts, especially dynamic properties [15,16]. Santos et al. [17] conducted laser melting of pure titanium powder and fabricated specimens with densities higher than 95%. While these samples showed comparable tensile strength to wrought material, their impact and torsional fatigue strengths were rather low because of porosity. Gong et al. [18], Edwards et al. [19], Wycisk et al. [20], and Simonelli et al. [21] also reported inferior uniaxial fatigue performance in Ti–6Al–4 V SLM parts due to porosity. Leuders et al. [22] suggested that micron-sized pores mainly affect fatigue strength, while residual stresses have a strong bearing on the fatigue crack growth. Li et al. [23] carried out compression fatigue tests on Ti–6Al–4 V mesh arrays (these can be regarded as parts containing

* Corresponding author at: 3DSIM LLC, Park City, UT 84098, United States.

E-mail address: brent.stucker@3dsim.com (B. Stucker).

Table 1

Process parameters used for SLM.

Parameter set	Scan speed (mm/s)	Energy density (J/mm ³)
SLM-OP 1	960	42
SLM-MP 2	540	74
SLM-MP 3	400	100
SLM-MP 4	1260	32
SLM-MP 5	1500	27

Note: Laser power (120 W), hatch spacing (0.1 mm), layer thickness (0.03 mm) were the same in all the cases.

Table 2

Process parameters used for EBM (the layer thickness was 0.05 mm in all the cases).

Parameter no.	Max current (mA)	Speed function index	Line offset (mm)	Focus offset (mA)
EBM-OP 1	21	98	0.1	3
EBM-MP 2	30	60	0.2	15
EBM-MP 3	20	180	0.2	5

deterministic defects) with very high porosity levels (60–85 vol.%). It was found that the fatigue strength increased with increasing relative density. Brenne et al. [24] conducted four-point-bend tests and fatigue tests on Ti-6Al-4 V cellular structures produced using SLM in as-built and heat treated (1050 °C/2 h/furnace cooling) conditions. Digital image correlation (DIC) techniques were utilized to investigate the local strains. Considerable improvements in bend and fatigue performance were reported after the heat treatment. Sun et al. [25] and Amin Yavari et al. [26] studied the effect of unit cell structure on the mechanical properties of Ti-6Al-4 V cellular parts. They have shown that the geometrical morphology of the defect or the porous structure can strongly influence the mechanical strength. Vandebroucke et al. [4] investigated the hardness of SLM-built Ti-6Al-4 V samples and showed that porosity can affect macro hardness, but not micro hardness. Heinl et al. [27] evaluated the compressive strength of non-stochastic cellular Ti-6Al-4 V structure fabricated by EBM. Murr et al. [28,29] also studied

EBM Ti-6Al-4 V cellular structures and stochastic foams. It has been shown that the stiffness of these structures having designed porosity varies with density, and varies inversely with porosity. Schwerdtfeger et al. [30,31] and Li et al. [32] investigated non-stochastic cellular auxetic structures (i.e., deterministic defects) built from Ti-6Al-4 V using EBM. They observed a good correlation between Young's modulus and Poisson's ratio, and relative density and internal structure. Similarly, Yang et al. [33] investigated the compressive properties of Ti-6Al-4 V auxetic mesh structures produced by EBM. They showed that re-entrant lattice structures possess superior mechanical properties compared to regular foam structures.

Many researchers have reported how process parameters influence defect generation in SLM and EBM [34–38]. In this work, we report the mechanical properties of SLM and EBM Ti-6Al-4 V samples containing various types and amounts of defects. Broadly, two types of defects are dealt with: (i) defects due to incomplete powder melting or improper fusion between successive tracks or layers, (ii) defects due to entrapment of gases or improper closure of a keyhole. Defects of the former type arise due to insufficient energy input, while the latter are caused by the use of excessive energy.

2. Experimental details

Ti-6Al-4 V powder (Grade 23) obtained from Advanced Powders and Coatings Inc., Canada, was used for SLM. The powder has an apparent density of 2.6 g/cm³ and a mean particle size of ~30 µm (D_{10} : 17 µm, D_{90} : 44 µm). For EBM, Ti-6Al-4 V powder (Grade 23) supplied by Arcam was used. This powder has an apparent density of 2.7 g/cm³ with a mean particle size of 73 µm (D_{10} : 47 µm, D_{90} : 99 µm). Both the powders are spherical. Note that the powder used in EBM is considerably coarser than that used in SLM.

SLM and EBM experiments were conducted using EOS M270 DMLS and Arcam S400 machines, respectively. Cylindrical bars (10 mm in diameter) were built in the Z orientation (ISO/ASTM 52921, 2013) using different combinations of process parameters, as shown in Table 1 (for SLM) and Table 2 (for EBM). In SLM, the energy density was varied at two levels above (parameter sets SLM-MP2 and SLM-MP3) and below

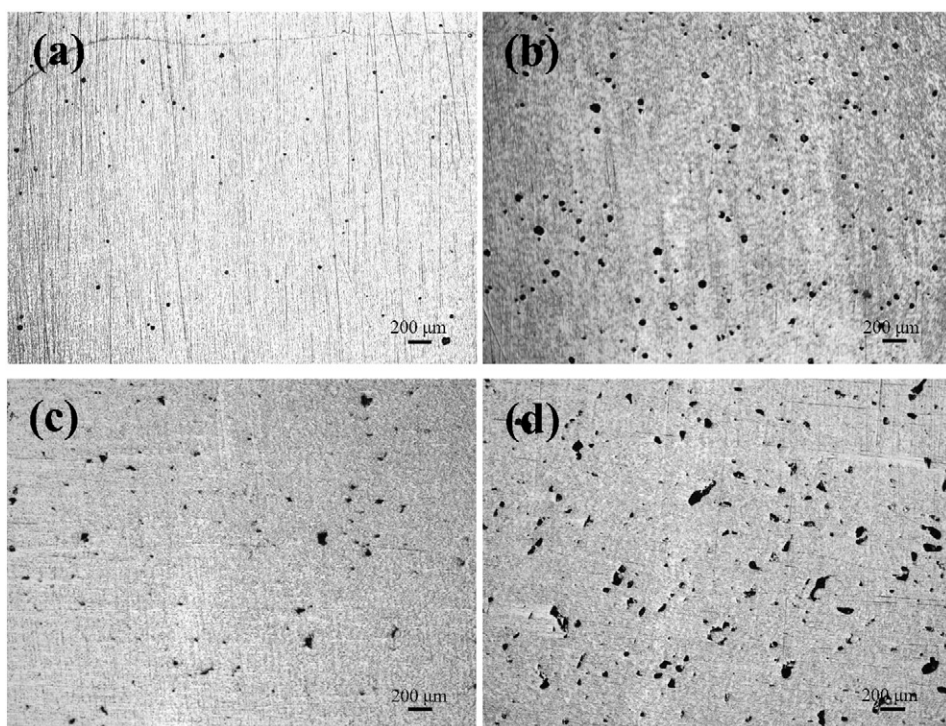


Fig. 1. Optical micrographs of SLM samples in as-polished condition: (a) SLM-MP2, (b) SLM-MP3, (c) SLM-MP4, (d) SLM-MP5.

Table 3

Results of bulk density measurements by the Archimedes method.

Parameter set	Density (g/cm ³)	Estimated porosity (vol.%)
<i>SLM</i>		
SLM-OP 1	4.41	0
SLM-MP 2	4.37	1
SLM-MP 3	4.21	5
SLM-MP 4	4.37	1
SLM-MP 5	4.20	5
<i>EBM</i>		
EBM-OP 1	4.41	0
EBM-MP 2	4.38	1
EBM-MP 3	4.22	5

Note: For porosity estimation, the nominal density of Ti–6Al–4 V was taken as 4.41 g/cm³. SLM-OP1 and EBM-OP1 samples contained some sparse pores, which, however, did not affect their density.

(parameter sets SLM-MP4 and SLM-MP5) the optimum energy density (parameter set SLM-OP1). This was done by changing the scan speed (V), which is related to energy density (E), as below:

$$E = \frac{P}{V * h * t}$$

where P is laser power, h is hatch spacing, and t is layer thickness. The optimum process parameters were determined in a previous study [35].

In the case of EBM, as detailed in Table 2, certain deviations (parameter sets EBM-MP2 and EBM-MP3) from the recommended machine/parameter settings for Ti–6Al–4 V (parameter set EBM-OP1) were attempted. These parametric variations were chosen based on a previous study on the effects of process parameters on defect generation in EBM [35]. Note that the parameters listed in Table 2 were the actual machine settings and/or control algorithms used for making the samples.

Specific values of beam current (the maximum value can be specified) and scan speed are continuously varied throughout the build according to the speed function setting. Line offset determines the distance between successive scan lines and focus offset determines the beam diameter (a higher focus offset results in a higher beam diameter).

No heat treatment was performed on any of the samples produced in the current study. Metallographic specimens were prepared using standard grinding and polishing procedures, and etched by Kroll's reagent (92 ml H₂O, 5 ml HNO₃, and 3 ml HF). An Olympus MX51 optical microscope was used for microstructural examination. The density of the samples made using different process parameters was measured using the Archimedes method as per ASTM B962–08. All the samples were lightly sand blasted and polished before density measurements. Hardness testing was done on a Rockwell C-Scale tester employing a diamond cone (Brale) indenter as per ASTM E18. Standard tensile and fatigue test specimens were machined from the samples built using various process parameters. Tensile tests were carried out as per ASTM E8 on an Instron 5569A tensile testing machine with Bluehill® 2 testing software using a crosshead travel speed of 2.5 mm/min. Tests were carried out using a static axial clip-on extensometer attached to the gage section of the specimen. For each process parameter set, six samples were tested. High cycle fatigue tests were performed as per ASTM E466 on a 10 kN Instron Electropulse 10000 fatigue testing machine with WaveMatrix™ testing software. Fatigue tests were conducted using sinusoidal loading (maximum stress = up to 750 MPa, stress ratio R = 0.1) at a frequency of 50 Hz. More than ten specimens were tested for each process parameter combination at different maximum stress levels. Fatigue testing was discontinued after 10⁷ cycles. All the tests were conducted at room temperature. After the tests, fracture surfaces were examined using a FEI Nova NanoSEM 600 Scanning Electron Microscope (SEM) to understand the role played by various defects in the fracture process.

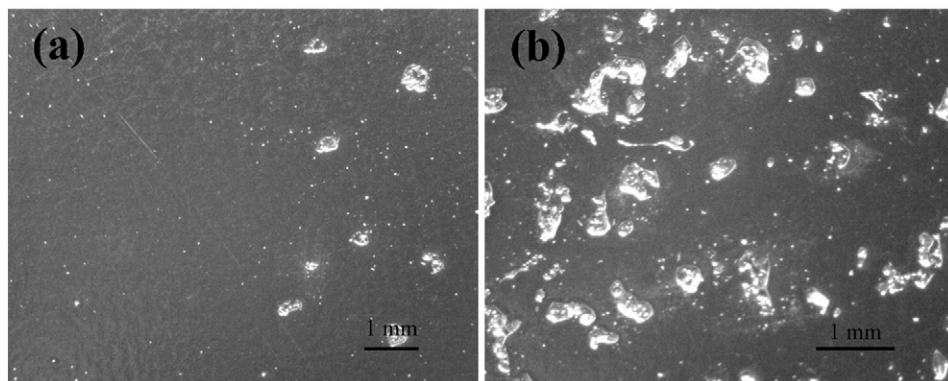


Fig. 2. Macrographs of EBM samples in as-polished condition: (a) EBM-MP2, (b) EBM-MP3.

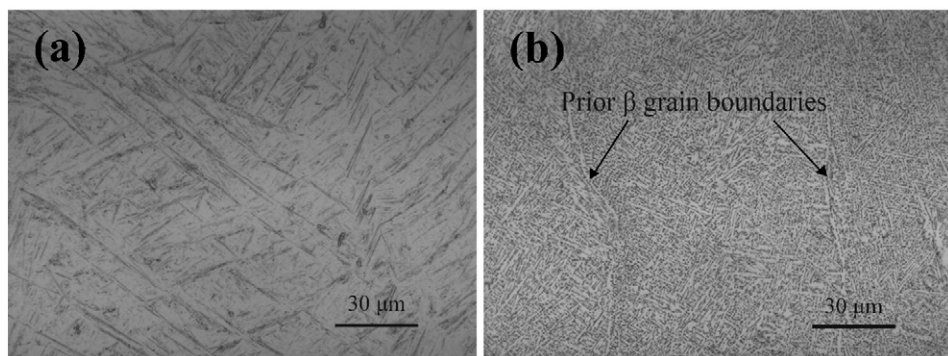


Fig. 3. Optical microstructures of SLM (a) and EBM (b) samples produced using optimum process parameters. Note the presence of α phase (grain boundary α) on prior β grain boundaries in (b).

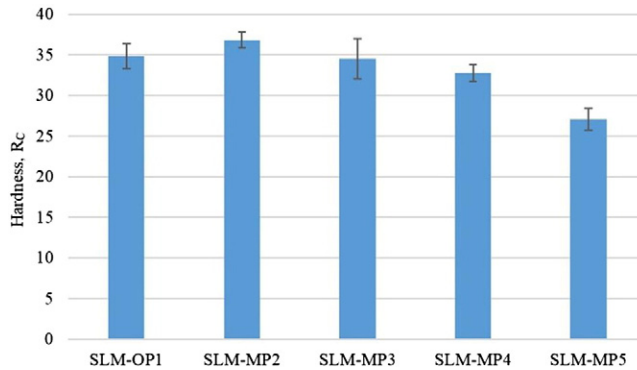


Fig. 4. Hardness of SLM samples.

3. Results and discussion

3.1. Microstructure

SLM samples produced using the optimum process parameters did not show any major defects, except for some sparse pores. Samples produced using lower or higher energy densities contained defects in different amounts, as can be seen in Fig. 1. When the energy density is increased by one level from the optimum, the samples developed small pores (less than 50 μm in size) (Fig. 1a). The pores became larger (up to $\sim 70 \mu\text{m}$) with further increase in the energy density (parameter set SLM-MP3) (Fig. 1b). Similarly, when the energy density was reduced by one level, the samples developed some pores (Fig. 1c), which are slightly more irregular and larger in size (up to 110 μm) than those found in the samples produced by increasing the energy density by one level above the optimum. With further decrease in the energy density (parameter set SLM-MP5), the pores became larger in size and more in number (Fig. 1d). The defects in these samples were also more irregular and larger (up to 250 μm in size).

The amount of porosity in all the SLM samples was estimated based on bulk density measurements using the Archimedes method. The results are given in Table 3. The type and nature of defects in SLM parts can be expected to vary depending on the process parameters. At very low energy density levels, pores or voids develop due to incomplete powder melting or improper fusion between successive tracks or layers. In contrast, when the energy density is excessive, the melt pool deepens and pores/voids develop due to entrapped gases or improper closure of the keyhole. Defects of the former type contain unmelted powder in them and samples containing such defects fare better in density

measurements than in microscopy. This explains why microscopy revealed relatively more defects in the samples produced using lower-than-optimum energy densities (SLM-MP4 and SLM-MP5) than those produced using higher-than-optimum energy densities (SLM-MP2 and SLM-MP3) at similar amounts of porosity estimated from the Archimedes method. The authors believe that the accuracy of Archimedes density measurements depends on the nature and type of defects in the parts. Archimedes density measurements tend to be more accurate and compare well with microscopic observations when most of the defects do not have entrapped powder in them (i.e., defects resulting from the use of excessive energy input) than when most of the defects are filled with unmelted powder (i.e., defects resulting from the use of insufficient energy input). Further, the results from Archimedes method can considerably vary depending on the surface roughness of the samples. Another issue is sensitivity. The SLM and EBM samples built using optimum parameters in this study indeed contained some sparse porosity defects as revealed in microscopy, but showed an Archimedes density equal to the nominal density of alloy Ti-6Al-4 V. While such samples can be regarded as “fully dense” for most practical purposes, they are not “flawless” and do contain some defects, which can be detrimental to their mechanical properties. Therefore, Archimedes density measurements cannot be entirely relied upon in assessing the quality of SLM or EBM parts. Overall, there is a need for developing methods for determining the density of SLM and EBM parts with greater precision and accuracy.

Density measurements on EBM-MP2 and EBM-MP3 samples indicated that they contained defects amounting to 1 and 5 vol.%, respectively. However, observations revealed that these samples were far more inferior in quality, containing large macroscopic voids filled with unmelted powder particles (because of insufficient energy input) (Fig. 2). Compared to the SLM samples, the size and number of defects in the EBM samples are clearly higher although their bulk densities as determined from the Archimedes method are comparable (because of the presence of more unmelted powder in EBM samples).

Representative optical micrographs of the SLM and EBM samples are shown in Fig. 3. All the SLM samples showed very similar microstructures consisting of primarily acicular martensitic alpha (α'), as can be seen in Fig. 3a. In contrast, the EBM samples showed fine lamellar α - β microstructure (Fig. 3b), suggesting diffusional transformation of the β phase during cooling from high temperature. This is understandable as the cooling rates in EBM are much lower than those in SLM (the powder bed in EBM is maintained at an elevated temperature, around 675 °C, throughout part fabrication). These microstructures are typical of SLM and EBM builds in Ti-6Al-4 V and have been discussed by many earlier investigators [12,39,40]. Overall, the results show that microstructure evolution during SLM and EBM processing of Ti-6Al-4 V

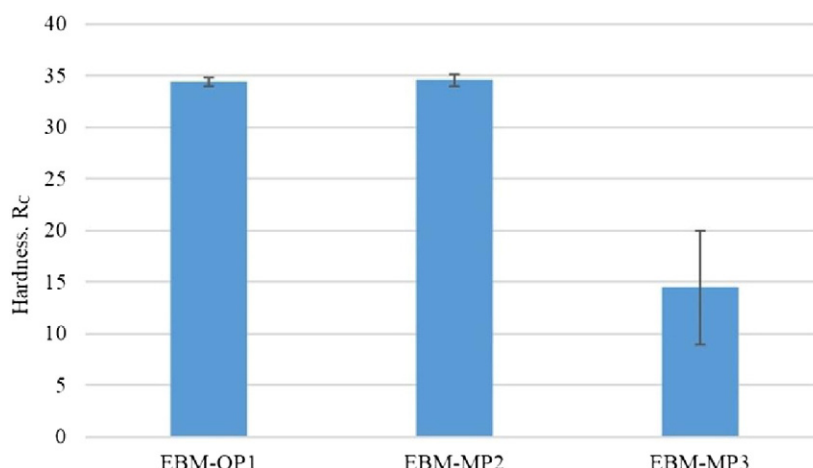


Fig. 5. Hardness of EBM samples.

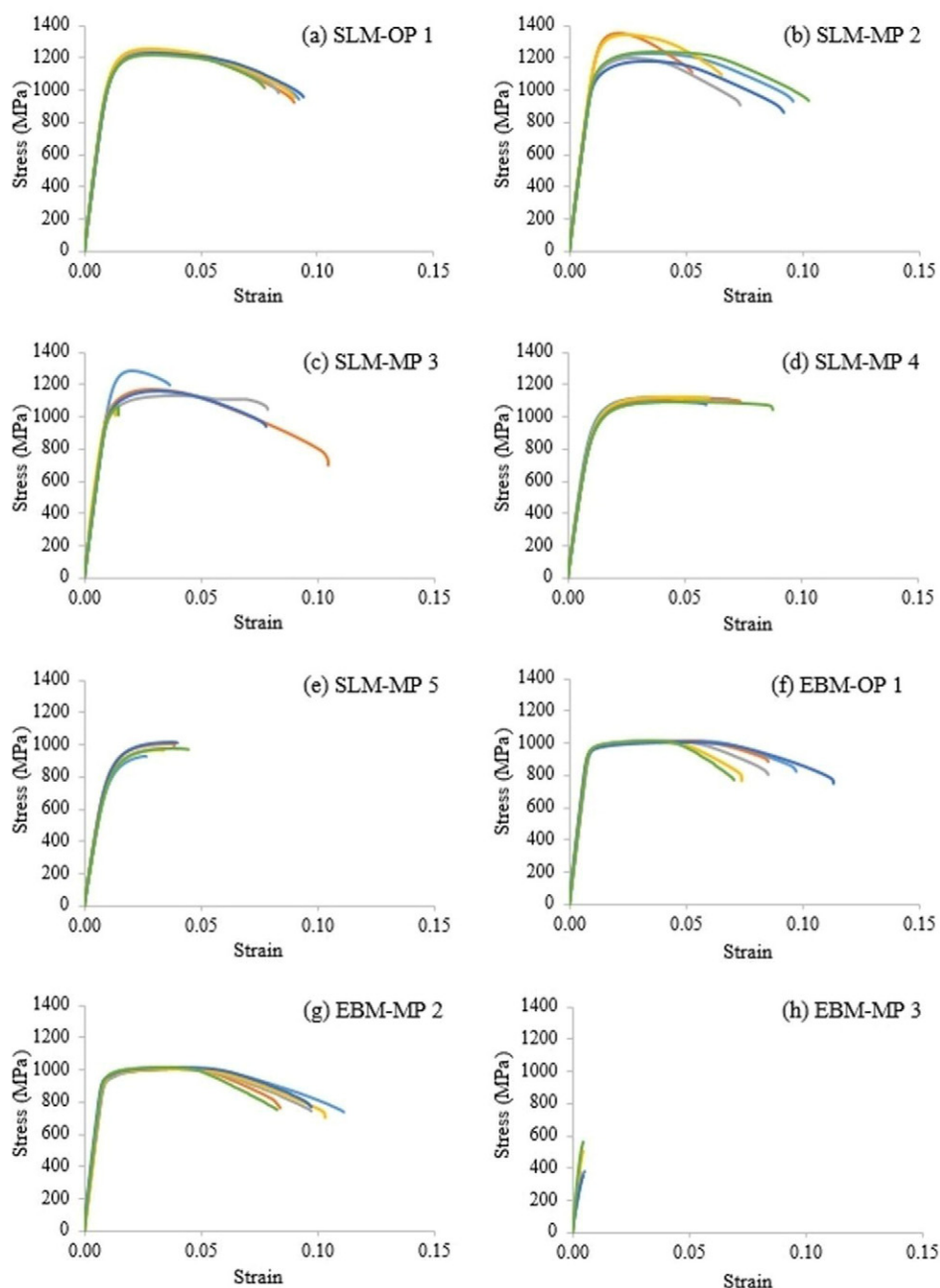


Fig. 6. Stress-strain plots of SLM- and EBM-produced Ti-6Al-4 V specimens.

Table 4
Tensile properties of SLM and EBM samples.

Parameter set	0.2% proof stress (MPa)	UTS (MPa)	Elongation (%)	Young's modulus (GPa)
<i>SLM</i>				
SLM-OP 1	1098 (15)	1237 (13)	8.8 (0.6)	109 (2.1)
SLM-MP 2	1150 (91)	1257 (74)	8.0 (2.0)	111 (1.4)
SLM-MP 3	1066 (91)	1148 (80)	5.4 (3.8)	109 (3.7)
SLM-MP 4	932 (16)	1112 (13)	6.6 (1.4)	95 (3.0)
SLM-MP 5	813 (23)	978 (32)	3.7 (0.6)	84 (3.0)
<i>EBM</i>				
EBM-OP 1	962 (4.0)	1012 (3.0)	8.8 (1.6)	121 (3.0)
EBM-MP 2	947 (11)	1011 (4.0)	9.0 (1.1)	120 (9.0)
EBM-MP 3	–	423 (88)	0.4 (0.1)	92 (20)

primarily depends on the cooling rate and defects such as pores and voids have little effect on the intragranular microstructure (phase constitution and morphology).

3.2. Hardness

The results of Rockwell hardness testing on SLM and EBM samples are shown in Figs. 4 and 5, respectively. SLM-OP1, SLM-MP2, and SLMP3 samples showed a similar hardness. Even SLM-MP4 samples showed only a slight drop in hardness, but SLM-MP5 samples showed significantly lower hardness. Among the three EBM samples, EBM-OP1 and EBM-MP2 samples showed more or less the same hardness, but EBM-MP2 samples showed drastically lower hardness. It may be also noticed that the hardness of SLM and EBM samples produced under optimum conditions is similar, notwithstanding the differences in their microstructure. These results show that small pores do not affect the hardness of Ti-

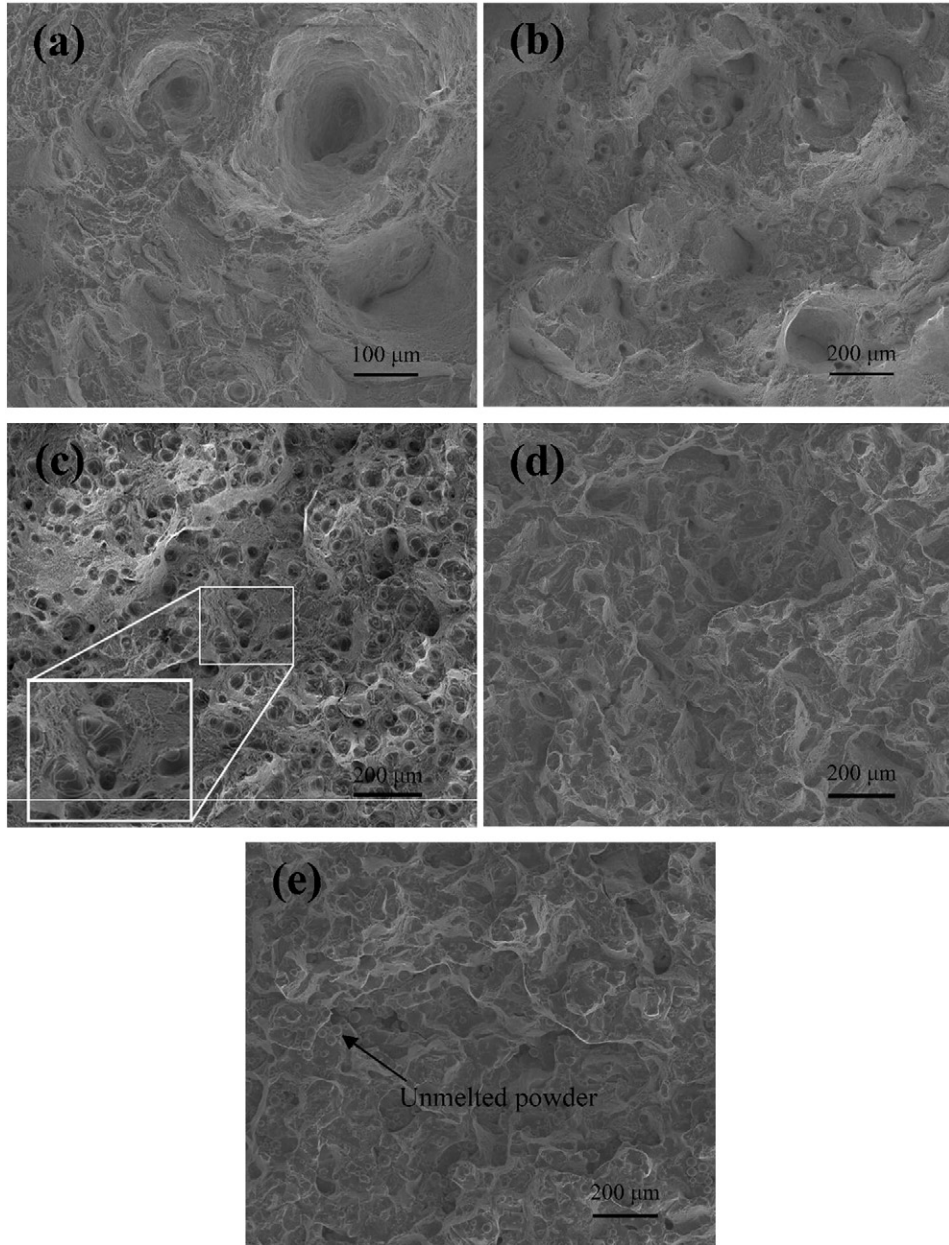


Fig. 7. Tensile fracture surfaces of SLM samples: (a) SLM-OP, (b) SLM-MP2, (c) SLM-MP3, (d) SLM-MP4, (e) SLM-MP5.

6Al–4 V parts produced by SLM and EBM. However, when the energy input is very low, the parts develop large voids due to incomplete powder melting, which impair their hardness significantly.

3.3. Tensile properties

Fig. 6 shows the stress–strain plots of SLM and EBM specimens. For each process parameter set, multiple specimens were tested. The average yield strength, ultimate tensile strength (UTS), Young's modulus and % elongation values are summarized in Table 4. The tensile properties obtained on SLM and EBM samples built under optimum conditions (SLM-OP1 and EBM-OP1) compare well with available published test data [12,41]. As reported by earlier investigators [40], the SLM samples showed higher yield and tensile strengths than the EBM samples because of their predominantly martensitic α microstructure. The SLM samples showed decent tensile ductility (as good as EBM samples), suggesting that their microstructure is not fully martensitic.

SLM samples produced using parameter set SLM-MP2 showed similar tensile properties to those produced under optimum conditions, while parameter set SLM-MP3 resulted in some drop in UTS and % elongation. Samples produced using parameter set SLM-MP4 showed further degradation, while those produced using parameter set SLM-MP5 showed the lowest strength and ductility. Overall, the defects generated due to insufficient energy input appear to be more detrimental to part mechanical properties than those generated due to excessive energy input. In other words, the results show that the SLM process is more tolerant to a little excess energy input than insufficient energy input. With regard to EBM, parameter set EBM-MP2 did not result in any significant reduction in tensile properties, but the samples built using parameter set EBM-MP3 performed very poorly in tensile tests.

Representative tensile fracture surfaces of various SLM and EBM samples are shown in Figs. 7 and 8, respectively. Both SLM and EBM samples produced under optimum conditions showed ductile dimpled rupture features (Figs. 7a and 8a). The fracture surfaces of SLM-MP2 and EBM-MP2 samples also appeared very similar to those of SLM-

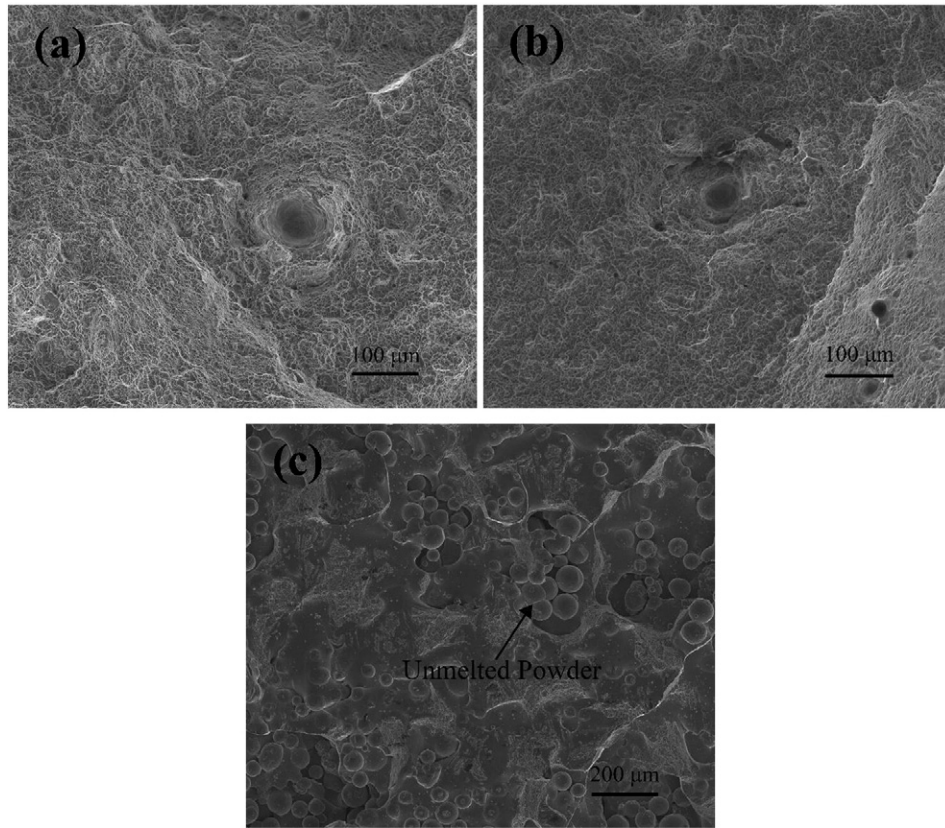


Fig. 8. Tensile fracture surfaces of EBM samples: (a) EBM-OP1, (b) EBM-MP2, (c) EBM-MP3.

OP1 and EBM-OP1 samples, respectively, but contained a few discernible pores and voids (compare Fig. 7a and b; Fig. 8a and b). The defects in SLM-MP3 samples could be readily seen on their fracture surfaces, as shown in Fig. 7c. SLM-MP4 samples showed ductile dimpled rupture features with some regions of brittle fracture corresponding to lack-of-fusion defects (Fig. 7d). Fracture surfaces of SLM-MP5 and EBM-MP3 samples revealed numerous unmelted powder particles, as can be seen from Figs. 7e and 8c, respectively.

3.4. Fatigue properties

The results of fatigue testing on SLM and EBM samples are shown in Figs. 9 and 10, respectively. All the samples, including those produced under optimum conditions, showed considerable scatter in fatigue life. The fatigue limit of SLM samples produced under optimum conditions

in this study was found to be considerably lower (350 MPa) than that (550 MPa) reported by Rafi et al. [40] for Ti-6Al-4 V SLM samples produced using EOS supplied Ti-6Al-4 V powder and EOS recommended process parameters. The Ti-6Al-4 V powder used in the current study has a different particle size distribution from the EOS Ti-6Al-4 V powder. Further, the process parameters used in the current study were also considerably different from those recommended by EOS. While detailed one-to-one comparisons are needed to ascertain the key differences, in terms of overall quality, the samples produced in the current study appear to be inferior to those in Ref. [40].

Among the SLM samples, SLM-MP2 samples showed comparable fatigue performance to SLM-OP1 samples. However, SLM-MP3 samples showed noticeable drop in fatigue lives and fatigue limit (300 MPa) due to the presence of pores in larger size and number. The samples built using lower-than-optimum energy densities (SLM-MP4 and

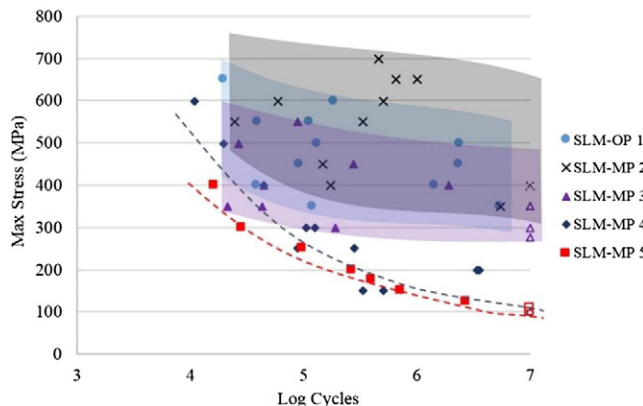


Fig. 9. Fatigue lives of SLM-produced Ti-6Al-4 V specimens.

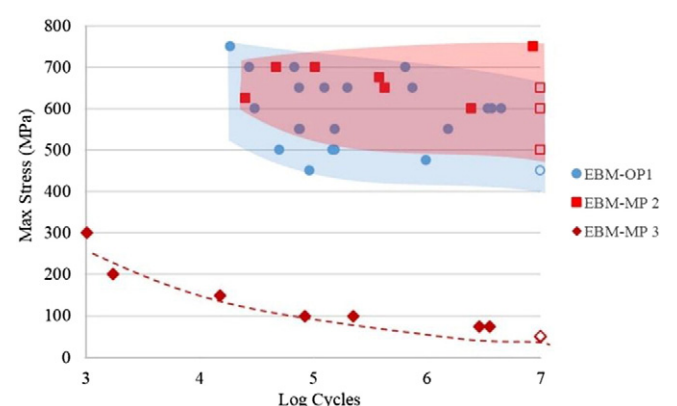


Fig. 10. Fatigue lives of EBM-produced Ti-6Al-4 V specimens.

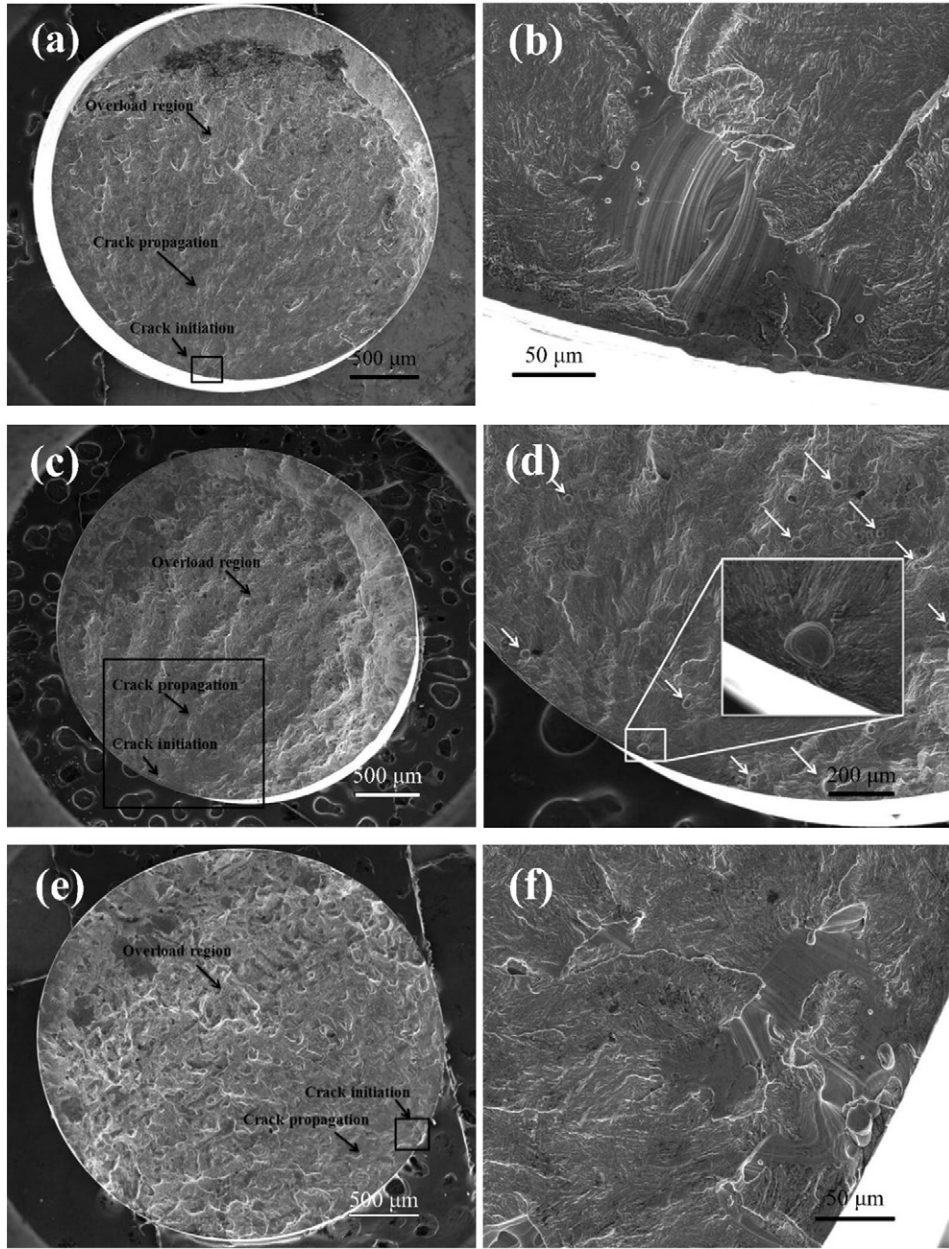


Fig. 11. Fracture surfaces of SLM fatigue specimens: (a) and (b) SLM-OP1, (c) and (d) SLM-MP2, (e) and (f) SLM-MP4. The images on the left are taken at low magnification and show the entire specimen cross-section. The rectangular boxes show the regions of crack initiation. White arrows show the defects. The images on the right show the fracture features at a higher magnification close to the crack origin.

SLM-MP5) showed a fatigue limit of around 100 MPa confirming that defects due to lack-of-fusion and incomplete powder melting are seriously detrimental to the fatigue performance. It should be noted that these samples show a very definite trend of increasing fatigue life with decreasing stress amplitude, unlike the other three sets of SLM samples. This suggests that lack-of-fusion defects in SLM-MP4 and SLM-MP5 samples are so seriously detrimental to fatigue performance that even the statistical nature of metal fatigue is defeated. In the case of EBM, EBM-OP1 and EBM-MP2 samples showed comparable fatigue lives, but the fatigue performance of EBM-MP3 samples is very poor with a fatigue limit of just 50 MPa. As in the case of SLM-MP4 and SLM-MP5 samples, EBM-MP3 samples showed a very regular trend of increasing fatigue life with decreasing stress amplitude, unlike EBM-OP1 and EBM-MP2 samples.

Representative fractographs of SLM and EBM fatigue fractured specimens are shown in Figs. 11 and 12, respectively. In all the specimens,

including those built using optimum parameters (Fig. 11a and b, Fig. 12a and b), cracks were found to initiate at a defect near the surface or subsurface. The fracture surfaces of SLM-MP2 specimens (Fig. 11c and d) revealed smaller and more regularly shaped defects compared to SLM-MP4 specimens (Fig. 11e and f). Spherical powder particles evidencing incomplete melting were also seen on the fracture surfaces of SLM-MP4 samples. These features can be seen more clearly in EBM-MP3 samples (Fig. 12c and d). Finally, the spherical defects evident on tensile (Fig. 7b) and fatigue (Fig. 11d) fracture surfaces of SLM-MP2 samples have a “stair” feature on their internal surface that may merit further investigation. The spherical defects could result from gas bubbles entrapped or generated when a high laser energy is applied to the melt pool, or from the pits generated by the recoater blade when removing welded particles [35,42,43]. But according to the morphological features and distribution, gas bubbles account for most of these defects in SLM-MP2 specimens.

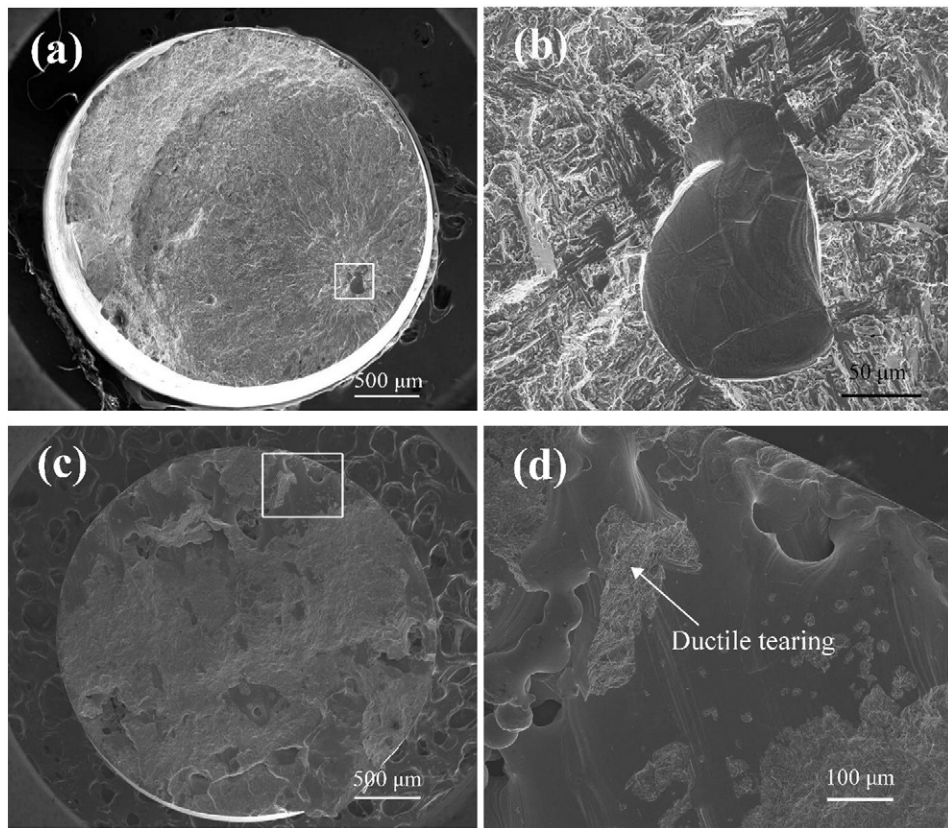


Fig. 12. Fracture surfaces of EBM specimens: (a) and (b) EBM-OP1, (c) and (d) EBM-MP3. The images on the left are taken at low magnification and show the entire specimen cross-section. The rectangular boxes show the regions of crack initiation. The images on the right show the fracture features at a higher magnification close to the crack origin.

4. Conclusions

In this study, SLM and EBM processes were used to produce Ti-6Al-4 V samples with different types and amounts of defects. The samples were subjected to hardness, tensile, and fatigue tests. Based on the findings of this study, the following conclusions can be drawn:

- Defect generation does not influence microstructure evolution in Ti-6Al-4 V during SLM and EBM. The microstructure is mainly governed by the cooling rate.
- Ti-6Al-4 V samples built using SLM show higher yield and tensile strengths than those produced using EBM because of their predominantly martensitic α microstructure. However, SLM and EBM samples show comparable tensile ductility, fatigue strength, and hardness.
- Density measurements using the Archimedes method are not satisfactory for assessing the quality of SLM and EBM samples, particularly when the samples are built using insufficient energy input. Samples may contain a significant amount of unmelted powder inside the defects, which contributes to density, but not to strength.
- In SLM samples, small pores or voids caused by the use of higher-than-optimum energy input are harmless when present in amounts up to 1 vol.%. However, tensile, fatigue, and hardness properties are considerably affected when these defects occur at the level of 5 vol.%.
- In SLM, defects caused by insufficient energy input have a strong bearing on the mechanical properties even when present in amounts as low as 1 vol.%. When such defects occur in higher amounts (to the level of 5 vol.%), the part mechanical properties tend to be very poor and unacceptable.
- In SLM, defects caused by excessive energy input are less detrimental to part mechanical properties than those caused by insufficient energy input.

- In EBM, any significant deviation from optimum process parameters results in relatively large defects and poor mechanical properties.

Acknowledgments

The authors gratefully acknowledge the support of the Office of Naval Research, awards N00014-09-1-0147 and N00014-10-1-0800, Technical Monitor: Dr. Ignacio Perez. The authors also express their gratitude to the staff of Rapid Prototyping Center at the University of Louisville for their assistance.

References

- I. Gibson, D.W. Rosen, B. Stucker, *Additive manufacturing technologies: rapid prototyping to direct digital manufacturing*, Springer, New York, 2009.
- T.H.C. Childs, C. Hauser, M. Badrossamay, Selective laser sintering (melting) of stainless and tool steel powders: experiments and modelling, *Proc. Inst. Mech. Eng. B J. Eng. Manuf.* 219 (2005) 339–357.
- G. Casalino, S.L. Campanelli, N. Contuzzi, A.D. Ludovico, Experimental investigation and statistical optimisation of the selective laser melting process of a maraging steel, *Opt. Laser Technol.* 65 (2015) 151–158.
- B. Vandenbroucke, J.P. Kruth, Selective laser melting of biocompatible metals for rapid manufacturing of medical parts, *Rapid Prototyp. J.* 13 (2007) 196–203.
- S. Price, B. Cheng, J. Lydon, K. Cooper, K. Chou, On process temperature in powder-bed electron beam additive manufacturing: process parameter effects, *J. Manuf. Sci. Eng.* 136 (2014) (061019-1–10).
- S. Sun, Y. Koizumi, S. Kurosu, Y. Li, H. Matsumoto, A. Chiba, Build direction dependence of microstructure and high-temperature tensile property of Co-Cr-Mo alloy fabricated by electron beam melting, *Acta Mater.* 64 (2014) 154–168.
- L. Thijs, F. Verhaeghe, T. Craeghs, J.V. Humbeeck, J.P. Kruth, A study of the microstructural evolution during selective laser melting of Ti-6Al-4 V, *Acta Mater.* 58 (2010) 3303–3312.
- N. Tolochko, S. Mozzharov, I. Yadroitsev, Balling processes during selective laser treatment of powders, *Rapid Prototyp. J.* 10 (2004) 78–87.
- R. Li, J. Liu, Y. Shi, M. Du, X. Zhan, 316 L stainless steel with gradient porosity fabricated by selective laser melting, *J. Mater. Eng. Perform.* 19 (2010) 666–671.

- [10] S. Biamino, A. Penna, U. Ackelid, S. Sabbadini, O. Tassa, P. Fino, et al., Electron beam melting of Ti-48Al-2Cr-2Nb alloy: microstructure and mechanical properties investigation, *Internet* 19 (2011) 776–781.
- [11] L. Facchini, E. Magalini, P. Robotti, A. Molinari, S. Höges, K. Wissenbach, Ductility of a Ti-6Al-4 V alloy produced by selective laser melting of prealloyed powders, *Rapid Prototyp. J.* 16 (2010) 450–459.
- [12] L. Facchini, E. Magalini, P. Robotti, A. Molinari, Microstructure and mechanical properties of Ti-6Al-4 V produced by electron beam melting of pre-alloyed powders, *Rapid Prototyp. J.* 15 (2009) 171–178.
- [13] E. Wycisk, C. Emmelmann, S. Siddique, F. Walther, High cycle fatigue (HCF) performance of Ti-6Al-4 V alloy processed by selective laser melting, *Adv. Mater. Res.* 816–817 (2013) 134–139.
- [14] G.V. Joshi, Y. Duan, J. Neidigh, M. Koike, G. Chahine, R. Kovacevic, et al., Fatigue testing of electron beam-melted Ti-6Al-4 V ELI alloy for dental implants, *J. Biomed. Mater. Res. B Appl. Biomater.* 101B (2013) 124–130.
- [15] T. Sercombe, N. Jones, R. Day, A. Kop, Heat treatment of Ti-6Al-7Nb components produced by selective laser melting, *Rapid Prototyp. J.* 14 (2008) 300–304.
- [16] Q. Liu, J. Elambasseril, S. Sun, M. Leary, M. Brandt, P.K. Sharp, The effect of manufacturing defects on the fatigue behaviour of Ti-6Al-4 V specimens fabricated using selective laser melting, *Adv. Mater. Res.* 891–892 (2014) 1519–1524.
- [17] E. Santos, F. Abe, Y. Kitamura, K. Osakada, M. Shiomi, Mechanical properties of pure titanium models processed by selective laser melting, 13rd Annual International Solid Freeform Fabrication Symposium, Austin TX 2002, pp. 180–186.
- [18] H. Gong, K. Rafi, T. Starr, B. Stucker, Effect of defects on fatigue tests of as-built Ti-6Al-4 V parts fabricated by selective laser melting, 23rd Annual International Solid Freeform Fabrication Symposium, Austin TX 2012, pp. 499–506.
- [19] P. Edwards, M. Ramulu, P. Edwards, M. Ramulu, Fatigue performance evaluation of selective laser melted Ti-6Al-4 V, *Mater. Sci. Eng. A* 598 (2014) 327–337.
- [20] E. Wycisk, A. Solbach, S. Siddique, D. Herzog, F. Walther, C. Emmelmann, Effects of defects in laser additive manufactured Ti-6Al-4 V on fatigue properties, *Phys. Procedia* 56 (2014) 371–378.
- [21] M. Simonelli, Y.Y. Tse, C. Tuck, Fracture mechanisms in high-cycle fatigue of selective laser melted Ti-6Al-4 V, *Key Eng. Mater.* 627 (2015) 125–128.
- [22] S. Leuders, M. Thöne, A. Riemer, T. Niendorf, T. Tröster, H.A. Richard, et al., On the mechanical behaviour of titanium alloy TiAl6V4 manufactured by selective laser melting: fatigue resistance and crack growth performance, *Int. J. Fatigue* 48 (2013) 300–307.
- [23] S.J. Li, L.E. Murr, Z.B. Zhang, X.Y. Cheng, Y.L. Hao, R. Yang, et al., Compression fatigue behavior of Ti-6Al-4 V mesh arrays fabricated by electron beam melting, *Acta Mater.* 60 (2012) 793–802.
- [24] F. Brenne, T. Niendorf, H.J. Maier, Additively manufactured cellular structures: impact of microstructure and local strains on the monotonic and cyclic behavior under uniaxial and bending load, *J. Mater. Process. Technol.* 213 (2013) 1558–1564.
- [25] J. Sun, Y. Yang, D. Wang, Mechanical properties of a Ti6Al4V porous structure produced by selective laser melting, *Mater. Des.* 49 (2013) 545–552.
- [26] S. Amin Yavari, S.M. Ahmadi, R. Wauthle, B. Pouran, J. Schrooten, H. Weinans, et al., Relationship between unit cell type and porosity and the fatigue behavior of selective laser melted meta-biomaterials, *J. Mech. Behav. Biomed. Mater.* 43 (2015) 91–100.
- [27] P. Heinl, C. Körner, R.F. Singer, Selective electron beam melting of cellular titanium: mechanical properties, *Adv. Eng. Mater.* 10 (2008) 882–888.
- [28] L.E. Murr, S.M. Gaytan, F. Medina, E. Martinez, J.L. Martinez, D.H. Hernandez, et al., Characterization of Ti-6Al-4 V open cellular foams fabricated by additive manufacturing using electron beam melting, *Mater. Sci. Eng. A* 527 (2010) 1861–1868.
- [29] L.E. Murr, K.N. Amato, S.J. Li, Y.X. Tian, X.Y. Cheng, S.M. Gaytan, et al., Microstructure and mechanical properties of open-cellular biomaterials prototypes for total knee replacement implants fabricated by electron beam melting, *J. Mech. Behav. Biomed. Mater.* 4 (2011) 1396–1411.
- [30] J. Schwerdtfeger, P. Heinl, R.F. Singer, C. Körner, Auxetic cellular structures through selective electron-beam melting, *Phys. Status Solidi B* 247 (2010) 269–272.
- [31] J. Schwerdtfeger, F. Schury, M. Stingl, F. Wein, R.F. Singer, C. Körner, Mechanical characterisation of a periodic auxetic structure produced by SEBM, *Phys. Status Solidi B* 249 (2012) 1347–1352.
- [32] S.J. Li, Q.S. Xu, Z. Wang, W.T. Hou, Y.L. Hao, R. Yang, et al., Influence of cell shape on mechanical properties of Ti-6Al-4 V meshes fabricated by electron beam melting method, *Acta Biomater.* 10 (2014) 4537–4547.
- [33] L. Yang, O. Harrysson, H. West, D. Cormier, Compressive properties of Ti-6Al-4 V auxetic mesh structures made by electron beam melting, *Acta Mater.* 60 (2012) 3370–3379.
- [34] B. Song, S. Dong, B. Zhang, H. Liao, C. Coddet, Effects of processing parameters on microstructure and mechanical property of selective laser melted Ti6Al4V, *Mater. Des.* 35 (2012) 120–125.
- [35] H. Gong, K. Rafi, H. Gu, T. Starr, B. Stucker, Analysis of defect generation in Ti-6Al-4 V parts made using powder bed fusion additive manufacturing processes, *Addit. Manuf.* 1 (2014) 87–98.
- [36] H. Gong, K. Rafi, N.V. Karthik, T. Starr, B. Stucker, Defect morphology in Ti-6Al-4 V parts fabricated by selective laser melting and electron beam melting, 24th Annual International Solid Freeform Fabrication Symposium, Austin TX 2013, pp. 440–453.
- [37] S. Zhang, Q. Wei, L. Cheng, S. Li, Y. Shi, Effects of scan line spacing on pore characteristics and mechanical properties of porous Ti6Al4V implants fabricated by selective laser melting, *Mater. Des.* 63 (2014) 185–193.
- [38] N. Hrabe, T. Quinn, Effects of processing on microstructure and mechanical properties of a titanium alloy (Ti-6Al-4 V) fabricated using electron beam melting (EBM). Part 2: energy input, orientation, and location, *Mater. Sci. Eng. A* 573 (2013) 271–277.
- [39] M. Simonelli, Y.Y. Tse, C. Tuck, Microstructure of Ti-6Al-4 V produced by selective laser melting, *J Phys Conf Ser.* 371 2012, p. 012084.
- [40] K. Rafi, N.V. Karthik, H. Gong, T. Starr, B. Stucker, Microstructures and mechanical properties of Ti-6Al-4 V parts made by selective laser melting and electron beam melting, *J. Mater. Eng. Perform.* 22 (2013) 3872–3883.
- [41] K. Rafi, T. Starr, B. Stucker, A comparison of the tensile, fatigue, and fracture behavior of Ti-6Al-4 V and 15–5 PH stainless steel parts made by selective laser melting, *Int. J. Adv. Manuf. Technol.* 69 (2013) 1299–1309.
- [42] L. Li, Repair of directionally solidified superalloy GTD-111 by laser-engineered net shaping, *J. Mater. Sci.* 41 (2006) 7886–7893.
- [43] W.E. King, H.D. Barth, V.M. Castillo, G.F. Gallegos, J.W. Gibbs, D.E. Hahn, et al., Observation of keyhole-mode laser melting in laser powder-bed fusion additive manufacturing, *J. Mater. Process. Technol.* 214 (2014) 2915–2925.

The Effects of Electron Beam Melting on the Microstructure and Mechanical Properties of Ti-6Al-4V and Gamma-TiAl

Tait McLouth¹, Yuan-Wei Chang¹, John Wooten², Jenn-Ming Yang¹

¹. Department of Materials Science and Engineering, University of California, Los Angeles, U.S.A.

². CalRam Inc., Simi Valley, CA, U.S.A.

Titanium alloys have been used extensively in the aerospace and biomedical industries due to their high strength to weight ratios, elevated temperature mechanical properties, excellent biocompatibility, and good corrosion resistance [1-4]. Alloys, such as Ti-6Al-4V (Ti-6-4) can be used for replacement hip joints, knee joints, and bone plates because of the aforementioned properties. Titanium-aluminum intermetallic alloys such as γ -TiAl are attractive for high temperature turbine engine components because of their good thermal stability and low density [5]. Recently, both of these alloys have been manufactured with additive manufacturing (AM) because traditional methods such as casting and forging present problems and limitations [5]. AM provides more design flexibility for titanium alloys, a great benefit when considering the complexity of certain parts made for biomedical implants or jet engines. Electron beam melting (EBM) is a powder processing AM technique that produces fully net shaped parts from a bed of powder, and it is the main focus of this study.

In this research, the microstructure and mechanical properties of both Ti-6-4 and γ -TiAl were studied before and after the EBM process. X-Ray diffraction (XRD), nanoindentation, and micropillar compression were performed to gain an understanding of the effects of the EBM manufacturing process. Microstructural evaluation was performed with the use of a scanning electron microscope (SEM). Figure 1 (a)(b) shows the microstructure of Ti-6-4 and γ -TiAl, respectively. Both alloys form a fine lamellar microstructure of alternating phases; these needle like Widmanstätten structures serve to strengthen the alloys by reducing crack propagation through the material.

Micropillars prepared by focused ion beam (FIB) milling were compressed by a nanoindenter in order to gather the yield strength and Young's modulus. Stress/strain curves for micropillars are shown in Figure 2(a) and (b) for Ti-64 and γ -TiAl, respectively. Tabulated values for the experimentally calculated compressive yield strengths, hardnesses, and Young's Moduli are shown in Table 1. From Table 1, it is clear that the EBM manufacturing process has a positive effect on the mechanical properties of Ti-6-4 and γ -TiAl. Compared to a cast sample of Ti-6-4 that underwent identical testing, the EBM sample displayed yield strengths that were 39% higher on average. This is due to the microstructure that is formed upon cooling. Specifically for Ti-6-4, the β phase that forms enhances the mechanical properties, as it has a higher strength than the α phase and also acts as a strengthening phase [6]. Referring to Figure 1, very fine spacing of the lighter β phase can be observed. The mechanical properties found for γ -TiAl agree well with calculated and experimental values from the literature with a Young's modulus of 179 ± 5 GPa.

From this research it can be concluded that the manufacturing process plays a significant role in the final mechanical behavior of a material. In the case of Ti alloys, there seems to be a strengthening effect due to the faster cooling rate and favorable microstructure that forms as a result. Future work to be performed will involve a TEM analysis of the deformation mechanisms of both materials as well as an analysis of the base powder from which EBM samples are produced.

References:

- [1] Y. Okazaki, S. Rao, Y. Ito, T. Tateishi, "Corrosion resistance, mechanical properties, corrosion fatigue strength and cytocompatibility of new Ti alloys without Al and V," *Biomaterials* 19 (1998) 1197-1215.
- [2] Y. Okazaki, E. Nishimura, H. Nakada, K. Kobayashi, "Surface analysis of Ti-15Zr-4Nb-4Ta alloy after implantation in rat tibia," *Biomaterials* 22 (2001) 599-607.
- [3] E. Eisenbarth, D. Velton, M. Müller, R. Thull, J. Breme, "Biocompatibility of beta-stabilizing elements of titanium alloys," *Biomaterials* 25 (2004) 5705-13.
- [4] M. Niinomi, "Biologically and Mechanically Biocompatible Titanium Alloys," *Mater. Trans.* 49 (2008) 2170-8.
- [5] S. F. Franzen, Joakim Karlsson, " γ -Titanium Aluminide Manufactured by Electron Beam Melting," Sanna Fager Franzen, Joakim Karlsson (2010).
- [6] William F. Smith, "Structure and Properties of Engineering Alloys", Second Ed. (New York, NY: McGraw-Hill, 1993) 201-245.

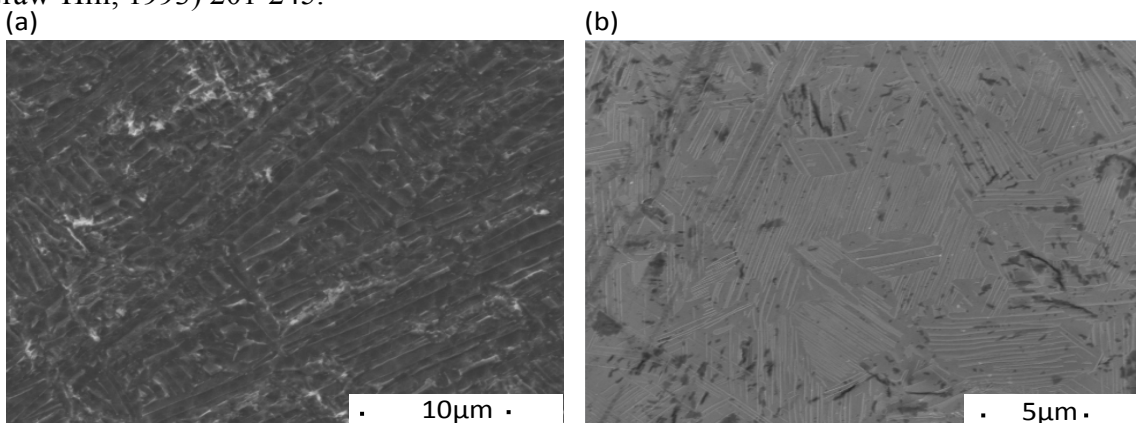


Figure 1: SEM images of microstructures for (a) Ti-6-4 showing the V rich β phase (lighter) and Al rich α phase (darker) and (b) γ -TiAl showing the α_2 - Ti_3Al phase (lighter) and γ -TiAl phase (darker)

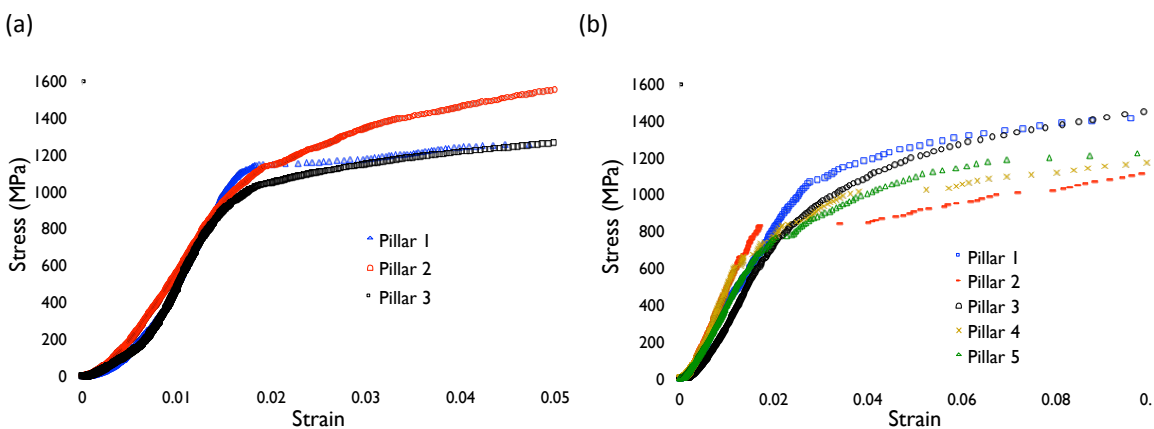


Figure 2: Micro-compressive stress-strain curves of (a) Ti-6-4 and (b) γ -TiAl

Material	Yield Strength	Young's Modulus	Hardness
EBM Ti-6-4	1135 ± 12 MPa	114 ± 6 GPa	4.5 ± 0.3 GPa
Cast Ti-6-4	812 ± 26 MPa	116 ± 2 GPa	4.1 ± 0.2 GPa
EBM γ-TiAl	620 ± 21 MPa	179 ± 5 GPa	5.3 ± 0.2 GPa

Table 1: Mechanical properties of tested samples

Rapid Manufacturing with Electron Beam Melting (EBM) – A manufacturing revolution?

Authors

Morgan Larsson, Technical Manager, Arcam AB

Ulf Lindhe, M.Sc., Manager of Marketing, Sales and Service, Arcam AB

Ola Harrysson, Ph.D., Assistant Professor, Industrial Engineering Department, North Carolina State University

ABSTRACT

The Electron Beam Melting technology is the result of intensive research and development and has a wide array of applications within areas such as Rapid Prototyping, Rapid Manufacturing, Tooling and Biomedical Engineering. The technology combines first-class material properties with high build speeds. The presentation will provide a basic understanding of the technology, technical status, applications and ongoing R&D.

Basic process & background

Arcam, founded 1997, has developed a unique Free Form Fabrication (FFF®) technology for Direct Manufacturing of fully dense parts from metal powder. The technology is based on Electron Beam Melting (EBM) and the parts are built up by melting the metal powder layer-by-layer.

The founders were prompted by a vision to revolutionize the art of manufacturing of complex parts. The technology is the result of intensive research and development and has a wide array of applications within areas such as Rapid Prototyping, Direct Manufacturing, Tools for Injection Molding and Die-Casting as well as Biomedical Engineering.

The technology offers a high level of geometric freedom together with first-class material properties. The CAD to Metal® technology provide fully dense metal with material properties identical with or close to the target metals used. Most conductive materials can be used although steel and titanium alloys the only materials available as per today. The strategy in the development is to combine excellent material properties with high build speeds.

With its ability to directly process complex geometries, the Electron Beam Melting process is ideal for direct manufacturing of complex parts in low volumes. The process enables customization of parts and parts optimized for the CAD to Metal process can feature geometries that cannot be achieved in other manufacturing technologies, thus providing superior performance in the part and value to the

customer. The process works directly from CAD data and is fast. The designer can have a fully functional detail within 24 hours from completion of the design. The process often requires significantly less lead-time than sand casting or investment casting.

The combination of Electron Beam Melting and vacuum provide high power and good environment for the process resulting in excellent material properties.

The major difference between the Electron Beam Melting process and methods such as Laser Sintering/Laser Melting is efficiency of the Electron Beam gun compared with a laser. The electron beam technology is several times more energy efficient than laser technology resulting in less power consumption and lower maintenance and manufacturing costs. Arcam is currently using a 4 kW EB gun on its standard machine. Reflection in the pool of melted metal is also a non-issue with electron beam technology.

The availability of sufficient power in the heat source in any fully melting freeform fabrication system is of key importance to achieve good material properties and high build speeds.

Electron Beam Melting (EBM)

The fundamental idea behind the CAD to Metal® technology is to build up metal details in layers of metal powder, each of which is melted by an electron beam to exactly the geometry defined by the computer model.

The part is first designed in a 3D CAD program. The file is transferred to pre-processing software where the model is sliced into thin layers. The parts are built up layer-by-layer by the Electron Beam Melting (EBM) process in a vacuum chamber. On completion of the CAD to Metal Process the net-shape part is cleaned and can be finished as necessary by conventional methods.

The electron beam is generated in an Electron Beam Gun situated on the top of a vacuum chamber. The Electron Beam Gun is fixed and the beam is deflected to reach the entire building area.

The electrons are emitted from a filament, which is heated to high temperature. The electrons are then accelerated to half the speed of light in an electric field. The beam of electrons is controlled with two magnetic fields. The first acts as a magnetic lens and is responsible for focusing the beam to the desired diameter. The second magnetic field deflects the focused beam to the desired point on the building table.

Advantages and disadvantages

Electron Beam Welding has become a vital technology in many industries. Some of its benefits include:

- Ability to achieve a high energy level in a narrow beam.
- Vacuum melt quality can yield high strength properties of the material.
- Vacuum environment eliminates impurities such as oxides and nitrides.
- Permits welding in refractory metals and combinations of dissimilar metals

Electron Beam Melting benefits from all of these factors in the same way. Compared with laser sintering/melting additional benefits include:

- Higher efficiency in generating the beam of energy resulting in lower power consumption as well as lower maintenance and installation costs
- High actual overall power resulting in high build speeds
- Deflection of the beam can be achieved without moving parts resulting in high scanning speed and low maintenance.

Some apparent disadvantages of electron beam technology are:

- Requires vacuum which adds another system on the machine which cost money and must be maintained [Added benefit: Vacuum eliminates impurities and provide a good thermal environment for freeform fabrication]
- Electron beam technology produces X-rays while in operation [Solution: The vacuum tank shields the rays perfectly if properly designed.]

Process availability and current use status

As per June 30th, 2003, 8 units have been built with a 9th system in production. Four of the systems are situated at Arcam while two beta-systems were installed at companies in Sweden during 2002. The present model was launched in December 2002 and during 2003 two of these systems have been installed. One system is in operation in Italy and one system at NC State University in Raleigh, North Carolina, USA.

The best applications, now and in the future

Present R & D is focusing on parts for high performance applications within automotive and aerospace industry as well as biomedical applications such as implants. Typical applications are complex parts manufactured in low volumes where casting and machining would require too much of lead-time, machine time or scrapping of material.

The technology can also be used to manufacture parts featuring geometries that cannot be achieved in other manufacturing technologies, thus providing superior

performance in the part and value to the customer. Examples of such applications are:

- Complex lattice/framework structures for lightweight design
- Internal cavities for lightweight design, weight distribution optimization and flow control
- Optimization of material and stress distribution
- Conformal cooling channels

The technology is used by teams within the car racing industry for fabrication of high performance parts and prototypes.

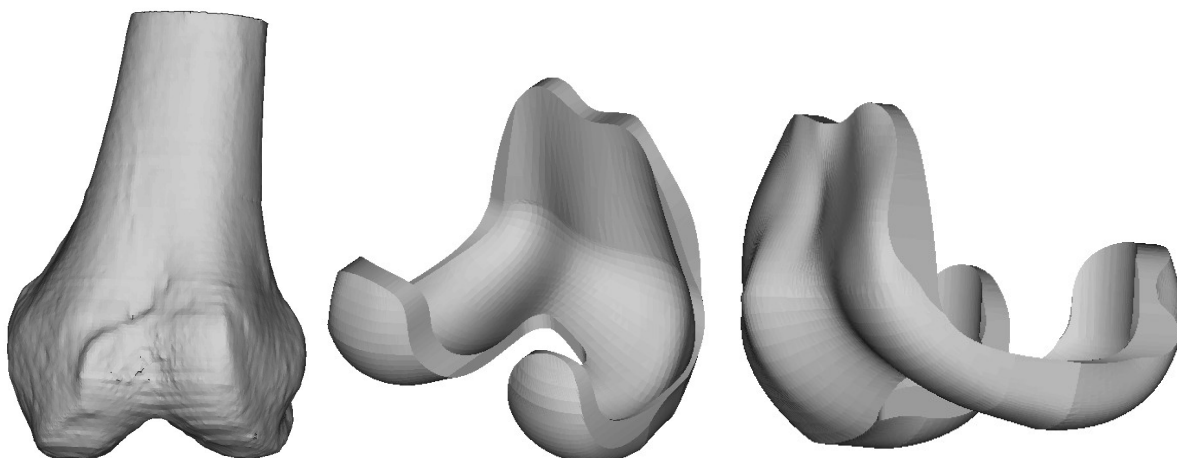
Fabrication of custom designed orthopedic implants can benefit from efficient freeform fabrication in metals such as commercially pure and alloyed titanium. There is a future for customized Knee- and Hip-implants that will provide better fitting and longer lasting prostheses and most areas of orthopedic implant surgery can benefit from customized implants.

North Carolina State University has several research projects related to customize implant technology. Areas of research include

- Optimize the bone-implant interface for better performance
- Reduce bone remodeling due to better stress distribution
- Customize implant due to size and shape of Tibia and Femur.
- Fabrication of implant components in titanium using the EBM-machine

Custom Implants

Each year over 500,000 Americans go through a hip or knee implant surgery to restore the function of a worn out joint. One of the main problems is that we are all different and the generic implants don't fit perfectly on most people, decreasing the longevity and the function of the implant. To improve the current generic implants, an effort has been made at North Carolina State University to design custom implants based on a Computed Tomography (CT) scan of the particular patient. The CT-scan is converted into a CAD-model of the patient's joint and a custom implant can be designed with optimal fit, shape and geometry.



The custom designed implant component could be fabricated through investment casting using an RP-pattern as a master, but would take a considerable amount of time and would be labor intensive, making the implant prohibitively expensive. Using the EBM-technology and the newly developed titanium alloy, the implant component could be fabricated in a matter of hours with very little labor involved using the same manual finishing as with conventional implant fabrication.

Plates for repair of severe bone fractures

Titanium and stainless steel plates are often used to repair and secure severe bone fractures on both humans and animals. The standard bone plates come in different sizes and are normally flat with evenly distributed holes. The surgeon spends a considerable amount of time in surgery to shape the bone plate to conform to the patient's specific anatomy using hand tools. This is an iterative process that prolongs the surgery, increasing the risk of trauma and infection. In many cases it is difficult to align the evenly distributed holes with the bone to attach the screws. In a new project at NCSU, custom designed bone plates are being developed using patient specific CT-scans and the EBM-technology. The surgeon will decide where to place the holes for the screws to achieve the optimal result and the plate is designed to perfectly conform to the curvature of the bone.

Materials

In theory, most conductive metals can be used in the process. To convert theory into reality Arcam is devoting significant resources to R&D in materials sciences in order to constantly develop and refine the CAD to Metal process for an increasing number of metals and alloys. Partners in materials R&D include companies and organizations such as

Chalmers University of Technology, Göteborg, Sweden
Max Planck Institute, Düsseldorf, Germany
North Carolina State University, Raleigh, NC, USA
Volvo Aero Corporation, Sweden

The CAD to Metal® process fully melts the metal powder in order to provide fully-dense metal with material properties identical with or close to the target metals used. Parts are built up in vacuum under strict temperature control.

Initial development of the technology was carried out with iron-based metals and the process has been verified for the following materials:

Tool Steel
Low Alloy Steel
Alloyed Titanium
Commercially Pure Titanium

Nickel Alloys

The current build volume that has been achieved is within a 200x200x160 mm envelope with massive parts in steel having a maximum size limitation of some 150x150x160 mm. The accuracy is within +/- 0.3 mm and is comparable to castings.

Mechanical Properties

	Ti6Al4V	H13
Hardness	30-35 HRc	48-52 HRc
Tensile Strength (Rm)	930 Mpa / 135 ksi	1300 Mpa / 190 ksi abt 1500 Mpa/ 220 ksi after heat treatment
Yield Strength (Rp0.2)	880 Mpa / 125 ksi	1000 Mpa /144 ksi
Modulus of elasticity	128 000 MPa	210 000 MPa
Elongation	> 10 %	N.A.
Microstructure	Lamellar alpha-phase with larger beta-grains. The material has a naturally aged condition directly from the process	Martensitic structure with a typical grain size between 10-30 mm due to fine uniform vanadium carbide dispersion.

As-Fabricated and Heat-Treated Microstructures of the Ti-6Al-4V Alloy Processed by Selective Laser Melting

T. VILARO, C. COLIN, and J.D. BARTOUT

Selective laser melting (SLM) is a rapid manufacturing process that enables the buildup of very complex parts in short delays directly from powder beds. Due to the high laser beam energy during very short interaction times and the high solidification rates of the melting pool, the resulting microstructure is out-of-equilibrium and particularly textured. This type of as-fabricated microstructure may not satisfy the aeronautical criterion and requires post heat treatments. Optimized heat treatments are developed, in one side, to homogenize and form the stable phases α and β while preventing exaggerated grain growth. In the other side, heat treatment is investigated to relieve the thermal stresses appearing during cooling. This study is aimed at presenting the various types of microstructure of the Ti-6Al-4V alloy after postfabrication heat treatments below or above the β transus. Tensile tests are then carried out at room temperature in order to assess the effect of the microstructures on the mechanical properties. The fine as-fabricated microstructure presents high yield and ultimate strengths, whereas the ductility is well below the standard. A strong anisotropy of fracture between the two loading directions is noted, which is attributed to the manufacturing defects. Conventional and optimized heat treatments exhibit high yield and ultimate strengths while the ductility is significantly improved. This is due to a new optimization of the process parameters allowing drastic reduction of the number of defects. These two heat treatments enable now a choice of the morphology of the grains between columnar or equiaxial as a function of the type of loading.

DOI: 10.1007/s11661-011-0731-y

© The Minerals, Metals & Materials Society and ASM International 2011

I. INTRODUCTION

SELECTIVE laser melting (SLM) process appeared in the late 1990s and is inspired from the stereolithography technique emerging in the late 1980s.^[1] These layer-by-layer processes were first used to produce prototypes, whereas the actual trend is to directly produce functional parts because of the permanent requirement of the industry to save manufacturing cost and time. The description of the process is done elsewhere and is not repeated here.^[2–4] Its success is directly linked with its ability to manufacture complex structures from a computer-aided design model and a wide range of materials in short delays without the need of expensive tools such as molds. Another advantage is that the powder bed is selectively molten; therefore, the nonirradiated powder can be fully recycled for further fabrication (“eco-conception process”). In order to attain a high level of density (≈ 99 pct) and mechanical properties comparable to the conventional fabrication routes such as foundry, the metallic powder is fully molten under the laser beam

in contrast to the selective laser sintering process, in which the melting point (T_m) or the solidus temperature of the material is never reached. This process is adapted more to the ceramic and polymer materials. Further, due to the high thermal gradient induced by the laser beam combined with high solidification rate, the resulting microstructure is out-of-equilibrium, very fine, and strongly textured whatever the nature of the material.^[5,6] Finally, the parts contain several defects such as lack of melting, some problems of scanning strategy, entrapped gas in solidified material, or residual stresses.^[7–9]

The titanium alloys and especially the Ti-6Al-4V alloy are widely used in the aeronautical industry for their high specific strength (ratio between the ultimate strength and its low density) but also for their high corrosion resistance at temperatures up to 773 K (500 °C). The high cost of the raw material has become an important driving force for the French aeronautical industry to manufacture near-net-shape components directly from additive processes. Nowadays, it exists in the literature in a few articles dealing with the as-fabricated microstructures of the titanium alloys by additive processes,^[10,11] but none of them deals with the modification of this metastable microstructure through heat treatments in order to satisfy the industrial requirements as well as the resulting mechanical properties.

This article is aimed at presenting the Ti-6Al-4V microstructure resulting from the SLM process. These microstructures are examined in terms of grain

T. VILARO, Engineer of Research, is with Poly-Shape, 43, rue d'Yerres, 94440 Villecresnes, France, and also with the Materials Centre of Mines ParisTech, CNRS UMR 7633, BP87, 91003 Evry, France. Contact e-mail: thomas.vilaro@ensmp.fr C. COLIN, Reader, and J.D. BARTOUT, Engineer of Research, are with the Materials Centre of Mines ParisTech, CNRS UMR 7633.

Manuscript submitted August 23, 2010.

Article published online May 19, 2011

morphology, size, and nature of phases. Specific heat treatments are then developed depending on the desired final microstructure and are compared to the more conventional treatments. Finally, mechanical tests are carried out at room temperature to determine the tensile properties of the as-fabricated as well as the various microstructures obtained after heat treatments.

II. EXPERIMENTAL PROCEDURES

The samples are manufactured on a Trumpf LF250 machine at Poly-Shape (Villecresnes, France) including a laser unit delivering a continuous laser power of 500 W. In contrast to most laser beams used in rapid manufacturing, the energy distribution is multimodal, which means that it presents two hot zones instead of the more conventional Gaussian heat distribution. The main process parameters such as the laser power P , the scanning speed V , the laser beam diameter \varnothing_l , the layer thickness ΔZ , and the hatching space H_s were previously optimized to obtain the lowest porosity level. It is worth mentioning that the aeronautical industry only accepts parts having less than 1 vol pct of porosity. These parameters are enumerated in Table I.

Because the solidified material is susceptible to containing a high level of residual stresses close to the substrate, the titanium substrate was preheated at 773 K (500 °C). At this temperature, it is expected to relieve the thermal stresses over a few millimeters. In fact, Combres shows that it is necessary to maintain the alloy during 10 hours at 773 K (500 °C) to relieve only 50 pct of the residual stresses.^[12] The oxygen content in the building chamber was maintained below 100 ppm to prevent melting pool oxidation and its oxygen enrichment, which is well known to stabilize the α phase.

The powder batch had a nominal size comprised between 20 and 55 μm with a Gaussian distribution centered on 35 μm . Its morphology was spherical thanks to the gas atomization process. Because it is well known that the oxygen stabilizes the α phase by increasing the β transus temperature, inductively coupled plasma–atomic emission spectroscopy (ICP-AES) analysis was carried out on a sample of powder. This type of analysis indicates that the oxygen present in solid solution of the

Ti-6Al-4V powder is 1300 ppm, well below the limit tolerated in the aeronautical industry for such material (2000 ppm). Differential thermal analysis (DTA), useful to determine the metallurgical transformation temperatures, was carried out on a sample of powder at 10 K/min (10 °C/min) from room temperature to 1723 K (1450 °C) under argon. This has permitted confirmation of the low oxygen content of the powder, because the β transus temperature is at 1263 K (990 °C).

A decision was made to assess the anisotropy of the process by testing two building orientations, longitudinal direction (LD) and transverse direction (TD), respectively. The LD gives rise to samples with a minimum of layers, because the largest length is parallel to the substrate. The samples built following the TD contain the highest number of layers, with the longest dimension perpendicular to the substrate. The layer overlapping strategy involves the rotation of the scanning direction of 90 deg at each new layer. This is essentially used to improve the metallurgical aspect of the parts by reducing the number of defects.^[13] At each layer, the scanning strategy involves two stages.

- (1) The filling stage comprises all scans located at the core of the samples. In this case, the surface to be scanned is divided into small squares ($5 \times 5 \text{ mm}^2$) in order to yield a more homogeneous thermal gradient induced by the laser beam, thus lowering the overall thermal stresses.^[5,9] Inside each square, each scan was 50 pct overlapped by its neighbor.
- (2) The contour stage comprises the only scan situated around the part. This stage is performed at last (after filling) with the process parameters as the filling stage.

To observe the microstructures, the samples are mechanically ground using SiC papers up to grid 1200 and then polished using diamond paste up to 1 μm . The etching solution used is the Kroll's reagent. Hardness tests are conducted upon a Buehler microhardness machine (Materials Centre of Mines ParisTech, Evry, France) with a force of 2 kg. All heat treatments are carried out under secondary vacuum (10^{-6} torr) with a heating rate of 10 K/min (10 °C/min). Tensile tests are carried out at room temperature with the elongation recorded both with strain gages and extensometer.

Table I. Process Parameters Used to Manufacture the Ti-6Al-4V Samples

Laser Power P (W)	Scanning Speed V (mm/s)	Laser Beam Diameter \varnothing_l (μm)	Layer Thickness ΔZ (μm)	Preheating Temperature T [K (°C)]	Hatching Space H_s (μm)	Oxygen Content O_2 (ppm)
160	600	220	40	773 (500)	200	<100

Table II. New Set of Process Parameters Used to Manufacture the Ti-6Al-4V Samples

Laser Power P (W)	Scanning Speed V (mm/s)	Laser Beam Diameter \varnothing_l (μm)	Layer Thickness ΔZ (μm)	Preheating Temperature T [K (°C)]	Hatching Space H_s (μm)	Oxygen Content O_2 (ppm)
200	500	220	30	773 (500)	200	<100

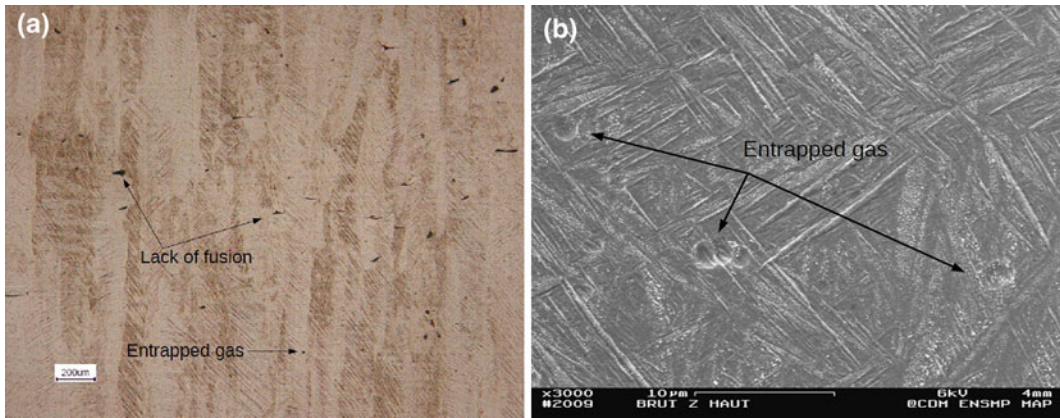


Fig. 1—(a) Optical micrograph illustrating the wide columnar grains of the as-fabricated microstructure and some typical manufacturing defects. (b) SEM image in the SE mode after chemical etching showing the out-of-equilibrium microstructure α' resulting from a rapid quenching from the β domain.

III. THE AS-FABRICATED MICROSTRUCTURE

The first observations are carried out with the optical microscope and permit to reveal the large columnar grains (150- μm wide over the entire height of the samples, Figure 1(a)). This type of microstructure is typical of direct manufacturing processes, which involve partial remelting of the previous layers.^[14] Indeed, when the laser beam scans the layer of powder, it remelts the top of the columnar grains, acting as a nucleus for the epitaxial growth of the strongly textured grains.^[14,15] Moreover, the time the melting pool remains liquid ($T > T_m$) before a complete solidification in the β domain ($T_m > T \geq T_\beta$), depending essentially on the solidification rate (\dot{T}) and the thermal gradient (G), acts on the epitaxial growth and especially the number of nuclei formed.^[16]

Even though accurate thermal measurements of the melting pool temperature as well as the thermal gradient in the building direction are not measured, the resulting microstructure does not evolve as a function of the height of the sample in contrast to what was noticed by Maisonneuve^[14] for the direct metal deposition (DMD) process and Murr *et al.*^[10] for the electron beam process (EBM). This microstructural evolution obtained in DMD comes from the fact that after a certain number of layers, the thermal dissipation through conduction in the substrate becomes negligible. However, the thermal conduction remains significant in the solid part and enables maintenance of this thermal gradient. Maisonneuve, with DMD, noted a high thermal gradient at the top of the wall at a great distance, because the thermal dissipation mainly occurs by convection and radiation, which are much less efficient than conduction.^[14] Longuet confirms this complex thermal behavior of the DMD process associated with the Ti-6Al-4V material thanks to numerical modeling.^[17] Furthermore, in SLM, as long as the part gets higher along the building direction, its cooling occurs through the nonmolten powder particles in contact with the part. This thermal conductivity is dependent on the porosity content, which is around 50 pct. Because of this source of thermal

dissipation, one can think that the temperature of the thermal gradient is, at most, close to 773 K (500 °C). Indeed, no phase transformation is observed during the building time. It can be deduced that lower thermal gradient temperatures are reached in SLM than DMD due to *smaller* melting pool size and lower linear energy (P/V) in comparison to the DMD and EBM processes.

Throughout the height of the samples, the microstructure is composed of the martensite α' phase. As shown in Figure 1(b), the size of needles is very fine (around 360 nm) because of the extremely high cooling rate from the β domain estimated around 10⁴ K/s in SLM. This value is in agreement with the lower cooling rates (10³ to 5·10³ K/s) involved in DMD as a function of the process parameters.^[17] This metastable microstructure was also noted by Murr *et al.* for the Ti-6Al-4V alloy produced by SLM^[10] and Elmer *et al.* for the welded Ti-6Al-4V alloy.^[18]

Such as the sample of powder, the oxygen content of a sample of SLM as-fabricated microstructure was analyzed by ICP-AES and then by DTA. Between the powder and the solid SLM processed material, a slight enrichment in oxygen (1300 → 1500 ppm) is noted, which is attributed to the presence of oxygen in the building chamber of the SLM machine, although it works under argon atmosphere and at level of oxygen below 100 ppm. The β transus does not vary between the powder and the solid SLM processed material and remains at 1263 K (990 °C).

As is also seen in Figure 1(a), some typical SLM defects are present. Nevertheless, the porosity content is determined by the Archimedes method and is found in all cases below 1 vol pct. Various types of defects are often encountered in SLM parts, but the most common can be described as follows.

- (1) The spherical entrapped gases, well known in casting, are usually very small (10 to 50 μm) and have two origins. On one hand, because the powder bed is around 50 pct porous, the gas present between the powder particles may dissolve in the melting pool and may remain after solidification because of

- the high cooling rate. One of the solutions to prevent this problem is to rise the apparent density of the powder bed by increasing the coordination number, as argued by Delannay *et al.*^[19] On the other hand, the melting pool temperature is generally very high due to the very intense laser beam. At this temperature, the solubility of the gas in the liquid metal is high, making its enrichment easier. To counteract this problem, diminishing the volume of liquid metal through smaller layer thicknesses or lower laser power is recommended. The other possibility is to reduce the gas pressure in the building.
- (2) The linear defects, known as lack of melting such as those observed in Figure 1(a), are very typical in additive manufacturing and much bigger than the gas bubbles (≈ 100 - to $150\text{-}\mu\text{m}$ long). They are due to improper optimization of process parameters or an inhomogeneous powder bed. Indeed, irregular thicknesses of the powder bed can lead to variable melting pool volume and temperature, which are in certain cases not thin enough to melt sufficiently the previous layers of material. This type of defect is very critical to the mechanical properties of the parts because of the high stress concentrations at the tip of the defect. It is of interest to avoid these defects if high mechanical properties are demanded. To do so, the thickness of the powder bed can be slightly reduced in order to melt less powder particles but more previously solidified material, enhancing the bonding between layers.

IV. HEAT TREATMENT OPTIMIZATION

The microstructure observed so far is not acceptable for conventional industrial application. Knowing that the mechanical responses of the material are in close relationship to the microstructure, it is of interest to either control the microstructure while the part is being manufactured, as possible with the DMD process,^[14] or to propose post heat treatments to fully restore homogeneous and stable microstructures.

A. Low-Temperature Strategy

This strategy must essentially relieve the thermal stresses resulting from the process without affecting considerably the microstructure. This condition is well suited to the parts that require high dimensional stability with reasonable mechanical properties in service. It involves a tempering treatment at medium temperature. During solidification, the melting pool volume shrinks as the solid front moves into the liquid from the fusion isotherm to its free surface. This volume reduction ($\Delta V_m = 6.7$ pct) obtained from relation 1 is constrained by the previous solid layers, which are directly in contact with the liquid metal. This generates thermal strains. Previous studies on this material have shown that it is possible to completely relieve the residual stresses at 1003 K (730 °C) during 2 hours.^[12]

$$\Delta V_m = 1 - \frac{\rho_l}{\rho_s} \quad [1]$$

where ρ_l and ρ_s are the density of liquid and solid at T_m , respectively. The standard aeronautical heat treatment (1003 K/2 h AC) is analyzed in terms of microstructure and hardness. This heat treatment involves the partial decomposition of the as-fabricated α' phase into the more stable phases $\alpha + s\beta$, as can be observed in Figures 2(a) and (b). This slight chemical contrast observed between the two phases in back scattered electron mode (BSE) mode is confirmed by electron probe microanalysis, where the atoms of vanadium diffused preferentially into the β phase. Microhardness measurements confirm this trend because a slight decrease is noted after 1003 K/2 h (730 °C/2 h) (344 HV2 ± 8 instead of 354 HV2 ± 8 for the as-fabricated microstructure). However, Gil^[20] showed that the complete decomposition is only obtained for temperature treatments above 1073 K (800 °C). Indeed, Figure 2(b) shows the presence of some needle α' phases resulting from the process, which are embedded in the more stable phases $\alpha + \beta$. It is worth mentioning that the width of the columnar grains did not evolve after this heat treatment and remains close to 150 μm .

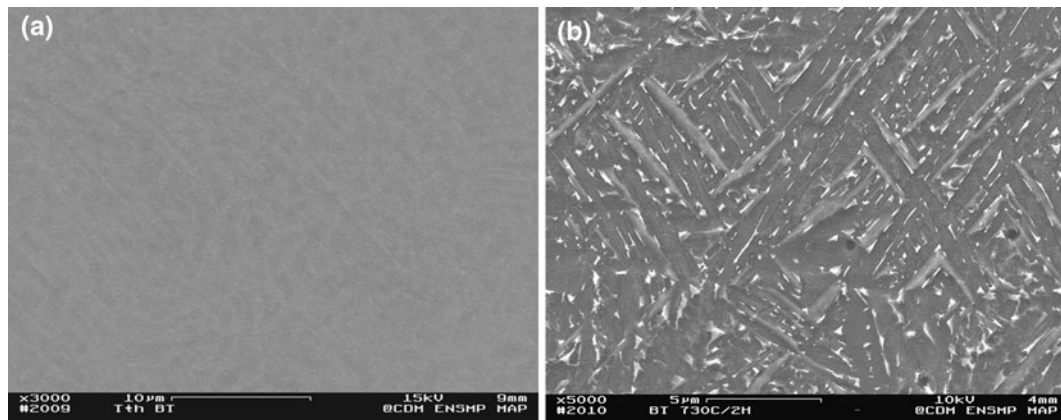


Fig. 2—SEM images (a) in BSE mode without etching and (b) in SE mode after etching illustrating the partial decomposition of the martensite α' from the as-fabricated microstructure toward the more stable phases $\alpha + \beta$ after annealing at 1003 K (730 °C) during 2 h.

B. High-Temperature Strategy

1. Solution treatment

This strategy fits with most industrial requirements, because it is dedicated to the parts demanding high mechanical properties. It involves a solution treatment followed by a tempering treatment to adjust the size, shape, volume fraction, and chemical composition of the strengthening phases.

The solution treatment is usually carried out below the β transus (± 1253 K or ± 980 °C) in order to avoid exaggerated grain growth thanks to the presence of the primary α phase (α_I) in conventional microstructure. Because the as-fabricated macrostructure is composed of relatively wide and long columnar grains as well as the martensite α' (no presence of primary α phase), supertransus solution treatment 1323 K/1 h WQ (1050 °C/1 h WQ) is compared to the more conventional subtransus treatment 1223 K/1 h WQ (950 °C/1 h WQ) in terms of grain morphology and size.

As shown by Ahmed and Rack,^[27] the supertransus solution treatment during 1 hour followed by water quenching (WQ) conducts the complete formation of a new α' martensite ($\beta \rightarrow \alpha'$). This type of martensite is referred to as new because the thickness of the α' needles is slightly thicker (1 μm instead of 360 nm) than the

as-fabricated α' needles. This increase is related to the difference in cooling rate between the SLM process and the traditional WQ. It is interesting to remember that in small and thin samples, WQ produces a cooling rate close to 1500 K/s in comparison to the air quenching of 500 K/s and the furnace cooling of 1 K/min.^[14] The microhardness confirms this change in the size of the needles because the finest microstructure gives rise to the highest hardness (354 HV2 ± 8 against 342 HV2 ± 12). It is worth mentioning that at this load (2 kg) the size of the indents is relatively small and does not take into account the effect of the grain size.

Concerning the grain morphology, the solution treatment above the β transus enables shearing of the long columnar grains usually seen in SLM parts, as shown in Figure 3. Indeed, above 1253 K (980 °C) and after a complete dissolution of the α' phase, the displacive transformation (without diffusion) of the body-centered-cubic phase (β) into the hexagonal phase (α') occurs after WQ with a shearing mechanism followed by nonthermal nucleation (without releasing energy). This reaction was previously brought forward by Combres.^[12] Therefore, the resulting equiaxial grains attain approximately 200 μm in diameter. Figure 3(a), in comparison to Figure 4(a), clearly illustrates this change

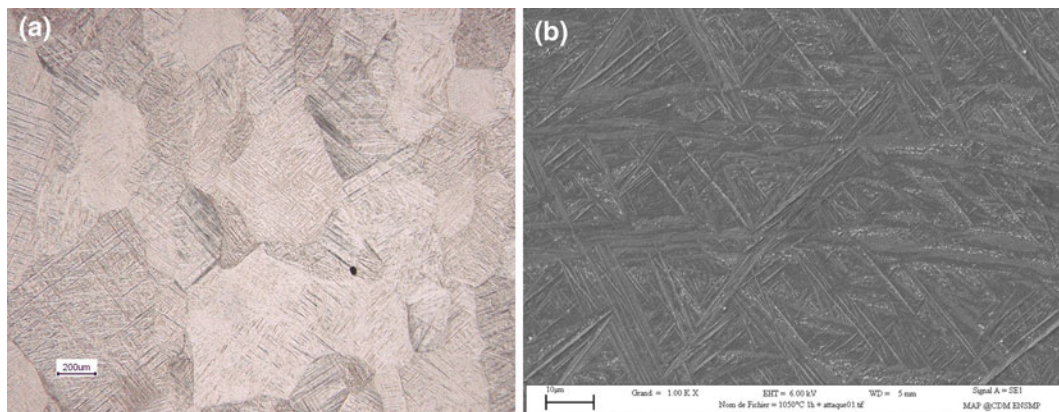


Fig. 3—Microstructures of the supertransus solution treatment 1323 K (1050 °C/1 h WQ): (a) optical micrograph showing the grain morphology and (b) SEM micrograph in the SE mode showing the α' needles.

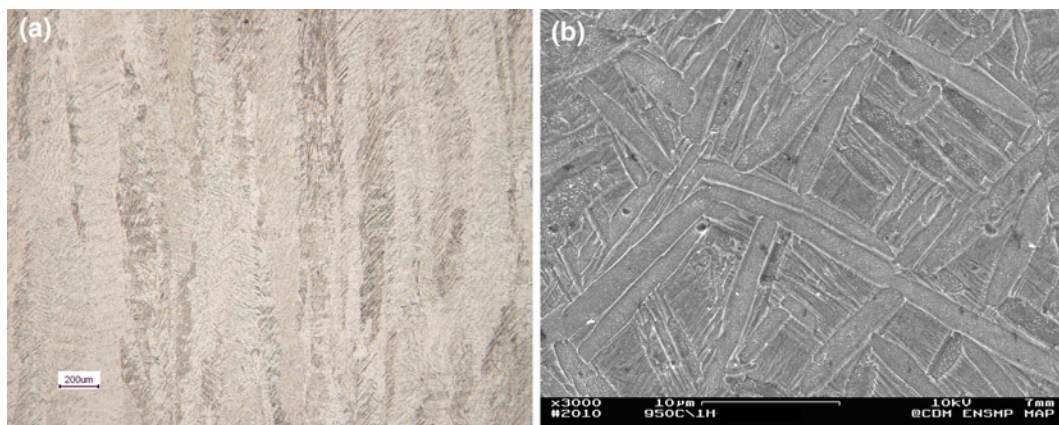


Fig. 4—Microstructures of the subtransus solution treatment 1223 K (950 °C/1 h WQ): (a) optical micrograph showing the grain morphology and (b) SEM micrograph in the SE mode showing the α , α' , and β phases.

in grain morphology (columnar → equiaxial), which is a function of the solution treatment temperature.

The subtransus solution treatment does not enable modification of the morphology of the grains. At this temperature, although it is thought that the as-fabricated α' phase is almost totally solutionized, the α phase resulting from the partial dissolution of α' hinders the movement of the grain boundaries, maintaining the long and wide columnar grains. It is only at temperatures above the β transus and with high cooling ($\beta \rightarrow \alpha'$) that the shearing mechanism takes place and leads to equiaxial grains.

The subtransus treatment leads to the gradual decomposition of the as-fabricated α' phase to a microstructure composed of alpha phase (α), beta phase (β), and a low volume fraction of a new martensite (α'') arising from the WQ ($\alpha' \rightarrow \alpha + \beta_r + \alpha''$) (Figure 4(b)). Here, the β_r phase represents the β phase poor in vanadium.

From that point, it is now possible to choose the morphology of the grains in accordance with the application of the parts. More precisely, it is the type of mechanical or thermal loading that will dictate the morphology of the grains to use. Usually, the columnar grains will be favored for creep tests, whereas equiaxial grains will be preferred for fatigue tests.^[22]

2. Tempering treatment

The optimization of this treatment is carried out on samples solution treated at 1323 K/1 h WQ (1050 °C/1 h WQ). The tempering temperature is varied from 973 to 1223 K (700 to 950 °C) for a fixed time of 2 hours. In all conditions, one sample is air cooled (AC) while the second is furnace cooled (FC) in order to distinguish the effect of the cooling rate on the nature of the phases present.

According to scanning electron microscopy (SEM) images in the BSE mode useful to reveal the chemical contrast, an increase in the tempering temperature leads to the gradual decomposition of the α' phase toward the more stable phases $\alpha + \beta$ when the samples are AC. The complete decomposition of this α' phase appears at 1073 K/2 h AC (800 °C/2 h AC). Obviously, the thickness of the lamellar α phase increases with the temperature, starting from 1 μm at 1023 K (750 °C) to 2.3 μm at 1223 K (950 °C). Moreover, it seems that for the samples treated at 1223 K (950 °C), some fine needles (α' phase) originating from β phase poor in vanadium reappear during air cooling. In contrast, during homogenizing at low temperature (≈ 973 K), the β phase arising from the partial decomposition of the new α' phase may reach a concentration in vanadium close to 15 wt pct and maintain its metastability at room temperature after air cooling. The resulting β phase is noted β_m . In the other side, other authors have noticed that after WQ from the $\alpha + \beta$ domain at intermediate temperatures (≈ 1073 K), the β phase being as rich as 10 wt pct in vanadium transforms into a soft orthorhombic martensite known as α'' phase, as illustrated in Figure 5.

In terms of the microhardness, Hadj Sassi^[24] and Combres^[12] observed an important loss of hardness after a treatment at 973 K (700 °C) during 15 hours for one and a consequent loss of yield strength after a treatment

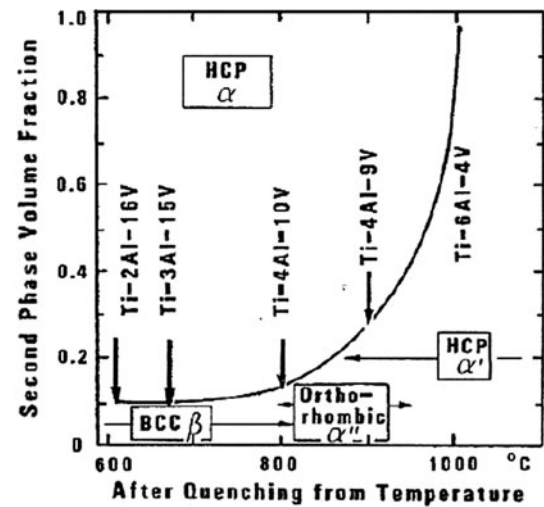


Fig. 5—Nature, composition, and volume fraction of the β phase in Ti-6Al-4V as a function of the water-quenched starting temperature^[23].

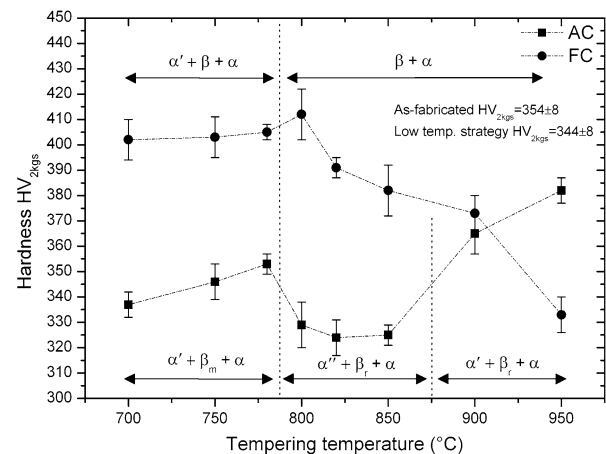


Fig. 6—Hardness evolution of the Ti-6Al-4V microstructure as a function of the tempering temperature after a solution treatment at 1323 K (1050 °C) during 1 h WQ, for both air and furnace cooling.

at 1073 K (800 °C) during 2 hours for the other, respectively. This softening range plays an important role in the ductility of the alloy, because it diminishes with an increase of the tempering temperature. According to Hadj Sassi, this decrease in ductility is due to the formation of the β phase, which becomes more abundant and poorer in vanadium, and later transforms in martensite α'' during air cooling. According to Combres, this loss of yield strength associated with a consequent increase in plastic deformation is caused by the precipitation of a soft orthorhombic martensite α'' phase very difficult to reveal by transmission electron microscopy observations. In this study, this important softening range appears between 1073 K and 1123 K (800 °C and 850 °C) for 2 hours, where the microhardness is comprised between 325 and 330 HV2, as seen in Figure 6. It is very important to note that this softening range does not arise when the cooling rate is significantly reduced (e.g., furnace cooling rate ≈ 1 K/min).

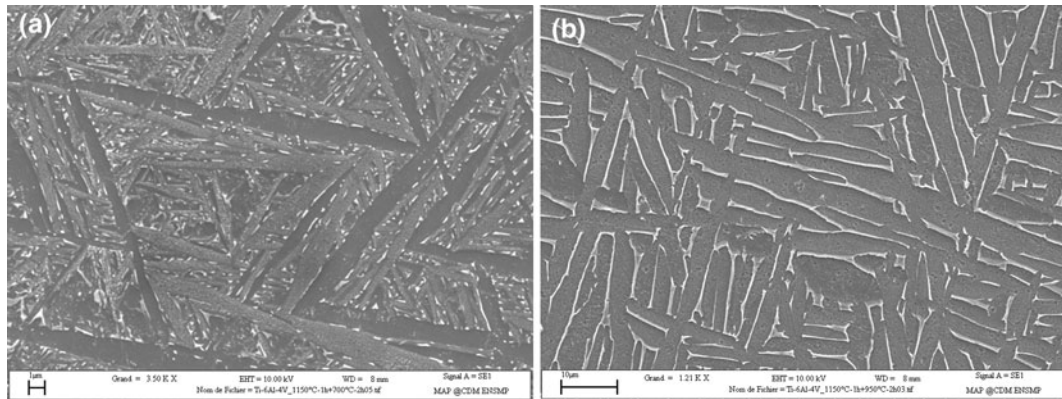


Fig. 7—Microstructures of the supertransus solution treatment 1323 K (1050 °C/1 h WQ): (a) SEM micrograph in SE mode of the 973 K (700 °C/2 h) (FC) tempering treatment and (b) SEM micrograph in the SE mode of the 1223 K (950 °C/2 h) (FC) tempering treatment.

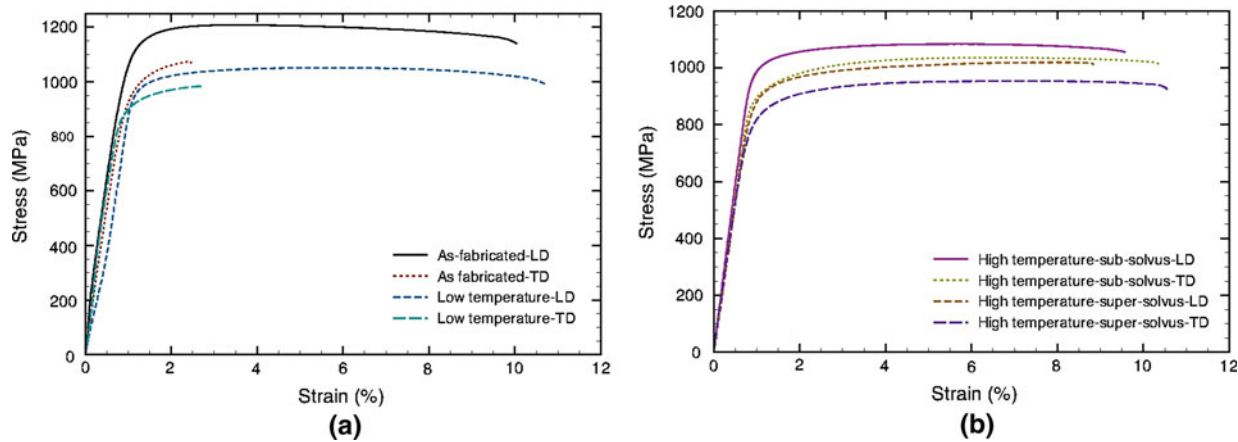


Fig. 8—Engineering stress-strain curves of the different microstructures: (a) the as-fabricated and the low-temperature strategy and (b) the high-temperature strategy (super- and subtransus) with the new process parameters.

It is clear that the difference in hardness HV2 between 973 K and 1953 K (700 °C and 780 °C) of the two cooling rates is directly linked to a more important volume fraction of the β phase after a rapid cooling (AC). In the case of near equilibrium cooling (FC), a greater volume fraction of β phase transforms to α phase while much more α' is decomposed (Figure 7(a)). Beyond 1053 K (780 °C) with a slow cooling, the hardness decreases continuously from 410 to 330 HV2 as the tempering temperature is increased. This can be attributed to the growth of the α lamellae. As shown in Figure 7(b), the width of the lamellae can attain 4.5 to 5 μm at 1223 K (950 °C) after FC. In opposite and beyond 1173 K AC (900 °C AC), the increase in hardness is due to the presence of the fine α' phase arising during cooling as well as the presence of the fine α phase.

V. MECHANICAL PROPERTIES

Flat tensile test specimens are first heat treated and then machined in accordance with the French Aeronautical Standard (CEAT TP5). The tensile tests are conducted at room temperature at a strain rate of

10^{-3} s^{-1} . The elongation is followed with an extensometer with initial gage length of 11 mm.

A. Tensile Properties of the As-Fabricated Microstructure

The LDs and TDs give rise to ultimate tensile strength and yield strength well above the conventional properties obtained for wrought Ti-6Al-4V. This comes from the extremely fine martensite α' microstructure resulting from the very high cooling rate from the β domain, as was also noted by Murr *et al.*^[10]

The ductility clearly shows the opposite trend, because in all cases, fracture occurs well below the conventional values and even those of the foundry route. From the σ - ϵ curves (Figure 8(a)) and the results recapitulated in Table III, it is clear that the SLM process exhibits a strong anisotropy as a function of the building direction. The LD direction permits reaching 7.6 pct of ductility, whereas the TD specimens fail below 2 pct, soon after reaching the plastic domain (Figure 8). Although the elongation is higher for the LD specimens, failure arises when they start to neck where the plastic flow becomes important in the loading direction.

Table III. Mechanical Properties at Room Temperature of the Different Microstructures as well as the Standard Processing Routes

	As-Fabricated		High-Temperature Supersolvus		High-Temperature Subtransus		Low Temperature			
	LD	TD	LD	TD	LD	TD	LD	TD	As Cast	Wrought
σ_u (MPa)	1206 ± 8	1166 ± 25	1019 ± 11	951 ± 55	1036 ± 30	1040 ± 4	1046 ± 6	1000 ± 53	980	995
$\sigma_{0.2}$ pct (MPa)	1137 ± 20	962 ± 47	913 ± 7	836 ± 64	944 ± 8	925 ± 14	965 ± 16	900 ± 101	865	930
ε (pct)	7.6 ± 2	1.7 ± 0.3	8.9 ± 1	7.9 ± 2	8.5 ± 1	7.5 ± 2	9.5 ± 1	1.9 ± 0.8	13.5	14
E (GPa)	105 ± 5	102 ± 7	96.7 ± 5	95 ± 4	103 ± 11	98 ± 3	101 ± 4	110 ± 29	/	/

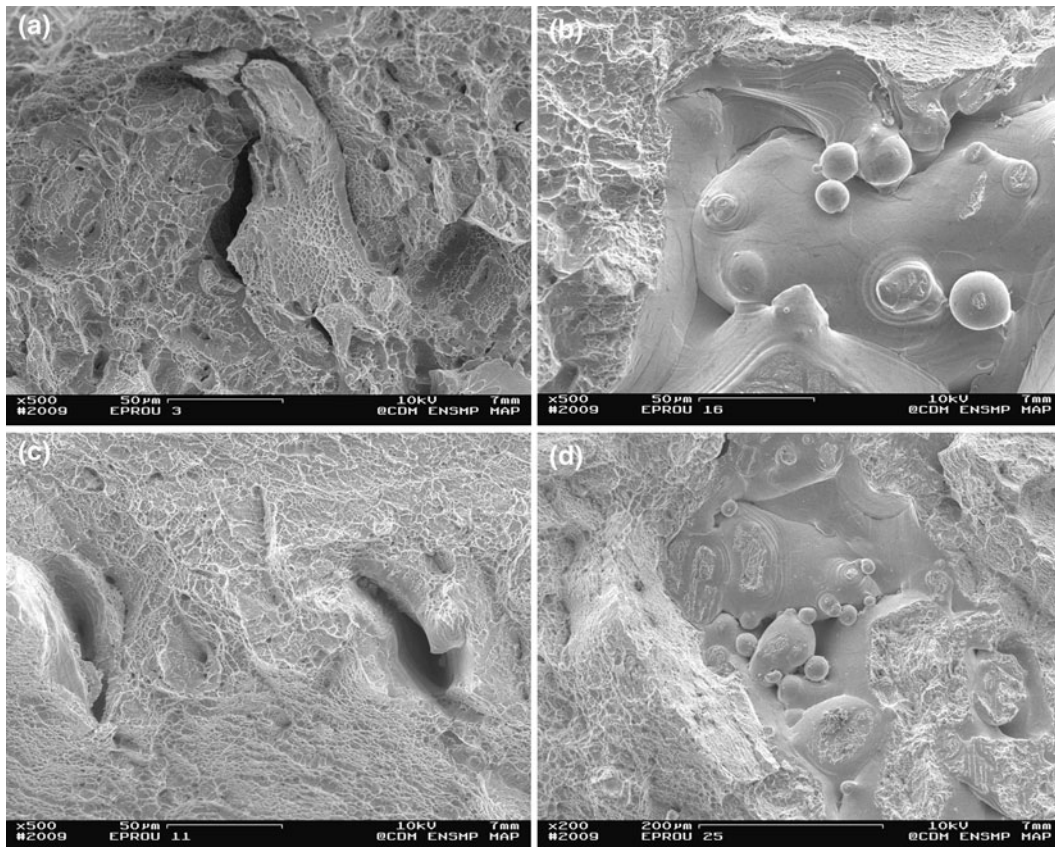


Fig. 9—Fracture surfaces of the tensile test specimens illustrating the presence of defects corresponding to the (a) LD and (b) TD of the as-fabricated microstructure, the (c) LD and (d) TD of the 1003 K/2 h AC (730°C/2 h AC) microstructure, the (e) LD and (f) TD of the 1423 K/1 h WQ + 1093 K/2 h AC (1150 °C/1 h WQ + 820 °C/2 h AC) microstructure, and the (g) LD and (h) TD of the 1223 K/1 h WQ + 973 K/2 h AC (950 °C/1 h WQ + 700 °C/2 h AC) microstructure.

A careful analysis of the fracture surfaces (Figures 9(a) and (b)) permitted revelation of the strong dependence of the mechanical behavior to the defects present in the structure. It is clear that the most critical are the defects with sharp angles such as those induced by the lack of fusion (Figures 9(a) and (b)).

According to the geometry and the orientation of the defects, the specimens tested in the LD direction pull upon the defect between two layers and thus tend to close it. This is true until the section starts to shrink. At this stage, the size of the defect becomes significant in comparison to the cross section, and locally, the stress attains a value well above the ultimate strength acceptable for the material. On the other side, the TD

specimens are the most critical because the loading direction opens up the defect; such is the case during fracture toughness testing in mode I. It is the reason why the as-fabricated TD samples show ductility of only 2 pct in comparison to 13.5 to 14 pct of the conventional processing routes.

B. Tensile Properties of the Low-Temperature Strategy

Thanks to the partial destabilization of the martensite α' phase, the ultimate tensile strength and the yield strength drop whatever the loading direction (LD and TD). This decrease in yield and ultimate strengths allows satisfaction of the aeronautical criteria, because the yield

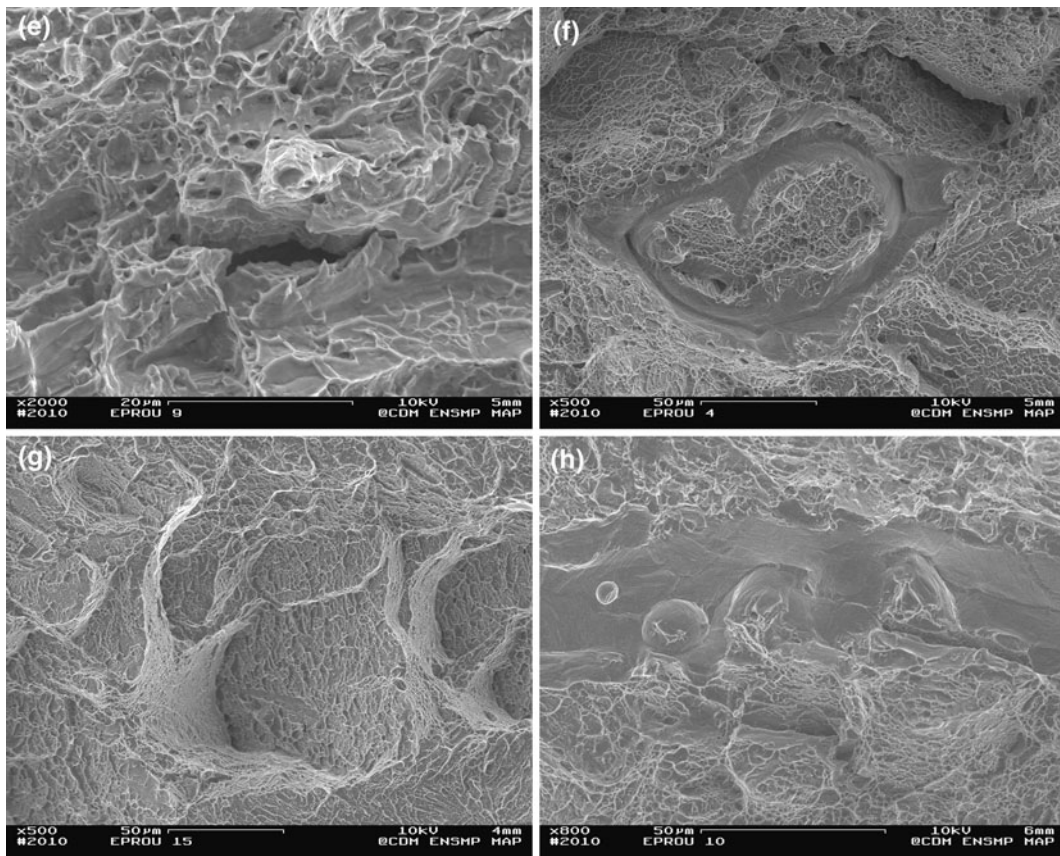


Fig. 9—Continued.

strength remains relatively high. Further, this loss of yield strength involves a slight increase in ductility even though the strong anisotropy is conserved. Once again, the fracture surfaces (Figures 9(c) and (d)) clearly show large critical defects to reach the elongation obtained by wrought material. The tensile properties of this strategy are listed in Table III.

C. Tensile Properties of the High-Temperature Strategy

Due to the poor ductility of the TD specimens, a new set of samples is manufactured with better optimized process parameters to reduce the number of defects. This is reached by reducing both the thickness of the powder bed and the scanning speed and by increasing the power of the laser, resulting in higher dilution of solid material. This new set of process parameters is listed in Table II. It is important to say that the as-solidified microstructure is still composed of the very fine martensite α' needles as well as the long and wide columnar grains. Indeed, the cooling rate of the new melting pool volume is expected to be of the same magnitude.

The tensile tests of the supertransus specimens give rise to yield and ultimate strengths comprised between the as-cast and wrought properties. In terms of the LD specimens, they are close to or above the wrought material, whereas the TD specimens present properties close to the as-cast state. Only the ductility remains

below in both cases, but it becomes very encouraging because it reaches 8 and 9 pct for the TD and LD directions, respectively. Despite a clear improvement, the fracture surfaces let some minor defects appear that are again at the origin of fracture. Such types of defects are illustrated in Figures 9(e) and (f).

The subtransus heat treatment usually undertaken leads to yield and ultimate strengths close to or above the wrought properties in both cases (LD and TD directions). However, the ductility is below this of the supertransus condition. Even in this condition, it is not possible to reach deformations close to the conventional processing routes because of the presence of defects on the fracture surfaces (Figures 9(g) and (h)).

VI. CONCLUSIONS

The high solidification rate imposed by the high scanning speed generates out-of-equilibrium microstructure (α' phase) throughout the height of the samples. Because the dissipation of the heat occurs essentially by conduction through the substrate in the first layer, the resulting microstructure is composed of wide columnar grains. These grains are conserved throughout the height of the samples, because the laser beam remelts the top of the grains at each new layer. This type of microstructure is very typical of additive processes.

Conventional and optimized heat treatments are compared in terms of the morphology of the grains and the phases present. This study shows that it is now possible to choose the morphology of the grains as a function of the type of loading of the parts. The subtransus treatment 1223 K/1 h WQ (950 °C/1 h WQ) can be useful to maintain the columnar structure inherent in the SLM process, while the supertransus 1323 K/1 h WQ (1050 °C/1 h WQ) treatment shears the columnar grains and results in equiaxial structure.

Evolution of the tempering temperature after supertransus solution treatment 1323 K/1 h WQ (1050 °C/1 h WQ) shows the existence of various domains illustrated by different hardnesses. Between 973 K and 1023 K (700 °C and 750 °C) during 2 hours AC, the microstructure is composed of α' + β_m + α phases. Between 1023 K (750 °C) and 1123 K/2 h AC (850 °C/2 h AC), an important loss of hardness is attributed to the appearance of the soft orthorhombic phase α'' . Beyond 1123 K/2 h AC (850 °C/2 h AC), the hardness increases drastically because of the presence of the α + β_r + α phases. This study also shows that these microstructural domains do not appear when the cooling rate is changed from AC to FC, because the microstructure has more time to evolve during cooling.

The as-fabricated microstructure generates reasonable tensile properties except the elongation, which is well below the as-cast material. There is a strong anisotropy between the two directions (LD and TD). It is maintained regardless of the microstructure and the heat treatment. This anisotropy is attributed to the important manufacturing defects and especially their orientations as a function of the loading direction. This is also the case for the heat-treated microstructures even though the effect is less pronounced for the high-temperature strategy thanks to the optimization of a new set of SLM parameters. This new process optimization including a reduction of the thickness of the powder bed as well as the scanning speed and an increase of the power of the laser permits dilution of more solid material and decreases the size and the number of critical defects.

The low-temperature strategy 1003 K/2 h AC (730 °C/2 h AC) leads to slightly lower yield strength and ultimate tensile strength than the as-fabricated microstructure, whereas the ductility is favored. However, this heat treatment can be applied to relieve the residual stresses that may deform the part during service temperature.

The high-temperature strategy (subtransus 1223 K/1 h WQ (950 °C/1 h WQ) or supertransus 1323 K/1 h WQ (1050 °C/1 h WQ)) increases the yield strength and ultimate tensile strength in comparison to the as-cast and wrought standards. Even though the ductility is improved in comparison to the first set of samples, it remains below the standard. This problem is clearly illustrated through the analysis of the fracture surfaces,

which shows the presence of defects at the origin of fracture. Careful optimization of the process parameters shows that it is possible to reach high tensile properties, but they will always be lower than those obtained from the conventional processing routes if significant manufacturing defects remain. The complete suppression of these critical defects might be achievable by carrying out hot isostatic pressing as is often the case to the parts elaborated by foundry.

ACKNOWLEDGMENTS

The authors are grateful to Stephane Abed (Poly-Shape) for providing the Ti-6Al-4V material. They acknowledge the ANRT foundation for helping in the funding of this study.

REFERENCES

1. G.N. Levy, R. Schindel, and J.P. Kruth: *Manufact. Technol.*, 2003, vol. 52, pp. 589–609.
2. M. Rombouts, J.P. Kruth, L. Froyen, and P. Mercelis: *Manufact. Technol.*, 2006, vol. 55, pp. 187–92.
3. I. Yadroitsev, I. Shishkovsky, P. Bertrand, and I. Smurov: *Appl. Surf. Sci.*, 2009, vol. 225, pp. 5523–27.
4. T. Vilaro, V. Kottman-Rexerodt, M. Thomas, and C. Colin: *Adv. Mater. Res.*, 2010, vols. 89–91, pp. 586–91.
5. J.P. Kruth, L. Froyen, J. Van Vaerenbergh, P. Mercelis, M. Rombouts, and B. Lauwers: *J. Mater. Process. Technol.*, 2004, vol. 149, pp. 616–22.
6. K.A. Mumtaz, P. Erasenthiran, and N. Hopkinson: *J. Mater. Process. Technol.*, 2008, vol. 195, pp. 77–87.
7. P.J. Maziasz: *Scripta Mater.*, 1998, vol. 39, pp. 1471–76.
8. N.W. Klingbeil, J.L. Beuth, R.K. Chin, and C.H. Amon: *Int. J. Mech. Sci.*, 2002, vol. 44, pp. 57–77.
9. M. Shiomi, K. Osakada, K. Nakamura, T. Yamashita, and F. Abe: *Manufact. Technol.*, 2004, vol. 53, pp. 195–98.
10. L.E. Murr, S.A. Quinones, and S.M. Gaytan: *J. Mech. Behav. Biomed. Mater.*, 2009, vol. 2, pp. 20–32.
11. S.H. Mok, G. Bi, J. Folkes, I. Pashby, and J. Segal: *Surf. Coat. Technol.*, 2008, vol. 202, pp. 4613–19.
12. Y. Combes: *Traitements Thermiques des Alliages de Titane, Techniques de l'Ingénieur*, M1335, 1995.
13. I. Yadroitsev, L. Thivillon, P. Bertrand, and I. Smurov: *Appl. Surf. Sci.*, 2007, vol. 254, pp. 980–83.
14. J. Maisonneuve: Ph.D. Thesis, ENSMP, Mines ParisTech, Paris, 2008.
15. X. Wu: *J. Eng. Mater. Technol.*, 2003, vol. 135, pp. 266–70.
16. M. Qian, J. Mei, J. Liang, and X. Wu: *Mater. Sci. Technol.*, 2005, vol. 21, pp. 597–605.
17. A. Longuet: Ph.D. Thesis, ENSMP, Mines ParisTech, Paris, 2010.
18. J.W. Elmer, T.A. Palmer, S.S. Babu, W. Zhang, and T. DebRoy: *J. Appl. Phys.*, 2004, vol. 95, pp. 8327–39.
19. F. Delannay, D. Pardo, and C. Colin: *Acta Mater.*, 2005, vol. 53, pp. 1655–64.
20. F.X. Gil: *J. Alloys Compd.*, 1996, vol. 234, p. 287.
21. T. Ahmed and H.J. Rack: *Mater. Sci. Eng.*, 1998, vol. A243, pp. 206–11.
22. D. Franois, A. Pineau, and A. Zaoui: *Comportement Mécanique des Matériaux*, Hermès Science Publications, Paris, 2009.
23. L.T. Lee: *Mater. Sci. Eng.*, 1990, vol. 128, pp. 77–89.
24. B. Hadj Sassi: Ph.D. Thesis, ENSTA ParisTech, Paris, 1977.

Effect of build direction on the fracture toughness and fatigue crack growth in selective laser melted Ti-6Al-4V

P. EDWARDS^{1,2} and M. RAMULU²

¹The Boeing Company, P.O. Box 3707 MC 02-HF, Seattle, WA 98124-2207, USA, ²University of Washington, Department of Mechanical Engineering, Box 352600, Seattle, WA 98195, USA

Received Date: 8 November 2014; Accepted Date: 27 February 2015; Published Online: 30 March 2015

ABSTRACT Experimental investigation was conducted to evaluate the fracture toughness and fatigue crack growth characteristics in selective laser-melted titanium 6Al-4V materials as a follow-on to a previous study on high cycle fatigue. For both the fracture toughness and crack growth evaluation, the compact tension specimen geometry was used. It was found that the fracture toughness was lower than what would be expected from wrought or cast product forms in the same alloy. This was attributed to the rapidly cooled, martensitic microstructure, developed in the parts. At low stress ratios, the crack growth rates were faster than in wrought titanium but became comparable at higher ratios. The fracture toughness appears to be higher when the crack is oriented perpendicular to the build layers. The difference in the average threshold and critical stress intensity values for the crack growth results for the three orientations was within the scatter of the data, so there was essentially no difference. The same was true for the empirically derived Paris Law constants. Residual stresses were likely to have overshadowed any variation in crack growth because of microstructural directionalities associated with build orientation.

Keywords additive manufacturing; fatigue crack growth; fracture toughness; selective laser melting; selective laser sintering; titanium.

NOMENCLATURE

K_{Ic}	= Plane strain fracture toughness
σ_{YS}	= 2% offset yield strength
K_R	= Resistance to fracture of as a function of crack extension (Δa)
a	= Crack length
Δa	= Crack extension
K_{app}	= Apparent fracture toughness computed from the maximum applied load on the K_R curve and initial crack length
K_c (R-Cruve)	= Critical stress intensity, or the onset of unstable crack extension on the K_R versus Δa
K_c (P_{max})	= K_R at the maximum applied load and crack length at that point
R	= Load ratio (max applied load/min applied load)
ΔK	= Stress intensity factor range
W	= Compact tension specimen width
B	= Compact tension specimen thickness
da/dN	= Crack length (a) growth per increasing number of load cycles (N)
C	= Paris law coefficient material constant
m	= Paris law exponent material
U	= Electric Potential
E	= Elastic Modulus
v	= Crack mouth opening displacement
P	= Applied load
y	= Probe Gage Length

Correspondence: M. Ramulu. E-mail: ramulum@u.washington.edu

INTRODUCTION

Titanium alloys are used for applications that require specific strength, relative to its weight, corrosion resistance or elevated operating temperature. However, the cost associated with producing wrought titanium material products and subsequent part fabrication is always a concern. Thus, there is constantly motivation to develop lower cost approaches to producing titanium components. One such approach is additive manufacturing, which is a layer-by-layer approach that can achieve complex geometry net-shapes, minimizing the waste of costly excess material incurred with traditional subtractive processes like machining. A number of additive manufacturing techniques are available. These techniques can be placed into two general categories: direct deposition and powder bed sintering.^{1,2} One of the powder bed approaches, selective laser melting (SLM), is capable of medium build rates, good repeatability and medium to high surface quality.³ In order to take advantage of such a process in the production of structural hardware, the mechanical performance of materials produced by this process must be well characterized.

Microstructures, which can offer insight into the expected mechanical performance, have been studied in Ti-6Al-4V alloy materials produced with SLM by several researchers.^{3–10} In general, the as-built condition exhibits fine martensitic acicular alpha morphology with elongated beta columnar grains that span across multiple build layers. Heat treatment, either stress relief or hot isostatic pressing (HIP'ing), after SLM allows the fine acicular alpha to precipitate into a more lamellar alpha + beta structure.^{3,9–11} These SLM microstructures are more similar to a weldment or casting than the equiaxed primary alpha grain structure in wrought Ti-6Al-4V mill products such as plate, sheet and forgings. As expected, this microstructure yields higher strengths and lower ductility than wrought material.^{3–10} In the as-built condition, higher strengths and lower elongations are obtained in SLM materials than Ti-6Al-4V castings. Heat treating improves ductility but decreases strength. The best combination of strength and ductility in Ti-6Al-4V SLM specimens was obtained by HIP'ing. Some researchers observed an influence of specimen orientation with respect to the build direction on tensile properties. This was primarily attributed to the elongated, directionally oriented (vertically), grain structure across build layers.^{8,10}

In addition to metallurgical and static performance evaluations, a few studies have been conducted on the high cycle fatigue performance of Ti-6Al-4V SLM materials as well.^{3,4,11} In all three studies, the fatigue performance of as-built SLM specimens was significantly lower than wrought materials. Leuders *et al.*³ found that heat treatment and HIP'ing both increased fatigue life. HIP'ing improved the life by an order of magnitude over

the as-deposited condition. Porosity was the primary cause for premature failure in the un-HIP'ed conditions, where 99.77% density was measured, while microstructure and tensile residual stresses present in the as-built condition played a secondary role. A similar result was observed in a previous study^{11,12} by this team, where poor fatigue performance was attributed to porosity, the as-deposited/un-machined surface condition and tensile residual stresses. In that study, a large variation in fatigue performance with build orientation was also observed. However, Chan *et al.*⁴ were able to show that when SLM specimens were machined, in the absence of porosity, the fatigue life became comparable with cast Ti-6Al-4V.

To date, only one study has been published on the fatigue crack growth in Ti-6Al-4V SLM.³ In the as-built condition with the crack plane oriented parallel to the build layers, the growth rates were highly scattered, or erratic, and lower than the reference wrought material curves. When the crack was oriented transverse to the build planes, the growth rates were less erratic. At low stress intensity ranges, the transversely oriented crack had higher growth rates than the reference material, but at higher stress intensities, the growth rates became more similar to the reference material. This was not the case in the parallel crack specimens. Heat treatment (both at 800 and 1050 °C) and HIP'ing brought the crack growth rates of the SLM specimens, in both orientations, in-line with the reference material. This was attributed to the reduction in tensile residual stress in the as-built condition. Residual stress was concluded to be the primary driver in fatigue crack growth rate performance in these Ti SLM specimens. It was also interesting to note that in the 1050 °C heat treated specimens, erratic crack growth rates, similar to the as-built condition, were observed, but this was not the case in the 800 °C or HIP'ed specimens. This was attributed to the more coarse lamellar grain size resulting from the higher heat treatment temperature that leads to greater crack path deflection during propagation. Thus, microstructure played a secondary role to residual stress in the crack growth performance. Porosity was determined not to have an influence on crack growth.

While there are a fair amount of data available on the microstructural characteristics and static performance of Ti-6Al-4V SLM and even a few works published on high cycle fatigue, there has only one study on the crack growth behaviour, and nothing has been published on another mechanical performance parameter that is critical in damage tolerant design, which is fracture toughness. Thus, the goal of this research is to evaluate the crack growth rates in Ti-6Al-4V SLM materials to augment the limited data available in that area and to provide the first fracture toughness assessment. This is a follow-

on study of Edwards and Ramulu,¹² where the high cycle fatigue performance was evaluated in addition to microstructures, surface conditions and residual stresses of Ti SLM materials. As in the study of Edwards and Ramulu,¹² parts were tested in the as-deposited condition, meaning that no post-process heat treatment or HIP would be performed. This was to determine the performance of components produced in the lowest cost condition, which is the goal of utilizing this process for the fabrication of titanium components over traditional methods.

EXPERIMENTAL PROCEDURE

This section will describe the experimental procedure used during this study. The SLM processing conditions used to fabricate all test materials will be summarized, and details regarding the raw powder titanium material are provided. The experimental test methods for evaluating the fracture toughness and fatigue crack growth rates will then be defined.

Material and processing

All test specimens were produced by SLM on an MTT 250 machine by an external collaborator on this project and provided for mechanical characterization. Specifics regarding the processing parameters and equipment are as follows: The machine features a fully welded vacuum chamber, enabling low-pressure atmospheric evacuation followed by a refill of the chamber with high purity argon gas. A soft blade evens out each fresh layer powder material across the surface of the bed before consolidation by the laser. The process parameters used to fabricate all specimens are given in Table 1.

The titanium powder material used in this study was a pre-alloyed plasma atomized Ti6Al-4V, grade 23. The powder is spherical in shape, and the measured particle size distribution was within 15–70 µm, but about 75% of the examined particle size ranged between 25 and 50 µm. The mean particle size was approximately 30 µm in diameter.

If the bed of the SLM machine is defined as the *x*-*y* plane of a Cartesian coordinate system, the vertical stacking direction of the layers would be the *z*-axis (Fig. 1). The traverse, or scan, direction of the laser beam changed by 67° in the *x*-*y* plane with every build layer. To evaluate the potential effect of build orientation on anisotropy of performance, specimens were built in three orientations. The specimen orientations built and tested in this study are shown in Fig. 1.

For both the fracture toughness and crack growth tests, the same compact tension specimen geometry was

Table 1 Selective laser melting process conditions

Parameter	Setting
Laser power	200 W
Beam wavelength	1070 nm
Point-to-point distance	50 µm
Exposure time	251 µs
Consecutive line scan distance	180 µm
Layer thickness	50 µm
Energy density	$11.1 \times 10^{-5} \text{ J/mm}^3$

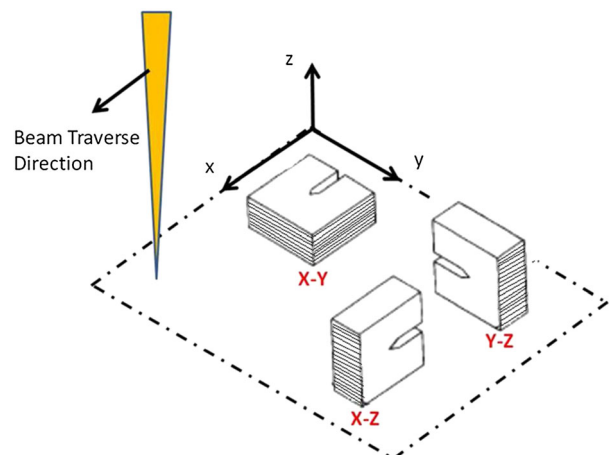


Fig. 1 Schematic of specimen build orientations in build chamber.

used. The C(T) specimens were fully machined from 65 × 65 × 5 mm blanks produced on the SLM machine. The final C(T) specimen geometry utilized a specimen width (W) of 50 mm and a B of approximately 4 mm after machining. Three specimens were produced in each of the three orientations for both fracture toughness and crack growth testing. One specimen in each orientation was produced in each build, or run of the machine, resulting in six total builds. For the Y-Z and X-Z orientations, the crack plane was parallel with the build layer plane. For the X-Y specimens, the crack plane was transverse to the build layers.

Fracture toughness

Plane stress fracture toughness testing was conducted using the *R*-curve method per ASTM 561-08. Fatigue pre-cracking of the C(T) specimens was done to achieve an initial crack length such that the crack length (*a*) to W ratio (*a/W*) requirement of 0.35–0.55 would be satisfied. Plane stress testing was conducted because the thickness of the specimens (B) was not sufficient to satisfy plane strain conditions. Thus, the results of the fracture toughness parameters computed will be dependent on the material thickness and crack size rather than the invariant material property of plane strain fracture

Table 2 Fracture toughness parameters and equations

Parameter	Equation/definition	Eq.
K	$\frac{P}{B\sqrt{W}}f\left(\frac{a}{W}\right)$	1
$f(a/W)$	$\frac{\left(2+\frac{a}{W}\right)\left[0.886+4.64\left(\frac{a}{W}\right)-13.32\left(\frac{a}{W}\right)^2+14.72\left(\frac{a}{W}\right)^3-5.6\left(\frac{a}{W}\right)^4\right]}{\left(1-\frac{a}{W}\right)^{3/2}}$	2
a/W	$(1.0010 - 4.6695U + 18.460U^2 - 236.82U^3 + 1214.9U^4 - 2143.6U^5)$	3
U	$\frac{1}{\sqrt{E \cdot B \cdot \left(\frac{a}{W}\right) + 1}}$	4
E_{corr}	$120.7 - 1065.3\left[\left(\frac{a}{W}\right)_{app}\right] + 4098\left[\left(\frac{a}{W}\right)_{app}\right]^2 - 6688\left[\left(\frac{a}{W}\right)_{app}\right]^3 + 4450.5\left[\left(\frac{a}{W}\right)_{app}\right]^4$	5

toughness, K_{IC} . For every C(T) specimen, the crack mouth opening displacement (v) was measured with a displacement gage along with the applied load (P) using the load cell built into the load frame. From this load versus displacement data, a K_R versus effective crack length curve was derived using the Equations in Table 2. The modulus (E_{eff}) is computed from the initial crack length (a_0) and the slope of the initial linear elastic portion of the Crack Mouth Opening Displacement (CMOD) (v) versus load (P) curve using Eqs (3) and (4). The crack length (a) along the rest of the CMOD versus load curve is then computed by multiplying the initial (E_{eff}) by the v/P value at that point along with the thickness (B) to obtain the apparent modulus (E_{app}). From this, a U_{app} and a/W_{app} are computed with Eqs (3) and (4). A corrected modulus (E_{corr}) is then obtained with Eq. (5) using a/W_{app} . This E_{corr} is then used to re-compute U and then finally a_{eff} with Eqs (3) and (4), again. K can be computed, using Eqs (1) and (2), and plotted against the crack length, a_{eff} , to obtain the K_R curve. From the K_R curve, the fracture parameters could be computed: K_C , K_{Cmax} and K_{app} . K_C is computed with the load and crack length at the onset of instability in the K_R curve, where it becomes tangent to the crack driving curve. Crack driving curves are generated by calculating K as a function of crack size for a series of constant applied loads. K_{Cmax} is computed at the maximum applied load and crack length at that point. K_{app} is determined from the maximum applied load and initial crack length. K_{app} is a conservative parameter typically used in the design of structures.

Crack growth rate

Crack growth testing was conducted per ASTM E647 (E 2011). Paris Law, Region II testing was performed at a frequency of 10 Hz and a load ratio of $R=0.1$ at constant load amplitude, resulting in an increasing ΔK as the crack grows. Testing was conducted on an Instron servo-controlled, hydraulically actuated, close loop test machine. An automated test system utilizing a personal computer and custom software provided the means for data acquisition and machine control. An electric potential

system consisting of a constant current supply and multiple gain amplifier was used to monitor continuously the physical crack length on each specimen. Electric potential probes were attached to the specimens on either side of the specimen notch. The gage length of these probes measured approximately $0.35 \times W$. Current leads were attached to the top and bottom of each specimen in order to provide a uniform current flux through the specimen gage section. During the test, the crack length of each specimen was continuously monitored by the automated test system using the electric potential technique. The crack length was found by passing a constant current through the specimens and measuring the potential drop between the two potential probes. The crack length, a , is related to the change in potential drop, U , by Johnson's equation (Eq. (6)). From the crack length computed by the potential drop, number of cycles and applied load, a da/dN versus ΔK crack growth curve was constructed. Paris law ($\frac{da}{dN} = C\Delta K^m$) constants, C and m , were then calculated from Region II of this the crack growth curve.

$$\frac{U}{U_0} = \frac{\cosh^{-1} \left[\frac{\cosh\left(\frac{\pi y}{2W}\right)}{\cos\left(\frac{\pi a_0}{2W}\right)} \right]}{\cosh^{-1} \left[\frac{\cosh\left(\frac{\pi y}{2W}\right)}{\cos\left(\frac{\pi a}{2W}\right)} \right]}, \quad (6)$$

where U_0 and a_0 are the initial values of potential and crack length, y is one half the probe gage length and W is the specimen width.

RESULTS

The load versus displacement (CMOD) curves from each of the fracture toughness specimens are given in Fig. 2a. R -curves derived from each of these CMOD are given in Fig. 2b. From these curves, it can be seen that the Y-Z orientation had the lowest toughness and the X-Y orientation had the best performance, in general. The X-Z orientation had one specimen that outperformed the X-Y

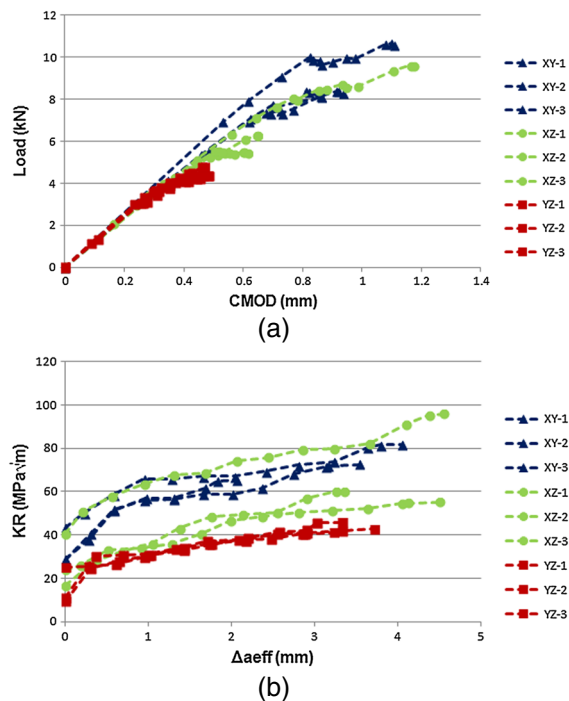


Fig. 2 Fracture toughness testing a) load versus CMOD and b) *R*-curves.

orientation, but the other two were lower. The X-Z and Y-Z orientations are more similar to each other when considering the build process than the X-Y orientation. The X-Z and Y-Z specimens are both in the “vertical” orientation where the crack is in the same plane as the build layers. The X-Y orientation is “horizontal,” and the crack runs perpendicular to the build planes. Thus, it was expected that the X-Z and Y-Z would be similar and the X-Y could be different. If one X-Z specimen that performed higher than the X-Y orientation is neglected, the X-Z and Y-Z orientations would both exhibit more similar responses. In this case, it would appear that cracks oriented parallel to the build planes are more detrimental than those oriented transversally.

The fracture toughness results extracted from the curves in Fig. 2 are summarized in Table 3. The values of K_c (*R*-curve), K_c (P_{\max}) and K_{app} are given for each

specimen as well as the averages and standard deviations for each orientation tested. As seen in the curves, the X-Y orientation appears to have the best performance where Y-Z has the lowest toughness. The X-Z orientation has the largest standard deviation mainly due to one specimen that performed significantly different than the other two.

Typical fracture surfaces for the *R*-curve specimens in each orientation are shown in Fig. 3. The X-Z and Y-Z fracture surfaces are fairly similar, showing a fibrous surface and small shear lips along the edges. The X-Z specimen shown was not the one that yielded significantly higher fracture toughness than the other two X-Z specimens or the Y-Z specimens. The X-Z specimen does appear to be somewhat less uniform fracture surface than the Y-Z specimen and even contains some anomalies, which may have been a discontinuity from porosity. Even so, the difference in K_{app} between these two specimens was approximately 9 MPa \sqrt{m} , with the X-Y specimen having 44.3 MPa \sqrt{m} and the Y-Z specimen having 35.1 MPa \sqrt{m} K_{app} , respectively, so relatively similar fracture surfaces would be expected.

The most interesting aspect of these fracture surfaces is the clear difference in morphology from one side of the X-Y specimen to the other (Fig. 3a). This is attributed to the fact that specimens in this orientation were built with one side of the specimen in direct contact with the substrate of the build chamber. It appears that this close proximity of the substrate yields a non-uniform part quality through the specimen thickness. If the X-Z or Y-Z specimens were sectioned close to the edge that was in contact with the substrate, a similar structure would be expected, but in these specimens, the crack was far away from the edge close to the substrate. This is likely another reason why the X-Y specimens generally had a different behaviour than the X-Z or Y-Z specimens. The X-Y orientation had higher toughness than the other orientations in general. It is unclear if this is completely attributed to the different structure obtained near the substrate or the fact that in the XY orientation, the crack is travelling across build layers rather than parallel to them as in the X-Z and Y-Z specimens. X-Y orientation specimens should be re-fabricated with a support structure to separate them farther from the substrate in order to investigate this effect further.

The crack growth results, plotted on a da/dN versus ΔK curve, for each specimen tested are given in Fig. 4. All orientations and specimens appear to have performed roughly the same. There was not any well pronounced Region I or III behaviour. The Y-Z orientation does have a more variable, scattered or erratic response than the other two orientations, but the overall trends are similar. Threshold and critical ΔK values are given in Table 4

Table 3 Fracture toughness results

Orientation	K_c (<i>R</i> -curve)		K_c (P_{\max})		K_{app}	
	Ave	STDEV	Ave	STDEV	Ave	STDEV
X-Y	66.9	2.6	72.8	8.5	62.3	4.2
X-Z	64.8	16.9	70.1	21.9	57.0	16.7
Y-Z	41.8	1.7	43.4	2.5	36.6	2.1

Ave, average; STDEV, standard deviation.

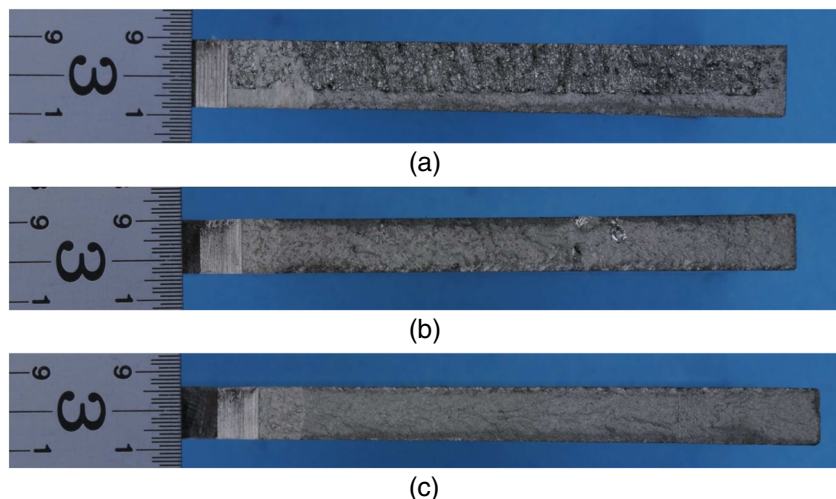


Fig. 3 Fracture surfaces for typical *R*-curve specimens in the a) X-Y, b) X-Z and c) Y-Z orientations.

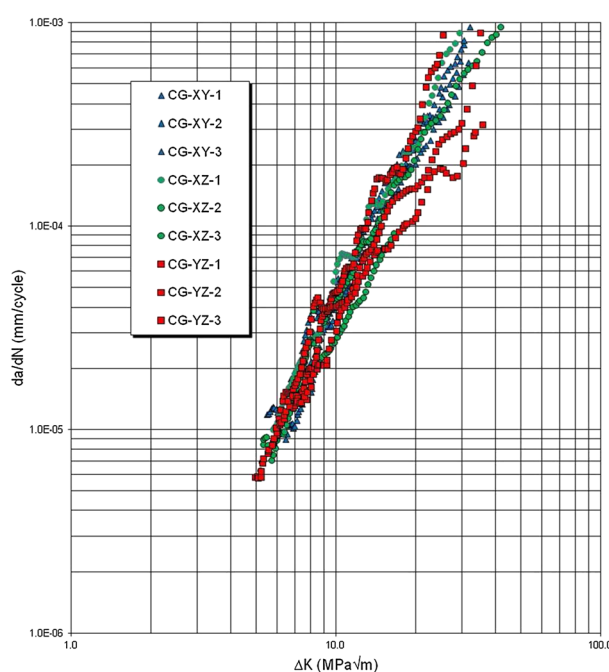


Fig. 4 da/dN versus ΔK crack growth curves.

along with the Paris law constants, C and m . Threshold values, ΔK_{th} , are on the order of $6 \text{ MPa}\sqrt{\text{m}}$, and ΔK_C

values are between 33 and $36 \text{ MPa}\sqrt{\text{m}}$. The m -values are between 2.4 and 2.6 .

DISCUSSION

In order to assess the performance of these Ti-6Al-4V materials, these results were compared with reference handbook data for two standard Ti-6Al-4V product forms: wrought mill annealed and cast Ti-6Al-4V.¹ Microstructural analysis of these SLM materials tested here was provided in a previous study.¹² In the as-deposited condition, Ti-6Al-4V SLM materials possess a fine acicular alpha, martensitic, structure within columnar beta grains, with an average width of $210 \mu\text{m}$ ($\pm 50 \mu\text{m}$), which extend vertically across multiple build layers. This was consistent with all previous research.^{3–11} The as-built SLM structure is probably most similar to a casting or weldment in titanium. However, castings generally exhibit a large prior beta grain structure (0.5 – 5 mm in size) and coarse lamellar alpha colonies via either slow cooling or post-process heat treatment. The individual alpha platelets are typically 1 – $3 \mu\text{m}$ in thickness and 20 – $100 \mu\text{m}$ in length, and the typical colony size range is 50 – $500 \mu\text{m}$.¹³ Typically, slower cooling rates, such as

Table 4 Average and standard deviation

Orientation	ΔK_{tb} (MPa $\sqrt{\text{m}}$)		ΔK_c (MPa $\sqrt{\text{m}}$)		C		m	
	Ave	STDEV	Ave	STDEV	Ave	STDEV	Ave	STDEV
X-Y	6.3	0.7	33.3	3.9	1.2E-7	7.6E-8	2.612	0.252
X-Z	5.8	0.8	36.0	22.6	1.7E-7	5.8E-8	2.366	0.274
Y-Z	5.9	1.0	33.4	3.6	2.1E-7	1.6E-7	2.451	0.632

Ave, average; STDEV, standard deviation.

in thick cast sections, result in microstructures with larger beta grains, a longer and thicker grain-boundary alpha phase, thicker alpha platelets and larger platelet colonies. These cast microstructures typically correlate to high fracture toughness and improved fatigue crack growth resistance, but lower fatigue crack initiation resistance and tensile elongation, relative to the fine (15–20 µm) equiaxed alpha grains present in mill annealed titanium, which is a preferable structure for the combination of strength and ductility as well as high cycle fatigue.¹ While SLM does result in solidification of a molten material, as in castings, the rapid cooling rates result in a finer structure. While cooling rates were not measured during this study to quantify “rapid,” other researchers⁵ have modelled the temperature distribution in a Ti-6Al-4 V SLM build, and from these data, cooling rates can be extracted. The SLM material cools from the molten state to below 700 °C in less than a second. SLM microstructures will be more similar to welds in Ti-6Al-4 V that also cool rapidly, such as those from electron beam welding, which exhibit fine martensitic structure with alpha platelets of approximately 1 µm thickness within prior beta grains that are on the order of 100–1000 µm in size depending on parameters that influence cooling rates (e.g. heat input and joint thickness).¹⁴ Welds with rapid cooling rates typically exhibit toughnesses below that of the mill annealed base metal, while welds with slower cooling rates yield increasing toughness levels that can be superior to the base metal.¹

With respect to the fracture toughness results (Fig. 2, Table 3), if one specimen in the X-Z orientation that performed significantly higher than the other X-Z or Y-Z specimens is neglected, the average K_{app} for the specimens tested in the “vertical” orientation, where the crack plane is parallel with the build layer plane, is 37–48 MPa \sqrt{m} . A handbook value for plane strain fracture toughness, K_{IC} , in wrought mill annealed Ti-6Al-4 V is approximately 65 MPa \sqrt{m} . Cast Ti-6Al-4 V has K_{IC} values of approximately 107 MPa \sqrt{m} in the as-cast condition to 109 MPa \sqrt{m} after HIP. The fracture toughness of electron beam welds in Ti-6Al-4 V ranges from 54 to 90 MPa \sqrt{m} .¹ The fracture toughness values of the SLM materials tested here approach that of wrought material and the low end of electron beam welds but fall well short of cast materials. However, the literature values cited are plane strain properties. The thickness of the specimens tested here were such that plane stress conditions were present. In plane stress, the role of the plastic zone at the crack tip is significant and will lead to higher toughness than plane strain, brittle and fracture. So, if thicker SLM specimens were tested to obtain plane strain properties that could be more directly compared with these literature values, even larger deficiencies would be expected. Thus, it appears that SLM Ti-6Al-

4 V has an inferior fracture toughness compared with conventional wrought or cast product forms. This is most likely due to the fine acicular alpha martensitic microstructure in the as-deposited condition,¹² which is typically strong, brittle and less tough. The X-Y, or “horizontal,” specimen orientation, where the crack plane is perpendicular to the build layers, showed a higher toughness on average than the “vertical” specimens (62 MPa \sqrt{m}), but it is unclear if this was attributed totally to the crack propagating across build layers or the different structure developed in this specimen because of the proximity of the specimen to the build chamber substrate (Fig. 3). Additional testing is needed on specimens in the “horizontal” orientation without this non-uniform microstructural condition associated with the proximity to the build chamber substrate.

In fatigue crack growth, the specimens tested here generally had the same performance trends, regardless of orientation (Fig. 4 and Table 4). The average threshold and critical values for ΔK for the three different specimen orientations were all within the scatter of the measurements implying that there is essentially no difference between the orientations. The same was true for the Paris Law constants, C and m , extracted from the da/dN curves. The most notable aspect of the results was the variable, or erratic, behaviour. This type of behaviour was seen in a previous study on the crack growth Ti-6Al-4 V SLM materials.³ In the as-deposited condition, the results of this previous study showed that the crack growth was significantly faster than baseline Ti-6Al-4 V. Heat treatment improved the performance to be more comparable with wrought material, mainly because of residual stress mitigation. In this current test, when compared with da/dN versus ΔK curves for wrought mill annealed Ti-6Al-4 V, which exhibits ΔK_{th} of 8–11 MPa \sqrt{m} and ΔK_c of 50–60 MPa \sqrt{m} ,¹ the SLM materials possess a lower threshold and critical value. However, in Region II, at ΔK of 20 MPa \sqrt{m} , the wrought material exhibits a da/dN of 1E-3 mm/cycle, and the SLM materials in this study exhibit a da/dN of 2E-4 mm/cycle. This actually represents an improvement to what was observed in the study of Leuders *et al.*³ where the entire as-deposited curve was faster than the base metal reference. Some benefit to crack growth transverse to the SLM build layers was seen as in the study of Leuders *et al.*³ compared with the crack growing parallel to the build layers. No noticeable difference in crack growth behaviour for cracks growing parallel versus transverse to the build layers was observed here. It is expected that the tensile residual stresses in this as-deposited condition (shown in the study of Edwards and Ramulu¹²) overshadowed any major influence of microstructure/orientation on the fatigue crack growth performance.

Compared with a previous study¹⁵ on the fracture toughness of Ti-6Al-4V parts produced using an electron beam heat source rather than a laser, where the fracture toughness was over $100 \text{ MPa}\sqrt{\text{m}}$ and crack growth rates were comparable with wrought materials, the results of this process appear to be inferior. Both are additive manufacturing processes, but the key difference is that the electron beam-based process is performed in an elevated temperature build chamber, which results in lower as-built residual stresses^{12,15} and a more annealed microstructure that is typically more ductile and tough. Without a post-process heat treatment on SLM materials, the rapidly cooled microstructure, high residual stresses and potentially less than 100% density could all lead to degraded performance. The study prior to this,¹² which investigated sub-surface characteristics and residual stresses, the same materials tested in this present study, showed high tensile residual stresses (over 400 MPa) and significant porosity. Build density was not measured, but significant porosity was observed. In a 20 \times magnification image, anywhere from 40 to 500 pores was observed. While it is unclear how this porosity would influence the fracture toughness and crack growth results measured here, but it is anticipated that porosity generally deteriorates mechanical performance, most prominently in high cycle fatigue because of premature crack initiation at pores that act as stress concentrations. It is expected that this degree of porosity would degrade the crack growth and toughness of the material as well. The tensile residual stresses present would also accelerate fatigue crack growth.

However, it was desired to test the SLM materials in this study in the as-deposited condition, with no thermal post-processing, to determine the performance of materials made with the lowest cost approach. It appears that the lack of post-processing does result in lower performance, so in order to utilize an SLM component in the as-deposited condition, an appropriate cost versus performance benefit assessment would be required. The cost versus benefit improvement of post-processing, like heat treatment, HIP, machining and peening, should be taken into consideration during the design of parts with this process in mind. In some cases, the improved performance yielded by post-processing may be needed, at added cost, but in others, it may not be required, enabling the lowest cost solution.

CONCLUSIONS

The following conclusions about Ti-6Al-4V SLM materials in the as-deposited condition can be drawn from the results of this study:

- The plane stress fracture toughness, regardless of crack orientation with respect to the build direction,

is lower than wrought and cast product forms as well as electron beam additive manufactured parts. This reduction is most likely attributed to the brittle martensitic structure obtained from rapid solidification of the material in the as-deposited condition.

- If the one outlier “vertical” fracture toughness specimen is neglected, the “horizontal” specimens exhibited higher fracture toughness than the “vertical” orientation. Thus, one can conclude that cracks orientated transversally to the build layers have higher toughness than those oriented parallel to the build layers. However, the “horizontal” specimens were essentially laying on the base of the build chamber, which is expected to have induced a sharp thermal gradient through the thickness of the specimen and thus an non-uniform microstructure through the thickness. It is unknown whether this was the reason for the improved performance or the crack orientation with respect to the build layers. More testing is necessary in “horizontal” specimens produced away from the build chamber substrate to obtain a uniform material.
- The threshold and critical stress intensities in the fatigue crack growth curves for these SLM materials are below that of wrought material, but in Region II, the SLM crack growth rates are actually slower than wrought material. Crack growth rates were also found to be highly variable, or erratic, which was consistent with previous research in materials produced by this process.
- The difference in crack growth rates between the three orientations tested was not discernible. Differences in threshold and critical stress intensity averages for each orientation were within the variation in the results for a given orientation. This was also the case for the Paris Law constants, C and m . Residual stresses likely overshadow any changes in crack growth behaviour as a function of build orientation and microstructural directionality.
- Post-process heat treatment or HIP’ing should be tested to validate the assumption that fracture and crack growth properties would be increased by microstructural modification and removal of residual stresses.

Acknowledgements

The authors of this paper would like to thank Dr Richard Hague, Dr Chris Tuck and everyone else who contributed to this work by fabricating specimens for testing from the Additive Manufacturing and 3D Printing Research Group at the University of Nottingham as well

as the United Kingdom's Technology Strategy Board and The Boeing Company for their support.

REFERENCES

- 1 Boyer, R., Welsch, G. and Collings, E. W. (1994) Materials and Properties Handbook Titanium Alloys. ASM International, Materials Park, OH, pp. 517–548.
- 2 Dutta, B. and Froes, F. H. (2014) Additive manufacturing of titanium alloys, Advanced Materials & Processes, February 2014.
- 3 Leuders, S., Thone, M., Riemer, A., Niendorf, T., Troster, T., Richard, H. and Maier, J. (2013) On the mechanical behavior of titanium alloy TiAl6V4 manufacture by selective laser melting: fatigue resistance and crack growth performance. *Int. J. Fatig.*, **48**, 300–307.
- 4 Chan, K., Koike, M., Mason, R. and Okabe, T. (2013) Fatigue life of titanium alloys fabricated by additive manufacturing techniques for dental implants. *Metall. Mater. Trans.*, **44A**, 1010–1022.
- 5 Thijs, L., Verhaeghe, F., Craeghs, T., Humbeeck, J. and Kruth, J. (2010) A study of the microstructural evolution during selective laser melting of Ti-6Al-4V. *Acta Mater.*, **58**, 3303–3312.
- 6 Kobryn, P., Moore, E. and Semiatin, S. (2000) The effect of laser power and traverse speed on microstructure, porosity, and build height in laser-deposited Ti-6Al-4V. *Scr. Mater.*, **43**, 299–305.
- 7 Kobryn, P. and Semiatin, S. (2001) The laser additive manufacture of Ti-6Al-4V. *JOM J. Miner. Met. Mater. Soc.*, **53**, 40–42.
- 8 Kobryn, P. and Semiatin, S. (2001) Mechanical properties of laser-deposited Ti-6Al-4V. In: *Proceedings of the Solid Freeform Fabrication Symposium 2001*, pp. 179–186.
- 9 Facchini, L., Magalini, E., Robotti, P., Molinari, A., Hoeges, S. and Wissenbach, K. (2010) Ductility of a Ti-6 Al-4 V alloy produced by selective laser melting of prealloyed powders. *Rapid Prototyping J.*, **16**, 450–459.
- 10 Koike, M., Greer, P., Owen, K., Lilly, G., Murr, L., Gaytan, S., Martinez, E. and Okabe, T. (2011) Evaluation of titanium alloys fabricated using rapid prototyping technologies – electron beam melting and laser beam melting. *Materials*, **4**, 1776–1792.
- 11 Qiu, C., Adkins, N. and Attallah, M. (2013) Microstructure and tensile properties of selectively laser-melted and of HIPed laser-melted Ti-6Al-4V. *Mater. Sci. Eng.*, **578**, 230–239.
- 12 Edwards, P. and Ramulu, M. (2014) Fatigue performance evaluation of selective laser melted Ti-6Al-4V. *Mater. Sci. Eng.*, **598**, 327–337.
- 13 Eylon, D., Newman, J. R. and Thorne, J. K. (1990) Titanium and titanium alloy castings, properties and selection: nonferrous alloys and special-purpose materials. In *ASM Handbook, Vol. 2*. ASM International, 634–646.
- 14 Wanjara, P., Brochu, M. and Jahazi, M. (2005) Ti-6Al-4 V electron beam weld qualification using laser scanning confocal microscopy. *Mater Charact.*, **54**, 254–262.
- 15 Edwards, P., O'Conner, A. and Ramulu, M. (2013) Electron beam additive manufacturing of titanium components: properties and performance. *J. Manuf. Sci. Eng.*, **135**, 011016–1.

DOI: 10.1002/adem.201100233

Analysis of Fracture Toughness and Crack Propagation of Ti6Al4V Produced by Selective Laser Melting**

By Brecht Van Hooreweder,* David Moens, Rene Boonen, Jean-Pierre Kruth and Paul Sas

This paper describes and analyzes fracture toughness and crack propagation of selective laser molten (SLM) components made from Ti6Al4V powder particles. The main goal of this research is to gain more insight in the fracture mechanisms of this relatively new material and to improve the static and dynamic behavior of cracked SLM-Ti components. At first, the SLM process parameters are optimized until the relative material density equals 99.7%. This is close to the relative density of vacuum arc remelted mill annealed standard oxygen titanium which is used as a reference for all experiments. A distinctive difference in phase morphology and texture of the microstructure is noticed between the SLM and the reference titanium. The fine acicular martensite phase of the SLM-Ti results in more brittle behavior and inferior fracture toughness. On the other hand, the fine grained microstructure leads to a large number of grain boundaries acting as obstacle points for crack propagation. Consequently, crack growth properties do not significantly differ between both. Microstructural analysis of the crack growth and final failure areas on the fractured surfaces is performed to study the failure mechanisms in more detail.

Selective laser melting (SLM) is an additive fabrication process in which layers of powder are spread and laser radiation is used to fully melt the powdered material. Molten and resolidified material forms parts, whilst un-molten material remains in place to support the structure.^[1–3] In comparison with conventional production techniques, the SLM process offers high geometrical freedom, short design and manufacturing cycle time, customized components, and a wide material range. Furthermore, the un-molten powder can be reused, leading to a highly efficient material use which is beneficial for components made from expensive materials like Ti-alloys. Additive manufacturing techniques like SLM are increasingly

being used to produce functional mechanical components subjected to complex load histories. A variety of applications can be found in the automotive, aerospace and biomedical industry.^[4–7] However, to be competitive with other production techniques, the mechanical properties of the resulting products must be sufficient to meet in service loading and operational requirements. The static and dynamic material properties of SLM-components can differ substantially from the properties of the same components produced by conventional techniques. This is due to the inherent complexity of SLM and the large quantity of process parameters such as layer thickness, energy density, scan strategy, scan speed, preheating temperature, etc., that have a strong influence on the mechanical properties of the final product. At present, material properties like tensile strength, yield strength, hardness, and impact toughness are well understood and published.^[8,9] On the other hand, very little has been reported in literature on the fracture toughness and crack propagation properties of SLM-components made from Ti6Al4V. The knowledge of these properties is limited and accurate design calculations are therefore not possible. In the present work, a first attempt has been made to address this by studying the static and dynamic behavior of cracked SLM-components made from Ti6Al4V. The experimental procedure is repeated on vacuum arc remelted (VAR) mill annealed standard oxygen Ti6Al4V to compare the results.

[*] B. Van Hooreweder, Dr. R. Boonen, Prof. J.-P. Kruth,
Prof. P. Sas
K. U. Leuven, Department of Mechanical Engineering (PMA),
Celestijnlaan 300b, B-3001 Leuven, (Belgium)
E-mail: Brecht.vanhooreweder@mech.kuleuven.be
Prof. D. Moens
Lessius Mechelen, De Nayer Institute, Department of Applied
Engineering in association with K. U. Leuven, Department of
Mechanical Engineering, J. De Nayerlaan 5, B-2860 Sint-
Katelijne-Waver, (Belgium)

[**] This research is funded by a Ph.D. grant of the Institute for the
Promotion of Innovation through Science and Technology in
Flanders (IWT-Vlaanderen). The author also gratefully
acknowledges Ir. L. Thijs for detailed analysis of the micro-
structure and Ing. O. Raeymaekers for his excellent master
thesis which formed the groundwork for this publication.

1. Materials

To analyze fracture toughness and crack propagation, both VAR standard oxygen mill annealed Ti6Al4V and SLM

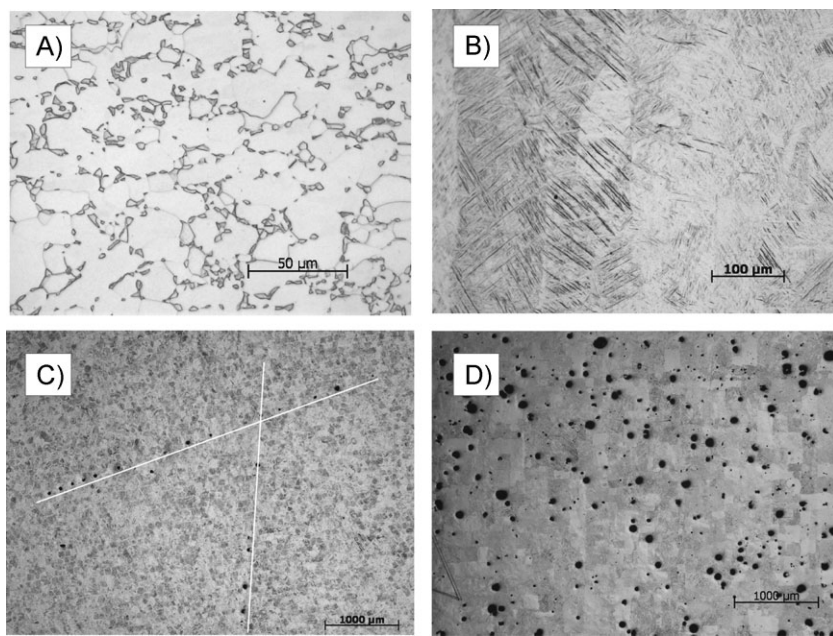


Fig. 1. Microstructure of Ti6Al4V: (A) VAR standard oxygen mill annealed ($d = 99.70\%$), (B) SLM with optimal scan-parameters ($d = 99.68\%$), (C) SLM with island scanning ($d = 99.43\%$), (D) SLM with suboptimal scan-parameters ($d = 97.06\%$).

Ti6Al4V was used. The microstructure from the VAR titanium strongly differs from that of the SLM titanium. Figure 1A shows the globular microstructure of the reference material resulting from a slow cooling process. During SLM on the other hand, high temperature gradients occur due to laser interaction, leading to a fine acicular α' -martensite phase with sharp needles as indicated in Figure 1B. Furthermore, epitaxial grain growth can be noticed on the sides of the test specimens, indicating vertical growth through the layers of the specimens in the direction of heat removal.^[10] This clear difference in microstructure can have a major impact on the fracture toughness and crack growth of the material. According to Lütjering,^[11] the most important microstructural parameter for Ti6Al4V is the α -colony size. With increasing temperature gradient, the α -colony size will decrease leading to improved yield stress but lower fracture toughness and faster crack propagation.

Another important parameter that has a major influence on the mechanical behavior of the final products is the density of the SLM-parts. A high density ensures fewer pores in the material leading to an improved resistance against crack growth and failure. A low density is characterized by many pores and inferior material properties. Moreover, the pores in the material often dominate the failure mechanisms, making it very difficult to predict or calculate the mechanical material behavior.^[12]

Figure 1C and D shows two examples of SLM material with low densities. Figure 1C indicates a specimen with low material density caused by the use of island scanning. By means of this scanning strategy, different small "islands" are scanned under various directions in one layer. This can be an effective approach to reduce residual stresses in the final

product. However, the overlap between the islands can cause inferior melting and aligned pores in the material as shown in Figure 1C. Consequently, the island scanning strategy will not be used in this study. Figure 1D indicates a low-quality SLM-product with a density of only 97.06% due to suboptimal scanning parameters. It is clear that these pores act as microscopic stress raisers which are associated to stress concentration factors in the range of 5–12. Not only does this facilitate the initiation of fatigue cracks, also cracks can propagate more rapidly through the material.

To optimize the production time and the density of SLM test specimens for fracture toughness and crack propagation experiments, the in-house developed SLM machine^[13] of the PMA division of K. U. Leuven was used to produce different cubical ($5 \times 5 \times 5 \text{ mm}^3$) blocks using different values for the laser power P (100, 200, 250 W), scan speed v (63–1600 $\text{mm} \cdot \text{s}^{-1}$), track distance h (53–145 μm), and layer thickness t (30, 60,

$90 \mu\text{m}$) while maintaining the same energy density E . This last parameter gives an indication of the energy supply during SLM and can be calculated using the previous parameters, $E = P/vht$ in $\text{J} \cdot \text{mm}^{-3}$. A bidirectional scanning strategy was used for all the specimens. After scanning the contour, the first layer is scanned in zigzag and each successive layer is rotated by 90° as indicated in Figure 2. The relative density of the different blocks was measured using the Archimedes principle leading to a maximal value of 99.7% and a set of optimal scan parameters as indicated in Table 1.

2. Experimental

All experiments are performed using CT-specimens with geometry as shown in Figure 3. The specimens of the reference material were extracted from a solid block according to the T-L

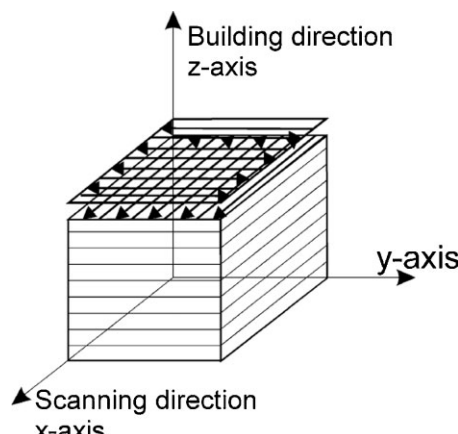


Fig. 2. Bi-directional scanning strategy.

Table 1. Optimal scan parameters.

Laser power <i>P</i> [W]	Scan speed <i>v</i> [mm · s ⁻¹]	Track distance <i>h</i> [μm]	Layer thickness <i>t</i> [μm]
250	1600	60	30

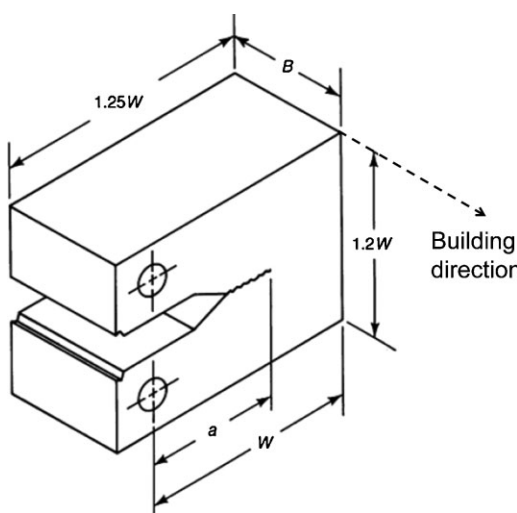


Fig. 3. Compact tension test specimen with straight trough notch.

direction using electrical discharge machining (EDM). For the SLM material, oversized blocks were produced using the optimal scanning parameters, the bidirectional scanning strategy, and building direction as illustrated in Figure 3. After this, EDM was used to remove the excess of material and to machine the straight trough notch. The relative density of 18 SLM-specimens was measured to be $99.73 \pm 0.036\%$, which is close to the maximum density of the optimization study. This high density ensures a product without pores as shown in Figure 1B. Furthermore, the low standard deviation gives an indication of the high degree of process-stability. The relative density of the VAR material was determined using 18 specimens to be $99.68 \pm 0.046\%$.

2.1. Fracture Toughness

Fracture toughness experiments were carried out according to the ASTM E399 standard [14]. The geometry of the test samples was determined using the expected fracture toughness K'_{1C} and the yield strength σ_{ys} :

$$(W - a) \geq 2.5 \left(\frac{K'_{1C}}{\sigma_{ys}} \right)^2 \quad \text{and} \quad B = a = 0.5 W$$

$$\rightarrow W \geq \frac{2.5}{0.5} \left(\frac{65}{950} \right)^2 \geq 23.41 \text{ mm}$$

$$\rightarrow W = 25 \text{ mm}, B = a = 12.5 \text{ mm}$$
(1)

For statistical data analysis, 10 specimens were tested for both the VAR and the SLM-material. At first, a 7.5 mm deep pre-crack was introduced at the notch root by purely reversed

cyclic loading at 10 Hz while making sure that $K_{max} < 0.8 \times K'_{1C} < 52 \text{ MPa} \cdot \text{m}^{0.5}$. After this, tensile tests were performed on the pre-cracked specimens with test speed of 1 mm · min⁻¹. These tensile curves were then used to construct a line with a slope of 95% of the linear part of the original curve. By doing so, the intersection between both curves could be found and the maximum force P_Q was determined in this point. Finally, the fracture toughness was calculated using Formula 2.

$$K_{1C} = K_Q = \frac{P_Q}{B\sqrt{W}} \frac{\left(2 + \frac{a}{W}\right)}{\left(1 - \frac{a}{W}\right)^{3/2}} \left(0.89 + 4.64 \left(\frac{a}{W} \right) - 13.32 \left(\frac{a}{W} \right)^2 + 14.82 \left(\frac{a}{W} \right)^3 - 5.6 \left(\frac{a}{W} \right)^4 \right) \quad (2)$$

2.2. Crack Propagation

Crack propagation experiments were carried out according to the ASTM E647 standard [15]. The geometry of the test samples is the same as for the fracture toughness specimens with exception of the thickness B which equals 0.25 W or 6.25 mm. For statistical data analysis, eight specimens were tested for both the VAR and the SLM material. At first, a 1 mm deep pre-crack was introduced at the notch root by purely reversed cyclic loading at 5 Hz. After this, the crack propagation test was started using a cyclic load in tension ($R = 0.1$) with fixed amplitude (ΔP) and fixed test frequency (5 Hz). For each load amplitude, a crack length (a) versus lifetime (N) curve was constructed. After that, da/dN ratios were calculated for each curve and ΔK values were determined using Formula 2 where P_Q was replaced by ΔP and a was replaced by $(a_1 + a_2)/2$. Finally, the values of da/dN were plotted versus ΔK on a double logarithmic scale to construct the crack propagation curve.

3. Results and Discussion

3.1. Fracture Toughness

For 10 specimens of the VAR material and 10 specimens of the SLM material, fracture toughness values were successfully determined according to the relevant standard. Hence K_q was set equal to K_{1C} and design values were defined according to a 95% confidence interval. The results of these calculations are summarized in Table 2.

The fracture toughness for the standard oxygen mill annealed titanium is close to the K_{1C} value of $64.9 \text{ MPa} \cdot \text{m}^{0.5}$

Table 2. Fracture toughness results.

	VAR Ti	SLM Ti
Specimens	10	10
Density [%]	99.68 ± 0.046	99.73 ± 0.036
K_{1C} [MPa · m ^{0.5}]	69.98 ± 3.53	52.4 ± 3.48
$K_{1C,95\%}$ [MPa · m ^{0.5}]	67.8	50.2

found in literature.^[16] This indicates that the experimental procedure is applied in the approved manner. Moreover, the standard deviation is within reasonable limits for fracture toughness testing. Table 2 also shows that the fracture toughness of the SLM material is around 3/4 from the fracture toughness of the VAR material. Since both densities are approximately the same, it is not likely that material imperfections such as pores or pollution by oxygen and nitrogen are the foundation for this inferior behavior of the SLM titanium. Hence the lower fracture toughness properties are almost certainly caused by the metastable microstructure consisting of a fine martensitic phase which causes an increase of the brittleness. If the rapid solidification of the titanium powder could be delayed, the ductility of the material would rise, leading to improved fracture toughness. This could be done by preheating the building chamber or the building platform. Furthermore, a suitable heat treatment could be applied to the test specimens in order to transform the metastable martensite phase into a biphasic α - β matrix with improved ductility.

3.2. Crack Propagation

Figure 4 shows the measured crack length as a function of cycles to failure for five different cyclic load levels applied to a CT specimen of the VAR titanium. It is clear that testing at different load levels is required to obtain data over a wide range of growth rates.

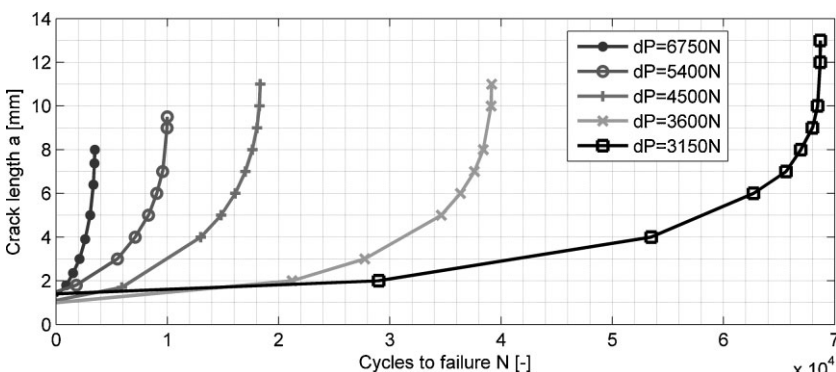


Fig. 4. Crack length a versus cycles to failure N for VAR-Ti using five different load cases.

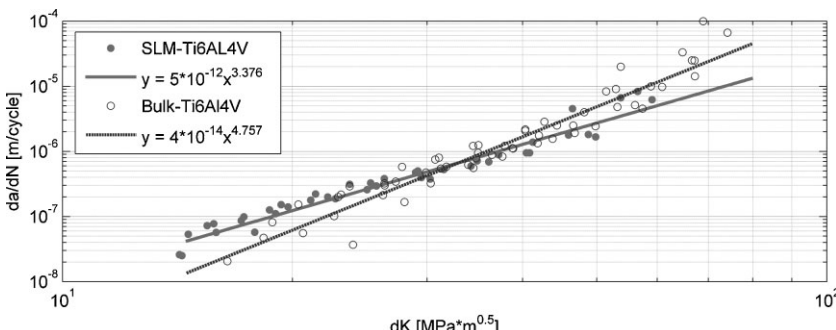


Fig. 5. Crack growth da/dN versus stress intensity range dK for VAR and SLM-Ti.

Table 3. Constants for the Paris equation.

	VAR Ti	SLM Ti
C [$m \cdot cycle^{-1}$]	4×10^{-14}	5×10^{-12}
m [-]	4.757	3.376

Figure 5 illustrates the data and least-squares fitted lines or fatigue crack growth rate curves $da/dN - dK$ for all the test specimens. For the mid-region of these lines, the Paris equation (Formula 3) can be solved leading to the Paris constants C and m as shown in Table 3.

$$\frac{da}{dN} = C(dK)^m \quad (3)$$

In general, the difference between the VAR and the SLM material is acceptable and values for C and m are close to the ones found in literature.^[17] To study the crack propagation more in detail, the microstructure of the fractured surfaces of the VAR titanium (A, B, C) and the SLM titanium (D, E, F) was examined using scanning electron microscopy as illustrated in Figure 6. The first column (A, D) shows a general overview, indicating the pre-crack (1), crack growth (2), and final failure (3) areas which appear to be featureless at low magnification. The crack growth phase (B, E) is characterized by ductile fatigue striations for the reference titanium and brittle crack

propagation showing small irregular facets and fine secondary cracks for the SLM titanium. For the final fracture surfaces the reference material shows ductile transgranular fracture caused by microvoid coalescence resulting in a dimpled appearance of the fracture surface (C). Also here, the SLM-titanium (F) shows less ductile dimples. The more brittle behavior of the SLM titanium is probably caused by the fine martensitic phase, leading to increased crack growth rates up to stress intensity range values of $30 \text{ MPa} \cdot \text{m}^{0.5}$.

Fine grained and martensitic microstructures like that of the SLM material tend to slow the propagation rate of small cracks due to the high density of grain boundaries acting as obstacle points.^[16–18] For cracks larger than 1 mm, this effect is reversed and crack propagation is increased. This phenomena is noticed for Ti6Al4V by many researchers including Lütjering and Yoder.^[18–20] The results in Figure 5 show increased crack propagation for the SLM-material with respect to the VAR-material up to a stress intensity range of $30 \text{ MPa} \cdot \text{m}^{0.5}$. This follows the theory as postulated by Lütjering *et al.* Once above $30 \text{ MPa} \cdot \text{m}^{0.5}$, the VAR material

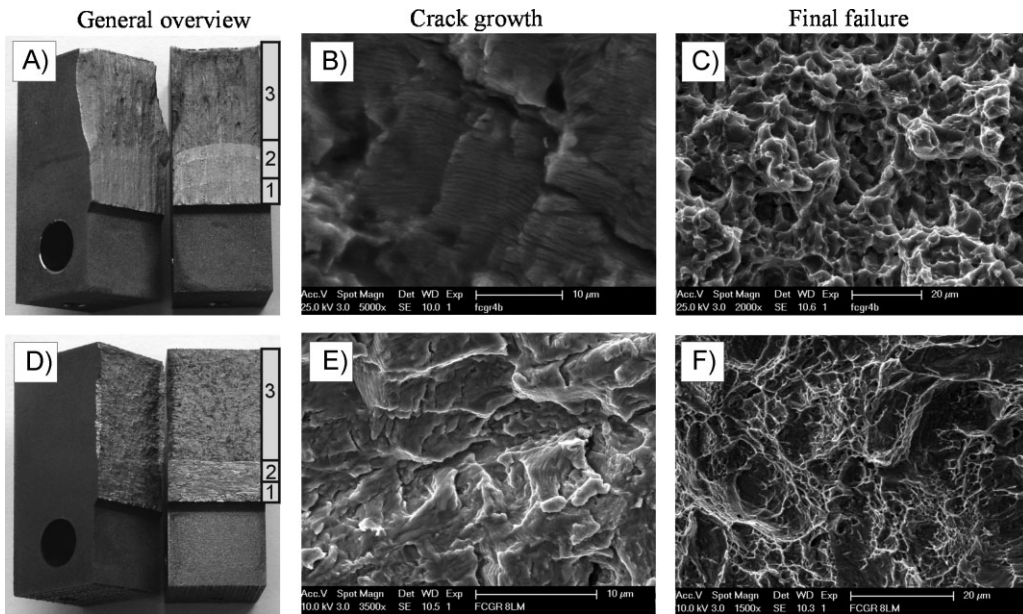


Fig. 6. General overview, crack growth, and final failure microscopy of fractured CT specimens from VAR titanium (A–C) and SLM titanium (D–F).

has a higher crack growth rate than the SLM material. Although the SLM material performs better in this region, it should be noticed that this curve will evolve more rapidly to an asymptote corresponding to $K_{\max} = K_C$ than the curve of the VAR material.

4. Conclusions

This paper describes the fracture toughness and crack propagation properties of SLM Ti6Al4V components. The in-house SLM apparatus was used with bidirectional scanning strategy and optimal process parameters to manufacture high quality test specimens with relative density of 99.7%. All experimental methods were repeated on VAR Ti6Al4V components to compare the results.

The SLM-Ti shows inferior fracture toughness values with respect to the reference material. Most likely, this is caused by the unstable and brittle microstructure consisting of a fine martensitic phase with sharp needles. On the other hand, this fine grained microstructure leads to acceptable crack growth properties due to the high density of grain boundaries acting as obstacle points for crack propagation.

Received: August 22, 2011

Final Version: September 30, 2011

Published online: November 2, 2011

- [1] J. P. Kruth, G. Levy, F. Klocke, T. H. C. Childs, *Ann. CIRP* **2007**, *56*, 730.
- [2] L. Lü, J. Fuh, *Laser-Induced Materials and Processes for Rapid Prototyping*, Kluwer, London 2001.

- [3] R. Noorani, *Rapid Prototyping: Principles and Applications*, Wiley, New Jersey, NJ 2005.
- [4] M. A. Lopez-Heredia, E. Goyenvalle, E. Aguado, P. Pilet, C. Leroux, M. Dorget, P. Weiss, P. Layrolle, *J. Biomed. Mater. Res. Part A* **2008**, *85A*, 664.
- [5] I. Yadroitsev, L. Thivillon, Ph. Bertrand, I. Smurov, *Appl. Surf. Sci.* **2007**, *254*, 980.
- [6] K. Osakada, M. Shiomi, *Int. J. Mach. Tools Manuf.* **2006**, *46*, 1188.
- [7] T. Gielis, M. Fleurinck, J. Bormans, B. Van Hooreweder, *Development of a monoblock titanium steering wheel for a solar powered race vehicle using SLM*. FISITA World Automotive Congress, 2010.
- [8] J. P. Kruth, M. Badrossamay, E. Yasa, J. Deckers, L. Thijs, J. Van Humbeeck, *Part and material properties in selective laser melting of metals*. 16th International Symposium on Electromachining, 2010.
- [9] E. Yasa, J. Deckers, J. P. Kruth, M. Rombouts, J. Luyten, *Experimental Investigation of Charpy Impact Tests on Metallic SLM Parts*. Int. Conf. Adv. Res. Virt. Rapid Prototyping, 2009, pp. 207–214.
- [10] L. Thijs, F. Verhaeghe, T. Craeghs, J. Van Humbeeck, J. P. Kruth, *Acta Mater.* **2010**, *58*, 3303.
- [11] G. Lütjering, *Mater. Sci. Eng.* **1998**, *A243*, 32.
- [12] B. Van Hooreweder, F. De Coninck, D. Moens, R. Boonen, P. Sas, *Polym. Test.* **2010**, *19*, 319.
- [13] J. Van Vaerenbergh, *Process Optimisation in Selective Laser Melting*, Ph.D. Thesis, UTWENTE, 2008.
- [14] ASTM E399, Standard test method for linear-elastic plane-strain fracture toughness K_{Ic} of metallic materials, annual book of ASTM standards, Pennsylvania, US 1995.

- [15] ASTM E647, Standard test method for measurement of fatigue crack growth rates, *annual book of ASTM standards*, Pennsylvania, US 1995.
- [16] E. W. Collings, *Materials Properties Handbook: Titanium Alloys*, ASTM International, Materials Park, OH 1994.
- [17] M. J. Donachie, *Titanium, a Technical Guide*, ASTM International, Materials Park, Ohio, USA 1988.
- [18] R. K. Nalla, B. L. Boyce, J. P. Campbell, J. O. Peters, R. O. Ritchie, *Metall. Mater. Trans. A* **2002**, *33A*, 899.
- [19] G. R. Yoder, L. A. Cooley, T. W. Crooker, *Eng. Fract. Mech.* **1983**, *17*, 185.
- [20] G. Lütjering, J. Albrecht, A. Gysler, in *Titanium: Science and Technology* (Eds: F. H. Froes, I. Caplan), TMS, Warrendale, PA 1993, pp. 1635–1646.

See discussions, stats, and author profiles for this publication at: <https://www.researchgate.net/publication/281728815>

Microstructure and mechanical properties of direct metal laser sintered Ti-6Al-4V

Article in South African Journal of Industrial Engineering · May 2015

DOI: 10.7166/26-1-1022

CITATIONS
33

READS
910

Some of the authors of this publication are also working on these related projects:



Qualification of Selective Laser Melting-produced Ti-6Al-4V for the biomedical and aerospace industries [View project](#)



Damage Characterisation of Thermal Power Plant Steels using Digital Image Correlation [View project](#)

MICROSTRUCTURE AND MECHANICAL PROPERTIES OF DIRECT METAL LASER SINTERED Ti-6Al-4V[†]

T.H. Becker^{1*}, M. Beck² & C. Scheffer³

^{1,3}Department of Mechanical and Mechatronic Engineering
Stellenbosch University, Stellenbosch
¹t.becker@sun.ac.za

²Zentralinstitut für Medizintechnik (IMETUM)
Technische Universität München, München

ABSTRACT

Direct metal laser sintering (DMLS) is a selective laser melting (SLM) manufacturing process that can produce near net shape parts from metallic powders. A range of materials are suitable for SLM; they include various metals such as titanium, steel, aluminium, and cobalt-chrome alloys. This paper forms part of a research drive that aims to evaluate the material performance of the SLM-manufactured metals. It presents DMLS-produced Ti-6Al-4V, a titanium alloy often used in biomedical and aerospace applications. This paper also studies the effect of several heat treatments on the microstructure and mechanical properties of Ti-6Al-4V processed by SLM. It reports the achievable mechanical properties of the alloy, including quasi-static, crack growth behaviour, density and porosity distribution, and post-processing using various heat-treatment conditions.

OPSOMMING

Direkte metaal-laser-sintering is 'n selektiewe lasersmeltvervaardigingsproses wat naby aan netto-vorm onderdele van metaalpoeiers kan produseer. Verskeie materiale is geskik vir lasersmeltvervaardiging, onder ander titaan, staal, aluminium en kobaltchrom legerings. Die doel van dié navorsing is om die materiaaleienskappe van lasersmeltvervaardigde onderdele te ondersoek. 'n Titaan legering (Ti-6Al-4V) wat dikwels biomediese en ruimte toepassings het, word voorgehou. Verder word die effek van verskeie hittebehandelings op die mikrostruktuur en meganiese eienskappe van die titaan legering, na dit lasersmeltvervaardiging ondergaan het, ondersoek. Die quasi-statiese kraakvoortplanting, digtheid- en poreusheidsverspreiding en die verwerking met verskeie hittebehandelingstoestande word bespreek.

[†] This is an extended version of a paper presented at the 14th International RAPDASA conference held at the Central University of Technology in South Africa in 2013.
* Corresponding author

1 INTRODUCTION

Direct metal laser sintering (DMLS), a selective laser melting (SLM) process, is a laser-based additive manufacturing (AM) technique that uses CAD models to create three-dimensional parts. The technique uses a high-powered laser to fabricate dense components from metal powder [1-3]. DMLS is capable of producing geometrically complex designs to high tolerances and with minimal material waste, while avoiding lengthy machining times. Furthermore, no tooling changes are required for different components to be manufactured on the same machine.

Over the past decade, increased material performance of SLM-manufactured components has allowed for a wide range of applications of the technique [4-6]. One such example is the use of DMLS to fabricate medical implants using Ti-6Al-4V, a titanium alloy that is typically characterised by high strength, low density, high corrosion resistance, and good biocompatibility [7-9]. The use of DMLS has demonstrated its versatility here, as it allows for the manufacture of geometrically complex and customised patient-specific implants. And due to the seamless CAD-to-manufacture transition, fast manufacturing of parts is possible [4].

There is significant concern, however, about the application of SLM-produced parts. For example, medical implants require strict material properties that have not yet been completely matched by SLM products [10]. The concerns about SLM-manufactured metals relate to internal stresses (resulting from steep temperature gradients and high cooling rates) that occur during the manufacturing process [11], the microstructure of as-built components and the resultant material performance [12], and the occurrence of pores [13]. DMLS parts do not normally have full density (although 99.8 per cent density can be achieved [10,11]), and they have an anisotropy due to the inherent layer-wise building procedure. Furthermore, little has been reported in the literature on heat-treatments, particularly for the application of Ti-6Al-4V in the biomedical industry. According to ASTM F1472 [14], as-built SLM-manufactured Ti-6Al-4V implants are currently may not be used in biomedical implants due to the presence of a martensitic microstructure [12] and the occurrence of porosity [13].

Previous studies by the author have indicated that high, non-uniform residual stresses are present in as-built DMLS Ti-6Al-4V samples that approached the yield strength of the material [11,15]. These stresses could easily be relieved, however, through heat-treatment. Studies by Vrancken et al. [12] on the microstructure and the influence of heat-treatment have shown that, due to the specific process conditions and thus the specific microstructure, SLM-produced parts require different heat-treatment from bulk alloy parts. They showed that the temperature, time, and cooling rate play an important role. Mechanical properties were dependent on the maximum heat treatment temperature where an increased maximum temperature resulted in a decline in the yield and ultimate tensile strength (UTS) and an increase in the fracture strain due to the transformation of the fine α' needles to a more coarse mixture of α and B . Similarly, work undertaken by Leuders et al. [13] has shown that porosity influences the fatigue life of SLM-manufactured Ti-6Al-4V: they identified a correlation between porosity and the fatigue behaviour in the high-cycle fatigue regime, where porosity vastly decreases fatigue life.

It follows that the successful industrial application of DMLS-manufactured Ti-6Al-4V components requires an investigation of material performance. Such a study should address the achievable mechanical properties of DMLS-manufactured Ti-6Al-4V, and post-treatment - such as heat-treatment - to improve the material performance. Characteristic quasi-static, crack growth and fatigue behaviour, residual stresses, and, most importantly, the microstructural interaction with the properties mentioned, should be investigated.

In this work, DMLS Ti-6Al-4V is post-processed through heat-treatment and hot isostatic pressing (HIP). The material performance is compared with the as-built and the wrought

material condition. A thorough testing procedure, combining porosity investigations using X-ray computed tomography (CT), quasi-static and dynamic mechanical loading, and microstructural characterisation is undertaken. Based on the findings, conclusions are drawn on the applicability of DMLS Ti-6Al-4V for biomedical implants.

2 EXPERIMENTAL METHODOLOGY

Fully characterising the material properties of DMLS-manufactured Ti-6Al-4V and the link between the DMLS process and the material properties requires a vast number of test specimens and test data, and a great deal of time. In this study, the focus was directed toward heat-treatment and the link between microstructure, as well as their link to the achievable tensile and dynamic mechanical properties of DMLS Ti-6Al-4V. This study did not consider any anisotropic affects that arise due to the inherent building process; samples were thus built in the XY plane orientation, according to the ISO/ASTM52921-13 designations.

All samples were made of Ti-6Al-4V, and were produced with an EOSINT M280 (EOS GmbH), which used a layer thickness of 30 μm and a 200W Yb-fibre laser. The scanning strategy is multidirectional with no further parameter descriptions supplied by EOS. The machine is installed at the Centre for Rapid Prototyping and Manufacturing at the Central University of Technology in Bloemfontein.

The experimental procedures presented in this study were conducted in ambient conditions. Heat-treatments and density determination (CT scans) were carried out at Stellenbosch University. Tensile tests and investigations in crack growth behaviour were conducted at the Centre for Materials Engineering at the University of Cape Town. Hot isostatic pressing (HIPing) was undertaken by Bodycote in Belgium.

2.1 Heat-treatment and microstructural evaluation

Ti-6Al-4V is an alpha-beta (α - β) alloy that is widely known to be suitable for heat-treatment, with many different microstructures obtainable through variations of heat-treatments. At room temperature, mill-annealed Ti-6Al-4V is about 90 per cent (volume) α , and the α phase thus dominates the physical and mechanical properties of this alloy; the β phase can be manipulated in amount and composition through heat-treatment.

The overall effects of processing history and heat-treatment on microstructure are complex, where the microstructure depends on both processing history and heat-treatment [16]. The microstructure that combines the highest static strength and ductility is not necessarily that which provides the optimum fracture toughness, fatigue strength, or resistance to crack growth. Typically, when wrought Ti-6Al-4V is heat-treated in the α - β temperature range and subsequently cooled, an equiaxed microstructure is formed that is categorised by the presence of globular (equiaxed) primary α in the transformed β (platelike) matrix. Similarly, a β structure is achieved by cooling from above the β transus to obtain an acicular or needle-like structure. The relative advantages of equiaxed and acicular titanium alloy microstructures include a higher ductility and formability, higher strength, and better low-cycle fatigue (initiation) properties for an equiaxed microstructure, as well as superior creep and crack growth properties and higher fracture-toughness values for an acicular grain structure [16].

Previous microstructure studies on SLM-produced Ti-6Al-4V have reported that the as-built material condition has a martensitic microstructure; the matrix is composed of acicular α phase, while no β phase is present [12]. It has also been reported that heat-treatment causes the transformation of the metastable martensite into a biphasic α + β matrix, with a morphology that depends on the heat-treatment [12]. These reported observations compare well with wrought Ti-6Al-4V, and the thought follows that DLSM Ti-6Al-4V can be tailored to achieve the desired mechanical properties that are comparable to wrought Ti-6Al-4V.

In this study, a total of four heat-treatments - including a recrystallisation anneal, duplex anneal, beta anneal, and HIP - were completed. Since Ti-6Al-4V will readily oxidise when heated above 427°C, heat-treatments were undertaken either in a vacuum furnace or with the use of ceramic coatings.

- Recrystallisation anneal (RA): Heated to 950°C, one-hour holding period, followed by a furnace cool.
- Hot isostatic pressing (HIP): heated to 915°C at 1000bar isostatic pressure, two-hour holding period, furnace cooling at 11°C/min.
- Duplex anneal (DA): heated to 950°C, one-hour holding period followed by air cooling, then heated to 700°C, two-hour holding period, followed by air cooling.
- Beta anneal (BA): heated to 1030°C, one-hour holding period followed by air cooling, then heated to 630°C, followed by air cooling.

2.2 Porosity and flaw investigations

The CT scanner is a General Electric Phoenix V|Tome|X L240 with an additional NF180 option. In this study, 5 mm diameter cylinders were scanned allowing for a voxel resolution of 3 μm^3 . One cylinder was scanned per post-processing condition.

2.3 Tensile strength and fracture toughness

Characterisation of the quasi-static properties was performed according to ASTM E8/E8M-11. Tests were conducted using the Zwick/Roell 1484 at ambient conditions. The tensile properties investigated were yield strength, ultimate tensile strength (UTS), percentage elongation at break, and Young's modulus. A minimum of five round tensile specimens (with a gauge diameter of 4.00 mm) were tested in the parallel to build direction. All tests were displacement controlled at a strain rate of 0.001/s.

The fracture toughness tests were conducted according to ASTM E399. To reduce the number of samples, fracture toughness tests made use of the samples used for crack growth rate investigations. The fatigue crack length was thus restricted to the range from 0.45 to 0.55 for K_{Ic} determination. Fracture toughness tests were displacement controlled at a rate of 1 mm/min, according to the standard. A minimum of five specimens (with a gauge diameter of 4.00 mm) were tested in the perpendicular to build direction.

2.4 Crack growth rate

An analysis of crack growth behaviour was conducted using compact tension specimens at ambient conditions with a stress intensity factor (K) ratio of $R \approx 0.1$. The specimens were manufactured according to ASTM E 647-08 with $W = 25$ mm and $B = 12.5$ mm. An optical microscope was used to monitor crack propagation, allowing for crack measurements to be taken every 0.1 mm. Five specimens were tested in the as-built condition, five in the recrystallisation annealed condition, and five in the HIPed condition, totalling 15 specimens. Tests were carried out at a frequency of 10 Hz.

3 EXPERIMENTAL RESULTS

3.1 Density evaluation

The experimental results of the CT scans are presented in Table 1. It shows that a near-full density of 99.79 ± 0.2 per cent and 99.94 ± 0.2 per cent for as-built and HIPed samples was achieved respectively. These values are in agreement with Knowles et al. [11], who determined a relative density of 99.7 per cent for DMLS Ti-6Al-4V using both Archimedes and optical measuring techniques. Figure 1 shows the CT scan of the as-built and HIPed samples that provide information on the porosity distribution and orientation. Scans in the as-built condition show an even porosity distribution, with no indication of a dependence on the layer distribution or sample orientation.

Table 1: Density of DMLS-manufactured Ti-6Al-4V. Relative density values given to $\pm 0.2\%$.

	HIPed	as-built
Density [g/cm3]	4,427	4,421
Relative density	99,94%	99,79%

No porosity is visible in the CT scans after the HIP process (Figure 1a), suggesting that any residual porosity is below the CT scan resolution limit of 3 μm . This is in agreement with the work done by Leuders et al. [13], who found a relative density of 100 per cent after the HIP process, measured using CT with a minimum resolution of 22 μm . They found that the mean relative density of as-built samples was 99.77 per cent.

3.2 Microstructure evaluation

Previous studies by Knowles et al. [11] have shown that the as-built microstructure has a very fine acicular (plate-like) morphology. This is attributed to the inherent rapid cooling of the material during DMLS, resulting in a beta-to-martensite transition. XRD analysis by Luca Facchini et al. [17] indicated the presence of only the α phase, which can be recognised as both the α phase and the α' martensite [18-20]. However, because of the very large solidification undercooling, the microstructure may be interpreted as martensitic. This microstructure morphology exhibits a high strength and hardness and low ductility, and can be detrimental to fracture toughness. However, martensite impedes dislocation motion, which leads to a strengthening effect that can improve fatigue crack propagation [16].

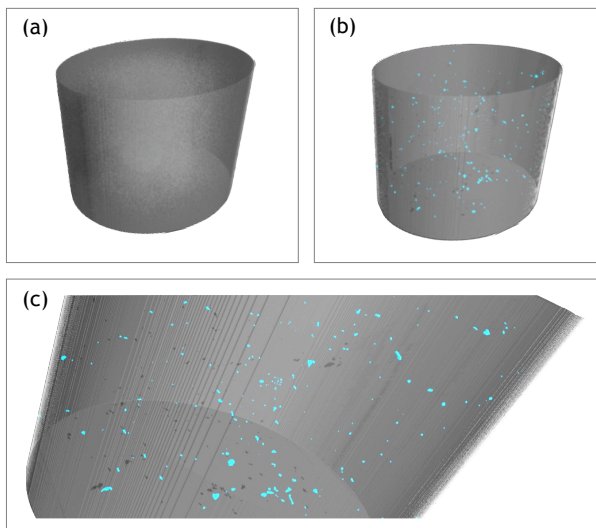


Figure 1: CT scan of a 3 mm diameter cylinder showing porosity (blue coloured) and distribution, where a) HIPped, b) as-built. a) After the HIP process the porosity was below the resolution limit of 3 μm . c) is an enlargement of b) to show the pore orientation and distribution.

Figure 2 shows the microstructures obtained through the aforementioned heat-treatment variations. The RA (Figure 2b, 950°C - furnace cooled) shows a microstructure transformed into a Plate-like $\alpha + \beta$, consisting of a small amount of equiaxed α . The HIPped condition (Figure 2d, 915°C - cooled at 11°C/min) shows a similar morphology; however, it consists of a larger grain structure and with less equiaxed α , which may be attributed to the faster cooling rate of the HIP treatment. The DA treatment (Figure 2a, 950°C - air cooled, followed by 700°C - furnace cooled) has transformed the microstructure into a matrix of equiaxed and acicular α and a small amount of intergranular β . Lütjering et al. [21] showed that the α colony size is a determining factor for the mechanical properties in wrought Ti-

6Al-4V. The coarsened α phase and larger α colony size result in a reduced tensile strength and an increased ductility, yet do not yield the best crack growth behaviour. Fine grains show a superior long through-crack fatigue crack growth behaviour and fracture toughness [16].

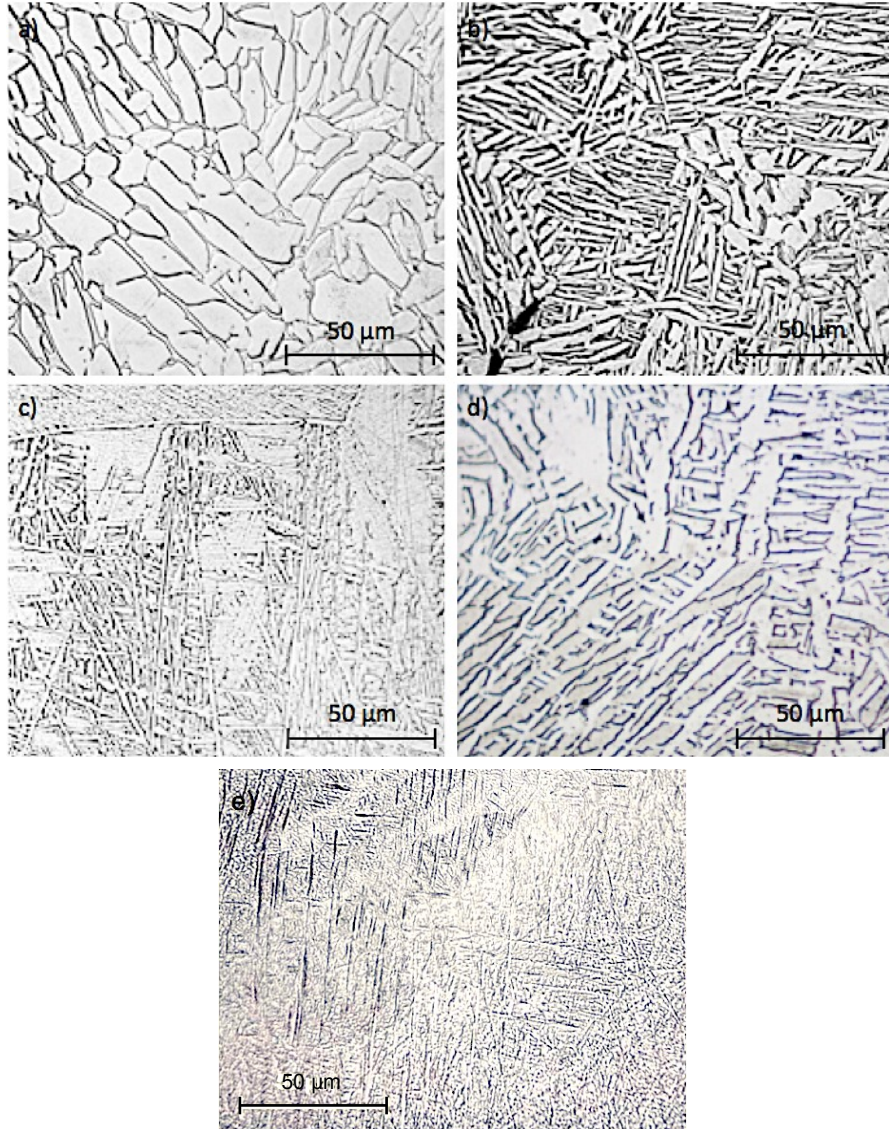


Figure 2: Microstructures obtained through various heat-treatments of DMLS Ti-6Al-4V.
(a) Duplex anneal (DA), (b) recrystallisation anneal (RA), (c) beta anneal (BA), (d) hot isostatic pressing (HIP), and (e) as-built condition.

The BA also produced changes on the microstructural level, as shown (Figure 2c, 1030°C - air cooled, followed by 630°C - air cooled). The microstructural change produced a fine microstructure consisting of acicular α (transformed β) with the α phase preferentially along the prior- β grains. The ‘fineness’ of this microstructure is evidence of a moderate cooling rate from above the β -transus. BA microstructures have the lowest fatigue crack growth rates, whereas mill-annealed microstructures yield the highest growth rates [16]. The structure of the Widmanstätten α plus retained β , or a mixture of this structure and α' , exhibit yield and tensile strengths superior to those of the mill-annealed wrought metal and a ductility and toughness greater than those of an entirely martensitic microstructure. A summary of the heat-treatments and resultant microstructure is provided in Table 2.

Table 2: Summary of heat-treatments and resultant microstructure

Heat treatment	Holding temperature	Cooling rate	Microstructure
As built	-	-	Fine acicular α' martensite
RA	950 °C	Furnace cooled	Plate-like $\alpha - \beta$, small amount of equiaxed α
HIP	915 °C	11 °C/min	Plate-like $\alpha - \beta$, small amount of equiaxed α
DA	960 °C and 700 °C	Air cooled and furnace cooled	Equiaxed and acicular α with intergranular β .
BA	1030 °C and 630 °C	Both air cooled	Widmanstätten $\alpha + \beta$ colony microstructure.

3.3 Tensile and fracture toughness properties

The achievable strengths for the post-treatments are summarised in Table 3. Standard deviations are ± 20 MPa for UTS and yield strength respectively, and ± 2 per cent for elongation at failure. The as-built samples achieved a high tensile strength of 1155 MPa. The RA, HIP, and DA show a decrease in tensile strength to 914, 960, and 871 MPa respectively. As expected, the BA results in a higher strength of 1008 MPa compared with the below β transus temperature heat-treatments. Similarly, the ductility (per cent elongation) increased through the various heat-treatments, with the DA achieving the highest per cent elongation of 11.5 per cent. These results are consistent with the microstructural observations in that the larger grain structures provided a decrease in strength and an increase in ductility.

The as-built material has a higher strength than the wrought metal, which can be attributed to the fine acicular microstructure. A study undertaken by Vrancken et al. [12] pointed out that, unlike wrought Ti-6Al-4V, the tensile strength decreases and ductility increases with increasing heat-treatment temperature. Wrought Ti-6Al-4V in the mill-annealed condition consists of an equiaxed microstructure; thus a β anneal transforms this microstructure to a lamellar $\alpha+\beta$, Widmanstätten α , or martensitic α' microstructure, depending on the cooling rate. The as-built microstructure is in a condition similar to a β anneal; a martensitic α as discussed in Section 3.2. Thus the various heat-treatments outlined - RA, HIP, and DA - essentially anneal a transformed β (which has undergone a severe cooling rate) to a lamellar $\alpha+\beta$ structure. The outcome of the heat-treatment primarily depends on the cooling rate (unless two or more heat-treatment cycles are undertaken, such as the DA or BA). It would be expected that, based on the understanding of the heat-treatment of wrought Ti-6Al-4V, the thickness of the grain boundary α is dependent on the cooling rate - decreasing with increasing cooling rate - and, when cooled from above the β transus, i.e. the as-built material state, the cooling rate determines the size of the α colonies and decomposition of martensite.

The fracture toughness results are also presented in Table 3. The as-built material condition resulted in surprisingly low toughness of $K_{Ic} = 37.5$ MPa/m. The HIP condition results in a stress intensity factor of $K_{Ic} = 57.8$ MPa/m, and the RA has the highest toughness of $K_{Ic} = 86.3$ MPa/m. These results are within 5 MPa/m.

The poor fracture toughness in the as-built condition may be explained by the martensitic microstructure and high UTS. Studies on the wrought material have shown that in a superior β transformed microstructure, an increase in UTS significantly decreased the toughness of the material, where an increase of about 20 per cent in UTS can halve K_{Ic} [16]. The low HIP fracture toughness is somewhat surprising when comparing the result with the RA toughness. It is not clear why the HIPed condition would result in a significantly lower toughness; it could, however, be attributed to a larger grain size.

Table 3: Ultimate tensile strength, elongation at failure and fracture toughness of Ti-6Al-4V. Wrought and P/M (powder metallurgy) results were taken from Donachie [16].

Process and heat-treatment	UTS [MPa]	% elongation at break	K _{IC} [MPa/m]
DMLS as-built	1155	4.1	37
Wrought Mill-annealed	930-970	17-19	44-66
DMLS Stress relief	1230	7.0	-
DMLS Recrystallisation anneal	914	10.3	86 [†]
DMLS Duplex anneal	871	11.5	-
DMLS Beta anneal	1008	8.4	-
Wrought Beta anneal	875-915	-	88-110
DMLS HIPed	960	8.5	58
P/M HIPed	937	17	85

3.4 Crack growth behaviour

The results obtained from crack growth measurements are shown in Figure 3. The data is compared with the results obtained by Leuders et al. [13], and shows excellent agreement (Leuders' data is based on samples built on a SLM 250HL machine from SLM Solutions GmbH). The data shows a considerable difference between the as-built and heat-treated material condition. The as-built condition has considerably poorer fatigue performance relative to the heat-treated condition (identified by the faster crack growth rate for a similar cyclic stress intensity factor value), and exhibits large scatter. Specimens in both the RA and the HIP condition have significantly less scatter and a similar behaviour to that of the wrought mill-annealed metal. The scatter in data may be attributed to high residual stresses that are present in the as-built state.

Similarly to the quasi-static properties, the processing and microstructure can have a large effect on the crack growth rate. Generally for wrought metal, BAed microstructures in near- α and α - β have the lowest fatigue crack growth rates, whereas mill-annealed microstructures yield the highest growth rates. A martensitic α microstructure can be advantageous; however, in the case of DMLS, the high residual stresses probably outweigh any advantageous microstructural effects. A recent study by Rafi et al. [22] showed an improved fatigue performance for as-built SLM samples compared with annealed cast samples. It is not clear in their study, however, whether any stress relieving was performed.

Furthermore, the HIPed samples show little, if any, improvement in fatigue crack growth. However, the work done by Leuders et al. [13] showed that for mean stress-based fatigue life investigations, the fatigue failures ranged from $27 \cdot 10^3$ to $290 \cdot 10^3$ cycles to failure for as-built and heat-treated samples. By contrast, none of the HIPed specimens failed during tests, which were interrupted at $2 \cdot 10^6$ cycles at a cyclic stress of 600 MPa. Clearly there is a strong interaction between fatigue life and porosity. Pores act as sites of increased stress, and thus act as crack initiation sites.

4 DISCUSSION

Ti-6Al-4V is one of the most widely-used titanium alloys, with an excellent combination of strength and toughness along with excellent corrosion resistance. Relying on the refinement of the grains upon cooling from the β region or the α -plus- β region develops the properties of this alloy, and subsequent low-temperature aging allows the martensite formed upon quenching to decompose.

Clearly, a significant improvement in the material performance of DMLS Ti-6Al-4V can be achieved using an appropriate treatment. Both ductility and toughness, as well as the crack growth characteristics, may be substantially improved. Although HIPing does not have a

[†] $P_{max}/P_Q \leq 1.1$ was not achieved.

direct effect on these properties, Leuders et al. [13] have shown that non-HIPed samples have a very poor fatigue life, where pores act as crack initiation sites.

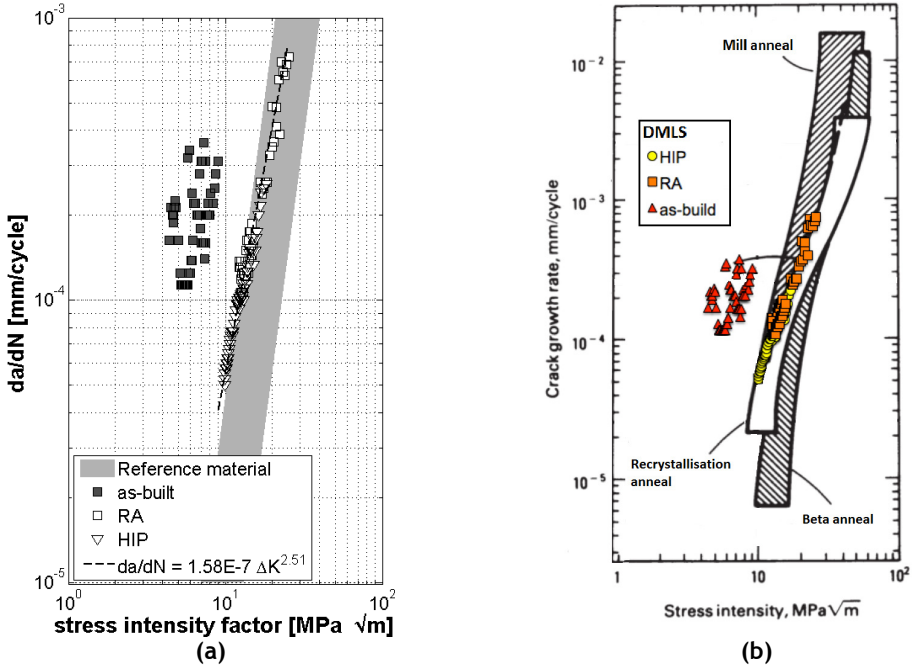


Figure 3: Crack growth curves for DMLS Ti-6Al-4V. (a) DMLS data in comparison with SLM-produced Ti-6Al-4V [13] (reference material). (b) DMLS data superimposed on to Ti-6Al-4V production methods data (data reproduced from Donachie [16]).

To obtain high strength with adequate ductility, one heat-treatment below the β transus is suggested. If higher fracture toughness is required, BA may be desirable. However, heat-treating Ti-6Al-4V in the β range can cause loss in ductility. As is typical for wrought Ti-6Al-4V, a heat-treatment just below the β transus can obtain an optimum balance of ductility, fracture toughness, and tensile strength.

It is important to realise that standard heat-treatments do not apply to DMLS material. In Ti-6Al-4V, the microstructure, and hence the mechanical properties, depend on the process history. Since as-built DMLS Ti-6Al-4V has a fine acicular morphology that results from the heating above the β transus, improper heat-treatment can result in undesirable properties. For example, α phase can form preferentially along the prior- β grains. Because cracks tend to propagate in or near interfaces, this type of structure can provide loci for crack initiation and propagation, and thus lead to premature failure. Correct BA microstructures have the lowest fatigue crack growth rates, whereas mill-annealed microstructures yield the highest growth rates (Figure 3b).

5 CONCLUSIONS

The aim of this study was to evaluate the achievable material performance of DMLS Ti-6Al-4V through heat-treatment. In order to establish a link between mechanical properties and heat-treatment, a comparison of the various heat-treated microstructures (and porosity) was undertaken. The findings presented in this study lead to the following conclusions:

- The tensile behaviour, fracture toughness, and crack growth behaviour compare well with the wrought material. As for most commercial SLM processes, a nearly-100 per cent dense material may be achieved.
- The material behaviour is directly related to its microstructure, which can be tailored by specific heat-treatments. The as-built condition has an unfavourable performance

- that is strongly inhibited by large residual stresses with an unfavourable martensitic microstructure.
- Due to the specific process conditions and hence microstructure, DMLS-produced parts may require heat-treatment that is different from the wrought material.

REFERENCES

- [1] Kumar, S. 2003. Selective laser sintering: A qualitative and objective approach, *Journal of Materials*, 55(10), pp 43-47.
- [2] Kruth, J.P., Froyen, L., Van Vaerenbergh, J., Mercelis, P., Rombouts, M. & Lauwers, B. 2004. Selective laser melting of iron-based powder, *Journal of Materials Processing Technology*, 149(1-3), pp 616-622.
- [3] Santos, E., Abe, F., Kitamura, Y., Osakada, K. & Shiomi, M. 2002. Mechanical properties of pure titanium models processed by selective laser melting, *Proceedings of the Solid Freeform Fabrication Symposium*, Austin, pp 180-186.
- [4] Agarwala, M., Bourell, D., Beaman, J., Marcus, H. & Barlow, J. 1995. Direct selective laser sintering of metals, *Rapid Prototyping Journal*, 1(1), pp 26-36.
- [5] Kruth, J.P., Mercelis, P., Vaerenbergh, J.V., Froyen, L. & Rombouts, M. 2005. Binding mechanisms in selective laser sintering and selective laser melting, *Rapid Prototyping Journal*, 11(1), pp 26-36.
- [6] Kim, G.D. & Oh, Y.T. 2008. A benchmark study on rapid prototyping processes and machines: Quantitative comparisons of mechanical properties, accuracy, roughness, speed, and material cost, *Proceedings of the Institution of Mechanical Engineers: Part B, Journal of Engineering Manufacture*, 222(2), pp 201-215.
- [7] Bartolo, P., Kruth, J.P. & Silva, J. 2012. Biomedical production of implants by additive electrochemical and physical processes. *CIRP Annals - Manufacturing Technology*, 61(2), pp 635-655.
- [8] Bibb, R., Eggbeer, D. & Williams, R. 2006. Rapid manufacture of removable partial denture frameworks, *Rapid Prototyping Journal*, 12(2), pp 95-99.
- [9] Evers, D. & Dotchev, K. 2010. Technology review for mass customisation using rapid manufacturing, *Assembly Automation*, 30(1), pp 39-46.
- [10] Vandenbroucke, B. & Kruth, J.P. 2007. Selective laser melting of biocompatible metals for rapid manufacturing of medical parts, *Rapid Prototyping Journal*, 13(4), pp 196-203.
- [11] Knowles, C.R., Becker, T.H. & Tait, R.B. 2012. The effect of heat treatment on the residual stress levels within direct metal laser sintered Ti-6Al-4V as measured using the hole-drilling strain gauge method, *Proceedings of the 13th international RAPDASA conference*, Sun City.
- [12] Vrancken, B., Thijs, L., Kruth, J.P. & Humbeeck, J. 2012. Heat treatment of Ti-6Al-4V produced by selective laser melting: Microstructure and mechanical properties, *Journal of Alloys and Compounds*, 541, pp 177-185.
- [13] Leuders, S., Thöne, M., Riemer, A., Niendorf, T., Tröster, T., Richard, H.A. & Maier, H.J. 2013. On the mechanical behaviour of titanium alloy TiAl6V4 manufactured by selective laser melting: Fatigue resistance and crack growth performance, *International Journal of Fatigue*, 48(1), pp 300-307.
- [14] ASTM standards. 2012. ASTM F136-12a Standard Specification for Wrought Titanium-6Aluminum-4Vanadium ELI (Extra Low Interstitial) Alloy for Surgical Implant Applications, UNS R56400.
- [15] Knowles, C.R., Becker, T.H. & Tait, R.B. 2012. Residual stress measurements and structural integrity implications for selective laser melted Ti-6Al-4V, *South African Journal of Industrial Engineering*, 23(3), pp 119-129.
- [16] Donachie, M. 2000. *Titanium: A technical guide*, 2nd edition. ASM international.
- [17] Facchini, L., Magalini, E., Robotti, P., Molinari, A., Höges, S. & Wissenbach, K. 2010. Ductility of a Ti-6Al-4V alloy produced by selective laser melting of prealloyed powders, *Rapid Prototyping Journal*, (16)6, pp 450-459.
- [18] Kubiak, K. & Sieniawski, J. 1998. Development of the microstructure and fatigue strength of two phase titanium alloys in the processes of forging and heat treatment, *Journal of Materials Processing Technology*, 78(1), pp 117-121.
- [19] Jovanovic, M.T., Tadic, S., Zec, S., Miskovic, Z. & Bobic, I. 2006. The effect of annealing temperatures and cooling rate on microstructure and mechanical properties of investment cast Ti-6Al-4V alloy, *Materials and Design*, 27(3), pp 192-199.
- [20] Malinov, S., Sha, W., Guo, Z., Tang, C.C. & Long, A.E. 2002. Synchrotron X-ray diffraction study of the phase transformations in titanium alloys, *Materials Characterization*, 48(4), pp 279-95.
- [21] Lütjering, G. 1998. Influence of processing on microstructure and mechanical properties of $\alpha+\beta$ titanium alloys, *Materials Science and Engineering*, A243(1), pp 32-45.
- [22] Rafi, H.K., Karthik, N.V., Gong, H., Starr, T.L. & Stucker, B.E. 2013. Microstructures and mechanical properties of Ti6Al4V parts fabricated by selective laser melting and electron beam melting, *Journal of Materials Engineering and Performance*, 22(12), pp 3872-3883.

See discussions, stats, and author profiles for this publication at: <https://www.researchgate.net/publication/259716135>

Electron Beam Additive Manufacturing of Titanium Components: Properties and Performance

Article in *Journal of Manufacturing Science and Engineering* · December 2013

DOI: 10.1115/1.4025773

CITATIONS
204

READS
5,658

3 authors, including:



P. Edwards
Tesla Motors
52 PUBLICATIONS 1,266 CITATIONS

[SEE PROFILE](#)



M. Ramulu
University of Washington Seattle
297 PUBLICATIONS 6,765 CITATIONS

[SEE PROFILE](#)

Some of the authors of this publication are also working on these related projects:



Abrasice Water Jet Machining of Hybrid Composites [View project](#)



PhD Thesis [View project](#)

P. Edwards

Boeing Research & Technology,
The Boeing Company,
Seattle, WA 98124
e-mail: Paul.D.Edwards2@boeing.com

A. O'Conner

Graduate Assistant
e-mail: apoc@u.washington.edu

M. Ramulu¹

Boeing-Pennell Professor of Engineering
e-mail: ramulum@u.washington.edu

Department of Mechanical Engineering,
University of Washington,
Seattle, WA 98195

Electron Beam Additive Manufacturing of Titanium Components: Properties and Performance

This research evaluates the fatigue properties of Ti-6Al-4V specimens and components produced by Electron Beam additive manufacturing. It was found that the fatigue performance of specimens produced by additive manufacturing is significantly lower than that of wrought material due to defects such as porosity and surface roughness. However, evaluation of an actual component subjected to design fatigue loads did not result in premature failure as anticipated by specimen testing. Metallography, residual stress, static strength and elongation, fracture toughness, crack growth, and the effect of post processing operations such as machining and peening on fatigue performance were also evaluated. [DOI: 10.1115/1.4025773]

Keywords: additive manufacturing, electron beam, titanium, fatigue, fracture

1 Introduction

With traditional manufacturing processes, such as machining from wrought plate, the design of the part is constrained by the geometries that can be feasibly produced by the machining process. An example of a small machined titanium bracket, or clip, is shown in Fig. 1(a). The machining process geometric producibility constraints often result in parts with more material, and weight, than is actually needed to safely support the design loads. However, the complex geometric build capabilities of additive manufacturing (AM) can provide nearly complete design freedom. By combining design optimization and AM, parts can be produced with material only where it is needed to transfer the required design loads, resulting in significant weight reductions. Figure 1(b) shows an example of the same bracket, Fig. 1(a), with a numerically optimized design that is 48% lighter than the machined part design.

Although AM holds promise for reducing the weight of aerospace structures, it must be shown that the mechanical performance of AM parts will meet stringent commercial aerospace design criteria. A number of AM processes are currently available [1,2] and most studies performed on titanium, specifically Ti-6Al-4V, are defined by their heat source, such as electron beam [3–12], Laser [12–23] or Arc [21,22], and how the raw material is supplied, such as layers of powder where selected regions are melted and the unmelted powder is subsequently removed [1–20] or when material, such as solid wire or powder, is directly deposited onto a base plate [21,22]. In order to utilize these AM technologies to leverage their ability to produce novel light weight designs for structural applications, the static, fatigue, and damage tolerance performance of specimens and components subjected to a variety of post processing conditions must be assessed and understood. AM of titanium is of particular interest due to its increased usage in aerospace structures for its thermal and galvanic compatibility with composites.

The static performance of Ti-6Al-4V parts produced by AM is dependent on the particular AM technique used, processing conditions, post deposition heat treatment, location in build envelope and orientation, among other variables. However, AM is generally found to be comparable to wrought Ti-6Al-4V ultimate strength,

yield strength, and elongation [3,8,12,20–22]. Related to the static properties, microstructures and hardness are also dependent on these same variables. Microstructures have been characterized as acicular alpha in prior beta grains [3,4], very fine lamellar [7], alpha laths in prior beta [6], or prior beta grains that grow across build layers [21,22]. Process conducted outside of an elevated temperature build chamber, like Laser and Arc, can result in martensitic structure [20]. Inhomogeneous microstructures due to the build direction can lead to the location and orientation dependence on the mechanical performance of the parts [5]. Heat treatment can reduce, or eliminate, residual stresses as well as coarsen the lamellar alpha structure and dissolve the martensite, which may lower the strength slightly, but recover ductility [20]. Heat treatment has a larger impact on laser processes [20] compared to electron beam [7] because electron beam processes are typically carried out in build chambers at temperatures ranging from 600 to 700 °C, which essentially stress relieves the parts *in situ*.

While microstructures and static properties are important, characterization of fatigue and damage tolerance performance is often more difficult, time consuming, and costly. In addition, it is challenging to clearly define, the most critical aspects in design for long life, safety critical, high performance structures, such as those in commercial aerospace. As with static properties, fatigue and damage tolerance are also dependent on similar process variables, but in fatigue, surface condition and porosity have the most

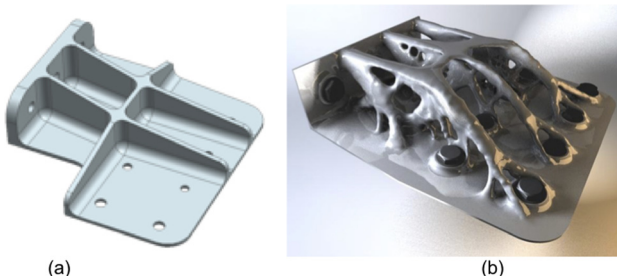


Fig. 1 (a) Typical titanium aerospace bracket made by machining from wrought material and (b) optimized design based on the loading conditions leveraging the build capabilities of additive manufacturing. Drawings are not to scale.

¹Corresponding author.

Manuscript received April 30, 2013; final manuscript received October 17, 2013; published online November 18, 2013. Assoc. Editor: Yung Shin.

significant impact on fatigue performance [7,8,20–22]. Leuders et al. [20] evaluated the fatigue and crack growth characteristics of Ti-6Al-4V manufactured by selective laser melting (SLM). It was found that in the as-built condition, the fatigue strength was significantly reduced due to porosity. However, when hot isostatic pressed (HIP'ed), the fatigue strength became more comparable to conventionally processed titanium alloys. With respect to crack growth, the controlling factor was internal residual stresses, but regardless of post process heat treatment the crack growth behavior was similar to wrought titanium. Chan et al. [8] studied the fatigue performance of Ti-6Al-4V ELI materials produced by both electron beam melting (EBM) and SLM with both as-built and electro discharged machined (EDM) surfaces. In all cases, the performance of wrought material was significantly better than EBM and SLM. EDM improved the fatigue performance, but still did not compare to the wrought titanium properties. Internal porosity was not observed and all fatigue crack initiations originated from rough features on either the as-built or machined surfaces. Facchini et al. [7] assessed the fatigue performance of Ti-6Al-4V specimens produced by EBM in the as-built and HIP'ed conditions. In the as-built condition, the fatigue life was similar to cast products and in the HIP'ed condition the fatigue strength became more comparable to wrought material. Brandl et al. [21,22] investigated the fatigue strength of wire deposited materials consolidated with both laser and arc heat sources. While there were low performing outliers due to near surface porosity, the fatigue strength was comparable to wrought material, ranging from 760 to 780 MPa in the as-built conditions to 840 MPa after heat treatment.

Even though several studies have been conducted on the fatigue performance of AM Ti-6Al-4V materials, there is still a need to generate more data in this area. Additionally, there is very limited information available on damage tolerance properties, such as fracture toughness and fatigue crack growth propagation. Furthermore, and more importantly, while specimen testing can provide insight into the expected performance of full-scale components, in fatigue, test coupon data is only good at estimating the life of test coupons [27]. When using fatigue properties derived from coupon testing for estimating the life of other structures, a life estimate within a factor of 2 would be exceptional and even one within an order of magnitude would not be considered abnormal. Life estimates of structures made from coupon test data should be verified by testing the actual structure, or component, of interest. Therefore, in this research, a typical aerospace component was built by AM and subjected to its design loads to validate the fatigue life trends developed by coupon testing.

Additionally, while using AM to minimize part weight is a primary motivation, manufacturing costs, and environmental impacts, must also be minimized. Post processing of AM parts, such as heat treatment, machining, and peening can all potentially improve part performance, but add to the total manufacturing cost and increase the net carbon footprint for the part. Thus, this study will also evaluate the effect of machining and peening on fatigue performance to try and gain an understanding of the cost versus benefit trade off for post processing AM titanium parts. Heat treatment was not used in this research since the AM process used, EBM, is conducted in a high temperature build chamber that effectively stress relieves the parts during build. Metallography, static properties, residual stress, fracture toughness, and crack growth behavior were also evaluated.

2 Experimental Setup and Procedure

All test specimens and parts were produced by EBM on an ARCAM A1 machine [24]. This machine builds up components by selectively melting layers, 700 μm in thickness, of titanium powder using an electron beam with power ranging from 50 to 3500 W with a spot size of 0.2–1.0 mm and a beam speed of 3 m/s. All processing was done in a vacuum chamber ($<1 \times 10^{-4}$ bar) at elevated temperature (700 °C) to minimize residual stresses during solidification and cooling of the melted layers. The exact processing

parameters were identified by the Boeing Company via a trial-and-error basis starting from the machine manufacturers recommended conditions to achieve optimal results. However, these exact processing conditions remain proprietary. The titanium powder material used in this study was a Ti-6Al-4V powder produced by plasma rotation electrode process (PREP). This produces powder with a spherical shape ranging between 100 and 300 μm in size.

Since parts are made in an elevated temperature build chamber to minimize residual stresses, specimens were not heat treated after depositing. While heat treating, either stress relief or hot isostatic pressing, after deposition could further stress relieve the parts and/or consolidate the materials, it was desired to test the specimens in the as-deposited condition since post processing such as this would add cost to the manufacturing process that may make AM cost prohibitive. Residual stress measurements would be made to ensure adequate levels of residual stresses were being achieved without post build heat treatment.

A variety of specimens were produced on the ARCAM machine for this study. At this point it is important to define the orientation of the specimens built. The base, horizontal plane, of the build chamber can be defined as the x and y directions of a Cartesian coordinate system, Fig. 2. The depth, or vertical dimension, of the build chamber is then in the z direction. With the ARCAM machine, the beam traverse direction rotates 90 deg with respect to the beam traversing direction after every layer. This negates any build orientation directional differences between the two horizontal directions, x and y , of the build chamber. Thus, rather than needing to build specimens in both the x and y directions to determine potential property variations due to orientation, only one set of horizontal specimens would be needed. Specimens built in the vertical, z direction would still be needed for comparison to those built in the horizontal directions.

Small cubes were built for metallographic analysis. These cubes were 10 mm × 10 mm × 10 mm in size. Samples were sectioned and mounted so that the microstructure of the materials could be examined with respect to all three build orientation directions, normal to the x - y , y - z , and z - x planes. After mounting, specimens were polished, etched, and photographed under high magnification. This metallographic analysis would provide insight into the build process and resulting mechanical properties.

Since it is desired to minimize manufacturing costs by avoiding a post build heat treatment and rely solely on the elevated build chamber temperatures to minimize residual stresses, it is necessary to measure the resulting as-built residual stresses. A 100 mm × 100 mm part in the horizontal plane of the build chamber was made with a thickness of 12 mm in the vertical direction. Residual stress measurements were made at the center of these samples on both the top and bottom sides at nominal depths of 13, 25, 51, 76, 127, 178, and 254×10^{-3} mm using X-ray diffraction in accordance with SAE HS-784.

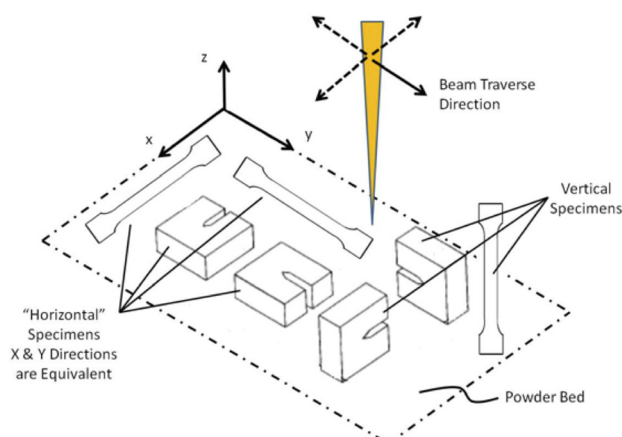


Fig. 2 Schematic of specimen orientation in machine

In this study 10 tensile specimens, were built to net shape, meaning no post process machining would be performed. Half were made in the horizontal orientation where the length and width directions of the specimens corresponded to the x and y directions of the build chamber with the thickness direction of the specimen in the vertical direction of the chamber. The other half of the specimens were built in the vertical direction, with the lengthwise direction of the specimens being in the vertical, z, direction of the chamber. All specimen dimensions (flat bar) and test conditions were in accordance with ASTM E 8. The overall dimensions of the tensile specimens produced were 200 mm in length, 20 mm wide, and 6 mm thick. In each test, the yield and ultimate strengths were recorded in addition to the elongation to failure. A clip on extensometer was used to measure elongation of the specimen gage section through failure.

Fracture toughness compact tension, (CT), specimens were fabricated per ASTM E 399 with $B = 40$ mm and $W = 80$ mm. 100 mm \times 100 mm \times 50 mm blocks were deposited and the CT specimens were then machined to net dimensions as opposed to building the CT specimens with the notch and loading pin holes directly during the AM process so that critical specimen dimensions could be controlled closely by precision machining. Five specimens were built in both the horizontal and vertical orientations, where the loading direction of the CT specimen corresponds to the indicated build orientation. The crack is then perpendicular to the specified build orientation.

Fatigue crack growth tests were performed per ASTM E647. For this test a standard CT specimen was used with the dimensions $W = 101.6$ mm and $B = 19.05$ mm. 125 mm \times 125 mm \times 25 mm blocks were deposited and then machined to the net specimen. Paris Law Region II testing was performed at a frequency of 10 Hz and a load ratio of $R = 0.1$ at constant load amplitude (increasing ΔK). Electric potential drop method was used to monitor the crack growth and the crack length measurement was verified using periodic optical measurements. Five specimens were built in both the horizontal and vertical orientations, where the loading direction of the CT specimen corresponds to the indicated build orientation. The crack is then perpendicular to the specified build orientation.

High cycle fatigue (HCF) specimens were made in a wide variety of conditions. Flat bar, low K_t (1.0), fatigue specimens were made in the vertical and horizontal orientations of the build chamber. Specimens were built via AM directly to net dimensions as well as machined to net dimensions from 250 mm long \times 40 mm wide \times 8 mm thick bars produced by AM to assess the difference in as-built surface finish and a machined finish. The final overall dimensions of the fatigue specimens were 200 mm long \times 30 mm wide \times 6 mm thick. Furthermore, in many fatigue critical applications titanium components are peened to induce compressive residual stresses at the surface and suppress fatigue crack initiation. Thus, some of the fatigue specimens machined to the net shape were also peened with 0.006 A intensity and 100% coverage. Five samples were made in each condition (as-built, machined, machined & peened) and orientation (horizontal and vertical) combination. Each specimen was tested at different constant maximum stress level, from 100 to 600 MPa, to failure in order to generate a rough S-N curve for that given condition/orientation. Testing of the samples was carried out per ASTM E466-07 at a frequency of 20 Hz and a load ratio of $R = -0.2$.

Typical bracket type parts were selected to be built and tested in fatigue to validate the results of the specimen tests for this study. Components were tested in both the as-built and machined conditions. Figure 3 shows the as-built part tested along with a component that was deposited with excess and subsequently machined to the net shape dimensions. Testing of the weight optimized design, Fig. 1(b), was not included in this particular study.

After fabrication, these test components were then drilled and fastened to a fixture, Fig. 4, designed to mimic the design loads for this component. Design loads and fastener requirements were provided by the project sponsor, but details remain proprietary.

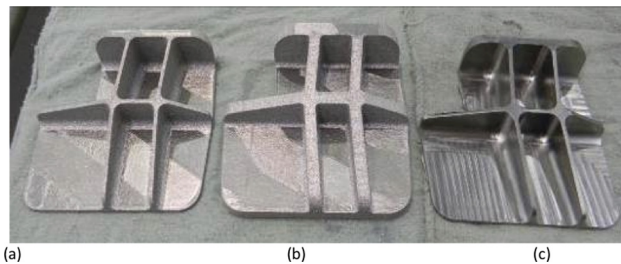


Fig. 3 Ti-6Al-4V egg crate/bracket prototype parts. (a) As-deposited, (b) deposited with excess, and (c) machined.



Fig. 4 Component fatigue test setup

All components were subjected to the design loads at a load ratio of $R = -0.39$ for $2 \times$ lifetimes (defined as 500,000 cycles). If the components survived $2 \times$ lifetimes at the design loads, the load was doubled and the parts were cycled for another lifetime. If failure still had not occurred after the double design load phase, the parts were then statically loaded to failure. The tests were carried out at room temperature and at a 10 Hz frequency.

3 Results

A 3D metallographic image of the Ti-6Al-4V material produced by EBM and a higher magnification image of the y-z plane orientation microstructure are given in Fig. 5. As expected, a transformed beta structure is observed as a result of solidification from the molten state. A columnar, or epitaxial, prior beta grain structure is also seen. These columnar grains point upward, in the z-direction, in the build and the columnar grains are continuous across multiple build layers. It is expected that this directionally dependent microstructure will result in anisotropic mechanical properties. Some small porosity was also observed.

Figure 6 shows a cross section of an as-deposited sample at the surface. This clearly highlights the as-built surface condition, which would be expected to result in poor high cycle fatigue performance due to the roughness and large number of potential crack initiation sites. This rough surface will likely have to be machined away for any part that would be subjected to fatigue loading, which will add to manufacturing costs. Machining complex part shapes produced by AM could even result in higher costs

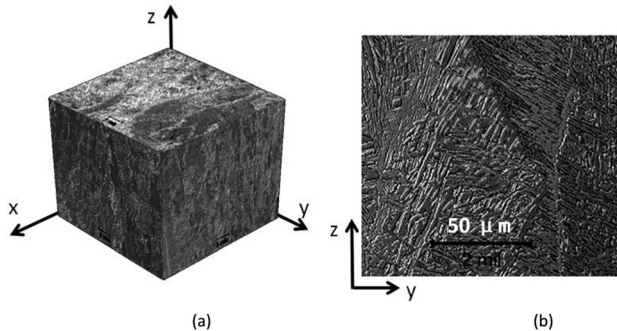


Fig. 5 (a) Microstructure cube and (b) high magnification microstructure of y-z plane

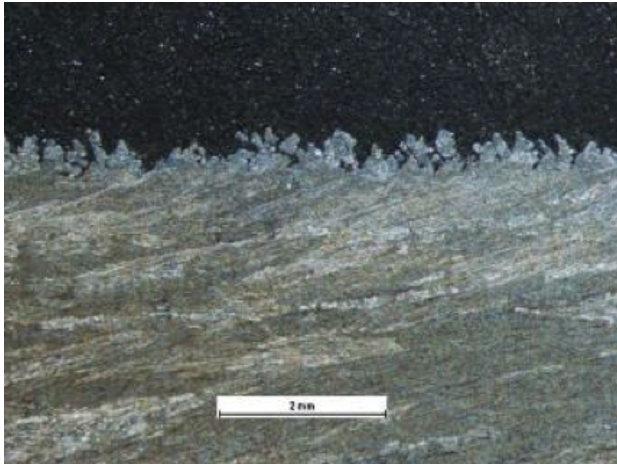


Fig. 6 Cross section at the surface of an ARCAM sample showing typical surface condition

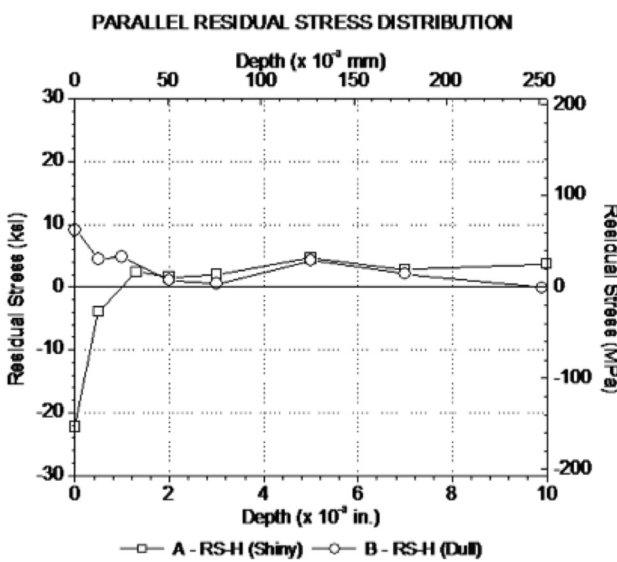


Fig. 7 Residual stress measurements in the x-direction as a function of depth taken from the top (a) and bottom (b) of EBM part

compared to machining from wrought material, unless the AM part geometry is so complex machining from wrought becomes impossible.

Residual stress measurements taken from the top and bottom of 100 mm × 100 mm × 12 mm thick specimens are given in Fig. 7.



Fig. 8 Fracture toughness specimen fracture surface

These results show that there are compressive residual stresses at the bottom of the sample and tensile stresses on the top of the part. Compressive residual stresses would be beneficial in fatigue while tensile stresses would be detrimental. After approximately 0.03 mm into the specimen, on both sides, the residual stresses reduce to nearly zero. Thus, for parts that are machined, residual stress should have a negligible effect on performance. This illustrates that the elevated build temperature used in the EBM process is effective at minimizing residual stresses and avoiding a mandatory post build stress relief.

Tensile properties for the specimens built in the horizontal and vertical orientations are given in Table 1. Both average values and standard deviations are given for the limited number of tensile specimens tested. In both orientations, the strength and elongations are lower than handbook values for wrought Ti-6Al-4V [25].

3.1 Fracture Toughness. The apparent fracture toughness values for both the horizontal and vertical orientations are given in Table 2. Values are given for both the average and standard deviation for the population of specimens tested in each

Table 1 Tensile properties

Orientation	UTS (MPa)		0.2% YS (MPa)		Elong %	
	Ave	Stdev	Ave	Stdev	Ave	Stdev
Horizontal	833	22	783	15	2.7	0.4
Vertical	851	19	812	12	3.6	0.9

Table 2 Fracture toughness properties

Orientation	Kq (MPa \sqrt{m})	
	Ave	Stdev
Horizontal	110	8.9
Vertical	102	7.4

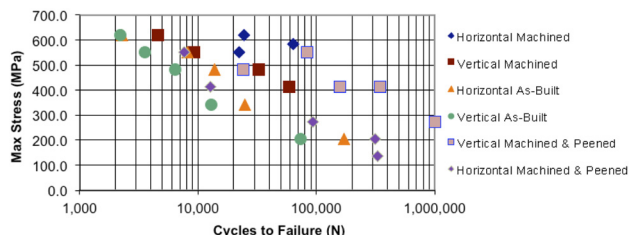


Fig. 9 Fatigue results $R = -0.2$, $K_t = 1.0$

orientation. For annealed Ti-6Al-4V, the fracture toughness is on the order of 66 MPa \sqrt{m} [25], thus these AM parts have superior fracture toughness. This is likely related to the coarse grained acicular alpha microstructure when compared to standard Ti-6Al-4V plate fine equiaxed structure. Apparent fracture toughness (K_q (MPa \sqrt{m}) is reported as opposed to K_{ic} due to a failed specimen geometry validity check. Predicating the correct fracture toughness specimen size is difficult as it depends on the yield strength. These tests resulted in higher fracture toughness and lower strengths than expected, which led to the invalid result. Thicker specimens ($W = 120$ mm and $B = 60$ mm) would likely be needed for a valid result.

A typical fracture surface is given in Fig. 8. Some porosity was observed on this fracture surface. While small porosity is not expected to have a large influence on the fracture toughness, it will be an issue in fatigue.

3.2 High Cycle Fatigue. The results of the fatigue testing are shown in Fig. 9 on a plot of maximum applied stress versus number of cycles to failure. Two specimen build orientations, vertical and horizontal, are given along with three different conditions, as-built, machined and machined then peened. Compared to wrought Ti-6Al-4V, which has a fatigue strength of approximately 750 MPa at 100,000 cycles [25] all build orientations and conditions have significantly lower fatigue strengths. Peening of the vertical build orientation specimens provided a noticeable improvement in fatigue strength at higher cycles, but this improvement was not seen on the horizontal peened specimens.

Fracture surface evaluation of the fatigue specimens in the as-deposited (net), machined and peened conditions for both build orientations are given in Fig. 10. The net specimens highlight the rough as-built surface finish that leads to multisite crack initiation and virtually no stable crack growth behavior before final fracture. In the machined condition, internal porosity was brought to the surface during machining, which then acted as the crack initiation

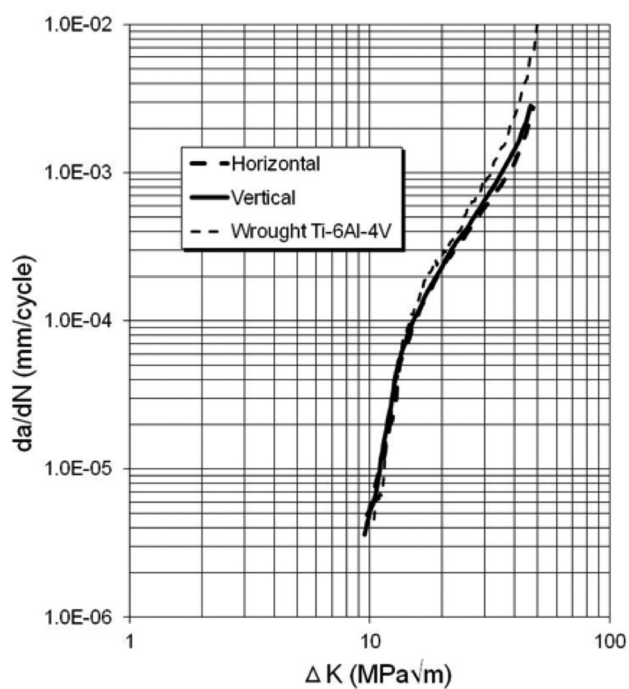


Fig. 11 Fatigue crack growth rate results $R = 0.1$

site instead of the rough surface finish. This is why no significant difference was observed between the as-deposited and machined conditions. By peening, the induced compressive residual stresses drove crack initiation to a sub-surface porosity defect for the vertical build specimens. However, for the horizontal specimen, it appears that a crack still initiated at near surface porosity.

3.3 Crack Growth. Fatigue crack growth curves for the Horizontal and Vertical orientation specimens are given in Fig. 11 along with base metal data obtained from a previous study [26] for comparison. The AM specimens in both orientations displayed essentially equivalent behavior with respect to each other. This indicates that there is no noticeable difference in crack growth rates as a function of specimen, crack, or loading orientation. Compared to wrought material, the additive parts behave similarly in the Region I, the threshold region. However, in Region II, the Paris Law Region, the additive curves deviate slightly from the wrought curve. The additive materials actually exhibit slower

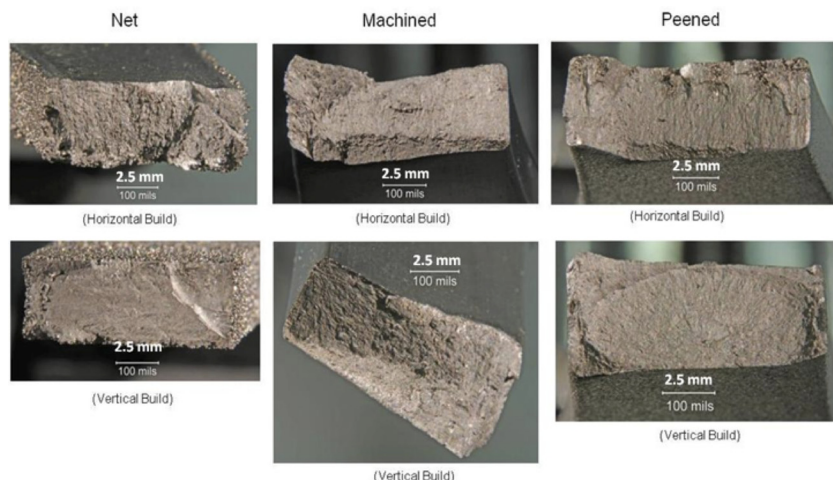


Fig. 10 ARCAM fatigue specimen fracture surfaces

crack growth rates for a given ΔK in Region II and as the crack load combinations, or ΔK , approach the point of instability and eventual fracture in Region III.

In the component testing of both the net shape and fully machined conditions, no parts failed at the design load before two lifetimes (500,000 cycles) were reached. When loads were doubled and the parts were cycled for another lifetime (250,000 cycles), they either still did not fail or failure occurred in the fasteners, Fig. 12. In one of the net shape parts, a fastener failed at 177 k cycles in the double design loading phase. This fastener was replaced and testing continued, but this same fastener failed again after an additional 32 k cycles. This fastener was replaced two more times, lasting 26 k and 19 k cycles each time, respectively. At this point, it was noticed that a crack had begun to form at this fastener hole, Fig. 12(b), and the testing was stopped. This was the only component tested where any kind of part failure was observed. It is expected that the number of cycles the replaced fastener lasted continued to decrease because the crack at the hole was growing throughout this process, which allowed the part to become more compliant and lead to more and more deflection of the fastener as the testing continued and the crack grew.

Several of the parts, both net and machined, which survived both the single and double design load testing for a total of three lifetimes (750,000 cycles) with no fastener failures, were then subjected to monotonic static loading to failure. In all of these static tests, failure occurred in the fasteners and not the parts. This component testing, both fatigue and static, suggest that even though the performance of Ti-6Al-4V AM materials was found to be lower than wrought material via specimen testing, fasteners are more susceptible to failure in structural component testing than the actual AM parts.

4 Discussion

The primary focus of this study was to evaluate the fatigue performance of Ti-6Al-4V materials produced by additive manufacturing with standard test specimens and to validate the applicability of the results to the fatigue performance of actual components. It was found that fatigue performance of the Ti-6Al-4V specimens was significantly reduced, on the order of 80%, compared to wrought material regardless of the condition (net, machined, and peened). In previously published research [7,8,20–22], it was found that the fatigue performance of Ti-6Al-4V AM materials could be equivalent to wrought material when porosity is avoided, the rough as-built surface condition is removed and, in the case of non EBM process, heat-treated. For this study, the fatigue life was limited by the rough surface in the net condition and then the sub-surface porosity in the machined and peened conditions. Peening was shown to improve the fatigue life in some specimens, but porosity defects present generally negated any benefit provided by peening in this set of experiments. If the porosity could be eliminated and the surfaces

machined, it is expected that the fatigue performance would increase to similar levels as seen by previous researchers.

The tensile properties (strength and elongation) reported here were lower than handbook values [25,27] for wrought material and other published studies [3,12,20] on the static properties of AM Ti materials. However, in this case, all tensile specimens were tested in the as-deposited condition. There was no post process machining, stress relief or HIP. In most all of the previous studies [3,10–14] tensile specimens were machined prior to testing. It is possible that the porosity, as-deposited surface finish and residual stresses may have all contributed to this difference. This highlights the importance of testing specimens in the same condition that parts will be used in. If it is desired to use AM parts in the as-built state to minimize weight and cost, tensile data from fully machined specimens could be misleading.

The fracture toughness of the AM materials tested in this study was consistent and/or superior to handbook values of 44–66 MPa m^{0.5} for wrought and 88–110 MPa m^{0.5} for transformed (cast type) Ti-6Al-4V [27,25]. This is attributed to the large, coarse grained, microstructure of the AM materials compared to the fine, equiaxed (wrought) material. With respect to crack growth, the AM materials had equivalent Region I and slightly improved Region II da/dN behavior compared to wrought material. The fatigue crack growth results obtained are consistent with that of the data on cast versus wrought titanium alloys published in Ref. 25 [p. 565]. Thus, for fracture and damage tolerant driven designs, AM appears to be a viable candidate manufacturing process. It should be noted that the porosity defects that degraded the fatigue properties had no noticeable effect on the fracture toughness or crack growth behavior.

This study also evaluated the microstructure and residual stress in Ti-6Al-4V AM materials. The observed microstructure was consistent with previous studies [12,13], consisting of columnar prior beta grains containing lamellar alpha laths that span multiple build layers. The directionality of the microstructure was expected to result in anisotropic material behavior. However, static strengths were less than 4% different between the horizontal and vertical direction. The elongation difference between these two directions was 25%, but this only corresponded to a 1% difference in measured elongation. For fracture toughness, there was a 7% difference between the two build orientations. There was no quantifiable difference between the build orientations seen in the fatigue or crack growth testing. Overall, the differences in properties with build orientation did not appear to be significant, but only a limited number of specimens were tested, so more tests would be required to obtain a more statistically meaningful comparison. Moreover, additional testing is required to provide statistically meaningful to all of the results presented here.

Residual stress measurements showed that there were small amounts of compressive and tensile residual stresses on as-deposited parts, but the depths of these stresses were shallow. After approximately 760 μm the residual stresses essentially went

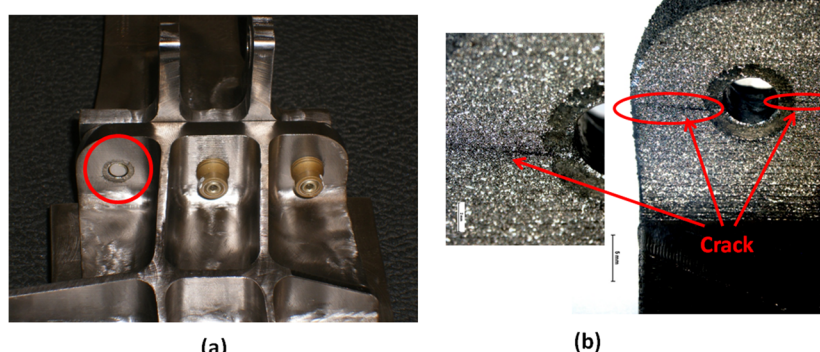


Fig. 12 (a) Location of repeat fastener failure and (b) crack initiated under the failed fastener

to zero. Post deposition machining of the part surface would remove these surface stresses. In the as-deposited net condition the rough surface finish likely overshadowed any tensile residual stress effects. These residual stress results support the conclusion that the elevated build temperature chamber used during fabrication of these parts using the EBM process is sufficient in minimizing residual stresses. However, for AM processes that do not use an elevated build chamber temperature, residual stresses will likely be higher and require post deposition heat treatment for stress relief. Stress relief or HIP'ing may also still be needed for EBM parts to reduce porosity and modifying the microstructure to improve mechanical performance.

Even though the fatigue performance of the specimens was inferior to wrought material and, would therefore, not likely be considered for use in the fabrication of fatigue critical components, the fatigue testing of parts, both net and machined, always resulted in fastener failure before part failure. This demonstrates that using AM, or any novel process, for the fabrication of fatigue driven components shouldn't be dismissed based solely on specimen test data. An opportunity for future research would be to test a part that has been optimized for weight based on the geometric build capabilities of AM. This was not possible due to logistical constraints for this particular program.

5 Conclusions

For the Ti-6Al-4V specimens and parts produced in this study by the Electron Beam Melting Additive Manufacturing process, it was found that:

- Fracture toughness and fatigue crack growth were comparable to literature properties of wrought Ti-6Al-4V.
- Residual stresses are low due to the elevated temperature in the build chamber, which minimizes temperature gradients during local melting and solidification. Thus, post process stress relief heat treatment is not required.
- The fatigue performance was significantly lower than handbook values for wrought Ti-6Al-4V. The rough surface finish in the as-deposited net condition and porosity in the machined conditions led to the premature failures. Peening provided little benefit.
- Structural components tested under design loads, and even double the design loads, for multiple design lifetimes, did not result in the premature failures expected based on coupon testing results. This shows that for fatigue driven designs, decisions should not be made solely on coupon data and structural element testing is needed to determine if a process such as this is acceptable for a given application.

Acknowledgment

The authors of this paper would like to thank Dr. Richard Hague, Dr. Chris Tuck and everyone else who contributed to this work from the Additive Manufacturing and 3D Printing Research Group at the University of Nottingham as well as the United Kingdom's Technology Strategy Board and The Boeing Company for their support.

References

- [1] Kruth, J. P., Leu, M. C., and Nakagawa, T., 1998, "Progress in Additive Manufacturing and Rapid Prototyping," *CIRP Ann.*, **47**(2), pp. 525–540.
- [2] Levy, G. N., Schindel, R., and Kruth, J. P., 2003, "Rapid Manufacturing and Rapid Tooling With Layer Manufacturing (LM) Technologies, State of the Art and Future Perspectives," *CIRP Ann.*, **52**(2), pp. 589–609.
- [3] Murr, L. E., Esquivel, E. V., Quinones, S. A., Gaytan, S. M., Lopez, M. I., Martinez, E. Y., Medina, F., Hernandez, D. H., Martinez, E., Martinez, J. L., Stafford, S. W., Brown, D. K., Hoppe, T., Meyers, W., Lindhe, U., and Wicker, R. B., 2009, "Microstructures and Mechanical Properties of Electron Beam-Melted Ti-6Al-4V," *Mater. Charact.*, **60**, pp. 96–105.
- [4] Murr, L. E., Gaytan, S. M., Ceylan, A., Martinez, E., Martinez, J. L., Hernandez, D. H., Machado, B. I., Ramirez, D. A., Medina, F., Collins, S., and Wicker, R. B., 2010, "Characterization of Titanium Aluminide Alloy Components Fabricated by Additive Manufacturing Using Electron Beam Melting," *Acta Mater.*, **58**(5), pp. 1887–1894.
- [5] Hrabe, N., and Quinn, T., 2013, "Effects of Processing on Microstructure and Mechanical Properties of a Titanium Alloy (Ti-6Al-4V) Fabricated Using Electron Beam Melting (EBM), Part 1: Distance From Build Plate and Part Size," *Mater. Sci. Eng., A*, **537**, pp. 264–270.
- [6] Hrabe, N., and Quinn, T., 2013, "Effects of Processing on Microstructure and Mechanical Properties of a Titanium Alloy (Ti-6Al-4V) Fabricated Using Electron Beam Melting (EBM), Part 2: Energy Input, Orientation, and Location," *Mater. Sci. Eng., A*, **573**, pp. 271–277.
- [7] Faccini, L., Magalini, E., Robotti, P., and Molinari, A., 2009, "Microstructure and Mechanical Properties of Ti-6Al-4V Produced by Electron Beam Melting of Pre-Alloyed Powders," *Rapid Prototyping J.*, **15**(3), pp. 171–178.
- [8] Chan, K., Koike, M., Mason, R., and Okabe, T., 2013, "Fatigue Life of Titanium Alloys Fabricated by Additive Manufacturing Techniques for Dental Implants," *Metall. Mater. Trans. A*, **44A**, pp. 1010–1022.
- [9] Harrysson, O., Deaton, B., Bardin, J., West, H., Cansizoglu, O., Cormier, D., and Little, D. M., 2005, "Evaluation of Titanium Implant Components Directly Fabricated Through Electron Beam Melting Technology," *Adv. Mater. Process.*, **163**(7), pp. 72–77.
- [10] Parthasarathy, J., Starly, B., Raman, S., and Christensen, A., 2010, "Mechanical Evaluation of Porous Titanium (Ti6Al4V) Structures With Electron Beam Melting (EBM)," *J. Mech. Behav. Biomed. Mater.*, **3**, pp. 249–259.
- [11] Heintl, P., Rottmair, A., Körner, A., and Singer, R. F., 2007, "Cellular Titanium by Selective Electron Beam Melting," *Adv. Eng. Mater.*, **9**(5), pp. 360–364.
- [12] Koike, M., Greer, P., Owen, K., Lilly, G., Murr, L., Gaytan, S., Martinez, E., and Okabe, T., 2011, "Evaluation of Titanium Alloys Fabricated Using Rapid Prototyping Technologies—Electron Beam Melting and Laser Beam Melting," *Materials*, **4**, pp. 1776–1792.
- [13] Thijss, L., Verhaeghe, F., Craeghs, T., Humbeeck, J., and Kruth, J., 2010, "A Study of the Microstructural Evolution During Selective Laser Melting of Ti-6Al-4V," *Acta Mater.*, **58**, pp. 3303–3312.
- [14] Faccini, L., Magalini, E., Robotti, P., Molinari, A., Hoeges, S., and Wissenbach, K., 2010, "Ductility of a Ti-6 Al-4 V Alloy Produced by Selective Laser Melting of Prealloyed Powders," *Rapid Prototyping J.*, **16**, pp. 450–459.
- [15] Kobryn, P., Moore, E., and Semiatin, S., 2000, "The Effect of Laser Power and Traverse Speed on Microstructure, Porosity, and Build Height in Laser-Deposited Ti-6Al-4V," *Scr. Mater.*, **43**, pp. 299–305.
- [16] Kobryn, P., and Semiatin, S., 2001, "The Laser Additive Manufacture of Ti-6Al-4V," *JOM*, **53**, pp. 40–42.
- [17] Kelly, S., and Kampe, S., 2004, "Microstructural Evolution in Laser-Deposited Multilayer Ti-6Al-4V Builds: Part I. Microstructural Characterization," *Metall. Mater. Trans. A*, **35**, pp. 1861–1867.
- [18] Mercelis, P., and Kruth, J., 2006, "Residual Stresses in Selective Laser Sintering and Selective Laser Melting," *Rapid Prototyping J.*, **12**, pp. 254–265.
- [19] Shiomi, M., Osakada, K., Nakamura, K., Yamashita, T., and Abe, F., 2004, "Residual Stress Within Metallic Model Made by Selective Laser Melting Process," *CIRP Ann.*, **53**(1), pp. 195–198.
- [20] Leuders, S., Thone, M., Riemer, A., Niendorf, T., Troster, T., Richard, H., and Maier, J., 2013, "On the Mechanical Behavior of Titanium Alloy TiAl6V4 Manufacture by Selective Laser Melting: Fatigue Resistance and Crack Growth Performance," *Int. J. Fatigue*, **48**, pp. 300–307.
- [21] Baufeld, B., Brandl, E., and Biest, O., 2011, "Wire Based Additive Layer Manufacturing: Comparison of Microstructural and Mechanical Properties of Ti-6Al-4 V Components Fabricated by Laser-Beam Deposition and Shaped Metal Deposition," *J. Mater. Process. Technol.*, **211**, pp. 1146–1158.
- [22] Brandl, E., Baufeld, B., Leynes, C., and Gault, R., 2010, "Additive Manufactured Ti-6Al-4V Using Welding Wire: Comparisons of Laser and Arc Beam Deposition and Evaluation With Respect to Aerospace Material Specifications," *Phys. Procedia*, **5**, pp. 595–606.
- [23] Santos, E. C., Osakada, K., Shiomi, M., Kitamura, Y., and Abe, F., 2004, "Microstructure and Mechanical Properties of Pure Titanium Models Fabricated by Selective Laser Melting," *Proc. Inst. Mech. Eng., Part C: J. Mech. Eng. Sci.*, **218**(7), pp. 711–719.
- [24] Arcam AB, "The Future in Implant Manufacturing," <http://www.arcam.com/wp-content/uploads/Arcam-A1.pdf>
- [25] Boyer, R., Welsch, G., and Collings, E. W., 1994, *Materials and Properties Handbook Titanium Alloys*, ASM International, Materials Park, OH, pp. 517–548.
- [26] Edwards, P., Petersen, M., Ramulu, M., and Boyer, R., 2010, "Mechanical Performance of Heat Treated Ti-6Al-4V Friction Stir Welds," *Key Eng. Mater.*, **436**, pp. 213–221.
- [27] Cameron, D. W., and Hoepplner, D. W., 1996, "Fatigue Properties in Engineering," *ASM Handbook: Fatigue and Fracture*, ASM International, Materials Park, OH, Vol. 19, p. 15.

SELECTIVE LASER MELTING OF BIOCOMPATIBLE METALS FOR RAPID MANUFACTURING OF MEDICAL PARTS

Ben Vandenbroucke, Jean-Pierre Kruth

Division PMA, Department of Mechanical Engineering,
Katholieke Universiteit Leuven, Belgium

Reviewed, accepted September 14, 2006

Abstract

In recent years, digitizing and automation have gained an important place in fabrication of medical parts. Rapid Manufacturing could be very suitable for medical applications due to their complex geometry, low volume and strong individualization. The presented study investigates the possibility to produce medical or dental parts by Selective Laser Melting (SLM). The SLM-process is optimized and fully characterized for two biocompatible metal alloys: TiAl₆V₄ and CoCrMo. This paper reports on mechanical and chemical properties and discusses geometrical feasibility including accuracy and surface roughness. The potential of SLM as medical manufacturing technique is proved by a developed procedure to fabricate frameworks for complex dental prostheses.

Introduction

Over the last decade Reverse Engineering, Computer-Aided Design, Computer-Aided Manufacturing and Rapid Prototyping (RE, CAD, CAM, RP) have been employed in medicine and dentistry [1]. Diagnostic tools have become increasingly more sophisticated and medical imaging technology can now present patient data with high precision. Virtual planning environments allow data visualization and manipulation. With RP there came a way to produce custom physical models of patient anatomy providing doctors the means for tactile interaction which facilitates preoperative planning of complex surgeries. In addition, RP-generated replicas act often as basis for customization of treatment devices such as craniofacial plates. RP-techniques are also used to create custom treatment aides such as dental drilling guides that transfer the digital planning to the patient in a reliable way. Because of technical improvements of Layer Manufacturing (LM) processes and due to the possibility to process all kind of metals Rapid Prototyping evolved to Rapid Manufacturing (RM) in recent years [2, 3]. Medical and dental applications could take advantage of this evolution by using LM techniques not only for plastic devices like visual anatomical models or one-time surgical guides, but also for functional implants or prostheses with long-term consistency made from a biocompatible metal.

This paper discusses the use of Selective Laser Melting (SLM) as RM technique for medical applications. SLM is a layer-wise material addition technique that allows generating complex 3D parts by selectively melting successive layers of metal powder on top of each other, using the thermal energy supplied by a focused and computer controlled laser beam [4, 5]. Medical and dental applications are very suitable to be produced by SLM due to their complex geometry, strong individualization and high aggregate price. Moreover, the manufacturing of multiple unique parts in a single production run enables mass customization.

To turn SLM into a manufacturing technique for implants or prostheses, some important conditions have to be fulfilled. The laser melted parts have to meet strict material requirements regarding mechanical and chemical properties and the process must guarantee high accuracy and appropriate surface roughness. In this study the SLM process is optimized and fully characterized according to these requirements for two biocompatible metal alloys, TiAl₆V₄ and CoCrMo. A dental prosthesis produced by SLM shows the potential of SLM as a medical manufacturing technique.

Materials and methods

In this study all test samples used to characterize the SLM process are produced on a M3 Linear machine from the German company Concept Laser GmbH. This machine is equipped with a diode-pumped Nd:YAG laser with beam spot size of 200 µm and maximum power of 95 W on the building platform. Two bio-metals are studied: a titanium alloy (Ti 90%, Al 6%, V 4%) and a cobalt-chromium alloy (Co 63%, Cr 29.53%, Mo 5%, Si 1%, Mn 0.5%, Fe 0.5%, N 0.3%, C 0.17%). Titanium and its alloys are used for many implants because of their high biocompatibility and high strength to weight ratio. For long time cobalt-chromium alloys are key materials for dentistry and nowadays they are also used for high-strength hip replacements and cardiovascular devices because of their high corrosion and fatigue resistance. The used titanium material is a commercial powder and the cobalt-chromium powder is made in house by IGAP (Induction melting Gas Atomization Process), which leads to spherical particles with very low amount of interstitial impurities. Fig. 1 shows the grain size distribution of both powders, determined by laser diffraction (Coulter analysis), and SEM micrographs indicate the morphology. Because of high reactivity of titanium to interstitial elements such as oxygen, nitrogen, carbon and hydrogen, the SLM process is carried out in a closed chamber continuously flushed with argon gas to reduce the oxygen level below 0.1%. Cobalt-chromium is processed in a nitrogen environment. A titanium base plate is used for titanium and a steel base plate for cobalt-chromium.

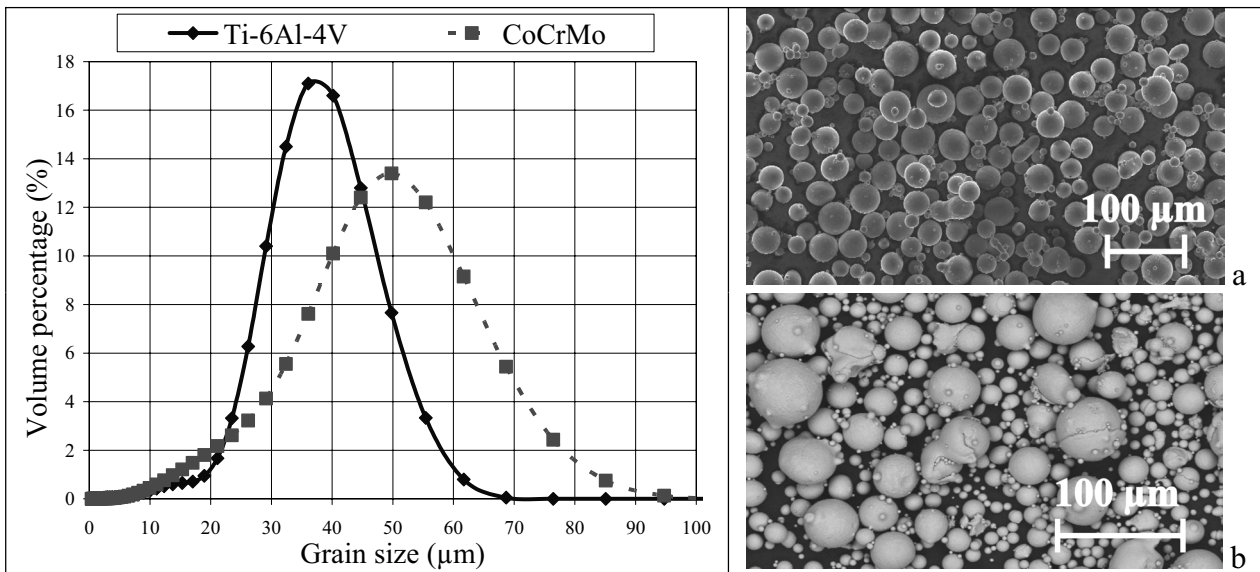


Fig. 1: Grain size distribution and micrographs of titanium (a) and cobalt-chromium (b) powder.

SLM is a complex thermo-physical process which depends on a lot of material, laser, scan and environmental parameters. For both selected materials, a parameter study has been performed to optimize the process regarding part density, since porosity has a harmful effect on the mechanical properties of the part. Four main process parameters are selected for experimentation: laser power, layer thickness, scan speed and hatching space. These factors determine the energy supplied by the laser beam to a volumetric unit of powder material, defined as energy density, an experimental quantity which has large influence on part density:

$$E_{density} = \frac{P_{laser}}{v_{scan} \cdot s_{hatching} \cdot t_{layer}}$$

where $E_{density}$ = energy density, P_{laser} = laser power, v_{scan} = scan speed, $s_{hatching}$ = hatching space, t_{layer} = layer thickness. Part density is measured according to the Archimedes principle by weighing the samples in air and subsequently in ethanol to measure the volume. A coating with lacquer avoids absorption of ethanol by the specimen. The density of the sample can be calculated based on the mass of the solid, the mass of the lacquer, the mass of the coated sample in ethanol, the density of ethanol and the density of the lacquer. Micrographs are taken and help to understand the presence and size of pores. All further tests characterizing the SLM process are performed with process parameters optimized for part density.

Specimens fabricated by SLM of TiAl₆V₄ are tested for their mechanical properties such as hardness, strength, stiffness and ductility to compare with values of bulk material from literature. Micro and macro hardness are measured on a universal testing machine using a Vickers indentation with a load of 100 g and 10 kg respectively. Each sample is measured on 10 different locations by indenting each time for 30 seconds. Mean and variance are calculated using a confidence limit of 95%. To investigate the influence of energy density, hardness is compared for samples produced with different process parameters. Tensile tests and three point bending tests are carried out using an Instron 4505 machine, according to the ASTM E 8M and ASTM B 528-83a standard respectively. For both tests four specimens, produced with optimized process parameters, are tested to check repeatability. Young's modulus, tensile and bending yield strength, ultimate tensile and bending strength and elongation at fracture are determined. Using the Grindo-Sonic system, the impulse excitation technique is employed to measure stiffness of two SLM samples produced with optimized process parameters. Young's and shear modulus are measured for a beam-shaped sample (40 x 12 x 4 mm³) and for a disc-shaped sample (Ø25 x 4 mm³), according to the ASTM E 1876-99 standard.

Both selected materials, TiAl₆V₄ and CoCrMo, are tested for their chemical properties. The corrosion behavior is of high interest to value biocompatibility. Both alloys are considered as corrosion resistant and biocompatible materials for dental implants or prostheses. Nevertheless, the very complex chemistry of the oral cavity may reveal surprises concerning corrosion processes. The corrosion characteristics are examined by static immersion tests according to the DIN EN ISO 10271 standard. Test specimens are stored in a corrosion solution (sodium chloride and lactic acid, each 0.1 mol/l with a pH value of 2.3) for 14 days. The solutions are exchanged after 1, 2, 7 and 14 days and analyzed by ICP-OES (Inductively Coupled Plasma-Optic Emission Spectrometry analysis) to determine the different ion emissions in function of time. Influence of manufacturing on corrosion behavior is investigated by comparing the emissions of five different cases, shown in Table 1. Each case differs regarding material (titanium / cobalt-chromium alloy) or production technique (SLM / milling / casting). For each case two series of two specimens are

tested. One series contains specimens blasted by glass beads or by compressed air and the other series contains specimens ground to a metallic gloss finish with 1200 particle silicon carbide paper. The blasted samples are more relevant but the ground samples should show smaller variance [6]. This experimental set-up leads to 80 solutions: 20 samples x 4 solutions/sample (after 1, 2, 7 and 14 days). Each solution is analyzed for ion emission of all relevant elements (see Table 1) and for each element the mean ion emission is calculated based on three ICP-OES measurements. As a result, corrosion rate of different elements in function of time can be discussed depending on material, manufacturing and finishing of the specimens.

Material	Manufacturing	Finishing	Number of samples	Relevant elements
TiAl ₆ V ₄	SLM	Blasted (glass)	2	Ti / Al / V / Fe
		Ground	2	
Cp Ti grade 2	Milling*	Blasted (air)	2	Ti / Fe
		Ground	2	
Cp Ti grade 1	Casting*	Blasted (air)	2	Ti / Fe
		Ground	2	
CoCrMo	SLM	Blasted (glass)	2	Co / Cr / Mo
		Ground	2	
CoCrMo	Casting*	Blasted (air)	2	Co / Cr / Mo
		Ground	2	

Table 1: Experimental set-up of specimens for corrosion tests (* produced in dental laboratory by standard methods).

Since the relatively high surface roughness of SLM parts could be an important drawback for some applications, a profound roughness analysis has been performed. The surface roughness depends on many factors: material, powder particle size, layer thickness, laser and scan parameters, scan strategy and surface post-treatment. Because of the stair effect due to the layer-wise production, surface roughness of a sloping plane depends on the sloping angle. In addition, roughness of top surfaces differs strongly from roughness of bottom surfaces. This paper discusses the influence of material, surface post-treatment, layer thickness, sloping angle and the difference between top and bottom surface. For both selected materials, three series of two blocks ($12 \times 12 \times 12 \text{ mm}^3$) are made by SLM with optimized process parameters. Each series differs for surface post-treatment. The first series contains samples as processed by SLM, the second series consists of samples blasted by glass beads and the third series contains samples post-treated by ultrasonic ceramic filing. For each sample the roughness of top and two side surfaces is measured along different directions as indicated on Fig. 2a. A benchmark model (Fig. 2b) is developed to test the influence of sloping angle and the difference between top and bottom surfaces. This benchmark contains top planes with sloping angle ranging from 0° to 90° and bottom planes with sloping angle ranging from 30° to 90° . For horizontal holes the sloping angle changes continuously. The benchmark is produced three times with layer thickness of $30 \mu\text{m}$. After glass blasting, the roughness of each sloping plane is measured on three line tracks. Similar benchmarks are produced and analyzed with higher and lower layer thickness ($50 \mu\text{m}$ – $20 \mu\text{m}$). All surface roughness tests are performed on a Taylor Hobson Form Talysurf and mean R_a and R_z values are calculated with a cut-off length of 2.5 mm, according to the DIN 4768 standard.

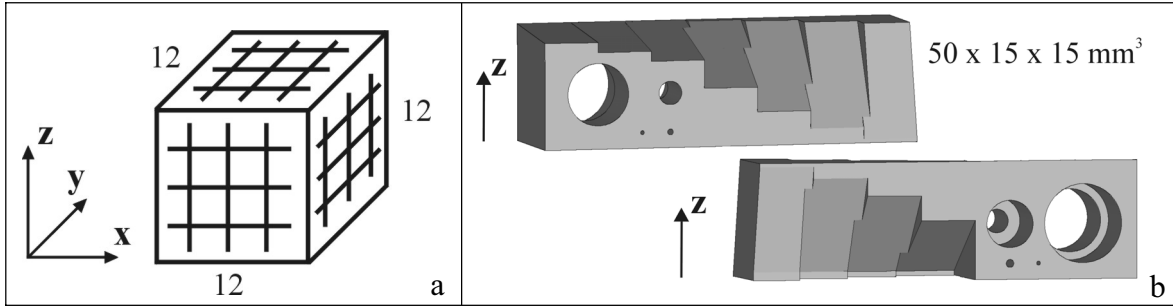


Fig. 2: (a) Indication of surface roughness measurements on blocks; (b) Benchmark model with different sloping angles for top and bottom planes (up: front view, down: back view).

To characterize SLM with regard to process accuracy and feasibility two benchmarks are designed, shown on Fig. 3. Both benchmarks are produced by SLM of TiAl₆V₄ and after glass blasting and ultrasonic ceramic filing, dimensional analyses are performed to find out feasible precision. These benchmarks are not only used to characterize the process limitations, but also to optimize process parameters iteratively. Offset and scaling factors, used to compensate for dimensional changes due to the laser beam spot size and for thermal distortions due to successive melting and resolidification, are optimized based on a few loops of benchmark tests. The first benchmark model (Fig. 3a) is used to find out process accuracy in x-, y- and z-direction and to measure the accuracy of cylinders and angled features. The presence of the thin plane with a thickness of 2 mm can indicate warpage due to thermal stresses. The second benchmark model (Fig. 3b) is developed to check the feasible precision and resolution of the process by small holes (ranging from 0.5 to 3 mm diameter), small slots (ranging from 0.5 to 3 mm thickness), small cylinders (ranging from 1 to 5 mm diameter) and thin walls (ranging from 0.5 to 3 mm thickness). Sharp edges with angles from 15° to 45° are added to the benchmark to test the influence of heat accumulation at the angle tips. All geometrical features of both produced benchmarks are measured three times by tactile probes on a NC 3D coordinate measurement machine, except for the smallest details which are measured on an optical micro-measurement machine.

Next to fulfilling the requirements on mechanical, chemical and geometrical properties, the breakthrough of SLM as a medical Rapid Manufacturing technique will depend on reliability, performance and economical aspects like production time and cost. These factors can not be characterized in general but will be investigated in this paper for the dental application.

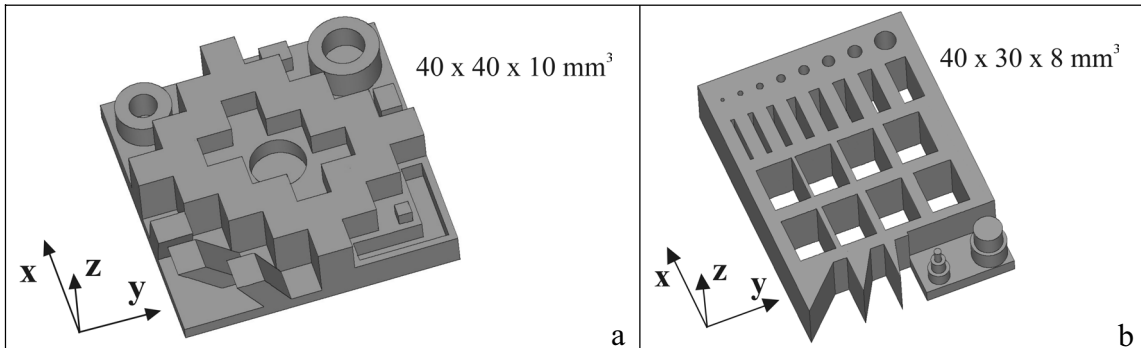


Fig. 3: (a) Benchmark to test process accuracy; (b) Benchmark to test feasibility of small details.

Results and discussion

By experience on SLM tests with other materials [7] and based on the physical properties of TiAl₆V₄, a rough estimation is made for the energy density needed to process the titanium alloy. Following parameter study optimizes this process more in detail to minimize porosity. Laser power and layer thickness are kept constant and scan speed and hatching space are varied. The laser is set at maximum power which corresponds with 95 W on the building platform. A layer thickness of 30 µm is used because of a mean particle size of 37 µm and a powder density of around 60%. Three settings of scan speed (90, 140, 190 mm/sec) combined with three settings of hatching space (100, 120, 140 µm) lead to an experimental set-up of nine cases. With a beam spot size of 200 µm the different hatching space settings correspond with different overlap settings of 50%, 40% and 30% respectively. Fig. 4 summarizes the outcome of this parameter study for titanium. For the three samples with a hatching space of 100 µm (overlap of 50%) the building process has been stopped because of too high top surface roughness leading to powder depositing problems. The other six samples are built successfully. For each case Fig. 4 indicates the measured part density and shows one micrograph proving porosity. The height of the vertical bar corresponds with the used energy density. Higher energy density leads to higher part density. For low energy input, successive scan tracks are not fully molten and large pores appear along the scan lines. Balancing part density versus process speed, a compromise is made leading to optimal process parameters: scan speed of 125 mm/sec and hatching space of 130 µm (35% overlap). With these parameters three samples are produced all leading to part density higher than 99.8%. For cobalt-chromium a similar parameter study has been performed. Table 2 shows the resulting optimal parameters compared with those for titanium. Because of physical properties of the material the process is easier to control for cobalt-chromium and higher part density is reached with higher build rate.

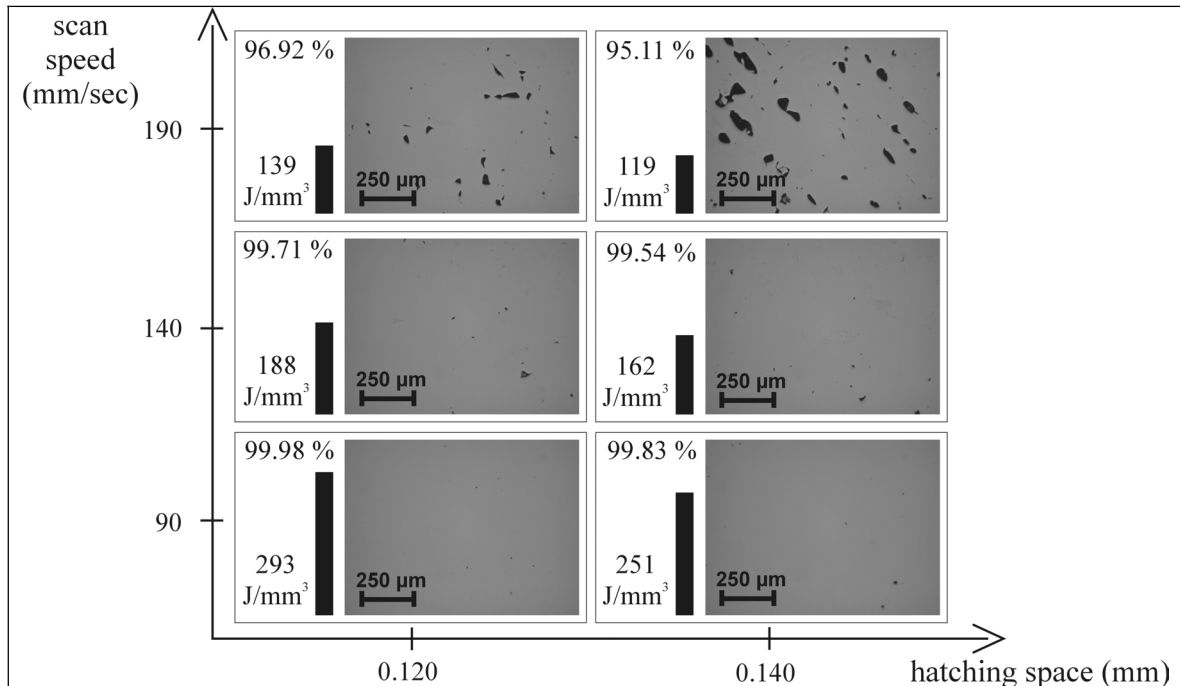


Fig. 4: Results of parameter study for TiAl₆V₄. Used energy density, measured part density and one micrograph are shown for each case.

Material	TiAl ₆ V ₄	CoCrMo
Melting temperature (°C)	1650	1330
Laser power (W)	95	95
Layer thickness (μm)	30	40
Scan speed (mm/sec)	125	200
Hatching space (μm)	130	140
Overlap (%)	35	30
Energy density (J/mm ³)	195	85
Build rate (cm ³ /h)	1.8	4.0
Part density (%)	> 99.8	> 99.9

Table 2: Optimized process parameters regarding part density and process speed for titanium and cobalt-chromium.

Fig. 5 shows the results of the hardness analysis for four titanium samples produced with different energy density. The circled measurement points correspond with the micro and macro hardness of the sample produced with optimized process parameters. The measured part density is indicated for each sample. Hardness increases with increasing energy density because of decreasing porosity. Because micro hardness is measured if possible at pore-free regions, micro hardness does not vary significantly for samples with part density higher than 99%. Since macro hardness is more dependent on porosity, the measured values are lower than those for micro hardness and energy density has a larger influence. Hardness values of bulk material from literature vary from 340 HV to 395 HV depending on thermal treatment. The hardness of SLM samples is higher, because during the process the melt pool cools down very rapidly when the laser beam has passed.

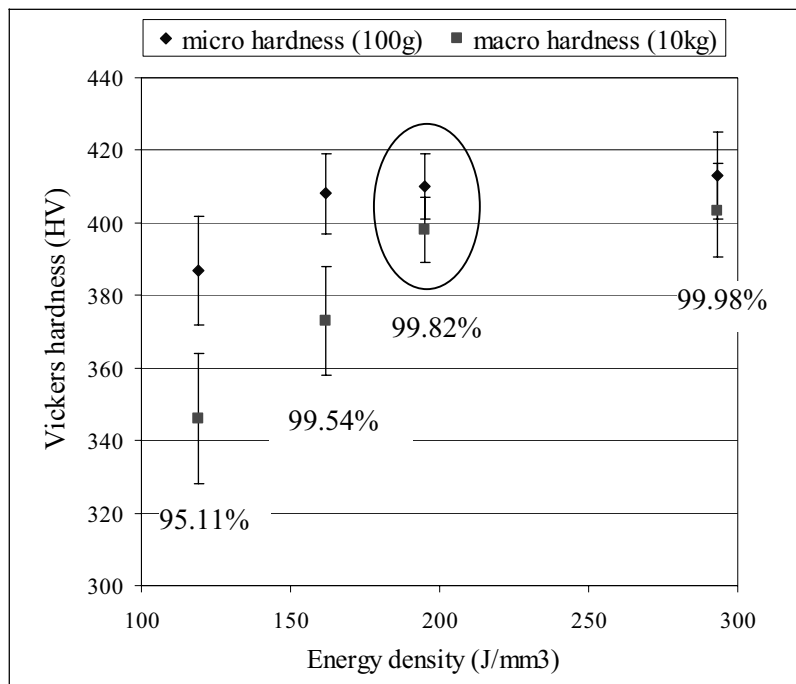


Fig. 5: Results of hardness analysis for TiAl₆V₄ (confidence limit 95%).

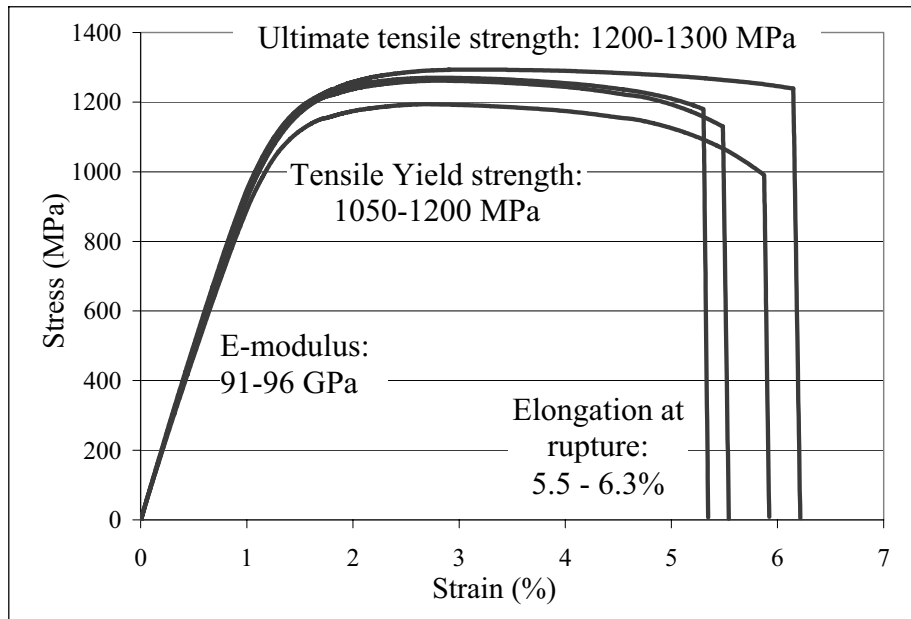


Fig. 6: Stress-strain graphs of tensile tests for TiAl_6V_4 samples.

Fig. 6 shows the stress-strain curves obtained by tensile tests on four titanium samples produced with optimized parameters. These graphs prove high repeatability for mechanical properties. Table 3 gives an overview of the results of all performed mechanical tests. The obtained mechanical properties of the SLM samples are compared with those of bulk material from literature. Properties of both annealed and solution treated aged (STA) bulk material are listed, but the SLM process links up best with the STA treatment. The results for SLM are similar to the stated properties of the bulk material, except for elongation at rupture which shows a lower ductility because of slight embrittlement due to the laser melting. This comparison proves that the SLM parts fulfill the mechanical requirements for manufacturing.

		SLM TiAl_6V_4	Annealed TiAl_6V_4	STA TiAl_6V_4
Archimedes	Density (kg/m^3)	4420	4430	4430
Vickers	Hardness (HV)	410 (micro) 400 (macro)	350	395
Tensile	Young's modulus (GPa)	94	110	110
	Tensile Yield strength (MPa)	1125	920	1100
	Ultimate tensile strength (MPa)	1250	1000	1200
	Elongation at rupture (%)	6	12	10
Bending	Young's modulus (GPa)	93	110	110
	Bending yield strength (MPa)	1900	1500	1800
	Ultimate bending strength (MPa)	2000	1900	2050
Grindo-Sonic	Young's modulus (GPa)	101	110	110
	Shear modulus (GPa)	38	44	44

Table 3: Results of mechanical tests on SLM samples compared to mechanical properties of bulk material from literature.

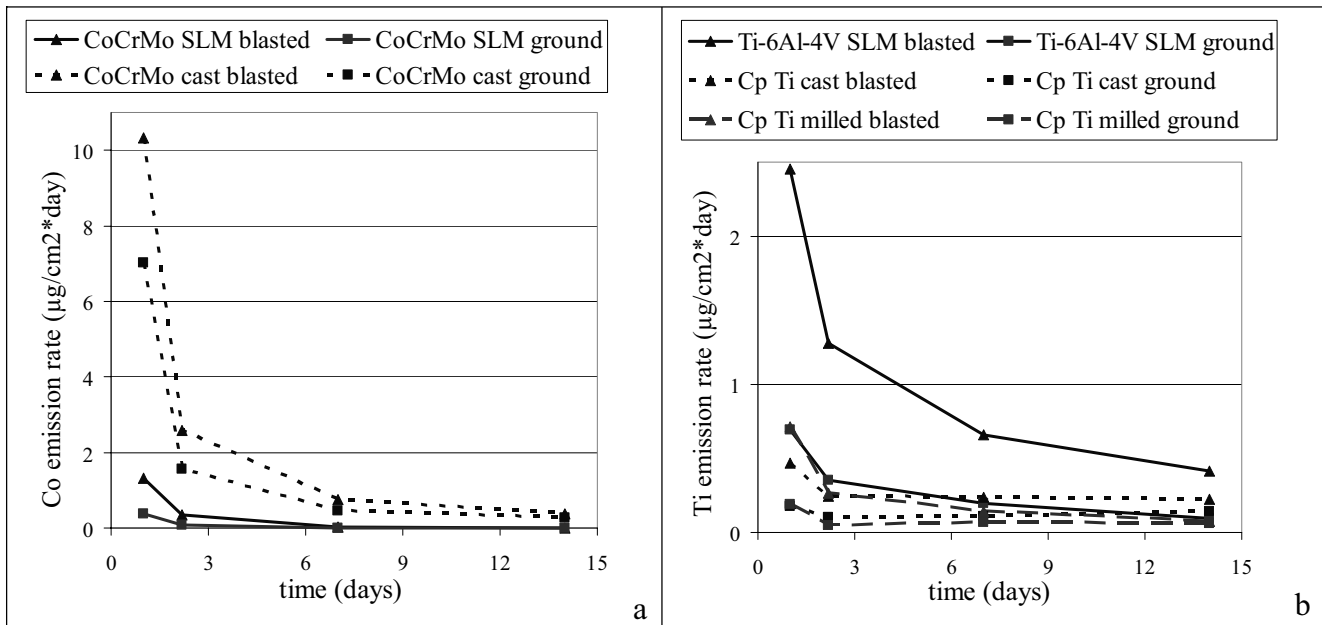


Fig. 7: Corrosion rates in function of time: (a) ion emissions of Co for cobalt-chromium variants, (b) ion emissions of Ti for titanium variants.

The corrosion rates of the cobalt-chromium variants are shown in Fig. 7a. The curves represent the emission of cobalt, since the corrosion of cobalt-chromium alloys is determined by this main component due to the passivating behavior of chromium. Only little chromium and molybdenum can be detected. Fig. 7b shows the corrosion rates of the titanium variants. The curves represent the emission of titanium. The emissions of aluminum and vanadium (for the SLM variant) have the same characteristics but are much lower than the emission of titanium. For all titanium variants only little iron can be detected. The emissions of all ions decrease rapidly within the first few days to approach a final low value. This demonstrates favorable corrosion behavior for all examined variants. After two weeks almost no difference is visible between the different variants and most concentrations come below the detection limit of the analyzing method. Because of the low ion releases, corrosion is influenced almost completely by the surface. Therefore, grinding of the test specimens reduces the ion release in every case. The cobalt-chromium variants are made from the same material and consequently, the different corrosion rates are due to manufacturing. The SLM test specimens show lower emissions than the cast specimens because the lower grain size of the SLM samples avoids deep penetration of the corrosion into the part. The SLM titanium variants are made from TiAl₆V₄ which is more sensitive for corrosion than pure titanium, because the passivating behavior of aluminum forces titanium to corrode. Therefore, milled and cast titanium variants, made from pure titanium grade 2 and grade 1 respectively, show lower corrosion rates.

Table 4 gives the results of the roughness analysis on titanium and cobalt-chromium blocks as indicated on Fig. 2a. For both top and side surfaces no significant differences are found regarding measurement direction. Simple surface post-treatments such as glass blasting and ultrasonic ceramic filing remove partial molten particles on the surface, leading to strong reduction of roughness. Although side roughness is determined by other factors, similar values to top roughness are measured. Cobalt-chromium samples show lower roughness than titanium samples.

		SLM TiAl ₆ V ₄		SLM CoCrMo	
		Top	Side	Top	Side
As processed	R _a (μm)	18	20	15	15
	R _z (μm)	92	110	87	90
Glass blasted	R _a (μm)	12	13	12	8
	R _z (μm)	70	81	66	43
Ultrasonic ceramic filed	R _a (μm)	10	11	7	5
	R _z (μm)	45	64	40	25

Table 4: Top and side surface roughness of titanium and cobalt-chromium SLM samples for different surface post-treatments.

Fig. 8a shows the influence of sloping angle and layer thickness on surface roughness and the difference between top and bottom surface roughness. These graphs are obtained by measurements on benchmarks (Fig. 2b) made by SLM of titanium. Some results can be explained by the stair effect, inherent to the layer-wise production of SLM. Theoretically, the stair size decreases proportionally with the cosine of the sloping angle, as illustrated on Fig. 8b. Consequently, the stair effect can be reduced by decreasing the layer thickness or by increasing the sloping angle. In both cases more stairs appear, but the size of the stairs becomes smaller, leading to lower surface roughness. This corresponds with the experimental findings on Fig. 8a. For very high sloping angles ($> 75^\circ$) roughness does not improve any further, because the stair effect does not play a role anymore and side effects cause the roughness to increase slightly. Top surface roughness (at 0°) improves strongly for smaller layer thicknesses because higher thermal conductivity and the presence of less powder lead to smaller and more stable melt pools. The effect of layer thickness on side surface roughness (at 90°) is less prominent because a good overlap between successive layers is still reached for a layer thickness of 50 μm.

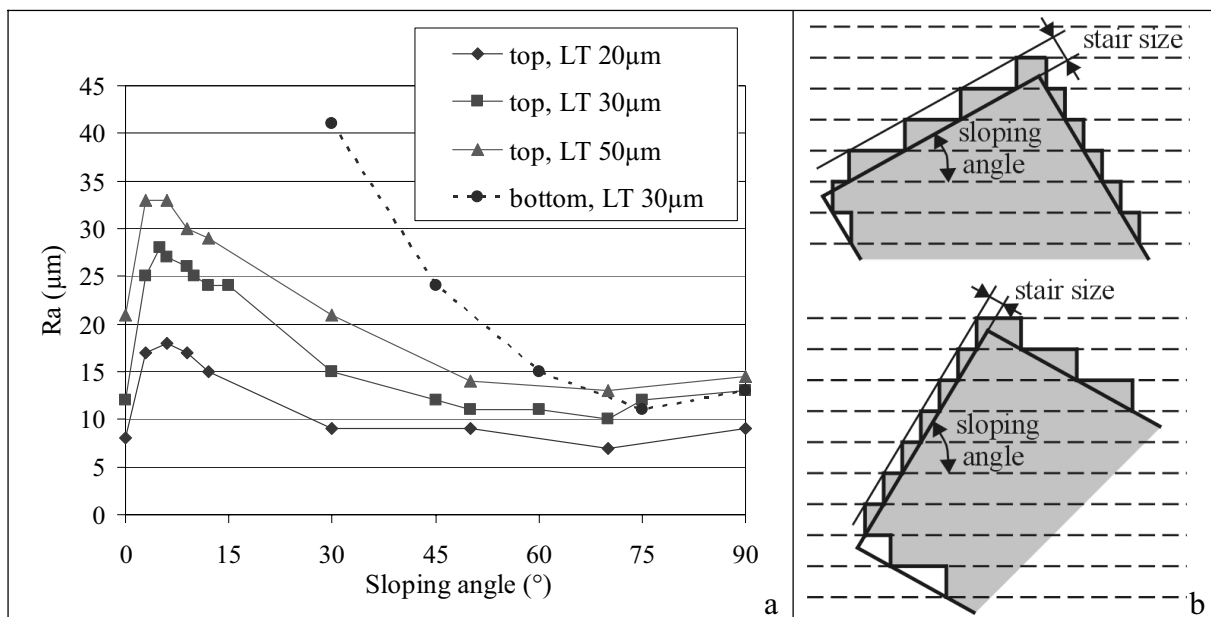


Fig. 8: (a) Surface roughness results in function of sloping angle, layer thickness (LT) and bottom/top surface; (b) Influence of sloping angle on stair effect.

Bottom or overhanging surfaces with a sloping angle below 60° have high roughness, as illustrated on Fig. 8a. Moreover, bottom surfaces with a sloping angle below 20° are not possible to make without support structures. These bottom surfaces are not finished well because of two reasons. Firstly, since the laser beam scans in loose powder instead of on solid material, thermal conductivity decreases and temperature increases leading to instable melt pools. Secondly, stalactite patterns are formed because the melt sinks in the loose powder by gravity. When overhanging surfaces with low sloping angle can not be avoided by tilting the part, specific laser parameters for the first few layers above the overhanging surface or support structures should be used. Horizontal holes, with a diameter higher than 8 mm, show bad roughness at the bottom because of the disadvantageous stair effect and at the top because of overhanging problems.

Table 5 shows the results of the dimensional analyses performed on the produced benchmarks (Fig. 3a) to test process accuracy in x-, y- and z-direction and to measure the precision of cylinders and angled features. Mean and maximum deviations between measured and designed dimensions are stated absolutely (μm) and relatively to the nominal dimension (%). The obtained accuracy fulfills the requirements of most medical and dental applications. All small features of the benchmark shown on Fig. 3b, are built successfully with high precision, except for the hole with diameter of 0.5 mm because the enclosed loose powder is melted by the surrounding heat.

Dental application

A fully digital procedure is developed for the design and manufacturing of personalized frameworks for complex dental prostheses by SLM of titanium or cobalt-chromium [8]. The framework is the metal base structure of the prosthesis and supports the artificial teeth (Fig. 9a). Such framework is screw-retained on oral implants placed in the jawbone of the edentulous patient. To avoid high stresses in the jawbone causing the oral implants to loose and to diminish the risk for colonization of bacteria resulting in infection and eventually bone loss, severe fit criteria below $40 \mu\text{m}$ are necessary at the framework-implant junctions [9]. The developed and patented procedure replaces conventional labor-intensive methods and consists of three main steps: the geometry capture of the implant positions, the digital design of the framework and the production of the framework by SLM. The procedure allows an efficient and customized manufacturing of the complex framework and guarantees the needed precision by optimal process parameters and an appropriate production strategy. The build time per framework declines for increasing number of frameworks produced during the same build, because powder depositing time is spread over all frameworks (Fig. 9b). When eight frameworks are produced during one production run, the build takes sixteen hours or two hours per framework, which is half of the build time when only one framework is produced. A lot of time and money can thus be saved by producing multiple unique frameworks in a single production run, leading to mass customization and to a lower price which competes with present-day market prices.

	x-direction		y-direction		z-direction		diameters		angles	
	mean	max	mean	max	mean	max	mean	max	mean	max
abs. (μm)	15	36	17	30	11	21	24	36	0.51°	1.33°
rel. (%)	0.25	0.97	0.30	1.40	0.21	0.52	0.38	0.90	x	x

Table 5: Summary of dimensional analyses performed to measure accuracy.

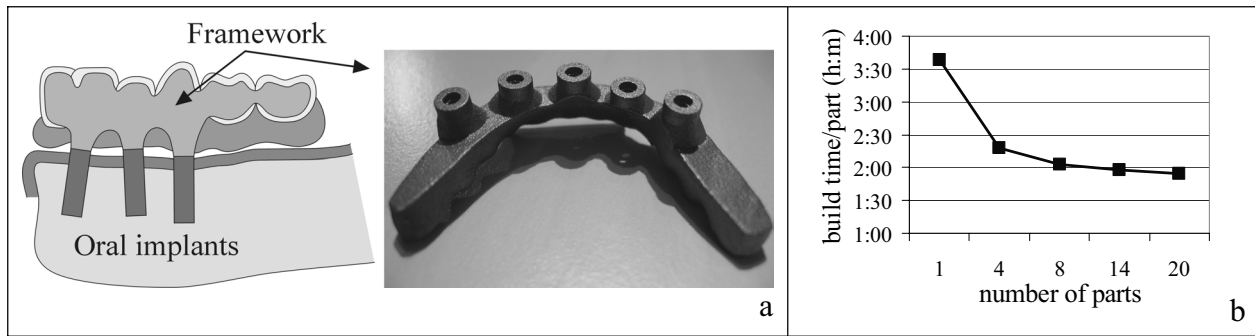


Fig. 9: (a) Scheme of implant-supported prosthesis and picture of framework produced by SLM of TiAl₆V₄; (b) Build time per framework versus number of produced frameworks.

Conclusions

Selective Laser Melting is fully characterized as medical Rapid Manufacturing technique for titanium and cobalt-chromium. The process parameters are optimized to minimize porosity, leading to part densities higher than 99.8% for TiAl₆V₄ and 99.9% for CoCrMo. Different mechanical tests prove that SLM parts fulfill the requirements on mechanical properties such as hardness, strength and stiffness. Chemical tests show favorable corrosion behavior. The influence of layer thickness and sloping angle on surface roughness is investigated, as well as the difference between top and bottom surface roughness. Dimensional analyses are performed on benchmarks showing process accuracy below 40 µm. A digital procedure is developed for the manufacturing of patient specific frameworks for complex dental prostheses, which proves that SLM allows an efficient production of medical or dental parts with strong economical potential.

Acknowledgments

This research is supported by a grant of ‘Fonds voor Wetenschappelijk Onderzoek Vlaanderen’.

References

- [1] I. Gibson, *Advanced Manufacturing Technology for Medical Applications*, Wiley ed. 2005, ISBN 0-470-01688-4.
- [2] G. Levy, R. Schindel, J.-P. Kruth, *Rapid Manufacturing and Rapid Tooling with Layer Manufacturing Technologies, State of the Art and Future Perspectives*, CIRP Annals 2003 Vol. 52/2.
- [3] J.-P. Kruth, B. Vandenbroucke, J. Van Vaerenbergh, P. Mercelis, *Benchmarking of Different SLS/SLM Processes as Rapid Manufacturing Techniques*, Proc. of 1st Int. Conf. of Polymers and Moulds Innovations, Gent, April 2005.
- [4] C. Over, W. Meiners, et al., *Selective Laser Melting a New Approach for the Direct Manufacturing of Metal Parts and Tools*, Proc. of SME conf. on Rapid Prototyping and Manufacturing, Cincinnati, May 2002.
- [5] J.-P. Kruth, P. Mercelis, J. Van Vaerenbergh, L. Froyen, M. Rombouts, *Binding Mechanisms in Selective Laser Sintering and Melting*, Rapid Prototyping Journal, Vol. 11, Issue no. 1, Jan. 2005, p. 26-36, ISSN 1355-2546.
- [6] R. Strietzel, A. Hösch, et al., *In Vitro Corrosion of titanium*, Biomaterials Vol. 19, 1998, p. 1495-1499.
- [7] J.-P. Kruth, L. Froyen, J. Van Vaerenbergh, P. Mercelis, M. Rombouts, B. Lauwers, *Selective Laser Melting of Iron Based Powder*, Proc. of 14th Int. Symp. On Electromachining, Vol. 2, 2004.
- [8] J.-P. Kruth, B. Vandenbroucke, J. Van Vaerenbergh, I. Naert, *Digital Manufacturing of biocompatible metal frameworks for complex dental prostheses by means of SLS/SLM*, Proc. of 2nd Int. Conf. on Advanced Research in Virtual and Rapid Prototyping, Leiria, Sept. 2005, p. 139-145.
- [9] J. Jemt, U. Lekholm, *Measurements of Bone and Framework Deformations Induced by Misfit of Implant Superstructures, a Pilot Study*, Clinical Oral Implants Research, Vol. 9, 1998, p. 272-280.

See discussions, stats, and author profiles for this publication at: <https://www.researchgate.net/publication/263895453>

Mechanical properties of alloy Ti-6Al-4V and of stainless steel 316L processed by Selective Laser Melting: Influence of out-of-equilibrium microstructures

Article in Powder Metallurgy · July 2014

DOI: 10.1179/1743290114Y.0000000092

CITATIONS

90

READS

2,182

7 authors, including:



Anne Isabelle Mertens

University of Liège

56 PUBLICATIONS 1,203 CITATIONS

[SEE PROFILE](#)



Sylvie Reginster

University of Liège

3 PUBLICATIONS 149 CITATIONS

[SEE PROFILE](#)



Paydas Hakan

University of Liège

10 PUBLICATIONS 222 CITATIONS

[SEE PROFILE](#)



Thierry Dormal

SIRRIS Belgium

14 PUBLICATIONS 352 CITATIONS

[SEE PROFILE](#)

Some of the authors of this publication are also working on these related projects:



Study about 316L+XC Composite Coatings [View project](#)



Metal Operating Losses for bushing in fibreglass industry [View project](#)

Mechanical properties of alloy Ti-6Al-4V and of stainless steel 316L processed by Selective Laser Melting: Influence of out-of-equilibrium microstructures

A. Mertens^{1a*}, S. Reginster^{1b}, H. Paydas^{1c}, Q. Contrepois^{1d}, T. Dormal^{2e}, O. Lemaire^{3f}, J. Lecomte-Beckers^{1g}

¹ University of Liege (ULg), Faculty of Applied Science, Department of Aerospace and Mechanics, Metallic Materials Science Unit, Chemin des Chevreuil, 1 B52/3, B 4000 Liège, Belgium

² Sirris Research Centre (Liège), Rue Bois St-Jean, 12, B 4102 Seraing, Belgium

³ CRM Group, Avenue Bois St-Jean, 21, B 4000 Liège, Belgium

^a anne.mertens@ulg.ac.be, ^b sylvie.reginster@ulg.ac.be, ^c hpaydas@ulg.ac.be, ^d quentin.contrepois@gmail.com, ^e thierry.dormal@sirris.be, ^f olivier.lemaire@crmgroup.be, ^g jacqueline.lecomte@ulg.ac.be

* Corresponding author

Abstract

Ti-6Al-4V and stainless steel 316L have been processed by selective laser melting under similar conditions, and their microstructures and mechanical behaviours have been compared in details. Under the investigated conditions, Ti-6Al-4V exhibits a more complex behaviour than stainless steel 316L with respect to the occurrence of microstructural and mechanical anisotropy. Moreover, Ti-6Al-4V appears more sensitive to the build-up of internal stresses when compared with stainless steel 316L, whereas stainless steel 316L appears more prone to the formation of “lack of melting” defects. This correlates nicely with the difference in thermal conductivity between the two materials. Thermal conductivity was shown to increase strongly with increasing temperature and the thermophysical properties appeared to be influenced by variations in the initial metallurgical state.

Keywords: Selective laser melting, Microstructure, Tensile properties, Thermal conductivity, Stainless steel, Titanium alloys

1. Introduction

Selective Laser Melting (SLM) was developed in the late 1990s as an economic layer-by-layer near-net-shape process allowing for the production of complex parts from a wide variety of materials including metallic alloys.^{1,2} Practically, a layer of powder is deposited in a bed and molten locally by a laser according to a computer-aided design model. The powder bed is then lowered, a fresh layer of loose powder is deposited and these steps are repeated until the part is completed.

While SLM brings about important advantages, it is also faced with a number of problems. Non-optimal processing parameters may cause the formation of defects such as porosities due to entrapped gas, lack of melting or poor wetting of a new layer on the material that was previously solidified.^{1,3,4} Another important feature of SLM is that the structure undergoes an ultra-fast cooling once the laser beam leaves the working zone, thus producing strongly out-of-equilibrium microstructures. High internal stresses may arise because of the high thermal gradients⁴ and because the contraction of a new layer upon cooling is constrained by the previous layers.⁵⁻⁷ Epitaxial growth of the grains from a given layer on the grains formed during the solidification of the previous layers may also occur.^{3, 8-11} These various factors can in turn affect the properties of metallic parts processed by SLM, e.g. by bringing about a strong anisotropy of the mechanical properties.^{3,9,11-13}

This study focuses on Ti alloy Ti-6Al-4V and on stainless steel 316L processed by SLM. These two alloys are of great practical significance, e.g. in biomedical applications.^{2,10} Moreover, Ti-6Al-4V is widely used in aeronautical applications and stainless steel 316L is very suitable for use in the energy and chemical industries. Previous works by the present authors have already shown that these two alloys exhibit fairly different behaviours in terms of the relationships between the processing parameters, the microstructures and the resulting mechanical properties.^{9,13} Following through on these observations, the present study aims at a systematic comparison of the processing of Ti-6Al-4V

and of stainless steel 316L by SLM, in relations with relevant thermophysical properties such as the thermal conductivity and the coefficient of thermal expansion (CTE).⁴⁻⁷ Indeed, it is hoped that such a careful comparison might shed more light into the role of phenomena such as epitaxial growth, out-of-equilibrium phase transformations and the build-up of internal stresses in determining the mechanical properties of metallic parts processed by SLM.

2. Experimental Procedure

A detailed description of the processing conditions for each alloy may be found elsewhere.^{9,13} The chemical composition of the Ti-6Al-4V alloy was Ti–5.91Al–4.20V (wt-%), with a particle size in the range of 25-50 µm. The composition of the AISI 316L stainless steel powder was Fe–0.019C–17.30Cr–10.90Ni (wt-%), with a particle size in the range of 10-45 µm. Samples for tensile testing were produced using a MTT SLM 250 laser melting deposition manufacturing system, in an argon purged production chamber, and following three different orientations ox, oy and oz with respect to the building direction (oz), as illustrated in Fig. 1. The layer thickness and the focus offset were optimised independently for each material, as summarised in Table 1. Other processing parameters were kept constant. The effect of a post-processing heat treatment at 640°C for 4 hours on alloy Ti-6Al-4V was also investigated. All Ti-6Al-4V specimens were heat treated simultaneously and under a protective atmosphere of Ar in order to minimise the risks of contamination.

Samples for metallographical examinations were embedded in resin and polished following standard practices. The overall quality and soundness of the produced parts have been assessed directly from observations of “mirror polished” samples, and the average volume fraction of porosities was determined by image analysis using the imageJ software. A more detailed microstructural characterisation was then carried out after etching with Kroll’s reagent (i.e. 5% HNO₃ and 5% HF in distilled water) for Ti-6Al-4V and with aqua regia (i.e. 55% HCl, 20% HNO₃ and 25% methanol) for

stainless steel 316L. Microstructural observations have been carried out by means of an Olympus BX60M optical microscope and a SEM-FEG FEI XL30 scanning electron microscope.

Uniaxial tensile tests have been performed according to the ISO 6892-1 B25: 2009 standard on samples 2.6 mm thick, 5 mm wide and with an initial gauge length of 35 mm. Average values of the yield stress, the ultimate tensile strength and the maximum uniform elongation have been obtained from the tensile stress-strain curves. The fractured surfaces have also been observed using SEM, in order to better understand the mechanisms leading to failure.

Thermophysical properties for the two alloys were determined in the temperature range between room temperature and 1000°C. Four sets of specimens were investigated. One set of representative samples of stainless steel 316L were taken from a plate. Three sets of specimens were considered for Ti-6Al-4V: one set produced by additive manufacturing (Ti-6Al-4V AM) and two sets from standard wrought materials (Ti-6Al-4V W1 and W2), so as to investigate the effect of the initial metallurgical state on the thermophysical properties. The CTE was measured by dilatometry, according to DIN 51045 standard, at a heating rate of 5°C/min. The thermal conductivity $\lambda(T)$ was obtained according to Laplace's equation

$$\lambda(T) = \alpha(T) * \rho(T) * c_p(T)$$

where $\alpha(T)$ is the thermal diffusivity (mm^2/s), $\rho(T)$ is the material density (g/cm^3) and $c_p(T)$ is the specific heat ($\text{J}/\text{g}*\text{K}$).

Practically, $\rho(T)$ was obtained from dilatometry tests. $C_p(T)$ was obtained from differential scanning calorimetry (DSC) measurements, at a heating rate of 10°C/s and using sapphire as a standard. Thermal diffusivity was measured by steps of 100°C, using a laser flash diffusivimeter. A more detailed account of the measurement procedures is provided elsewhere by A. Rassili et al.¹⁴

3. Results and discussion

3.1. Ti-6Al-4V

Fig. 2 shows optical micrographs (in cross section) of the Ti-6Al-4V samples processed according to three different orientations, as schematically represented in Fig. 1. These micrographs present some spherical porosities, typically associated with gas bubbles trapped in the build during solidification.^{1,3,15} However, the average volume fractions of these porosities remain well below 0,5%, which is considered acceptable.

As previously reported,^{3,8,9} alloy Ti-6Al-4V first solidifies in the β (BCC) structure. Moreover, the primary β grains of a given layer tend to grow epitaxially on the grains of the previous layers, thus assuming an elongated morphology parallel to the direction for maximum heat conduction. This elongated morphology is clearly to be seen parallel to the building direction in the samples processed in the oy direction (Fig. 2(c)), but not in the samples processed in the ox direction as shown in Fig. 2(a) and (b) that were taken from two different specimens to illustrate the reproducibility of this phenomenon. This suggests that the primary β grains in the ox samples may actually be tilted as a consequence of a tilt in the direction of maximum heat conduction with respect with the building direction.⁸ It has been previously established⁸ that specific processing conditions (laser scanning velocity, scanning strategy, ...) could lead the direction for maximum heat conduction to tilt with respect to the building direction, causing in turn a tilt in the growth direction of the primary β grains. However, the scanning strategy used in the present case did not favour such a tilt, since it involved a rotation of the scanning direction by an angle of 79° between two successive layers,⁹ and it is rather suspected that the cause of this phenomenon should be found in a combined effect of parts geometry and of the orientation of the Ar flow following the ox direction (Fig. 1). Indeed, it seems possible that the Ar flowing above the melt surface could affect its evaporation and hence influence heat conduction processes inside the build.¹⁶ Finally, Fig. 2(d) shows a cross section through a specimen processed in the oz direction, i.e. a cross section perpendicular to the elongated primary β grains.

Upon subsequent cooling below the β transus temperature (i.e. $\pm 995^\circ\text{C}$), due to the very high cooling rates, the primary β grains transform into a fine martensitic α' (HCP) structure that can also be observed in the four micrographs of Fig. 2.^{3,8,17}

Table 2 summarises the values of the tensile properties for samples oriented following the different directions presented in Fig. 1, with and without post-processing annealing at 640°C for 4 hours (only for the ox direction, in the latter case). Comparison of properties measured for the as-received and for the annealed samples oriented along ox clearly shows that the thermal treatment brings about a significant improvement of the ductility while causing only a slight decrease in strength. Heat treatment of Ti-6Al-4V parts produced by SLM has more classically been carried out at higher temperatures i.e. 780°C and above. In the latter case, the heat treatment have been shown to induce significant microstructural changes such as a coarsening of the α' laths or a partial transformation of α' to β .^{3,4} On the contrary, annealing at 640°C for 4 hours was not observed to cause significant microstructural change and its beneficial effect on ductility was ascribed to the relaxation of internal stresses.⁹

Table 2 further shows that the annealed tensile specimens processed following three different orientations exhibit a very strong anisotropy as far as the elongation is concerned. Anisotropy had been reported previously between samples oriented along the building direction or in the deposition plane. Mechanical anisotropy could then be ascribed to the very strong anisotropy of the primary β grains that were elongated parallel to the building direction. Lack of melting defects, oriented perpendicularly to the building direction were also demonstrated to play a role in anisotropy of the fracture behaviour of samples parallel or transverse to the building direction.³ However, to the best of our knowledge, only few reports existed so far of a mechanical anisotropy between two sets of Ti-6Al-4V specimens oriented perpendicularly to each other in the deposition plane.⁹ In this case, the anisotropy of elongation between the ox and oy specimens was ascribed to their microstructural

difference, i.e. to a tilt of the primary β grains with respect to the building direction in the ox samples.

3.2. Stainless steel 316L

Fig. 3(a) shows a representative optical micrograph of stainless steel 316L samples. Etching with aqua regia reveals semi-circular shapes perpendicular to the building direction, that correspond to the successive individual melt pools. Two different types of porosities can be observed. Spherical pores associated with gas bubbles are randomly distributed inside the melt pools. The second type of defects, bigger in size and elongated in shape, is localised between melt pools corresponding to two successive layers. These elongated defects remain scarce in the ox and oy specimens. But they are present in a much greater number in the oz specimens, as reflected by the volume fraction of porosities that is two to three times higher in the oz specimens when compared with the ox and oy specimens (Table 3). These elongated defects are generally associated with unmolten powder particles (Fig. 3(b)) and they can be ascribed to insufficient melting of the new layer and/or insufficient remelting of the previously solidified material.^{1,13,18} Fig. 3(b) further illustrates the typical cellular morphology associated with Cr segregation during the solidification of stainless steel 316L and similar steel grades under ultra-fast cooling conditions.¹⁹

The average values of the tensile properties obtained for the three different processing orientations (Fig. 1) are summarised in Table 3. All samples exhibit reasonable ductility, so that no post-processing heat treatment was deemed necessary in this case. Ox and oy samples, on the one hand, exhibit very similar properties, along with a typical ductile fracture behaviour. Oz specimens, on the other hand, exhibit significantly lower strengths and elongations. This deterioration of the mechanical properties of the oz samples can be ascribed to their greater volume fraction of “lack of melting” defects, but also to the very detrimental orientation of these defects with respect to the

tensile loading direction.^{3,13} This is further supported by the SEM fractograph of Fig. 4 that clearly shows the “lack of melting” defects as the cause of failure of the oz specimens.

3.3. Ti-6Al-4V and stainless steel 316L: comparison and influence of the thermophysical properties

From the results discussed in the two previous sections, some major differences can be highlighted between Ti-6Al-4V and stainless steel 316L processed by SLM under similar conditions. (i) Ti-6Al-4V is more sensitive to the build-up of internal stresses when compared with stainless steel 316L. (ii) Ti-6Al-4V also appears more prone to the occurrence of microstructural and mechanical anisotropy both in the building direction and in two perpendicular direction inside the deposition plane.

Stainless steel 316L, on the other hand, is more sensitive to the occurrence of a microstructural and mechanical anisotropy in relation with “lack of melting” defects. Efforts put into modelling the build-up of internal stresses and the thermal history of SLM parts have shown that the materials CTE and thermal conductivity are likely to play a role.^{5,6} The present section hence aims more particularly at comparing these thermophysical properties for both alloys in order to shed more light into their differences.

Fig. 5 shows the evolution of the CTE as a function of temperature between room temperature and 1000°C for the four sets of samples i.e. one set of stainless steel 316L and three sets of Ti-6Al-4V (Ti-6Al-4V W1, W2 and AM). Stainless steel 316L exhibits a CTE that is twice higher than the CTE for the three sets of Ti-6Al-4V samples. On the other hand, the three sets of Ti-6Al-4V samples exhibit fairly similar behaviour except in the 900°C-1000°C temperature range where the AM samples exhibit a higher CTE. The two sets of wrought materials exhibit a coarser microstructure than the AM sample, and they contain moreover a significant volume fraction of equiaxed α grains. Such a difference in the starting microstructure has been shown to influence phase transformations upon reheating⁴, and this is in turn likely to reflect on the values of the CTE.

The influence of the initial metallurgical condition on the thermophysical properties is further confirmed when comparing the curves of the thermal conductivity vs temperature for the three sets of Ti-6Al-4V specimens (Fig. 6). The AM samples again exhibit a higher apparent thermal conductivity than the W1 and W2 samples in the higher temperature range. Besides, it is worth noting that, for all samples, the thermal conductivity strongly increases with increasing temperature. These facts are neglected by a number of models that assume constant (i.e. room temperature) values for the thermal conductivity throughout processing.⁶

Fig. 6 further shows that stainless steel 316L exhibits a much higher thermal conductivity than the Ti-6Al-4V alloy, over most of the investigated temperature range. As a consequence, smaller thermal gradients may be expected in stainless steel 316L, hence its lower sensitivity to the build-up of internal stresses when compared to Ti-6Al-4V. However, as a drawback of its higher thermal conductivity, stainless steel 316L might cool down more efficiently by heat conduction through the part, and this might have contributed to some extent to the formation of “lack of melting” defects that had not been observed in alloy Ti-6Al-4V.

4. Conclusions

1. Ti-6Al-4V and stainless steel 316L have been processed by SLM under similar conditions, and their microstructures and mechanical behaviours have been compared in details.
2. Ti-6Al-4V appears more sensitive to the build-up of internal stresses when compared with stainless steel 316L, whereas stainless steel appears more prone to the formation of “lack of melting” defects. This correlates nicely with the difference in thermal conductivity between the two materials. On the other hand, higher values of the CTE *per se* do not seem to favour high internal stresses.
3. Under the investigated conditions, Ti-6Al-4V exhibits a more complex behaviour than stainless steel 316L with respect to the occurrence of microstructural and mechanical anisotropy.

4. Thermophysical properties appear sensitive to variations in the initial metallurgical state, possibly due to changes in the transformation behaviour.

Acknowledgements

The authors wish to acknowledge the financial support of the European Fund for Regional Development and the Walloon Region under convention FEDER 1784 TipTopLam, and of the Interuniversity Attraction Poles Programme initiated by the Belgian Science Policy Office, contract IAP7/21 “INTEMATE”. The authors also wish to thank Mrs S. Salieri and Mr A. Martinez-Aguilera (ULg), and the Additive Manufacturing Team from the Sirris Research Centre for their help with samples preparation.

References

1. J.-P. Kruth, G. Levy, F. Klocke and T.H.C. Childs: ‘Consolidation phenomena in laser and powder-bed based layered manufacturing’, *Annals of the CIRP*, 2007, **56**, 730-759
2. T. Marcu, M. Todea, L. Maines, D. Leordean, P. Berce and C. Popa: ‘Metallurgical and mechanical characterisation of titanium based materials for endosseous applications obtained by selective laser melting’, *Powder Metall.*, 2012, **55**, 309-314
3. T. Vilaro, C. Colin and J.D. Bartout: ‘As-fabricated and heat-treated microstructures of the Ti-6Al-4V alloy processed by selective laser melting’, *Metall. Mater. Trans.*, 2011, **42A**, 3190-3199
4. B. Vrancken, L. Thijs, J.-P. Kruth and J. Van Humbeeck: ‘Heat treatment of Ti6Al4V produced by selective laser melting: microstructure and mechanical properties’, *J. Alloys Compd.*, 2012, **541**, 177-185
5. K. Dai and L. Shaw: ‘Thermal and stress modeling of multi-material laser processing’, *Acta Mater.*, 2001, **49**, 4171-4181

6. A.H. Nickel, D.M. Barnett and F.B. Prinz: 'Thermal stresses and deposition patterns in layered manufacturing', *Mater. Sci. Eng. A*, 2001, **A317**, 59-64
7. M. Shiomi, K. Osakada, K. Nakamura, T. Yamashita and F. Abe: 'Residual stress within metallic model made by selective laser melting process', *Annals of the CIRP*, 2004, **53**, 195-198
8. L. Thijs, F. Verhaeghe, T. Craeghs, J. Van Humbeeck and J.-P. Kruth: 'A study of the microstructural evolution during selective laser melting of Ti-6Al-4V', *Acta Mater.*, 2010, **58**, 3303-3312
9. A. Mertens, Q. Contrepois, T. Dormal, O. Lemaire and J. Lecomte-Beckers: 'Ti alloys processed by selective laser melting and by laser cladding: microstructures and mechanical properties', Proc. 12th European Conf. on Space Structures, Materials & Environmental Testing, Noordwijk, The Netherlands, March 2012 (European Space Agency special publication ESA SP-691, July 2012)
10. I. Yadroitsev, P. Krakhmalev, I. Yadroitsava, S. Johansson and I. Smurov: 'Energy input effect on morphology and microstructure of selective laser melting single track from metallic powder', *J. Mater. Process. Technol.*, 2013, **213**, 606-613
11. T. Niendorf, S. Leuders, A. Riemer, H. A. Richard, T. Tröster and D. Schwarze: 'Highly anisotropic steel processed by selective laser melting', *Metall. Mater. Trans.*, 2013, **44B**, 794-796
12. I. Tolosa, F. Garciandia, F. Zubiri, F. Zapirain and A. Esnaola: 'Study of mechanical properties of AISI 316 stainless steel processed by "selective laser melting", following different manufacturing strategies', *Int. J. Adv. Manuf. Technol.*, 2010, **51**, 639-647
13. A. Mertens, S. Reginster, Q. Contrepois, T. Dormal, O. Lemaire and J. Lecomte-Beckers: 'Microstructures and mechanical properties of stainless steel AISI 316L processed by selective laser melting', Proc. Conf. Thermec 2013, Las Vegas (NV), December 2013, in press

14. A. Rassili, M. Robelet and J. Lecomte-Beckers: ‘Chapter 3 Identification of suitable steels’, in ‘Thixoforming steel’ (eds H. Atkinson and A. Rassili), 37-65; 2010, Aachen, Shaker Verlag GmbH
15. P.A. Kobryn, E.H. Moore and S.L. Semiatin: ‘The effect of laser power and traverse speed on microstructure, porosity, and build height in laser-deposited Ti-6Al-4V’, *Scr. Mater.*, 2000, **43**, 299-305
16. F. Verhaeghe, T. Craeghs, J. Heulens and L. Pandelaers, ‘A pragmatic model for selective laser melting with evaporation’, *Acta Mater.*, 2009, **57**, 6006-6012
17. T. Ahmed and H.J. Rack: ‘Phase transformations during cooling in $\alpha+\beta$ titanium alloys’, *Mater. Sci. Eng. A*, 1998, **A243**, 206-211
18. J.P. Kruth, L. Froyen, J. Van Vaerenbergh, P. Mercelis, M. Rombouts and B. Lauwers: ‘Selective laser melting of iron-based powder’, *J. Mater. Process. Technol.*, 2004, **149**, 616-622
19. J.W. Elmer, S.M. Allen and T.W. Eagar: ‘Microstructural development during solidification of stainless steel alloys’, *Metall. Trans.*, 1989, **20A**, 2117-2131

Tables

Table 1 Processing conditions

Material	Layer thickness (μm)	Focus offset (mm)	Laser power (W)	Travel speed (mm/s)	Hatch spacing (μm)
Ti-6Al-4V	30	2	175	710	120
SS 316L	60	1	175	700	120

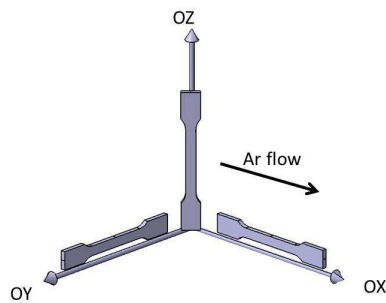
Table 2 Tensile properties of the Ti-6Al-4V samples

Samples	Yield strength (MPa)	Ultimate tensile strength (MPa)	Maximum uniform elongation (%)
ox as processed	1166 ± 6	1321 ± 6	2.0 ± 0.7
ox annealed	1104 ± 8	1225 ± 4	7.4 ± 1.6
oy annealed	1140 ± 43	1214 ± 24	3.2 ± 2.0
oz annealed	1152 ± 11	1256 ± 9	3.9 ± 1.2

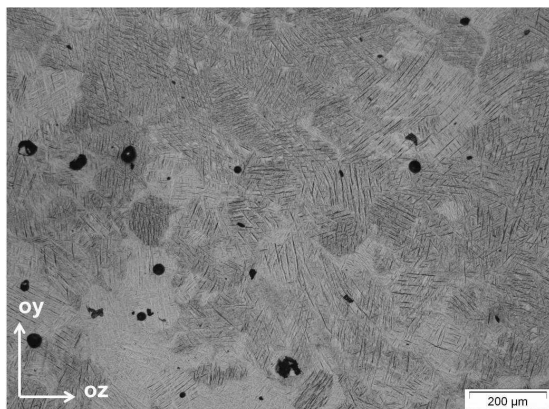
Table 3 Volume fractions of porosities and tensile properties of the stainless steel 316L samples

Samples	Volume fraction of porosities (%)	Yield stress (MPa)	Ultimate tensile strength (MPa)	Maximum uniform elongation (%)
ox	2.5 ± 1.0	534 ± 6	653 ± 3	16.2 ± 0.8
oy	3.3 ± 1.0	528 ± 4	659 ± 3	16.6 ± 0.4
oz	6.2 ± 2.6	444 ± 27	567 ± 19	8 ± 2.9

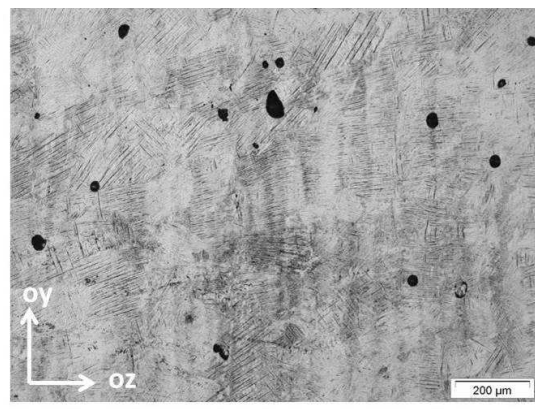
Figures



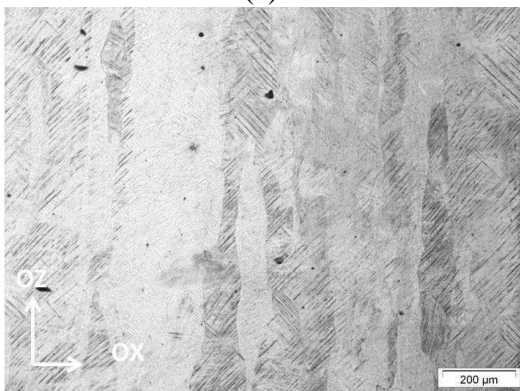
1. Schematic representation of the various orientations of the tensile samples with respect to the building direction (oz).



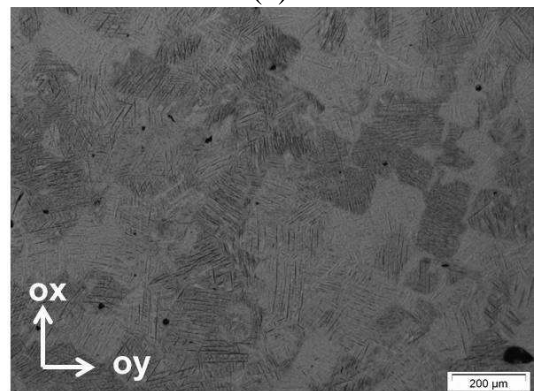
(a)



(b)

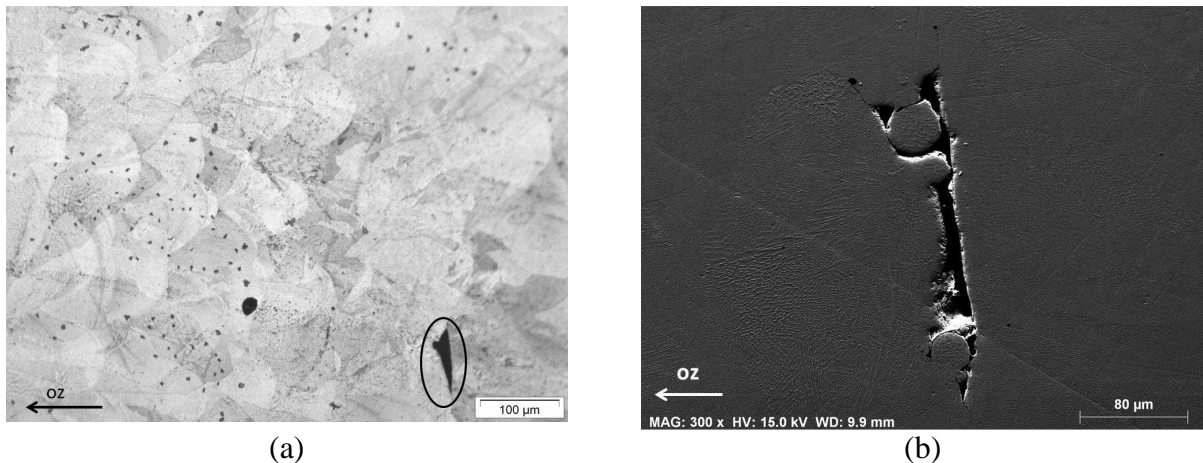


(c)

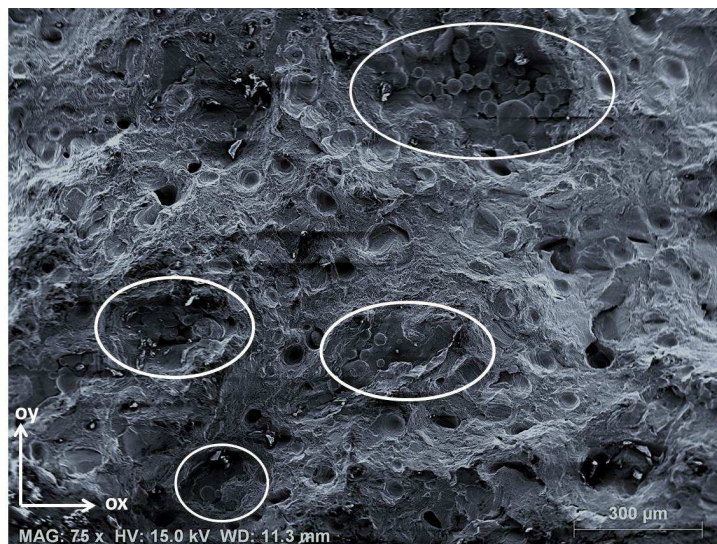


(d)

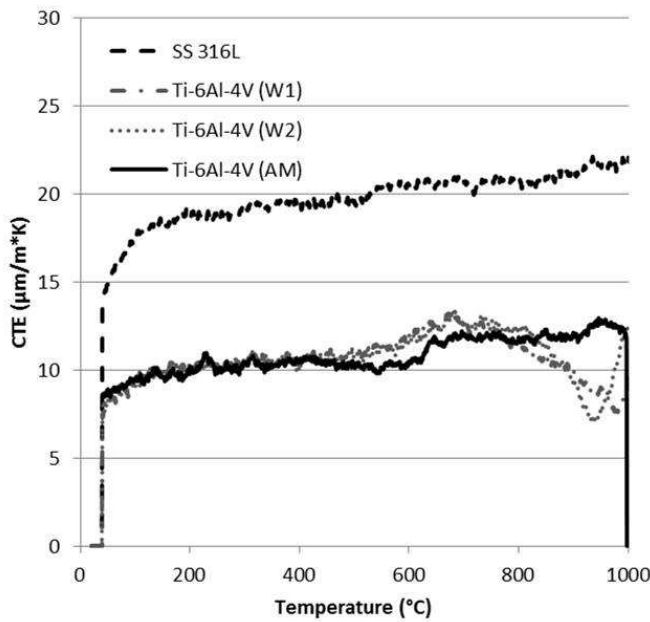
2. Optical micrographs of the cross section of Ti-6Al-4V specimens processed following three different orientations, as represented in Fig. 1. (a) - (b) in the ox direction, (c) in the oy direction and (d) in the oz direction.



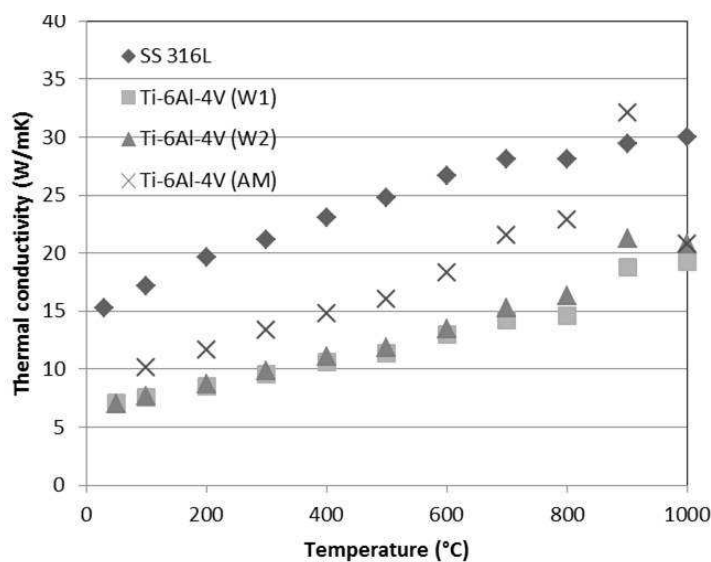
3. (a) Optical micrograph of a stainless steel 316L sample processed in the oy direction (the black circle marks a wetting defect), (b) SEM micrograph of a stainless steel 316L sample processed in the oz direction showing a wetting defect associated with a lack of fusion, as indicated by the unmolten powder particles.



4. Representative fractograph of a stainless steel 316L sample fabricated in the oz direction. "Lack of melting" defects are highlighted by white circles.



5. Evolution of the CTE as a function of temperature, for four sets of samples: stainless steel 316L, Ti-6Al-4V W1, T-6Al-4V W2 and Ti-6Al-4V AM



6. Evolution of the thermal conductivity as a function of temperature, for four sets of samples: stainless steel 316L, Ti-6Al-4V W1, Ti-6Al-4V W2 and Ti-6Al-4V AM

Structural, mechanical and in vitro characterization of individually structured Ti–6Al–4V produced by direct laser forming

Dirk A. Hollander^{a,1}, Matthias von Walter^{a,*1}, Tobias Wirtz^b, Richard Sellei^a, Bernhard Schmidt-Rohlfing^a, Othmar Paar^a, Hans-Josef Erli^a

^aDepartment of Trauma Surgery, University Hospital Aachen, Pauwelsstr. 30, 52074 Aachen, Germany

^bFraunhofer Institute of Laser Technology, Aachen, Germany

Received 5 April 2005; accepted 11 July 2005

Available online 22 August 2005

Abstract

Direct laser forming (DLF) is a rapid prototyping technique which enables prompt modelling of metal parts with high bulk density on the base of individual three-dimensional data, including computer tomography models of anatomical structures. In our project, we tested DLF-produced material on the basis of the titanium alloy Ti–6Al–4V for its applicability as hard tissue biomaterial. To this end, we investigated mechanical and structural properties of DLF-Ti–6Al–4V. While the tensile and yield strengths of untreated DLF alloy ranged beyond 1000 MPa, a breaking elongation of $6.5 \pm 0.6\%$ was determined for this material. After an additional post-DLF annealing treatment, this parameter was increased two-fold to $13.0 \pm 0.6\%$, while tensile and yield strengths were reduced by approx. 8%. A Young's modulus of 118.000 ± 2.300 MPa was determined for post-DLF annealed Ti–6Al–4V. All data gained from tensile testing of post-DLF annealed Ti–6Al–4V matched American Society of Testing and Materials (ASTM) specifications for the usage of this alloy as medical material. Rotating bending tests revealed that the fatigue profile of post-DLF annealed Ti–6Al–4V was comparable to casted/hot isostatic pressed alloy. We characterized the structure of non-finished DLF-Ti–6Al–4V by scanning electron microscopy and observed a surface-associated layer of particles, which was removable by sandblasting as a finishing step. We manufactured porous specimens with nominal pore diameters of 500, 700 and 1000 μm . The diameters were reduced by the used DLF processing by approx. 300 μm . In an in vitro investigation, we cultured human osteoblasts on non-porous and porous blasted DLF-Ti–6Al–4V specimens to study morphology, vitality, proliferation and differentiation of the cells. The cells spreaded and proliferated on DLF-Ti–6Al–4V over a culture time of 14 days. On porous specimens, osteoblasts grew along the rims of the pores and formed circle-shaped structures, as visualized by live/dead staining as well as scanning electron microscopy. Overall, the DLF-Ti–6Al–4V approach proved to be efficient and could be further advanced in the field of hard tissue biomaterials.

© 2005 Elsevier Ltd. All rights reserved.

Keywords: Titanium alloy; Rapid prototyping; Structure; Mechanical properties; Osteoblast; Cell spreading

Abbreviations: ASTM, American Society for Testing and Materials; DLF, direct laser forming; HIP, hot isostatic pressing; HOB, human osteoblasts; ILT, Fraunhofer Institute of Laser Technology; PBS, phosphate-buffered saline; RP, Rapid prototyping; SEM, scanning electron microscopy; SLS, Selective Laser Sintering; XTT, sodium 3'-[1-(phenylaminocarbonyl)-3, 4-tetrazolium]-bis (4-methoxy-6-nitro) benzene sulfonic acid hydrate

*Corresponding author. Tel.: +49 241 8088848;
fax: +49 241 8082415.

E-mail address: UC-labor@ukaachen.de (M. von Walter).

¹These authors contributed equally to the work.

1. Introduction

Rapid prototyping (RP), also known as solid freeform fabrication, is a strategy to directly generate physical objects with defined structure and shape on the basis of virtual 3D model data. Among diverse established RP technologies, selective laser sintering (SLS) [1] or selective laser powder remelting/direct laser forming (DLF) [2] offers the advantage to make use of an extended range of basic materials including polymers,

metals and ceramics. Comparing SLS and DLF techniques, SLS results in objects with sub-optimal bulk density due to partial melting and immediate sintering of the particles of the basic material. During DLF, on the other hand, the basic material particles are completely melted and fused in the laser focus resulting in objects with a density of almost 100%, resulting in a higher mechanical strength.

In principle, the DLF process can be subdivided into the following steps (Fig. 1). The structural information of the given 3D model is processed layer-wise. To this end, the model is split into layers with a defined thickness. In the production unit, the structure of the respective layer is selectively melted into a powder bed of the chosen material by a scanning laser beam. After the short exposure to the laser spot, the molten zones quickly solidify. In the next step, the production platform is lowered one layer thickness, a new powder layer is spread and scanned. The scanning orientation is altered by 90° after each layer. This process is repeated until the complete batch of layers has been transferred, resulting in a solid analog of the original 3D model, which usually only requires minimal surface finishing. Excessive basic material can be saved and reused, which additionally reduces manufacturing costs.

The prospect of instantaneously generating tailored parts via SLS/DLF has aroused much interest in the field of orthopedical and trauma surgery, where prostheses and implants have to be individually shaped in many cases. This is conventionally achieved by machining (e.g. milling, turning), which is time- and material-consuming and does not allow the realization of complex volumetric pore structures. With SLS/DLF technology, on the other side, parts with user-defined complexity can be fabricated almost realtime. The required 3D models can be directly derived from multiplanar 3D imaging of anatomical structures.

While SLS-fabricated implants on the basis of polymers, polymer/ceramic composites and ceramics are investigated since the 1990s [3–6], the realization of metal-based implants by DLF is a more recent approach. At the Fraunhofer Institute of Laser Technology (ILT), Aachen, a DLF strategy has been developed to manufacture hard tissue implants on the basis of titanium and its alloys [7]. In our present investigation, DLF titanium with various structures, porosities and post-DLF treatments is produced and investigated with regard to hard tissue substitution, which comprises structural characterization, mechanical testing as well as in vitro investigation. The aim of the project is to help establish the DLF technique as an alternative to conventional manufacturing in the field of metallic hard tissue biomaterials. In this publication, we present structural and mechanical properties of DLF-

fabricated titanium including tensile strength, rotating bending fatigue and Young's modulus. As in vitro model, we used human osteoblast culture to investigate spreading, vitality, proliferation and differentiation of the cells on DLF titanium.

2. Materials and methods

2.1. DLF production

Ti-6Al-4V-powder with a particle size of 25–45 µm was used as basic material. Processing was carried out in an argon atmosphere using a Nd:G laser system. For mechanical testing, round tensile specimens according to DIN 10002-1 with diameters of 4 mm and lengths of 20 mm (overall length: 54 mm) were fabricated. Additionally, for fatigue property testings, round specimens according to DIN 50113-A with diameters of 4 mm and lengths of 60 mm were manufactured. For the fabrication of specimens for mechanical testing the DLF process was set to exclusively produce dense parts (>99.5%). For tensile testing, some of the specimens underwent an annealing heat treatment which was carried out at 950 °C for 30 min in order to homogenize the metallic microstructure. The specimens were built with an oversize of 1 mm in diameter. Adjacent finish turning was conducted in order to match standard surface and tolerance requirements. Both types of round specimen were built up in a lying position which means that their longitudinal axis was parallel to the substrate's surface. For the in vitro experiments, discs with a thickness of 2 mm and a diameter of 20.5 mm were manufactured. Porosity was modelled according to a regular offset array of parallel cylindrical pores.

2.2. Mechanical testing

For all mechanical tests, specimens were DLF-processed in oversize and turned to match the appropriate dimensions. Tensile testing was conducted on the basis of DIN 10002-1. The main focus of mechanical testing was to determine basic material properties to match with American Society for Testing and Materials (ASTM) standards required for Ti-6Al-4V implants [8]. Untreated and post-DLF annealed DLF-Ti-6Al-4V was tested and compared to the literature results for wrought annealed Ti-6Al-4V. For each condition, three specimens were tested.

In order to determine fatigue properties of DLF-Ti-6Al-4V under standard geometric and environmental conditions 28 specimens were fabricated in charges of four pieces. All 28 specimens were annealed and adjacently turned into shape. Subsequent fatigue testing was carried out according to DIN/EN 50113 rotating bending fatigue testing standards at 50 Hz testing frequency. In each charge specimens were tested until failure starting with constant stresses from 500 to 700 Mpa. Moving from one specimen to the next, stresses were reduced successively to 350–450 Mpa. Using this procedure, a complete array of stresses and corresponding cycles to failure was covered with up to 1×10^7 cycles.

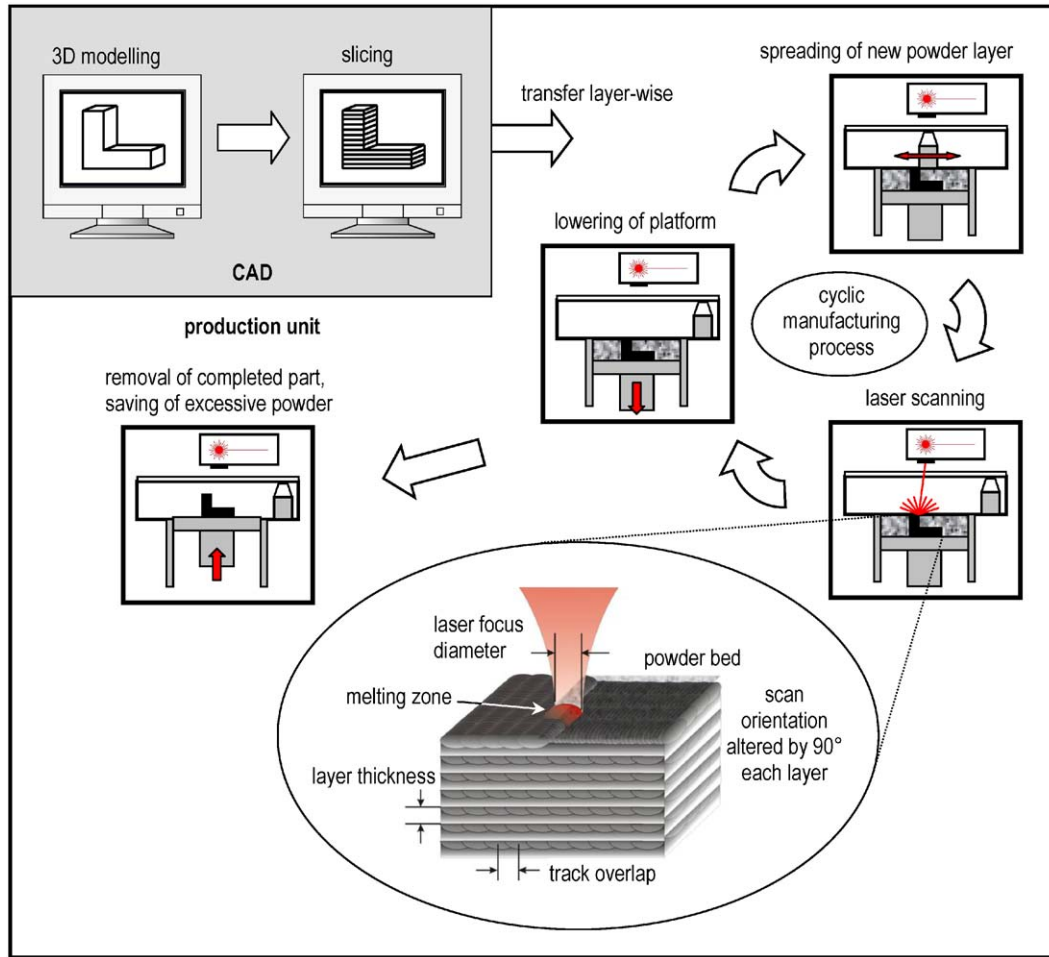


Fig. 1. Rapid prototyping of metal objects by direct laser forming (DLF), scheme.

2.3. In vitro experiments

Human primary osteoblasts (HOB) were isolated from cancellous bone which was obtained from femur heads after hip arthroplasty. Informed consent of the patients had been obtained before. Patients with generalized infections or known bone pathologies were excluded. The osteoblasts were cultured according to an established method [9]. All cultures were maintained at 37 °C in a humidified atmosphere supplied with 5% CO₂. Medium change was carried out twice a week. Cells were counted using a Casy counter (Schärfe System GmbH, Reutlingen, Germany). One cell donor was used for each experiment.

All Ti-6Al-4V discs were sonicated in acetone for 10 min to remove fatty residues. The discs were autoclaved, rinsed with sterile PBS/amphotericine B and transferred into 12-well culture dishes. Prior to cell contact, the specimens were equilibrated in culture medium for 10 min. Onto each specimen, 5 × 10⁴ cells were seeded. Standard cell culture dishes were used as control. The cultures were incubated at 37 °C in a humidified atmosphere containing 5% CO₂. The medium was replaced twice a week. At 3, 7 and 14 days after seeding, the cultures were assayed as follows. The discs were transferred into new 12-well dishes to separate them from dish-adhered

cells. To assess metabolic activity and vitality of the HOB cultures, XTT assays (colorimetric assay based on the oxidation of the tetrazolium derivate XTT by vital cells, Roche, Switzerland) and subsequent vital staining (live-dead staining procedure using fluoresceine/propidium iodide double labelling, both ICN Biomedicals GmbH) combined with fluorescence microscopy were performed. Finally, alkaline phosphatase was determined using an enzymatic photometric assay including the substrate 4-nitrophenyl phosphate (Sigma) according to a described method [10].

In all quantitative determinations, triple estimates were used. All numeric data are given as means and standard deviations.

3. Results

3.1. DLF manufacturing

With the established DLF strategy, parts ranging from simple discs to more complex objects like cylinders with regular porosity were produced (Fig. 2a), which took 3 h per single part. For a batch of 40 discs with a

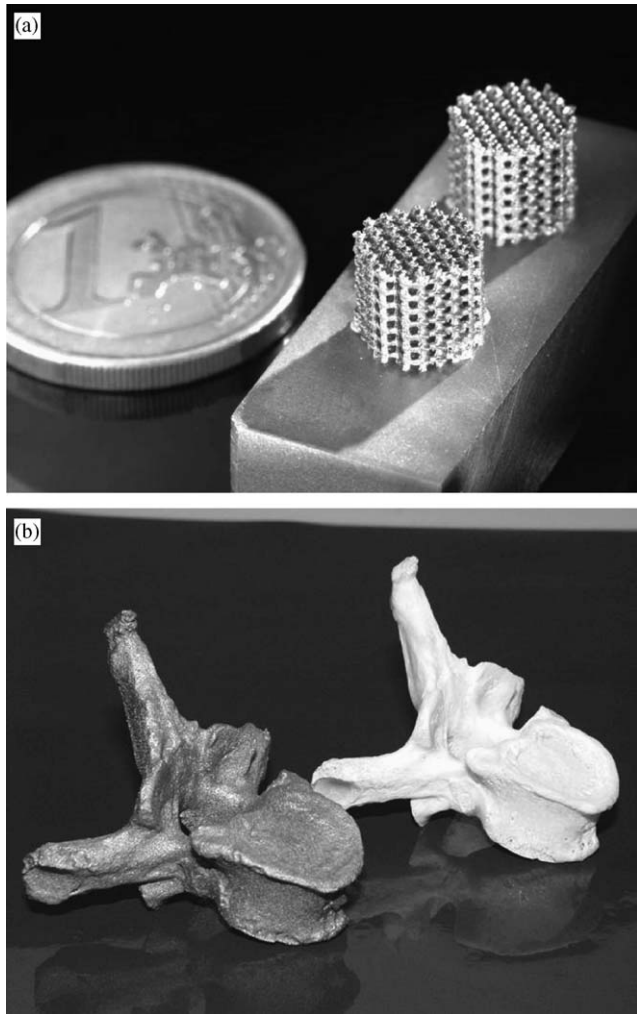


Fig. 2. Examples of DLF-fabricated Ti-6Al-4V parts, cylinders with cubic pore pattern (a), production time approx. 3 h, human vertebra (b) with original (right) and Ti-6Al-4V analog (left), production time approx. 12 h.

height of 3 mm and a diameter of 20 mm, the production time was approx. 7 h. To demonstrate the potential of the DLF technology, we scanned the model of a human vertebra and produced a titanium analog via DLF (Fig. 2b), which took approx. 12 h.

Unfinished, the surface of DLF-fabricated objects typically had a granulated appearance, as visualized by scanning electron microscopy (SEM, Fig. 3a). Parts of the surface area were covered with spherical particles which had diameters from 25 to 45 μm . Macroscopically, we noticed a sedimentation of metal powder in incubation vessels in which DLF parts had been stored, which indicated that the observed particles were only loosely associated with the surface. As a consequence, further DLF batches underwent corundum and glass pearl blasting in order to remove the particle layer. The surface of blasted DLF material appeared to be almost particle-free (Fig. 3b) and showed a groove-like structuring. Additionally, small pinpoint defects were

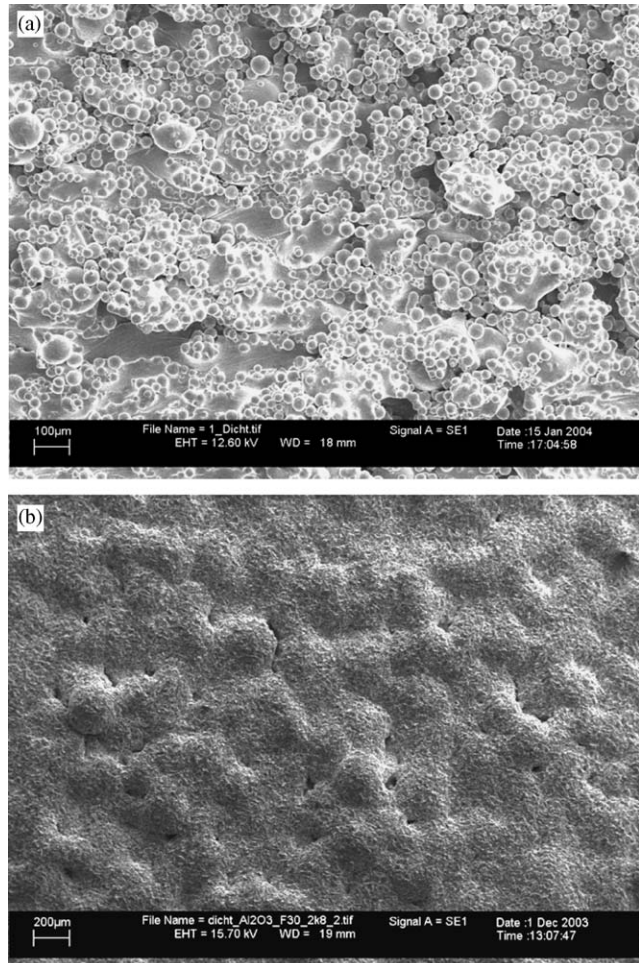


Fig. 3. DLF-fabricated Ti-6Al-4V, SEM imaging of surface before (a) and after sandblasting (b). Note the layer of globular particles on the untreated material, which was completely removed after the treatment.

observed. After storage of such treated material, no visible sedimentation occurred in the respective vessels. We established sandblasting as a standard finishing step.

We produced discs with parallel cylindrical pores in a regular offset pattern and characterized them by SEM to estimate the resolution and accuracy of the DLF process. A SEM image of a disc with a nominal pore diameter of 1000 μm is shown in Fig. 4. The actual diameters of two of the pores were estimated. The circle was added to compare the nominal and actual dimension of one of the pores. In comparison with the nominal diameter, the actual pore diameter was reduced to approx. 700 μm . In other terms, the rims of the pores were thickened in the range of 150 μm . A comparable range of reduction was observed in DLF batches with nominal pore diameters of 500 and 700 μm , which resulted in actual diameters of approx. 200 and 400 μm , respectively (not shown). This result indicated that the DLF process caused a defined overhang during

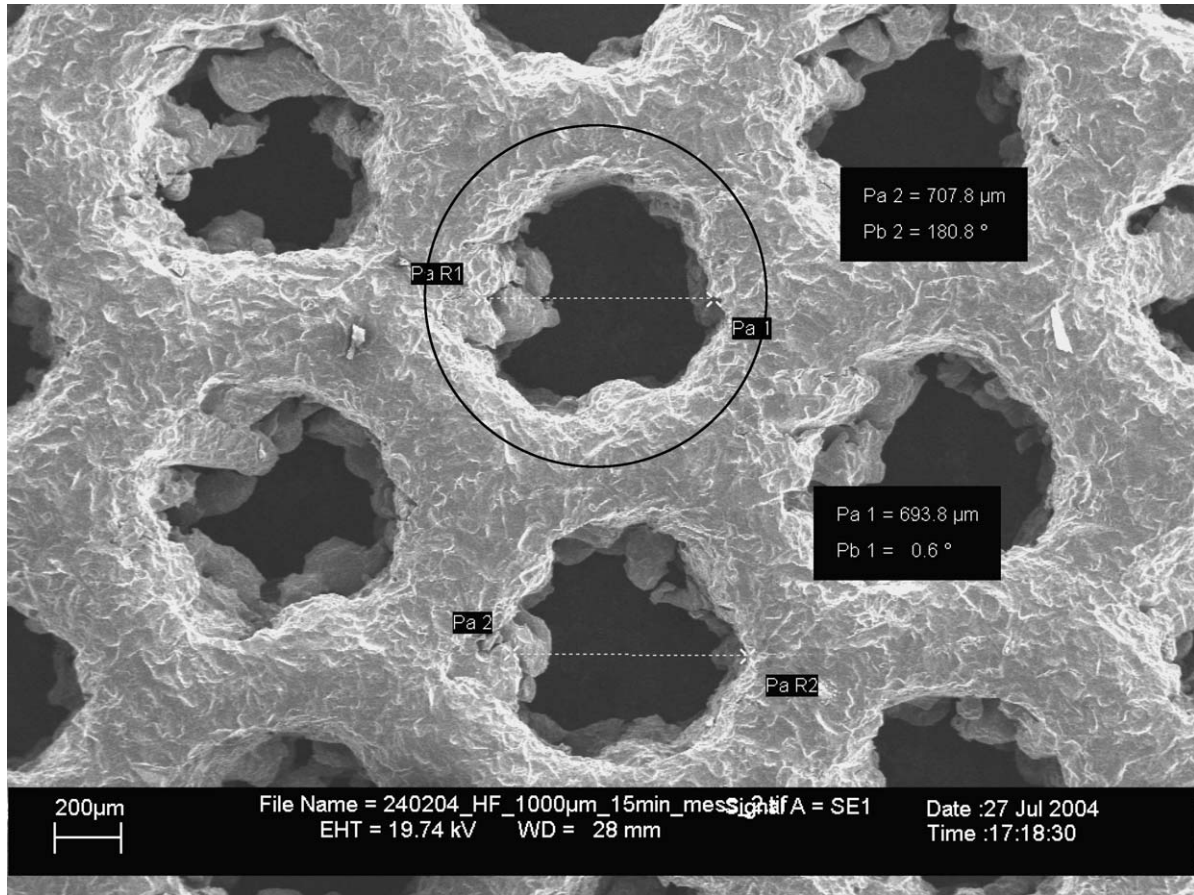


Fig. 4. DLF-fabricated porous Ti-6Al-4V disc with a nominal pore diameter of 1000 μm (indicated as black circle), measurement of actual pore diameters. The nominal pore dimensions were reduced to approx. 700 μm , indicating a defined processing overhang of approx. 150 μm .

sintering. While the pores were continuous and roughly cylindrical, the inner surface of the pores had an irregular appearance with some structures protruding into the pore lumens (dimensions max. 300 μm).

3.2. Mechanical testing

3.2.1. Tensile testing and Young's modulus

We tested tensile and yield strengths of DLF-Ti-6Al-4V with regard to ASTM specifications for the usage of this alloy as a medical material. The results are shown in Fig. 5. Tensile and yield strengths of untreated DLF-Ti-6Al-4V were 1211 ± 31 and 1100 ± 12 MPa, respectively, which clearly surpassed ASTM limits (860 and 795 MPa). With $6.5 \pm 0.6\%$, the breaking elongation of this material was below the respective ASTM limit (10%). Therefore, a set of DLF specimens underwent an additional annealing heat treatment. While the breaking elongation of this annealed DLF-Ti-6Al-4V was increased approximately two-fold to $13.0 \pm 0.6\%$, tensile and yield strengths were reduced by approximately 8% in comparison to untreated material (1042 ± 20 and 960 ± 19 MPa, respectively), but did not fall below the

ASTM limits. All tensile testing data derived from annealed DLF-Ti-6Al-4V matched the mentioned ASTM specifications and were in the same range as respective values derived from conventionally wrought annealed titanium alloy, which is shown for comparison. We conclude that annealing of DLF-fabricated Ti-6Al-4V increased ductility, while tensile and yield strengths were moderately impaired by this treatment. Both untreated and annealed DLF material conditions showed a Young's modulus of 118.000 ± 2.300 MPa (standard: 110.000 MPa).

3.2.2. Rotating bending fatigue testing

Post-DLF annealed Ti-6Al-4V underwent rotating bending fatigue testing. The results are shown in a standard Woehler diagram (Fig. 6). The array displayed contains all 28 tested experimental configurations of tensile strain and corresponding cycles to failure. The variation observed especially in the low cycles area ($< 10^7$ cycles) ranged up to ± 110 MPa. The high cycle fatigue strength was 375 ± 25 MPa. In comparison to traditional fabrication technologies such as casting, casting/hot isostatic pressing (HIP) and

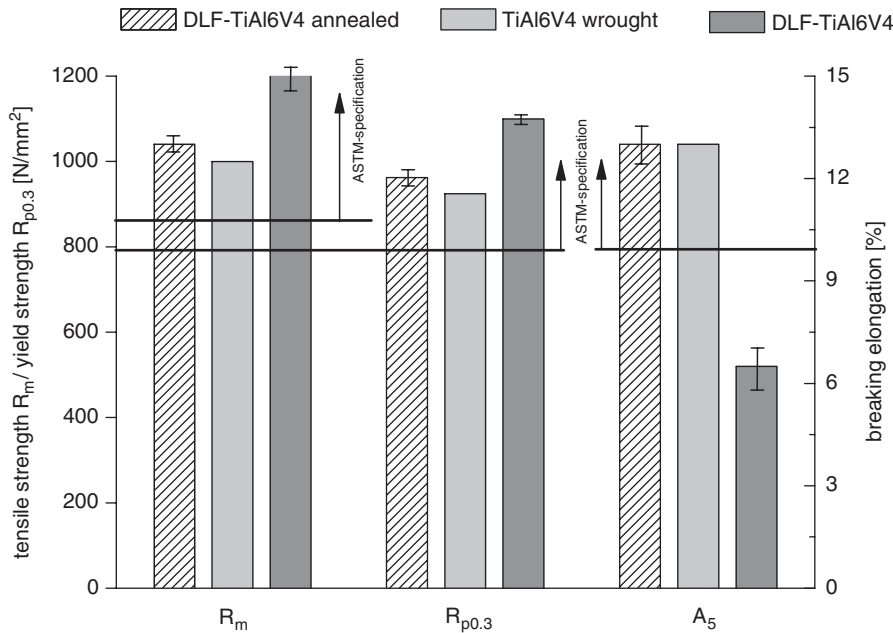


Fig. 5. Tensile and yield strengths and breaking elongation of DLF-Ti–6Al–4V before and after post-DLF annealing treatment in comparison to wrought annealed Ti–6Al–4V. Annealed DLF-Ti–6Al–4V surpassed the recommended ASTM limits of all investigated parameters.

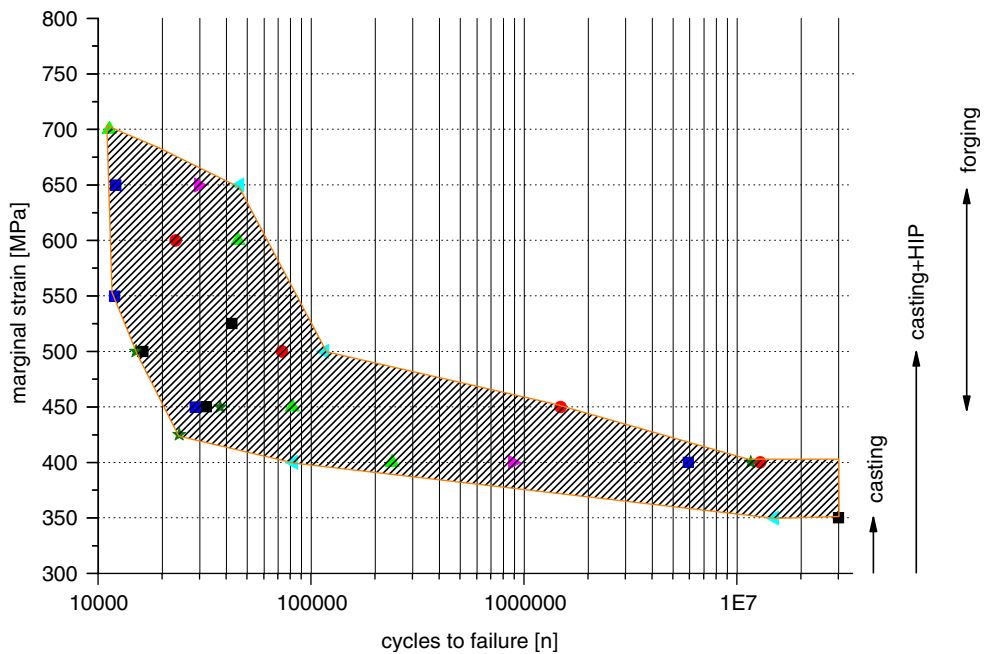


Fig. 6. Rotating bending fatigue testing of annealed DLF-Ti–6Al–4V. Ranges of casted, casted/hot isostatic pressed and forged titanium alloy are shown on the right hand. Fatigue characteristics of the DLF material ranged above casted and below forged Ti–6Al–4V.

forging, rotating bending fatigue of DLF-Ti–6Al–4V was in the same range as casted/HIP-treated alloy.

3.3. In vitro experiments

Human osteoblasts (HOB) were cultured on sandblasted DLF-fabricated Ti–6Al–4V discs for 3, 7 and 14

days. Standard cell culture plastic was used as control. Triple estimates were used. The HOB cultures underwent XTT assaying to investigate proliferation of the cells. Over 14 days of culturing, the relative XTT activity of HOB grown on DLF material was increased approx. 2.5-fold, which pointed out that the cultures were vital and proliferating. Vitality of the cells was proved by

live/dead staining, which showed that vital cells had grown on the DLF material with only few isolated disrupted individuals (Fig. 7a). Spreading of single HOB on the surface was moderately less in comparison with cell culture plastic, which was used as control (Fig. 7b). Alkaline phosphatase was clearly detectable in the HOB cultures by the used enzymatic assay, which indicated osteoblast-specific differentiation of the cultures.

To investigate the influence of porosity, we cultured HOB on porous DLF-Ti–6Al–4V discs with nominal pore diameters of 500, 700 and 1000 μm, respectively. After 14 days, live/dead staining was performed to visualize the structure of HOB cultures. The specimens of the 500 μm group were apparently overgrown with cells (Fig. 7c). The cultures covered most of the pores and hid them from external view. In contrast, the HOB cultures on the specimens of the 700 and 1000 μm group did not completely overgrow the pores, but showed a circular-shaped growth pattern along the pore rims (1000 μm group, Fig. 7d). Some of the pores were completely filled with cells. SEM imaging corroborated the live/dead staining results (Fig. 7e,f). Again, an orientation of the cells along the pore rims and a vortex-like appearance was evident on the specimen with 1000 μm pores. The in vitro experiments demonstrated that DLF-fabricated Ti–6Al–4V allowed structure-oriented growth of human osteoblasts on its surface.

4. Discussion

While the RP method SLS has been described since the last decade [1], establishment of the related DLF is still under way. The performance of DLF processing depends on several parameters, which include dimension of the laser focus, power rating of the laser, scanning speed, average particle size of the used material powder, layer thickness, track overlap (Fig. 1) and process atmosphere conditions. At the ILT, DLF processing of Ti–6Al–4V is being optimized taking into account each of the mentioned parameters. Main focus is on proper material processing to reach homogeneous material deposition with a resulting density as close as possible to 100%, which is a premise for higher mechanical strength. The actually used DLF configuration proved to be effective for the rapid fabrication of individually structured Ti–6Al–4V parts with a resolution of 150 μm. The results gained from static mechanical testing of DLF-Ti–6Al–4V were satisfactory since tensile and yield strengths matched ASTM specifications, with the addition that post-DLF annealing was necessary to surpass the ASTM limit for breaking elongation. While the moderate reduction of tensile and yield strengths after annealing was expected, this did not lead to an exclusion according to ASTM criteria. On the other side, the fatigue test results did not fully comply with expecta-

tions. Taking into consideration that the fabrication process is carried out under inert gas atmosphere and thus no chemical contamination should occur, the question arises whether high cycle fatigue strength is comparable with casted parts rather than forged parts. Therefore, the main effort is put in investigations regarding chemical composition and microstructure composition to understand and improve the combination of process guidance and corresponding mechanical properties. Since the specimens used for mechanical testing were turned after DLF manufacturing, no statement can be made on the effect of surface structuring/defects of raw DLF material on the mechanical properties.

According to the microscopical characterization of the presented products, the resolution of the actually used DLF configuration was estimated to be approx. 150 μm, which equals the observed overhang at structure rims. Regarding the prospect of a porous biomaterial for hard tissue replacement, the described resolution allows pore structuring in a triple-digit micron range, which covers the dimensions considered to be effective for bone tissue ingrowth [11,12].

Unfinished, the surface of the DLF products was covered with loosely bound spherical metal particles. These particles were most likely remnants from the used basic material powder and may have sintered partially to the bulk material. With regard to the prospected use as biomaterial, the release of surface-associated particles *in vivo* would probably cause inflammation due to macrophage activation. Thus, finishing the DLF products by sandblasting was inevitable. While the grooves observed on the treated surface were caused by the sandblasting itself, the pinpoint defects were thought to be small isolated surface-accessible pores, which assumably have a negligible significance concerning the overall surface properties. Taking into consideration that the process time for rather complex parts like the human vertebra was assumably far below the prospected time for conventional fabrication, this additional step was thought to play a minor role concerning the total production time. On the other side, we assume that this finishing method may not be able to remove particles out of complex volumetric pore systems. Therefore, alternative methods have to be considered, which cover the entire accessible surface of the object. We currently compare sandblasting with chemical etching.

The in vitro experiments showed that DLF-fabricated sandblasted Ti–6Al–4V allowed spreading and growth of vital human osteoblasts on its surface, which was comparable to the well-known biological characteristics of conventionally fabricated Ti–6Al–4V [13–15]. We conclude that the DLF manufacturing process did not lead to any disadvantageous alteration of the chemical/biological properties of the material.

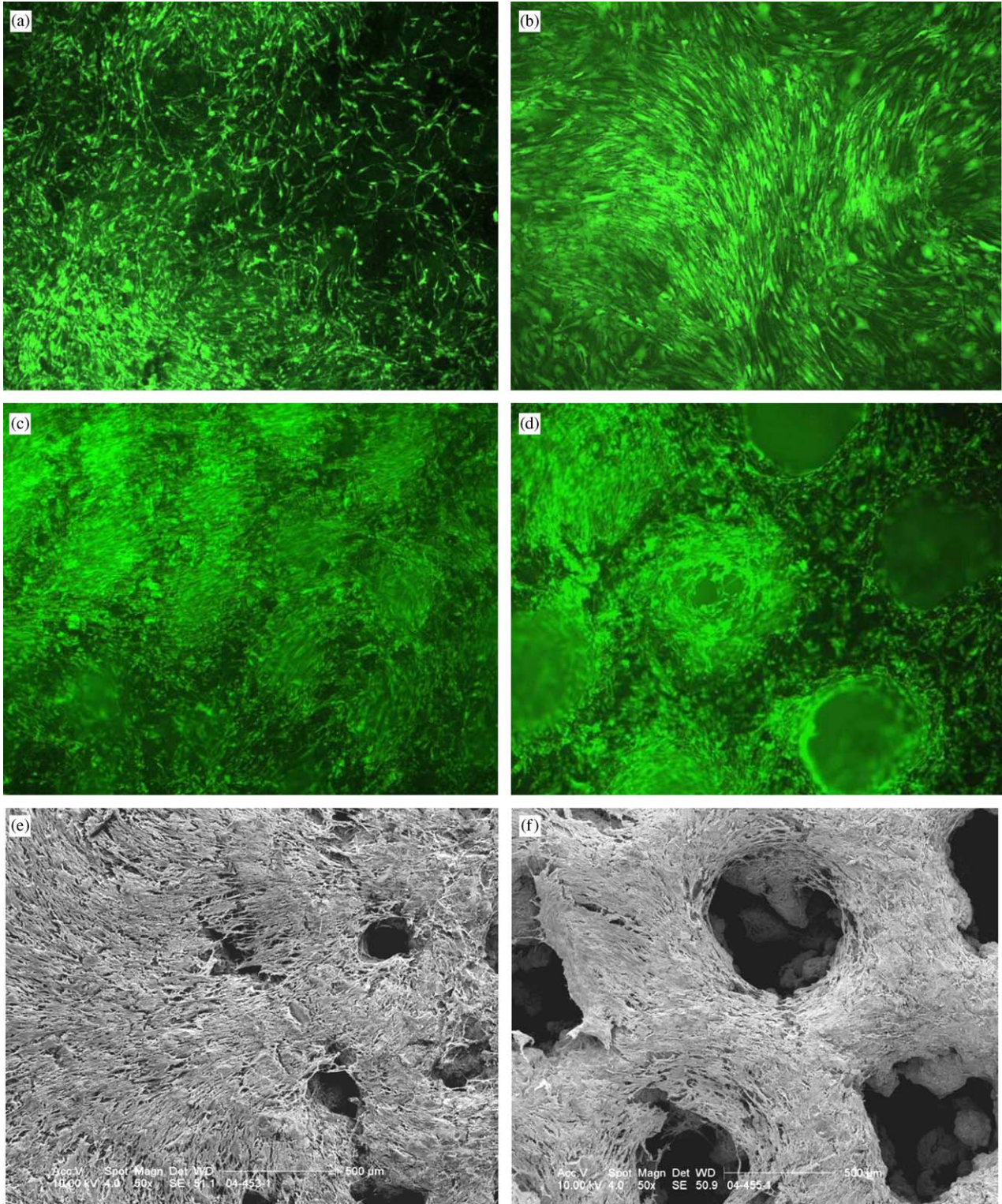


Fig. 7. DLF Ti-6Al-4V in vitro, human osteoblasts after 14 days of culturing, live/dead stain of cells on non-porous material (a) and cell culture plastic as control (b), live/dead stain of culture on porous substrate with a nominal pore diameter of 500 μm (c) and 1000 μm (d), SEM images from the same specimens (e, f). Some of the pores were filled with cells, which had grown along the pore rims in a circular-shaped manner.

As a conclusion, we state that the RP technique DLF proved to be reasonable and effective for the production of tailored Ti-6Al-4V parts, bearing in mind that additional treatment including annealing

and surface blasting was necessary in order to meet essential mechanical and surface criteria recommended for biomaterials in the field of hard tissue substitution.

Acknowledgments

We thank Mrs. Raby for excellent technical assistance. This work was supported by the German Federal Ministry of Education and Research (BMBF), Projektträger Jülich, Förderkennzeichen 03N4032.

References

- [1] Zong G, Wu Y, Tran N, Lee I, Bourell DL, Beaman JJ, et al. Direct selective laser sintering of high-temperature materials. In: Proceedings of the solid freeform fabrication, 1992. p. 72–85.
- [2] Meiners W, Over C, Wissenbach K, Poprawe R. Direct generation of metal parts and tools by selective laser powder Remelting (SLPR). In: Proceedings of the solid freeform fabrication symposium, Austin, Texas, 1999.
- [3] Berry E, Brown JM, Connell M, Craven CM, Efford ND, Radjenovic A, et al. Preliminary experience with medical applications of rapid prototyping by selective laser sintering. *Med Eng Phys* 1997;19(1):90–6.
- [4] Leong KF, Cheah CM, Chua CK. Solid freeform fabrication of three-dimensional scaffolds for engineering replacement tissues and organs. *Biomaterials* 2003;24(13):2363–78.
- [5] Tan KH, Chua CK, Leong KF, Cheah CM, Gui WS, Tan WS, et al. Selective laser sintering of biocompatible polymers for applications in tissue engineering. *Biomed Mater Eng* 2005;15(1–2):113–24.
- [6] Antonov EN, Bagratashvili VN, Whitaker MJ, Barry JJA, Shakesheff KM, Konovalov AN, et al. Three-dimensional bioactive and biodegradable scaffolds fabricated by surface-selective laser sintering. *Adv Mater* 2005;17(3):327–30.
- [7] Over C. Generative Fertigung von Bauteilen aus Werkzeugstahl X38CrMoV5-1 und Ti-6Al-4V mit “Selective Laser Melting”. Dissertation, Rheinisch-Westfälische Technische Hochschule Aachen, Shaker Verlag, Aachen, 2003.
- [8] Annual Book of ASTM Standards. Medical devices and services, Section 13, vol. 13.01. 2004.
- [9] Hughes J, Aubin JE, Arnett TR, Henderson BL, editors. Methods in bone biology. London: Chapman & Hall; 1997. p. 1–49.
- [10] Sodek J, Berkman FA. Bone cell cultures. *Meth Enzymol* 1987;145:303–24.
- [11] Hulbert SF, Young FA, Mathews RS, Klawitter JJ, Talbert CD, Stelling FH. Potential of ceramic materials as permanently implantable skeletal prostheses. *J Biomed Mater Res* 1970;4(3):433–56.
- [12] Schliephake H, Neukam FW, Klosa D. Influence of pore dimensions on bone ingrowth into porous hydroxylapatite blocks used as bone graft substitutes. A histometric study. *Int J Oral Maxillofac Surg* 1991;20(1):53–8.
- [13] Williams DF. Titanium and titanium alloys. Boca Raton, FL: CRC Press; 1981.
- [14] Puleo DA, Holleran LA, Doremus RH, Bizios R. Osteoblast responses to orthopedic implant materials in vitro. *J Biomed Mater Res* 1991;25(6):711–23.
- [15] Ku CH, Pioletti DP, Browne M, Gregson PJ. Effect of different Ti-6Al-4V surface treatments on osteoblasts behaviour. *Biomaterials* 2002;23(6):1447–54.



Microstructure and tensile properties of selectively laser-melted and of HIPed laser-melted Ti–6Al–4V



Chunlei Qiu*, Nicholas J.E. Adkins, Moataz M. Attallah

School of Metallurgy and Materials, University of Birmingham, Edgbaston, Birmingham B15 2TT, UK

ARTICLE INFO

Article history:

Received 27 February 2013

Received in revised form

25 April 2013

Accepted 27 April 2013

Available online 7 May 2013

Keywords:

Selective laser melting

Hot isostatic pressing

Titanium alloys

Microstructure

Tensile behaviour

ABSTRACT

Ti–6Al–4V samples have been prepared by selective laser melting (SLM) with varied processing conditions. Some of the samples were stress-relieved or hot isostatically pressed (HIPed). The microstructures of all samples were characterised using optical microscopy (OM), scanning electron microscopy (SEM) and X-ray diffraction (XRD) and the tensile properties measured before and after HIPing. It was found that the porosity level generally decreased with increase of laser power and laser scanning speed. Horizontally built samples were found to have a higher level of porosity than vertically built samples. The as-fabricated microstructure was dominated by columnar grains and martensites. HIPing closed the majority of the pores and also fully transformed the martensite into α and β phases. The as-fabricated microstructure exhibits very high tensile strengths but poor ductility with elongation generally smaller than 10%. The horizontally built samples show even lower elongation than vertically built samples. HIPing considerably improved ductility but led to a reduction in strength. With HIPing, the SLMed samples were found to show tensile properties comparable with those thermomechanically processed and annealed samples.

Crown Copyright © 2013 Published by Elsevier B.V. All rights reserved.

1. Introduction

Selective laser melting is one of the new additive manufacturing techniques that emerged in the late 1980s and 1990s [1], which has been widely reviewed elsewhere [2]. This layer-by-layer process was first used to produce prototypes, but the trend is towards direct manufacture of components because of its ability to net-shape manufacture complex structures from a computer-aided design model in a wide range of materials without the need of expensive tooling and machining so that the delay between design and manufacture is minimised. Another advantage is that powder is melted only locally by the laser and the rest of the powder can be recycled for further fabrication. This technology, therefore, is of particular interest to aerospace or biomedical industries where complex components or structures are usually required and processing of them using conventional route (cast+forging +machining) is usually time-consuming and expensive. However, this new manufacturing technique also needs to deal with some frequently observed problems. In terms of SLM of aerospace materials such as nickel-based superalloys [3–6] and Ti-based alloys [7–16], the common issues include cracking (especially for high γ' volume fraction nickel-based superalloys) [3,4],

porosity [4,8], residual stresses due to the high thermal gradient induced by rapid melting and cooling [5,8,9], columnar grain structure and strongly textured microstructures [4–11], and anisotropy in mechanical properties [5,10–11]. All of these issues have been well recognised but it is also noted that there is still considerable debate about the origins for some of the issues. Thus, in terms of the formation of pores in SLMed Ti alloys such as Ti–6Al–4V, Vilaro et al. [10] attributed spherical pores to gas entrapment during melting and rapid solidification and the linear/flat pores to be the result of lack of melting. Das [17] suggested that the formation of flat or irregular-shaped pores is due to incomplete homologous melting and solidification. Thijss et al. [8] argued that the pore formation may be due to an accumulation in powder denudation around the melt pool within a layer and an accumulation of the surface roughness across the layers. There is also concern that the gas bubbles which were entrapped in some of the original powder may be carried over to the build to form pores. In this paper, we tried to look into the internal structure of pores in SLMed samples and the laser scanned tracks to better understand the formation mechanism for porosity. As far as the anisotropy in mechanical properties of SLMed Ti–6Al–4V is concerned, it is generally attributed to the presence of build defects such as porosity [10,12]. However, the influence of other factors such as microstructure and the stress loading direction relative to the grain orientation have not been fully understood.

Moreover, it is noted that considerable study on the influence of post-SLM heat treatments on the microstructure and mechanical

* Corresponding author. Tel.: +44 121 414 5163; fax: +44 121 414 7890.
E-mail address: c.qiu@bham.ac.uk (C. Qiu).

properties of SLMed Ti-6Al-4V has been conducted [10–13]. However, the influence of post-SLM hot isostatic pressing (HIPing) on the microstructure and mechanical properties of SLMed samples, aimed at improving structural integrity, microstructural and mechanical capability for industrial application, has not been fully investigated.

In this work, Ti-6Al-4V samples were fabricated by using a unique SLM scanning strategy where the build is divided into a number of square islands which are then randomly scanned in an attempt to produce a more even heat distribution. The structural integrity, surface roughness, microstructural development and the tensile properties of as-fabricated samples were examined while the influence of processing parameters, island size, stress relief heat treatment and HIPing was also investigated.

2. Experimental

The material used in this study is gas atomised Ti-6Al-4V powder supplied by TLS in the size range of 20–50 µm. A Concept Laser M2 Cusing SLM system which employs an Nd:YAG laser with a wavelength of 1075 nm and a maximum laser output power of 200 W measured in continuous wave mode was used to prepare samples for microstructural characterisation and mechanical testing. As mentioned above, this system operates an island scanning strategy in which the build is divided into a number of square 'islands'; see Fig. 1. The islands are scanned randomly and the scan direction is rotated by 90° between neighbouring islands. When the island scanning at each layer is complete, a contour scan is performed around the build in an attempt to improve the surface finish. A laser beam with a spot size (d) of 150 µm in diameter and a hatch spacing (i.e. the distance between two neighbouring scan vectors) of 75 µm within islands have been used. The overlap of the scan vectors between two neighbouring islands is 0.15d and the overlap between the contour scan vector and the nearest raster scan vector is 0.25d. In attempt to avoid defect build up between layers, the island pattern is moved by 0.2D (D is the side length of the square islands) away from the sides of the previous island each layer. Samples were built on 245 mm × 245 mm × 30 mm Ti substrates. After building of each layer, the build platform was dropped by 20 µm before a new layer of powder was moved over the previous layer. Powder was delivered by a coater at 70 mm/s which gives a powder feed rate of around 1.5 g/s for the current setting up.

Initial process optimisation was performed on cubic samples (12 mm × 12 mm × 12 mm). Once the minimum porosity condition

was identified, the samples were scaled-up into cylindrical specimens with a diameter of 12 mm and a length of 70 mm or to a rectangular prism (12 mm × 12 mm × 70 mm) and were built both vertically and horizontally for detailed characterisation (see Fig. 2). A range of laser power (150–200 W) and laser scan speeds (800–1500 mm/s) have been investigated. The parametric study mainly focused on an island size of 1 mm × 1 mm. However, the influence of island size on structural integrity and microstructural development was also studied and a series of island sizes such as 1 mm × 1 mm, 3 mm × 3 mm, 5 mm × 5 mm and 8 mm × 8 mm were investigated.

Some of the as-fabricated samples were stress relieved at 600 °C and 700 °C, for 2 h followed by furnace cooling to limit stress-induced distortion of samples when being removed from the substrates. Some samples were further HIPed at 920 °C/103 MPa/4 h followed by furnace cooling to reduce porosity and also to optimise the microstructure. Metallographic specimens were prepared using conventional methods and examined using an optical microscope (OM) and scanning electron microscope (SEM) in a JEOL 7000 FEG-SEM microscope to reveal the pore size, distribution and morphology. To show porosity distribution over a large area of the samples, tens of OM frames were stitched to develop a whole picture of a single section. Porosity level was evaluated by measuring the area fraction (A_f) of pores using Image J software. The samples were further examined using X-ray

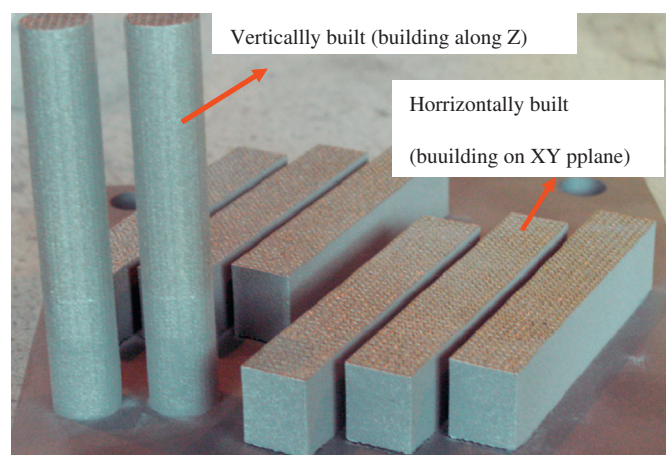


Fig. 2. A photograph showing the vertically built and horizontally built samples.

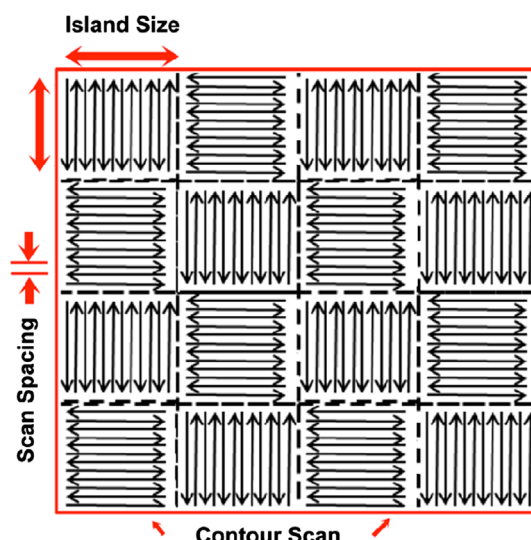


Fig. 1. The 'islands' scanning strategy on the Concept Laser M2 Cusing SLM system, and the typical chessboard morphology on the surface of a Ti-64 rectangular build.

diffraction and etched in an etchant containing 50 ml distilled water, 25 ml HNO₃ and 5 ml HF for microstructural investigation using OM and SEM. Surface roughness of the as-fabricated samples was measured by surface profilometry in a Surfcomber SE 1700 machine.

Tensile tests were performed at room temperature using a computer-controlled electric screw driven Zwick/Z100 tensile testing machine on as-fabricated and HIPed samples. Cylindrical specimens were used for the tensile testing. The vertically and horizontally built samples were tested along their axis and the tests were conducted under strain control mode with a strain rate of $1.0 \times 10^{-4} \text{ s}^{-1}$. Tensile fracture surfaces were examined using SEM.

3. Results

3.1. Characterisation of as-received powder

Fig. 3 shows secondary electron SEM images of the Ti-6Al-4V alloy powder and the particle size distribution. It can be seen that the powder particles with different sizes are distributed homogeneously. The powder particles are generally spherical but occasionally some irregular-shaped particles could be observed; see **Fig. 3(b)**. Moreover, large powder particles usually have some satellite particles with diameter smaller than 10 μm . The particle microstructure shows a typical needle-like martensitic structure (see **Fig. 3(c)**) due to the rapid cooling during gas atomisation (GA). Occasionally, pores are present in some of the powder particles probably due to gas being entrapped in these particles during GA. The powder particle size distribution analysis in **Fig. 3(d)** suggests that more than 90% of the powder particles fall in the size range of 20–50 μm , which is generally consistent with the specification. The average diameter of the particles was found to be 35.5 μm and the median size 36.5 μm . The figure also shows a very small fraction (< 5%) of particles with sizes smaller than 10 μm which obviously corresponds to the satellite particles as mentioned above; also see **Fig. 3(b)**. These very fine particles together with the irregular-shaped particles, due to their small volume fraction, do not seem to affect the overall powder flowability significantly in the present

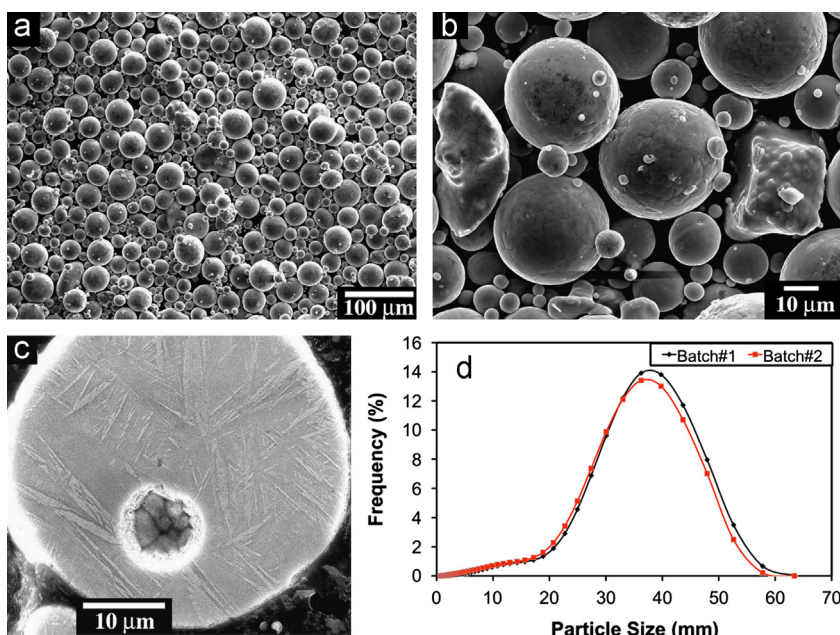


Fig. 3. Secondary electron SEM images showing (a) most of the powder particles are spherical and that particles with different sizes are distributed homogeneously, (b) some irregular-shaped powder particles, (c) a gas bubble and martensitic needle structure present in the as-received powder, and (d) powder particle size distribution.

work since the powders were found to spread evenly during SLM process.

3.2. Porosity and sample surface morphology

Fig. 4 shows the dependence of porosity fraction of cube samples on laser power for three different scan speeds, f_1 , f_2 and f_3 . It can be seen that within the range of processing parameters investigated, the porosity fraction decreased generally with increased laser power and laser scanning speed. It seems that with high laser powers (150–200 W) and thin powder layer thickness (20 μm) used in the current study, the laser scanning can go faster without causing increased porosity, which at the same time obviously improves the building efficiency. However, with further increased scanning speed while keeping the laser power constant, the porosity level may inevitably rise due to decreased energy input and lack of fusion. The dependence of porosity level on processing condition suggests that most of the pores formed in the as-fabricated samples should not be attributed to the inheritance of gas-filled pores that have been present in the gas-atomised powder.

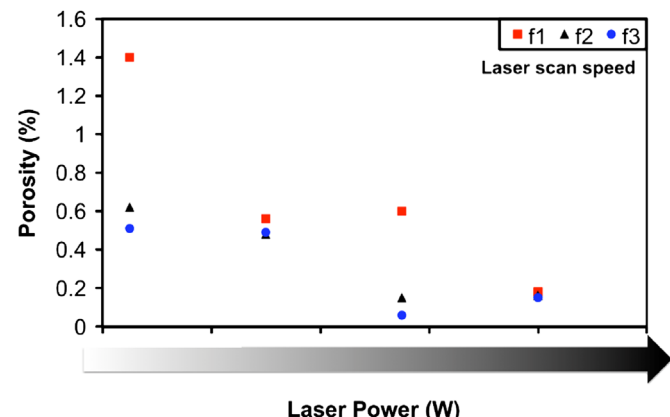


Fig. 4. Dependence of porosity level (area fraction) on laser power and laser scan speed ($f_1 < f_2 < f_3$).

The minimum porosity level that can be achieved in the present cubic samples is around 0.1%. However, when applying the optimum condition developed based on the study of cubic samples to the fabrication of big cylindrical or elongated samples, it was found that the horizontally built samples tend to have a higher level of porosity than vertically built samples, as shown in Fig. 5. The pores appear to form mainly at the interface between two adjacent layers and show a size ranging from 10 μm to 50 μm in diameter; see Fig. 6. The pores are generally near-spherical and show ridges inside. In terms of the morphology, the current pores are very different from the typical pores that are due to incomplete re-melting and lack of fusion [10,17]. The latter are usually either flat or irregular-shaped with sharp angles.

Fig. 7 shows the influence of island size on porosity level of samples that have been prepared under an identical processing condition. There is no obvious difference among the samples fabricated with different island sizes; the porosity fraction for all the samples is around 0.1%. Moreover, the influence of island size on the side surface roughness of the as-fabricated samples is very limited; the samples show an average roughness Ra between

13.3 μm and 15.5 μm . A typical roughness curve for the samples built with different island sizes is shown in Fig. 8. The roughness measurement results suggest that a fairly good surface finish could be achieved by SLM.

Fig. 9 shows the top surfaces of the samples prepared with different island sizes. The sample prepared with 1 mm \times 1 mm islands shows a very different surface feature from the samples prepared with bigger islands. The former contain a smooth region associated with a rippled rough area within each single island whereas the latter generally show an alternate pattern of a smooth island and a neighbouring rough island on the surfaces. It seems that for 1 mm \times 1 mm islands, they are so small that the molten material might have been moved with laser beam moving from one side to the other which led to the pile-up of material towards one side. This also to some extent reveals the turbulence of molten material ahead caused by the high speed movement of laser beam. The alternation of smooth and rough surface regions for samples fabricated with bigger islands is believed to be due to the difference in powder distribution and laser scanning direction in different islands. As we can see in Fig. 9(b-d), the rough islands

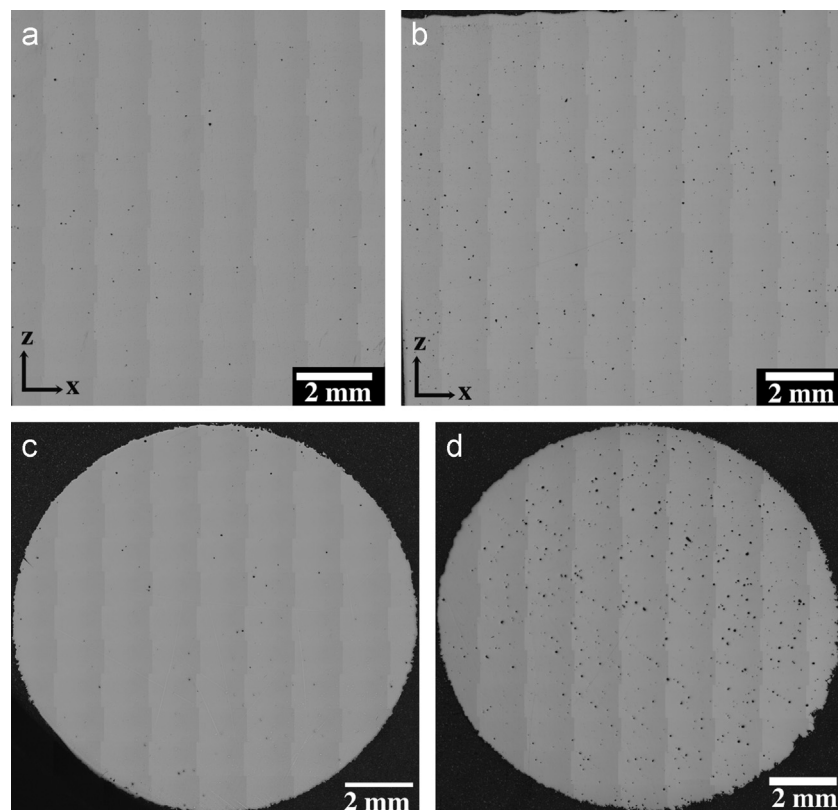


Fig. 5. Optical micrographs of longitudinal sections of (a) vertically built (porosity area fraction $A_f < 0.1\%$) and (b) horizontally built cylindrical samples ($A_f = 0.35\%$); the mid-sections of (c) vertically built ($A_f < 0.1\%$) and (d) horizontally built ($A_f = 0.9\%$) cylindrical samples. The grey vertical lines in the figures are stitching lines between stitched frames.

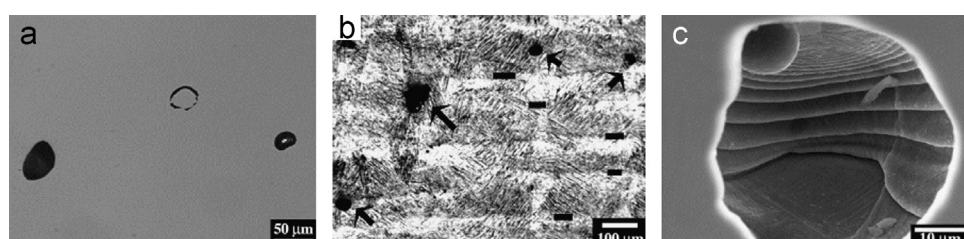


Fig. 6. The size, locations and morphology of pores in as-fabricated samples, (a) and (b) optical micrographs; (c) secondary electron SEM images. The arrows in (b) show the pores present in the as-fabricated samples and the horizontal short lines show the interface between layers.

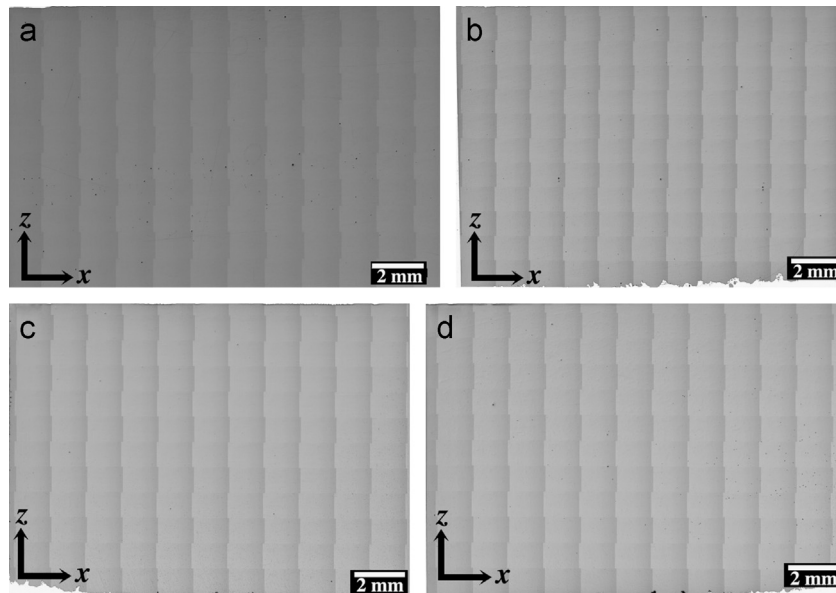


Fig. 7. Optical micrographs of samples built with different island sizes, (a) $1\text{ mm} \times 1\text{ mm}$, $A_f=0.04\%$; (b) $3\text{ mm} \times 3\text{ mm}$, $A_f=0.08\%$; (c) $5\text{ mm} \times 5\text{ mm}$, $A_f=0.03\%$; (d) $8\text{ mm} \times 8\text{ mm}$, $A_f=0.14\%$.

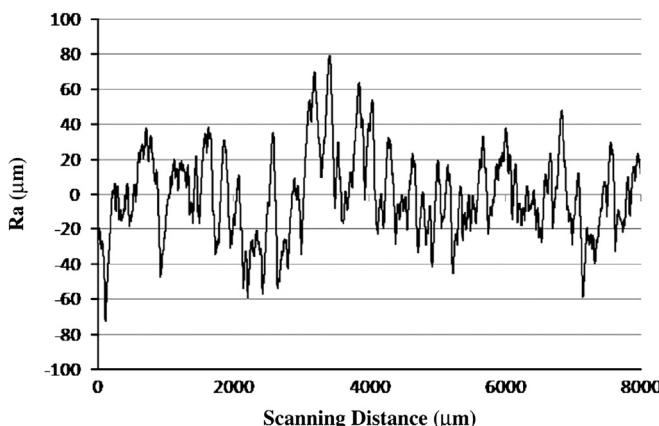


Fig. 8. A typical roughness curve for the side surfaces of samples fabricated with different island sizes.

contain ridges (corresponding to the laser scanned tracks) and valleys (corresponding to the overlaps between two laser scanned tracks). The valleys would be filled with more powder in the following layer and with island shift between layers these rough islands would become smooth during the laser scanning of the following layer whereas for the smooth islands, ridges and valleys may be formed in the following layer building. In addition, some pores could be directly observed right in the middle of laser scanning tracks; see Fig. 9(e–g). These pores are open, suggesting that they were not formed due to gas entrapment during SLM. Instead, we can see clearly the material spread over the surface of the previous layer but the solidification fronts at the pores do not seem to get connected, which may be either due to insufficient feeding of molten material to the solidification fronts or because the localised surface was not fully re-melted and the molten material failed to spread continuously or completely over the surface before solidification was completed. These pores would obviously remain in the builds as defects during the subsequent building. Quite a few incompletely melted particles are also present on the top surfaces. Gu et al. [18] suggested that these particles are due to balling but it is also possible that they are simply due to those particles that were splashed when the laser beam hit the

powder layer (which usually happens) and that may have been partially melted and dropped back to decorate the hot build surfaces. Also, it is noted that balling usually leads to the formation of irregular-shaped pores in the build [17] but in the present study this was not observed.

HIPing has been performed on the SLMed samples to further reduce porosity level. Its influence on the porosity level of SLMed samples is shown in Fig. 10(a–b). It is obvious that HIPing has closed almost all the porosity in as-fabricated samples. To find out whether the closed pores could be reopened during a post-HIP heat treatment (which is usually highly likely if the pores are filled with gas and the heat treatment temperature is high [19]), a high temperature heat treatment (at $920\text{ }^{\circ}\text{C}/4\text{ h}$) has been conducted on the SLMed and HIPed samples and the result is shown in Fig. 10(c). The heat treatment does not lead to obvious increase in porosity level, which again suggests that most of the pores in as-fabricated samples are not due to gas entrapment in molten material during SLM.

3.3. Microstructure

Fig. 11 shows the microstructure of as-fabricated Ti-6Al-4V samples. It can be seen that both vertically and horizontally built samples are dominated by columnar grains which tend to elongate along the building direction (i.e. Z direction). These columnar grains usually grow over many layers of building and can easily reach 3 mm in length with a width of only 0.2–0.3 mm, giving rise to an aspect ratio of 10–15. Within the grains, martensitic needles are obvious. These needles are generally inclined at about 40° to the building direction and very often show a herringbone pattern (highlighted by the red lines). This, according to reference [13], is due to a special Burgers relation between α/α' phase and β phase which dictates the α' growth orientation during fast cooling of SLM.

Fig. 12 shows the microstructure of post-SLM heat treated and HIPed samples. The needle structure still dominates in these samples. When samples were annealed at $700\text{ }^{\circ}\text{C}$, alpha plates started forming at the boundaries of some of the original martensitic needles although a significant number of needles could still be observed. The alpha plates appear to be horizontal, e.g., normal to the building direction. This is consistent with the previous

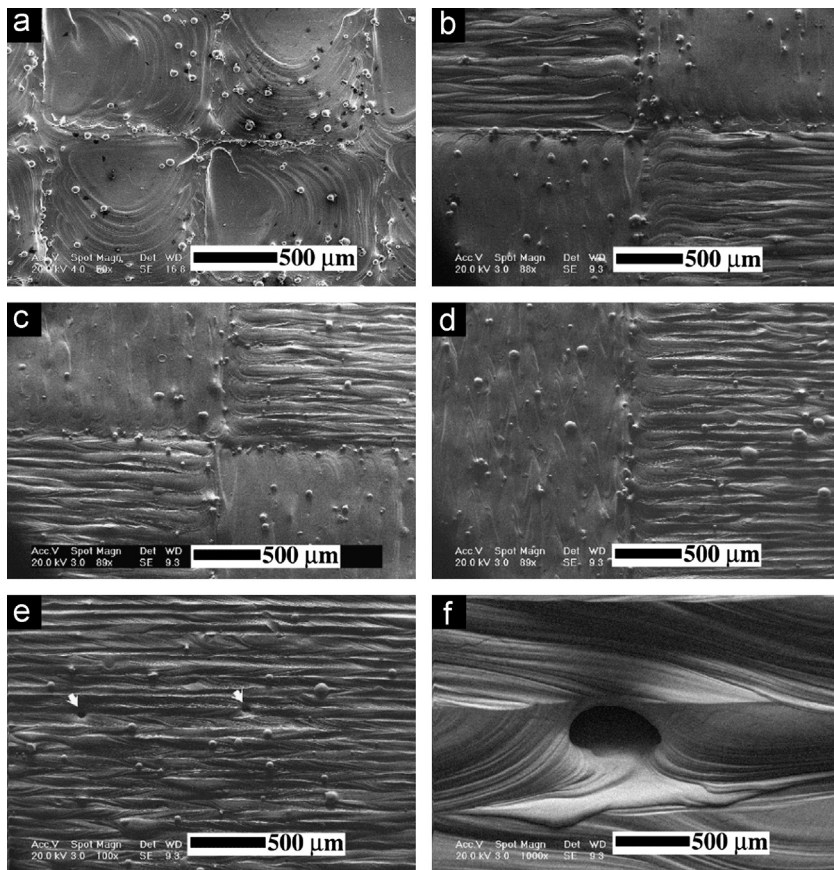


Fig. 9. Secondary electron SEM images of top surfaces of the samples that were fabricated with different island sizes, (a) 1 mm × 1 mm; (b) 3 mm × 3 mm; (c) 5 mm × 5 mm; (d) 8 mm × 8 mm; (e and f) showing that some pores were directly observed on the laser scanned tracks. The arrows show the solidification fronts at a pore.

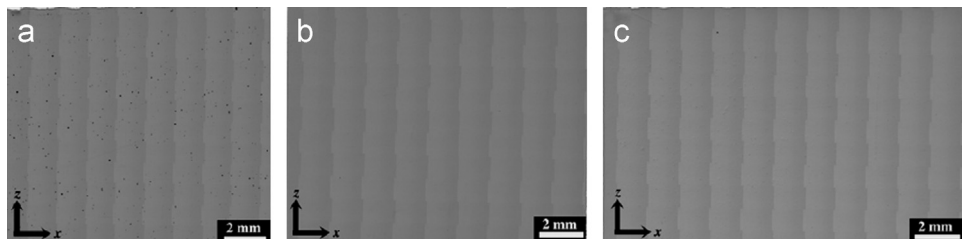


Fig. 10. Optical micrographs of (a) As-fabricated, horizontally built sample, $A_f=0.35\%$; (b) SLMed+HIPed sample, $A_f<0.01\%$ (c) post-HIP heat treated sample, $A_f=0.01\%$.

observation on the formation of alpha plates from martensitic structure in SLMed samples [9]. In the stress relieved and HIPed samples, the horizontal plates are present throughout together with some remaining needles; see Fig. 12(c). These needles, however, have been transformed into alpha plates given the high HIPing temperature (920 °C) used as shown by XRD analysis shown below. The OM observation results are consistent with the SEM observation as can be seen in Fig. 13 where the fine needle structure dominates in as-fabricated samples while alpha plates are predominant in HIPed samples. By virtue of atomic number contrast in the back scatter electron SEM image, those bright particles or plates observed in Fig. 13(c) could be attributed to beta phase. XRD was further used to characterise the microstructure and the result is shown in Fig. 14. It can be seen that neither the as-fabricated nor the stress-relieved (600 °C) samples displayed any β peaks. However, following stress relief at 700 °C or HIPing, β peaks start to appear. Moreover, a slight shift in the α -phase peaks to lower 2θ angles was observed following stress relief, suggesting that the $\alpha' \rightarrow \alpha$ transformation has occurred during stress relief. HIPing, however, moves the α -phase peaks to

larger 2θ angles with respect to 700 °C stress relief towards 600 °C stress relief, which may be due to the solute redistribution at high HIPing temperature.

3.4. Tensile properties and fracture mechanisms

Fig. 15 shows the tensile testing results for as-fabricated and HIPed samples. It can be seen that the as-fabricated samples generally show high 0.2% yield strength (> 1000 MPa) and ultimate tensile strength (UTS, ~1200 MPa) but exhibit fairly low elongation ($< 10\%$). HIPing resulted in a limited decrease in both the 0.2% yield strength and UTS but led to a considerable improvement in ductility for both orientations (vertical and horizontal). With the improvement in ductility through HIPing, the SLMed samples become more competitive as compared with the conventionally hot worked and annealed Ti-6Al-4V. Actually, the current SLMed and HIPed samples show even higher 0.2% yield strength (925–1000 MPa) and UTS (1000–1100 MPa) than the hot worked and annealed samples which exhibit a typical 0.2% yield strength of 790 ± 20 MPa and a UTS of 870 ± 10 MPa [9]. The

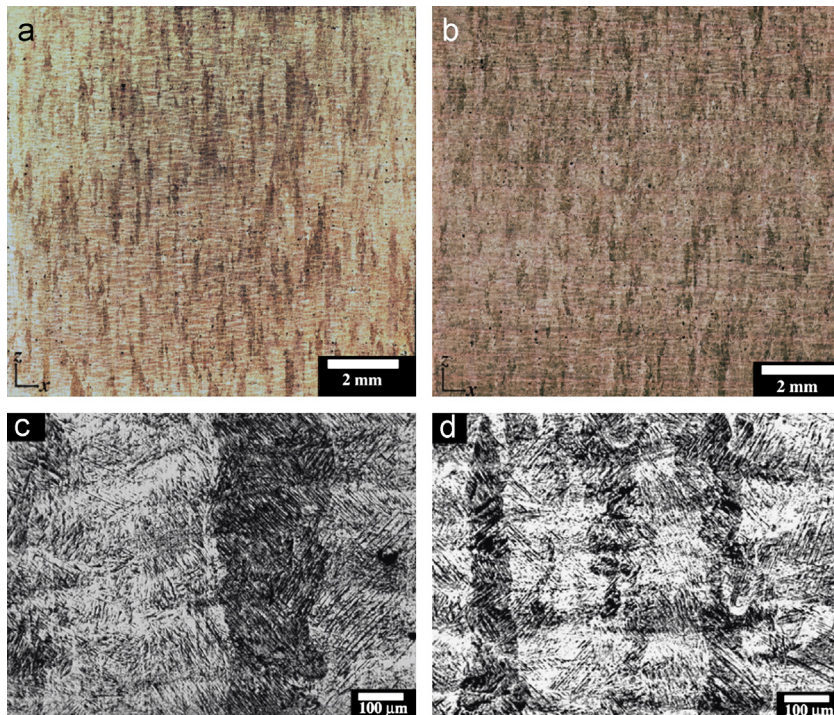


Fig. 11. Optical micrographs showing predominant columnar grain structure in (a and c) vertically built samples and (b and d) horizontally built samples. The zigzag lines show the growth orientations of martensitic needles. (For interpretation of the references to color in this figure, the reader is referred to the web version of this article.)

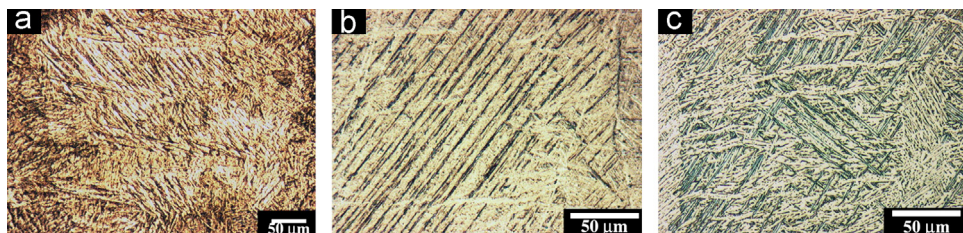


Fig. 12. Optical micrographs showing microstructure of (a) SLMed sample that was annealed at 600 °C, (b) SLMed sample that was annealed at 700 °C, showing that alpha plates formed at the boundaries of the original martensitic plates, and (c) SLMed and HIPed sample.

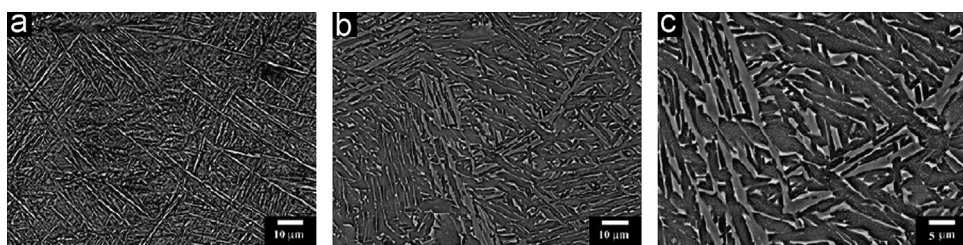


Fig. 13. Back scattered SEM micrographs showing (a) martensitic needle-like microstructure in as-fabricated samples; (b and c) microstructure of SLMed and HIPed samples.

ductility with elongations of 12–18% for the SLMed+HIPed samples is also comparable to the latter which generally show an elongation around 18%. Moreover, the elimination of porosity by HIPing as shown above would be good for other mechanical properties such as fatigue.

Also, according to the figure, the vertically-built specimens seem to show a generally higher elongation than the horizontally-built ones for either as-fabricated (7–10% against 4–6%) or HIPed condition (15–18% against 12–13%). The mechanical anisotropy in laser fabricated Ti-based alloys has been well recognised in previous reports but most of them attributed this to the manufacturing defects such as porosity [10,12]. In the present work, porosity can be almost fully closed by HIPing but the anisotropy in ductility still remains after HIPing, which suggests that there is

another mechanism leading to the anisotropy in ductility as discussed later. To better understand this issue, an investigation on the fracture surfaces has been carried out.

Fig. 16 shows the fracture surfaces of as-fabricated and HIPed samples. It can be seen that the fracture surfaces of the horizontally built specimens contain a significant number of opened up pores. In addition, the fracture surface is characterised by lamellar/cleavage fracture pattern (see Fig. 16(b)). By contrast, the fracture surfaces of vertically built specimens show a generally ductile morphology with a much lower number of pores; see Fig. 16(c–d). No obvious pores could be observed on the fracture surfaces of SLMed and HIPed specimens despite building orientations. However, the horizontally built and HIPed samples still show layered fracture morphology as compared with the fairly ductile fracture

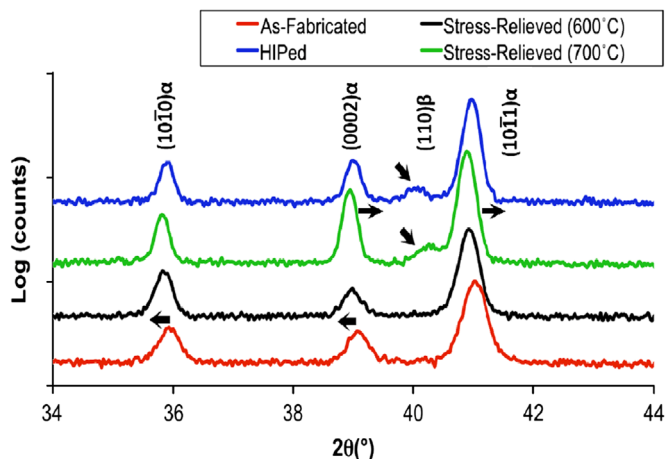


Fig. 14. XRD results for as-fabricated samples, stress-relieved samples and HIPed samples.

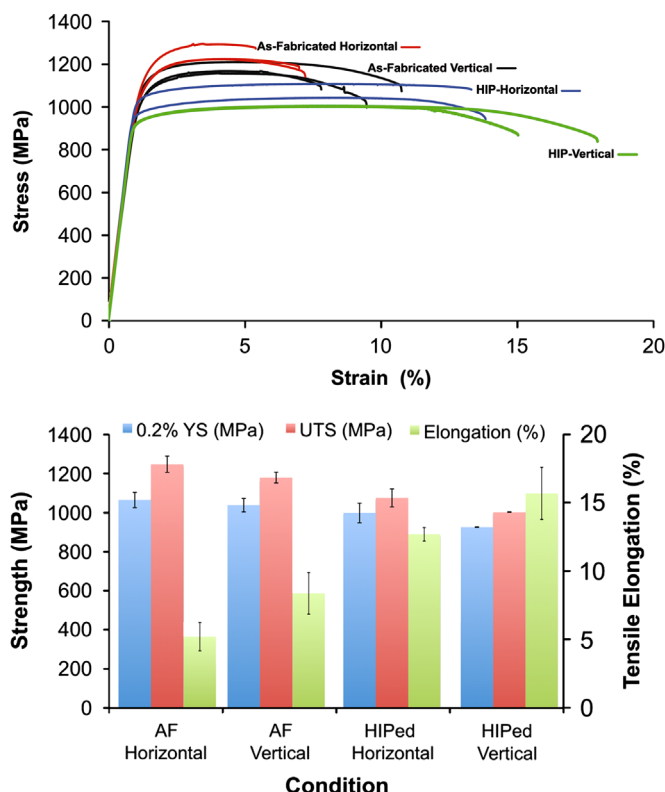


Fig. 15. Tensile properties of as-fabricated and SLMed+HIPed samples with different orientations; the horizontally and vertically built samples were tested with tensile axis along their longitudinal directions.

morphology of the vertically built and HIPed samples. Given that the microstructure of both vertically-built and horizontally-built samples is very similar, the difference in fracture mode is obviously associated with the difference in testing direction relative to the microstructural (especially columnar grain) orientation. This will be discussed in the following section.

4. Discussion

The observations have shown that both the details of the laser processing and post processing heat or HIP treatments can have significant effects on the microstructure and properties of laser

processed Ti-6Al-4V. As mentioned in the introduction there is considerable debate over the origin of the pores observed in laser processed samples and this aspect will be discussed first, before discussing the microstructures observed and the influence of post laser treatment on the porosity, the microstructure and the tensile properties.

4.1. Porosity in laser processed samples

There are clearly several different types of pores present in laser fabricated samples and whilst some of these may have been already present in the as supplied powder, the majority appear to have been formed by other mechanisms. Some of the spherical pores may be those which have been carried over from pores in the powder and other spherical pores will have been formed by gas becoming entrapped in molten metal as it solidifies during SLM. As noted above only a small fraction of pores re-open when the samples are heated to the temperature at which they were HIPed, confirming that the majority is not gas-filled. There are also flat or irregular-shaped pores which are usually formed at the interface between adjacent layers and are normally due to lack of fusion [10,17]. These kinds of pores are not observed in the current study. Instead, near-spherical pores are predominant. These pores contain ridges in internal surfaces and neither of these shapes is likely to have been formed by gas. The pores are probably formed during laser scanning and could be associated with incomplete re-melting of some localised surfaces of previous layers which slows down the spreading of molten material and are simply small volumes where molten metal was unable to penetrate. This analysis is consistent with the direct observation of pores on the laser scanning tracks; see Fig. 9(f). Open pores were found on the surfaces, further suggesting that they are not due to gas entrapment. The ridges on the inside surfaces of the pores (see Fig. 6) seem to represent the progress of solidification fronts in regions where no further feeding of molten metal occurs and that their contours reflect the complex turbulence of molten material within the solidifying region.

4.2. Influence of processing conditions on microstructure

The microstructures of all samples, i.e. the vertically and horizontally built and those built with different island sizes were all characterised by columnar crystals which in the as-grown state were martensitic, but these columnar crystals are along the axis of vertically-built samples but at right angles in the horizontally built samples. The only other obvious differences observed were in the pore densities in the vertically and horizontally built samples, where the horizontally built samples contained a significantly higher fraction of pores throughout their build height and that increased laser power and scanning speed were found to reduce porosity level.

The difference in porosity level between vertically and horizontally built cylinders and the influence of laser scan speed and laser power on pore density suggests that the detailed thermal history is important with vertically built samples (with smaller sections to be scanned at each layer) retaining heat for longer (which may be good for the re-melting of the surfaces of previous layers and for the bonding between layers), thus forming fewer pores as is observed with higher powers. The influence of laser scanning speed on porosity level in this study may have been realized by affecting the turbulence of molten pool. It is suggested that the melt pool is less stable when scanning at lower speed [8]. With increased laser scanning speed, the melt pool would become more stable and the melt spreading may be more continuous and homogeneous and thus would suppress the development of discontinuity on the laser scan tracks like those shown in Fig. 9(e–f). But if the laser scanning goes too fast, the resultant low energy input may lead to the formation of lack-of-fusion pores.

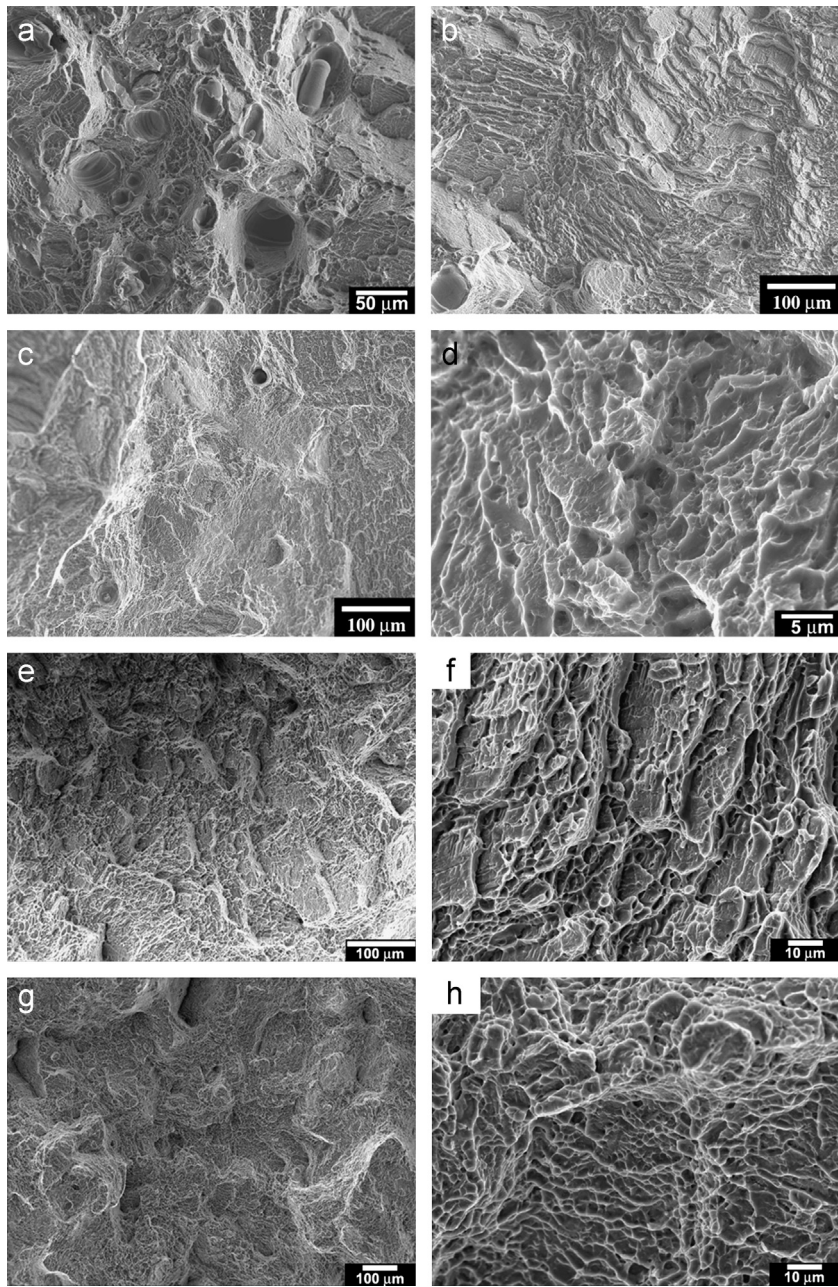


Fig. 16. Secondary electron SEM images of fracture surfaces of (a and b) horizontally built samples; (c and d) vertically built samples; (e and f) horizontally built and HIPed samples and (g and h) vertically built and HIPed samples.

Heat treatments or HIPing after laser fabrication have significant effects on the microstructure. The most obvious effect is the formation of an alpha+beta microstructure from the martensitic microstructure when heat treatment (or HIPing) is carried out at a sufficiently high temperature. The X-ray observations show beta is formed after heat treating at 700 °C although the overall morphology of the martensitic structure is maintained until large alpha plates are formed at higher temperatures. The other obvious effect of HIPing is the closure of the pores.

4.3. Strength and ductility

The properties of the horizontally and vertically built laser-fabricated samples differ only slightly. Any influence that the presence of pores would have on the tensile properties seems to be less than the influence of the orientation of the columnar grains

with respect to the tensile test direction. The vertically built samples are tested with the columnar grains parallel to the stress axis and the horizontally built samples are tested with the stress axis perpendicular to the length of the columnar grains. The fact that this difference in elongation between vertically and horizontally built samples is maintained after HIPing confirms the conclusion that the pores present in the as-built samples do not influence the tensile properties significantly. In previous work, pores which can be several hundred microns or even several millimetres in diameter, are caused by incomplete fusion between layers and thus they usually lie at interfaces between layers with flat or irregular morphology [10,17]. These pores could be easily torn apart and act as crack initiation sites when they are under tension-tension stresses whereas under compression stresses they would be closed, which obviously leads to the anisotropy in mechanical properties.

The difference in the properties is thus mainly due to the fact that the columnar grains are along the length of the tensile samples of the vertically built samples but at right angles in the horizontally built samples. This dependence of ductility on the columnar grain orientation is consistent with the SEM observation on fracture surfaces where the horizontally built samples, even after HIPing, showed generally more planar and faceted fracture morphology than the vertically built samples which exhibited a fairly dimpled ductile fracture mode. Further work is required to clarify the difference in fracture behaviour.

5. Conclusions

- (i) Near-spherical pores were found in as laser-processed Ti–6Al–4V alloys and could be mainly attributed to incomplete re-melting of some localised surface areas of the previous layer and to the insufficient feeding of molten metal to solidification fronts.
- (ii) The extent of porosity decreased with increase of laser power and laser scanning speed. Horizontally built samples showed a higher level of porosity than vertically built samples, which may be due to the difference in the thermal history.
- (iii) The microstructure in SLMed samples was dominated by columnar grains and fine martensitic needles mainly due to rapid melting and solidification.
- (iv) The as-fabricated samples have high strengths but poor ductility with horizontally built samples having poorer ductility than vertically built samples. The anisotropy in ductility is mainly due to the difference in the orientation of the columnar grains with respect to the tensile test direction.
- (v) HIPing closed almost all of the porosity and completely transformed the martensitic structure into α and β phases. This led to considerable improvement in ductility but caused reduction in strengths. With HIPing, the SLMed samples showed tensile properties comparable to those of thermomechanically processed and annealed samples.

Acknowledgements

The work shown in this paper was financially sponsored by Technology Strategy Board (TSB), UK and Rolls-Royce, plc. Thanks

are given to Professor Michael H. Loretto for useful discussion and help and to Mr. Luke Carter for support and help in operating the machine in the beginning.

References

- [1] G.N. Levy, R. Schindel, J.-P. Kruth, *Manuf. Technol.* 52 (2003) 589–609.
- [2] E.C. Santos, M. Shiomi, K. Osakada, T. Laoui, *Int. J. Mach. Tools Manuf.* 46 (2006) 1459–1468.
- [3] F. Abe, K. Osakada, M. Shiomi, K. Uematsu, M. Matsumoto, *J. Mater. Process. Technol.* 111 (2001) 210–213.
- [4] K.A. Mumtaz, P. Erasenthiran, N. Hopkinson, *J. Mater. Process. Technol.* 195 (2008) 77–87.
- [5] T. Vilaro, C. Colin, J.D. Bartout, L. Naze, M. Sennour, *Mater. Sci. Eng. A* 534 (2012) 446–451.
- [6] K.N. Amato, S.M. Gaytan, L.E. Murr, E. Martinez, P.W. Shindo, J. Hernandez, J. Collins, F. Medina, *Acta Mater.* 60 (2012) 2229–2239.
- [7] J.-P. Kruth, M. Badrossamay, E. Yasa, J. Deckers, L. Thijs, J. Van Humbeeck, Part and material properties in selective laser melting of metals, in: 16th International Symposium on Electromachining, Shanghai, 2010.
- [8] L. Thijs, L. Verhaeghe, T. Craeghs, J.V. Humbeeck, J.-P. Kruth, *Acta Mater.* 58 (2010) 3303–3312.
- [9] L. Facchini, E. Magalini, P. Robotti, A. Molinari, S. Hoges, K. Wissenbach, *Rapid Prototyp. J.* 16 (2010) 450–459.
- [10] T. Vilaro, C. Colin, J.D. Bartout, *Metall. Mater. Trans. A* 42 (2011) 190–199.
- [11] E. Yasa, J. Deckers, J.-P. Kruth, M. Rombouts, J. Luyten, *Virtual Phys. Prototyp.* 5 (2010) 89–98.
- [12] E. Chlebus, B. Kuźnicka, T. Kurzynowski, B. Dybała, *Mater. Charact.* 62 (2011) 488–495.
- [13] B. Vrancken, L. Thijs, J.-P. Kruth, J.V. Humbeeck, *J. Alloys Compd.* 541 (2012) 177–185.
- [14] L.E. Murr, S.A. Quinones, S.M. Gaytan, M.I. Lopez, A. Rodela, E.Y. Martinez, J. Mech. Behav. Biomed. Mater. 2 (2009) 20–32.
- [15] D.A. Hollander, M.V. Walter, T. Wirtz, R. Sellei, *Biomaterials* 27 (2006) 955–963.
- [16] L. Mullen, R.C. Stamp, W.K. Brooks, E. Jones, C.J. Sutcliffe, *J. Biomed. Mater. Res. Part B: Appl. Biomater.* 89 (2009) 325–334.
- [17] S. Das, *Adv. Eng. Mater.* 5 (2003) 701–711.
- [18] D.D. Gu, Y.-C. Hagedorn, W. Meiners, G.B. Meng, R.J.S. Batista, K. Wissenbach, R. Poprawe, *Acta Mater.* 60 (2012) 3849–3860.
- [19] H.V. Atkinson, S. Davies, *Metall. Mater. Trans. A* 31 (2000) 2981–3000.

Mechanical Properties of Laser-Deposited Ti-6Al-4V

P.A. Kobryn and S.L. Semiatin

Air Force Research Laboratory, AFRL/MLLMP,
Wright-Patterson Air Force Base, OH 45433-7817

Abstract

Laser additive manufacturing is a solid-freeform-fabrication process which is being investigated for titanium-component manufacturing and repair based on its cost-reduction potential and flexibility. Laser additive manufacturing also has the potential to improve mechanical properties due to the high cooling rates involved. However, the effect of the layered manufacturing process and any lack-of-fusion porosity and texture on the magnitude and anisotropy of mechanical properties is of concern. Hence, a preliminary effort was undertaken to assess these effects for bulk Ti-6Al-4V deposits manufactured using the LENSTM process. Tension, fatigue, and crack-growth tests were performed on both stress-relieved and HIP'ed deposits in three primary directions. The results were compared to published data for conventionally processed Ti-6Al-4V castings and forgings.

Introduction

Laser additive manufacturing is a solid-freeform-fabrication method which can be used to manufacture solid metallic components directly from CAD files. During laser additive manufacturing, powder is fed into a melt pool which is produced by a sharply-focused laser beam. Parts are built in a layer-by-layer fashion by rastering the laser and powder source across the substrate. Laser additive manufacturing has many potential applications, including production of functional prototypes, short-run component fabrication, component repair, and fabrication of functionally-graded materials.

Laser additive manufacturing is particularly attractive for the fabrication of titanium aerospace components because it can greatly reduce the buy-to-fly ratio and lead time for production, two factors which impact cost. Thus, a number of recent efforts have been undertaken to develop titanium laser-additive-manufacturing processes [1,2,3,4,5]. Much of the focus of this prior research has been on equipment development and mechanical property measurements [1,2]. Acceptable processing parameters have been determined largely through trial-and-error approaches. On the other hand, only limited work has been done to establish the relationship between process parameters and the structure of deposits [3,4,5]. Such an understanding is critical for both process design and control.

The work reported here is part of a larger effort to establish the effect of process parameters and input materials on deposit structure, texture, and mechanical properties. The results of efforts to characterize the effect of process parameters on structure have been described elsewhere [4,5]. The results of an initial investigation of mechanical properties in bulk Ti-6Al-4V deposits formed using the LENSTM process are described here with a focus on the relationship between properties and structure.

Materials and Procedures

Materials: The materials used in this investigation consisted of gas-atomized prealloyed Ti-6Al-4V powder made by Crucible Research and 13.23-mm-thick hot-rolled Ti-6Al-4V plate with an equiaxed-alpha microstructure. The powder had a composition (in weight percent) of 6.24 aluminum, 3.92 vanadium, 0.104 oxygen, 0.006 hydrogen, 0.007 nitrogen, 0.038 carbon, 0.047 iron, balance titanium and a mesh size of -100, +325 (particle sizes between 45 and 150 μm). The plate had a composition (in weight percent) of 6.19 aluminum, 3.89 vanadium, 0.20 oxygen, 0.0074 hydrogen, 0.01 nitrogen, 0.02 carbon, 0.12 iron, balance titanium. Prior to deposition, the plate was lapped on both sides to a surface finish of 12 to 14 μm and degreased using acetone and alcohol.

Test Material Fabrication: Two 76 mm x 76 mm x 76 mm cubes were formed in a LENS™ system using the powder and substrate material described in the previous section and the operating parameters recommended by the system manufacturer. One cube was stress relieved in vacuum for 2 hours at 700 - 730°C, while the other cube was hot isostatically pressed (HIP'ed) for 2 hours at 900°C and 100 MPa. Six cylindrical dogbone tension specimens (total length = 76 mm; gauge length = 13.5 mm; gauge diameter = 5 mm) and two ASTM E 399 compact tension specimens were extracted from each cube in each of the three primary deposition directions (Figure 1).

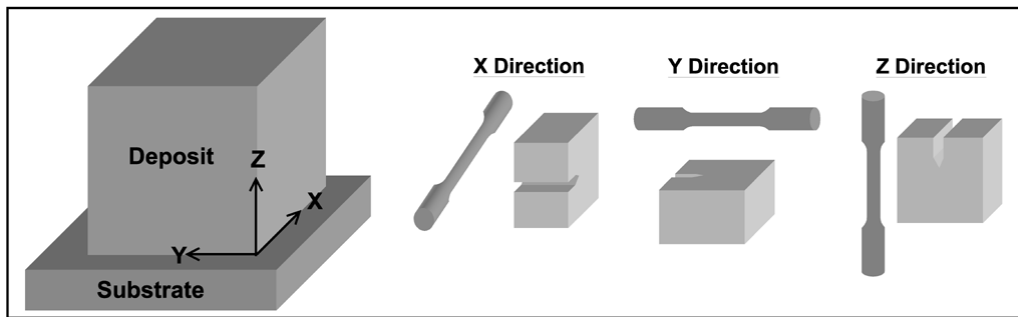


Figure 1. Illustration of the deposit geometry and the corresponding primary deposition and test-specimen directions.

Material Characterization: Remnants from each cube were sectioned, mounted, and polished using standard metallographic preparation techniques. The macrostructures and microstructures were characterized via light microscopy to assess the extent of porosity, the prior-beta grain morphology and grain size, and the morphology and scale of the transformed-beta microstructure. The crystallographic texture of the Ti-6Al-4V material produced via LENS™ was measured at a distance of approximately 6 mm from the substrate-deposit interface. It was determined using a scanning electron microscope (SEM) equipped with an electron-backscatter-diffraction (EBSD) analysis system [6].

Mechanical Testing: Standard tension tests were performed on three of the six dogbone specimens from each direction in each cube to determine the tensile yield and ultimate stresses, total elongation, and elastic modulus. The remaining dogbone specimens were used to perform fatigue tests for use in constructing an S-N fatigue curve. The compact tension specimens were used to determine fracture toughness values (i.e., $K_{I,C}$ or K_q). The fracture surfaces of all of the specimens were examined to establish the gross failure modes.

Data Analysis: The measured mechanical properties were analyzed to determine differences between different material conditions (i.e., stress-relieved vs. HIP'ed) and test directions (X, Y, and Z). The resulting tension data were also compared to published A-basis design properties for wrought, mill-annealed Ti-6Al-4V plate [7], while the fatigue and fracture-toughness data were compared to published scatterbands for cast and for wrought Ti-6Al-4V product forms [8]. Similarities and/or differences were reconciled based on the observed microstructures and texture.

Results

Microstructure/Texture: Both the stress-relieved material and the HIP'ed material contained columnar prior-beta grains with a grain size of approximately 155 μm (Figure 2a,b). A macroscopic banding (similar to that observed in previous Ti-6Al-4V material produced via LENSTTM [4]) was also evident in both materials. However, the stress-relieved material contained significant lack-of-fusion porosity while the HIP'ed material contained none. This result indicated that the selected processing conditions did not produce fully consolidated material, but that porosity which did form was closed to the surface and therefore healed during HIP.

Both materials also possessed a Widmanstätten transformed-beta microstructure (Figure 2c,d); however the alpha laths in the stress-relieved material were finer than those in the HIP'ed material. This difference was expected because the higher temperature used during HIP allows the alpha phase to coarsen, while the lower temperature used for stress relief does not. Such a difference in coarseness of the alpha phase would be expected to have a noticeable effect on mechanical properties, particularly tensile strength [8].

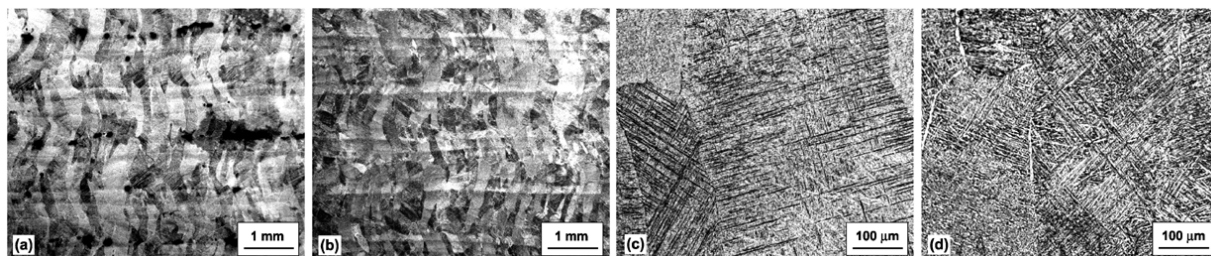


Figure 2. Photographs showing the (a,b) macrostructures and (c,d) microstructures of the (a,c) stress-relieved and (b,d) HIP'ed deposits.

The measured crystallographic texture was consistent with that which would form as a result of epitaxial growth of *columnar* beta grains from the substrate (i.e., showing the influence of both a solidification-induced <100> fiber texture and the texture of the beta-annealed substrate). However, the texture was found to be relatively weak (i.e., maximum of 2.5 times random in the alpha phase) [10].

Static Tension Test Results: The tension-test results provided insight into the effect of the deposition process and post-deposition HIP on mechanical properties (Table 1). For example, the deposits exhibited significant yield-strength anisotropy in both the stress-relieved and the HIP'ed conditions. The X- and Y-direction yield strengths were higher than those in the Z direction. However, this anisotropy was much greater in the stress-relieved condition than following HIP.

Table 1. Average Tensile Properties of Bulk Ti-6Al-4V Produced via the LENSTM Process.

Condition	Test Direction	Yield Strength (MPa)	Ultimate Strength (MPa)	Total Elongation (%)	Elastic Modulus (GPa)
Stress Relieved	X	1065	1109	4.9	116
Stress Relieved	Y	1066	1112	5.5	116
Stress Relieved	Z	832	832	0.8	112
HIP'ed	X	946	1005	13.1	118
HIP'ed	Y	952	1007	13.0	118
HIP'ed	Z	899	1002	11.8	114

The large anisotropy in the stress-relieved deposit was a direct result of the distribution of lack-of-fusion porosity in the material. Due to the layered nature of the LENSTM process, lack-of-fusion porosity tended to form primarily along the *planar* inter-layer boundaries (Figure 2a). Hence, the effective load-bearing area in tension tests perpendicular to the layer boundaries was significantly reduced, and the measured yield stress (which assumes full-density material) was correspondingly reduced. While additional lack-of-fusion porosity can also form at the inter-line boundaries *within* each layer, such porosity appeared to occur less frequently (Figure 2a). Additionally, because the line direction was alternated by 90° with each subsequent layer, inter-line porosity would be expected to have been distributed more evenly throughout the deposit and therefore have had a much smaller effect on strength. The amount of porosity and deformation observed in the fractured specimens (Figure 3) supported these conclusions. While the X- and Y-direction specimens exhibited large amounts of deformation and little porosity, the Z-direction specimens exhibited very little deformation and extensive porosity. The relative ductility of each of the three directions was further illustrated by the relative values of ultimate strength and total elongation in Table 1. While the X and Y directions had significant differences between their yield and ultimate stresses and had approximately 5% total elongation, the Z direction had no measurable difference between its yield and ultimate stresses and less than 1% total elongation.

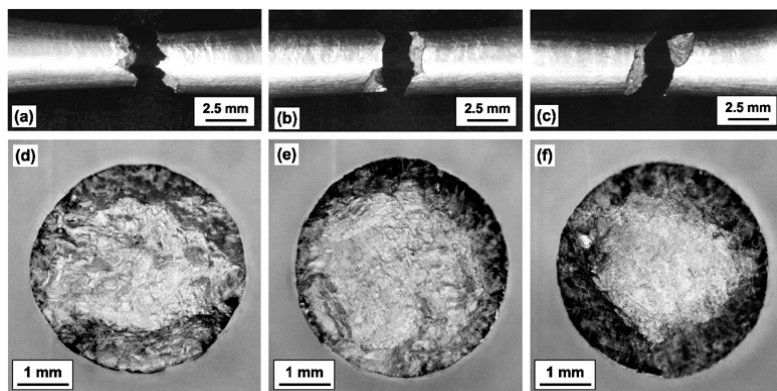


Figure 3. Macrographs of (a,b,c) broken specimens and (d,e,f) fracture surfaces of tension-test specimens cut from the stress-relieved deposit in the (a,d) X direction, (b,e) Y direction, and (c,f) Z direction.

Because the HIP'ed deposit was essentially porosity free (Figure 2b), a much smaller yield-strength anisotropy was observed. The specimens from all three directions exhibited significant ductility, as illustrated by the large amount of deformation observed in the fractured specimens (Figure 4) and the large, similar values of ultimate strength and total elongation. Hence, the yield-strength anisotropy is most likely *not* a result of porosity which might have remained incompletely healed after HIP. Instead, it is probably due to some form of mechanical

or crystallographic texture. While further research is required to determine the precise effect of various forms of texture on properties, some general comments can be made. One potential cause of the observed anisotropy is the mechanical texture due to the columnar grain morphology. In lamellar titanium microstructures, the effective slip length (which has a large, inverse effect on yield strength) is determined by the alpha colony size which, in turn, is limited by the prior-beta grain size [10]. In a columnar microstructure, the effective grain size is much smaller in directions perpendicular to the columnar grains than in the direction parallel to them. Hence, one would expect the yield strength to be lower in the direction parallel to the columnar grains (which in this case is the Z direction). Another possible cause of anisotropy is crystallographic texture [11]. Due to the high anisotropy of the hexagonal crystal structure, texture can greatly affect mechanical properties in titanium alloys. Because the texture of Ti-6Al-4V LENSTM deposits is markedly affected by the <100> fiber texture which forms during columnar solidification, a difference in texture between the Z direction and the X and Y directions would be expected and was indeed observed [9]. However, the effect of this texture on properties is not straightforward and requires further investigation.

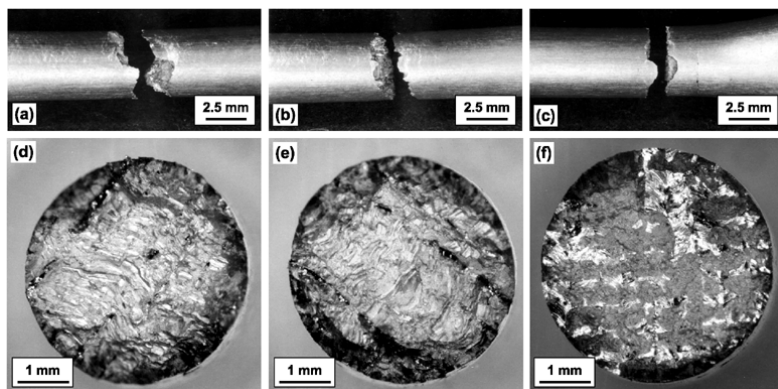


Figure 4. Macrographs of the (a,b,c) broken specimens and (d,e,f) fracture surfaces of tension-test specimens cut from the HIP'ed deposit in the (a,d) X direction, (b,e) Y direction, and (c,f) Z direction.

Another interesting observation was the significant difference in strength and ductility for the stress-relieved and HIP'ed material conditions. Focussing on the X- and Y-direction results, the stress-relieved material was stronger yet less ductile than the HIP'ed material. The difference in strength was likely a result of the difference in alpha-platelet thickness between the two materials with the coarser HIP'ed material being weaker. The difference in ductility was probably due to the presence of porosity in the stress-relieved material.

The Z-direction tension properties of these materials showed interesting comparisons to published design properties for wrought, mill-annealed Ti-6Al-4V (Table 2). While the strength and ductility of the stress-relieved material were severely limited by porosity, the yield strength was not particularly low when compared to the wrought material. Considering the much higher strengths and ductilities observed in the X and Y directions, it appears that the LENSTM process actually may offer improvements in tensile strength provided that the material can be fabricated *without* porosity. However, even if HIP is required to heal porosity, a modest improvement in strength relative to wrought properties can be achieved without a significant loss of ductility.

Table 2. Measured Z-Direction Tension Properties of Bulk Ti-6Al-4V Produced via the LENSTM Process versus Published A-Basis Design Properties for Wrought, Mill-Annealed Ti-6Al-4V Plate [7].

Condition	Yield Strength (MPa)	Ultimate Strength (MPa)	Total Elongation (%)	Elastic Modulus (GPa)
Stress Relieved	832	832	0.8	112
HIP'ed	899	1002	11.8	114
Wrought	827	896	10	110

Tensile Fatigue Test Results: The tensile fatigue test results revealed the expected trends in view of the distribution of porosity in the deposits (Figure 5). The stress-relieved material had much lower fatigue strengths than the HIP'ed material and also displayed an anisotropy. The Z-direction fatigue strengths were significantly lower than those in the X and Y directions. When compared to alternate product forms, the fatigue strength of the HIP'ed material was similar to that of wrought product, indicating that no debit in fatigue strength would need to be considered in component design.

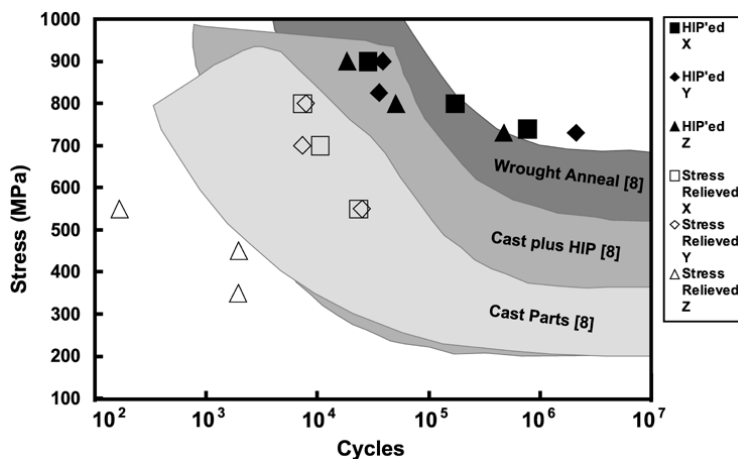


Figure 5. Comparison of measured fatigue strengths for Ti-6Al-4V deposits in both the stress-relieved and HIP'ed conditions to published scatterbands for Ti-6Al-4V castings and forgings (Reference 8).

Compact Tension Test Results: The compact tension results further demonstrated the effect of lack-of-fusion porosity on mechanical behavior. In the stress-relieved specimens, a strong anisotropy was again observed (Figures 6 and 7). In the X-direction specimens (Figure 6a,d), the crack did not begin at the notch tip, but instead at the nearest layer of lack-of-fusion porosity. From there, the crack grew rapidly with little plastic deformation thus resulting in a very low fracture toughness (Figure 7). In the Y and Z directions, the porosity layers were not in the same plane as the crack; thus, larger fracture toughnesses were obtained (Figure 7). In addition, an unusual phenomenon occurred in the Z-direction specimens (Figure 6c,f). The crack propagated along the original plane for a significant distance and then began to propagate along the layers of porosity at an angle 90° from the original plane. Nevertheless, these specimens exhibited the highest toughness values for the stress-relieved material (Figure 7).

In contrast, the HIP'ed specimens exhibited a much smaller level of anisotropy (Figures 7 and 8). The Z-direction toughness was slightly higher than that for the other directions. Significant ductility and nominally planar cracks were observed in all three directions (Figure 8).

Hence, the cause of the observed anisotropy is likely related to the same source as the observed yield-strength anisotropy.

Finally, upon comparing the toughness of these materials to those of other product forms, the toughness of the stress-relieved material fell below published values for wrought and cast product forms, while that of the HIP'ed material lay within the range of published values.

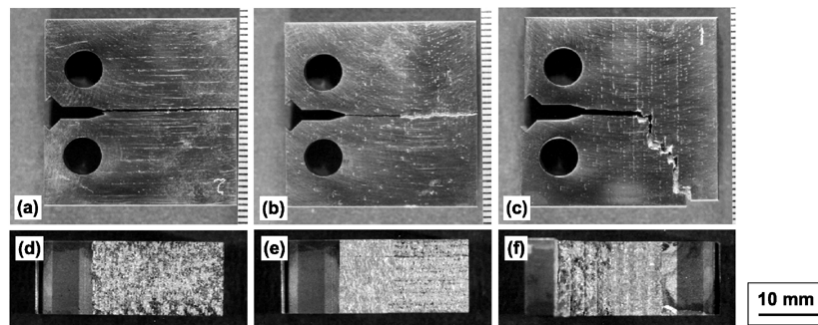


Figure 6. Macrographs showing the (a,b,c) broken specimens and (d,e,f) fracture surfaces of the compact-tension specimens from the stress-relieved deposits in the (a,d) X direction, (b,e) Y direction, and (c,f) Z direction.

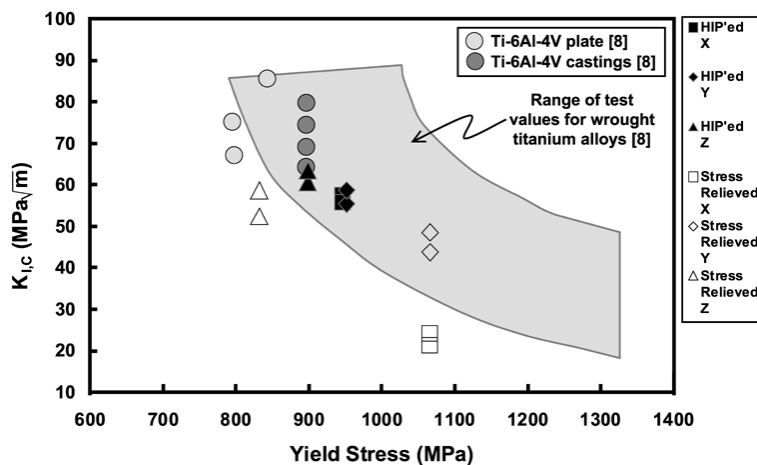


Figure 7. Comparison of measured $K_{I,C}$ and yield-strength values for Ti-6Al-4V deposits in both the stress-relieved and HIP'ed conditions to a published scatterband for wrought Ti-6Al-4V (Reference 8).

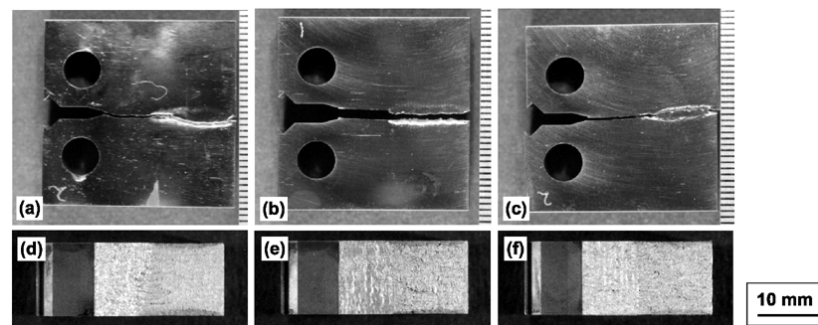


Figure 8. Macrographs showing the (a,b,c) broken specimens and (d,e,f) fracture surfaces of the compact-tension specimens from the HIP'ed deposits in the (a,d) X direction, (b,e) Y direction, and (c,f) Z direction.

Summary and Conclusions

The effect of microstructure and texture of laser-deposited Ti-6Al-4V on mechanical properties was investigated by conducting tension, fatigue, and fracture toughness tests. From this work, the following conclusions were drawn:

1. Lack-of-fusion porosity has a significant effect on both the levels and anisotropy of mechanical properties.
2. HIP appears to be effective in healing lack-of-fusion porosity.
3. The yield strength can show a noticeable anisotropy due to residual deposition porosity (in the stress-relieved condition) and mechanical and/or crystallographic texture (in both conditions).
4. The static tensile strength and ductility, fatigue strength, and fracture toughness of HIP'ed Ti-6Al-4V produced via LENSTTM compare favorably to those of wrought products.

Acknowledgements

This work was conducted as part of the in-house research activities of the Metals Processing Group of the Air Force Research Laboratory's Materials and Manufacturing Directorate. The support and encouragement of the Laboratory management and the Air Force Office of Scientific Research (Dr. C.S. Hartley, program manager) are gratefully acknowledged. The assistance of P. Gorman of Optomec Design Co. and W. Capshaw of ICE Prototyping in fabricating the deposits, D. Maxwell in performing the mechanical tests, S. Short, J. Vann, and R. Lewis in preparing and analyzing the metallographic specimens, and M. Glavicic in performing the OIM analysis is also much appreciated.

References

- [1] Schriempf, J.T., Whitney, E.J., Blomquist, P.A., Arcella, F.G., *Advances in Powder Metallurgy and Particulate Materials*, v. 3, Princeton, NJ: Metal Powder Industries Federation, 1997:21-51.
- [2] Keicher D.M., Miller, W.D., *Hard Coatings Based on Borides, Conference: Carbides & Nitrides: Synthesis, Characterization & Applications*, San Antonio, TX, USA, 16-19 Feb. 1998, Warrendale, PA: TMS, 1998: 369.
- [3] Brice, C.A., Schwendner, K.I., Mahaffey, D.W., Moore, E.H., Fraser, H.L., *Proceedings of the 10th Solid Freeform Fabrication Symposium*, University of Texas at Austin, Austin, TX, USA, Aug. 1999.
- [4] Kobryn, P.A., Moore, E.H., and Semiatin, S.L., *Scripta Materialia*, v. 43, no. 4, 2000.
- [5] Kobryn, P.A. and Semiatin, S.L., *Proceedings of the 11th Solid Freeform Fabrication Symposium*, University of Texas at Austin, Austin, TX, USA, Aug. 2000.
- [6] Adams, B.L., Wright, S.I., and Kunze, K., *Metall. Trans. A*, v. 24A, 1993: 819.
- [7] MIL-HDBK-5H, Battelle's Columbus Labs, Columbus, OH, 1998.
- [8] Donachie, M. J. Jr., ed., *Titanium: A Technical Guide*, ASM International, 1988.
- [9] Kobryn, P.A., Glavicic, M.G., and Semiatin, S.L., AeroMat 2001, Long Beach, CA, June 13th, 2001.
- [10] Lütjering, G., *Mater. Sci. Eng. A*, v. A243, 1998: 32.
- [11] Williams, J.C. and Starke, E.A. Jr., in: G. Krauss, ed., *Deformation, Processing, and Structure*, ASM, 1984: 279.



LANE 2012

Material properties of Ti6Al4V parts produced by laser metal deposition

Jun Yu*, Marleen Rombouts, Gert Maes, Filip Motmans

VITO (Flemish Institute for Technological Research), Materials Technology, Boeretang 200, 2400 Mol, Belgium

Abstract

This paper presents our recent progress on the applications of laser metal deposited (LMD) Ti6Al4V parts. The microstructure of the fabricated parts shows prior columnar β grains consisting of acicular α' martensite. The yield and ultimate tensile strengths of the fabricated parts are superior to those of cast and annealed wrought material, while the elongation is lower. On-line monitoring and control of the LMD process was performed by monitoring the pool area and feedback controlling the laser power in order to decrease heat accumulation. The substrate dilution is diminished and the decreased heat accumulation reduces its effects on the microstructure.

© 2012 Published by Elsevier B.V. Selection and/or review under responsibility of Bayerisches Laserzentrum GmbH
Open access under CC BY-NC-ND license.

Keywords: laser metal deposition; titanium alloy; oxygen content; monitoring and control

1. Motivation / State of the Art

Laser metal deposition (LMD) – also called laser engineering net shape (LENS), direct metal deposition (DMD) or laser solid forming (LSF) – is a process that has a unique capability to build up complex three dimensional features in an additive way on existing components. During this process, a laser source is used to melt metal-based powders delivered in a transport gas stream by means of a coaxial nozzle on to a metal substrate. A shielding gas stream is applied to constraint the powder stream and gives a primary protection from the atmosphere to the melt pool.

The main application area in industry for LMD technology is to build up or to repair high-value components. In these cases, titanium alloys play an important role, such as in building up titanium rudders or repairing titanium turbine blades. Ti6Al4V alloy, a α/β titanium alloy with high strength, low weight ratio and outstanding corrosion resistance, has a large number of applications in aerospace and

* Corresponding author. Tel.: +32-14-335696 ; fax: +32-14-321186 .
E-mail address: : jun.yu@vito.be .

automotive as well as in surgery, medicine, chemical plants, power generation, oil and gas extraction, sports,... [1-3]. LMD of near-net-shape Ti6Al4V components using the solid freeform fabrication route has capacity to meet the requirements of low cost, short cycle and high performance for the production and repair of complex shaped parts.

The background of this paper is using titanium alloy Ti6Al4V powder to produce functional components directly or to build up functional structures on existing parts. In this case, the knowledge of the bulk mechanical properties of the LMD material is really important. The microstructure of these components differs substantially from conventional material due to the rapid solidification, which results in a fine grain-sized microstructure. Although these microstructural features often bring out improvements in properties, rapidly solidified microstructures in commercial alloys that were designed to be used in conventionally processed condition do not necessarily show superior properties [4].

This paper shows the present research progress on LMD Ti6Al4V parts. The titanium alloy Ti6Al4V parts were built without the use of an inert gas chamber but with local protection using an argon gas flow provided by the powder nozzle. Their oxygen content was measured after LMD process and the microstructure, the mechanical properties of the built parts are presented too. A monitoring and control system is adopted to on-line monitor the process and assure the parts' quality by controlling the laser power on-line. Its effects on dilution and heat accumulation are presented as well. Some related works, like titanium parts built in the glove box as well as with heat treatment, are ongoing and will be presented in the near future.

2. Experiment

The experiments were carried out using a 7 kW IPG fiber laser with out-coupling fiber with a diameter of 600 μm . The use of a focal lens with a focal length of 250 mm and a collimator lens with a focal length of 125 mm results in a laser spot diameter of 1200 μm on the substrate. The laser spot has a top-hat energy distribution and the powder was transported through a coaxial nozzle (Fraunhofer-Institut für Lasertechnik) continuously with argon shielding gas stream (the shielding gas flow rate shown in Table 1 represented as Q_s). Specimens were built on Ti6Al4V flat substrates with a thickness of 10 mm. In addition, SKM-DCAM software is used for generating CNC program with specified tool paths.

In order to fabricate parts with good dimensional and shape accuracy, for each layer, the powders were deposited firstly along the contour and then the interior along raster deposition pattern that was rotated 90 degree between each layer. There was a 0.3 mm overlap between raster and contour paths and 0.6mm (50%) overlap between raster paths. Table 1 shows the experimental processing parameters, in which, P , V , D , F , η , Q_s and hc are the laser power, scan speed, spot diameter, powder feed rate, overlap, shield gas flow rate and layer thickness, respectively. The chemical compositions of titanium alloy Ti6Al4V from the supplier are shown in Table 2.

Table 1. Experimental processing parameters in present study

Para. Sets	P (W)	V (mm/min)	D (mm)	F (g/min)	η	Q_s (L/min)	hc (mm)
1	380	1000	1,2	1,43	50%	10,5	0,4
2	470	1000	1,2	1,43	50%	10,5	0,5
3	570	1000	1,2	1,43	50%	10,5	0,5
4	520	1500	1,2	1,98	50%	10,5	0,5
5	570	1500	1,2	1,98	50%	10,5	0,5

Table 2. Chemical compositions of titanium alloy Ti6Al4V from supplier (wt%)

Al	V	C	Fe	O	N	H	Ti
0,019	0,006	0,017	0,53	0,092	0,010	0,004	Bal.

The microstructure was studied by optical microscopy and X-ray Diffraction (Siemens D500). The specimens were etched using a solution of hydrochloride acid, nitric acid and hydrofluoric acid. The hardness was obtained by Vickers indentation measurements using a load of 1 kg. The mechanical properties were determined by tensile testing (Instron 5582) using an extensometer according to ASTM E-8M standard. Three parts produced under identical conditions have been subjected to tensile testing shown in Fig. 1(a), in which, the image of the milled part is also illustrated. These parts are 20*100 mm² and 10 mm high and then are milled to the final dimension (see Fig. 1(b)) prior to tensile testing.

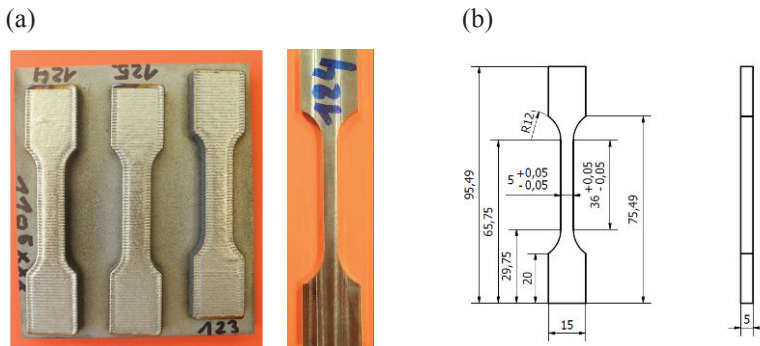


Fig. 1. Tensile test (a) specimens including a representative of the milled parts; (b) dimensions (in mm) of the milled part

A melt pool based monitoring and control system (Fraunhofer IWS, Dresden) constituting of a CCD camera (E-MAqS) for monitoring the melt pool area and a laser process control system (LompocPro) for real-time control of the laser power has been applied. Preliminary experiments encompassing laser cladding of single lines, layers and 3D parts have been carried out.

3. Results and Discussion

Figure 2(a) shows the particle morphology for the Ti6Al4V powder. The particle size is around 30~80 μm and some pores are occasionally present in the particles. Figures 2(b)~(d) show cross-section of three fabricated specimens with a dimension of 15*10*5 mm³ using the processing parameters sets 1-3 in Table 1, respectively. Pores and bad-bonding defects can only be found when using the lowest laser power 380W, i.e. set 1 in Table 1 (big magnification, area 1).

The macrostructure shows prior columnar β grains which are oriented more or less in the building direction, as shown in Fig. 3(a)~(c). The prior β grains grow epitaxially and get a little coarser with the laser power increase. The microstructure is composed of acicular α' -martensite as shown in Fig. 4. This can be proved by the evidence mentioned in the literature [5] comparing the hcp lattice parameters. In present study, the measured lattice parameters are $a=0.293$ nm and $c=0.467$ nm determined by X-ray diffraction, which correspond well to the lattice parameter values given in the literature [6] for the α' phase, i.e. $a=0.29313$ nm and $c=0.46813$ nm. In addition, Murr et al. [7-9] and Koike et al. [10] have

demonstrated that selective laser melting (SLM)/laser beam melting (LBM) fabrication of Ti6Al4V components exhibits α' martensitic or α'/α microstructures in contrast to primarily α/β microstructures for electron beam melting (EBM) fabricated Ti6Al4V components because during LBM a higher cooling rate is imposed on the material than during EBM. The α' phase is beneficially produced by the rapid cooling through diffusionless transformation. In fact, the cooling rate during LMD is around 10^6 °C/min at the current process parameters. This is even much higher than the cooling rate of water quenching which is around 10^5 °C/min [11] and in general produces α' martensitic microstructure [12-14].

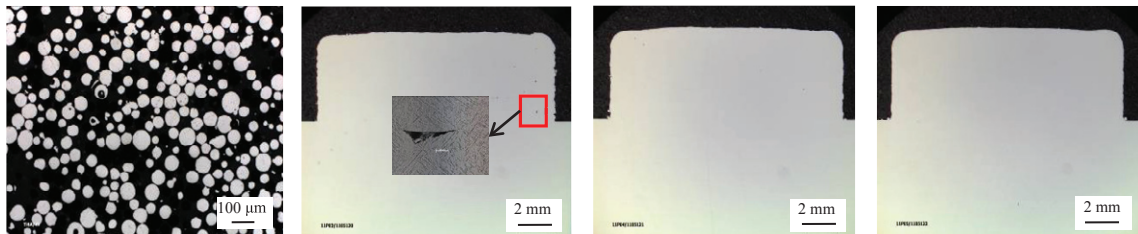


Fig. 2. Particle morphology and cross-sections of the specimens (a) Ti6Al4V particles and cross-sections of Ti6Al4V specimen using parameter (b) set 1, (c) set 2 and (d) set 3 in Table 1

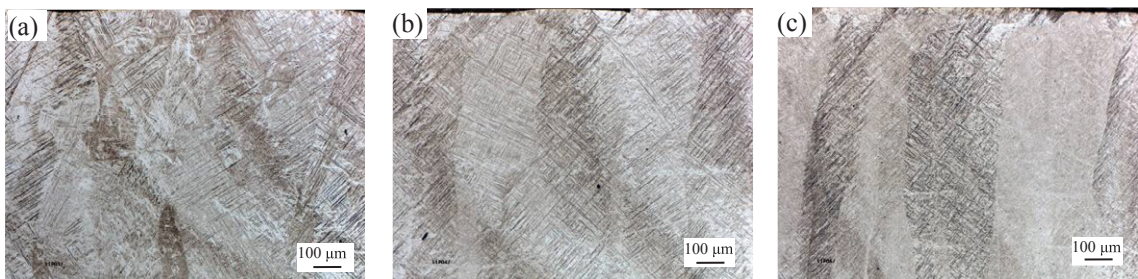


Fig. 3. Macrostructures of LMD Ti6Al4V specimens using different parameter sets; (a) parameter set 1; (b) parameter set 2; (c) parameter set 3 in Table 1

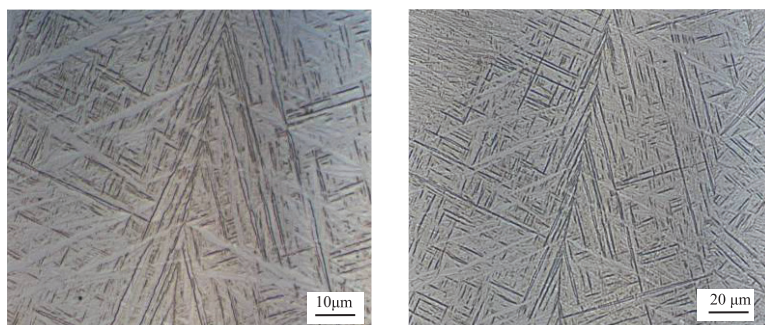


Fig. 4. Microstructures of LMD Ti6Al4V specimen using parameter set 1 in Table 1 (big magnification of Fig. 3 (a))

Figure 5 shows the hardness test results for the specimens in Fig. 2(b)~(d) including the testing positions as well. The points 1-10 in Fig. 5(a) are located on the substrate (Ti6Al4V) and the others are on the fabricated specimen. The hardness of the fabricated specimen is around 360 ± 10 HV and higher than the forging substrate plate. The laser power didn't have significant influence on the hardness of the fabricated specimens under current experimental conditions with the laser power being changed from 380 W to 570 W.

Laser metal deposition can produce high melt pool temperature and much heat accumulation leading to bad oxidation of the fabricated parts at high heat inputs. Hence, the parameter set 2 with laser power 470W was adopted to fabricate tensile test parts, taking into account the protection of the parts against oxidation as much as possible. In this case, three tensile test parts were fabricated under identical conditions (see Fig. 1(a)). The density of these three parts was measured using Archimedes method. The results are $4.421\text{g}/\text{cm}^3$, $4.417\text{g}/\text{cm}^3$ and $4.419\text{g}/\text{cm}^3$, respectively and in average, the relative density can be up to 99.8%. One of these parts was tested for oxygen level using instrumental gas analysis (IGA). The result was 0.13 wt% and shows a 0.038 wt% increase comparing with of the powder.

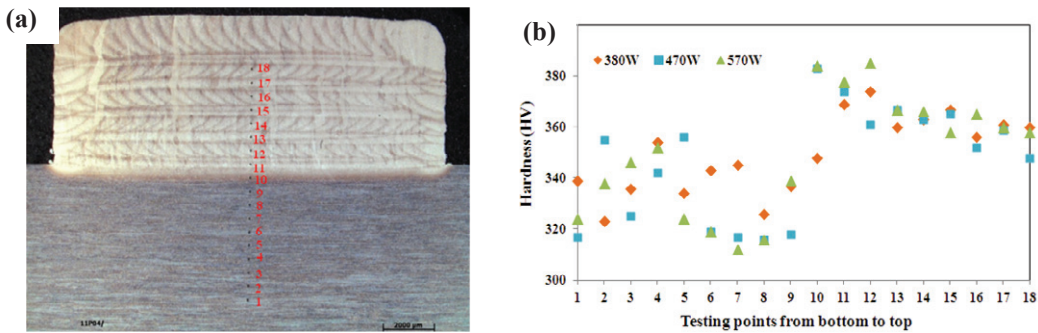


Fig. 5. Hardness test for Ti6Al4V specimens (a) the test points (b) hardness with the use of different laser powers

The mechanical property results of the fabricated parts are shown in Fig. 6 with respect to yield strength, ultimate tensile strength (Fig. 6(a)) and elongation (Fig. 6(b)). As a reference, the data for cast [15] and annealed wrought material were introduced [16]. The yield and ultimate tensile strengths of the three LMD parts are 976 ± 24 MPa and 1099 ± 2 MPa, respectively, which are higher than for cast and annealed wrought material. The elongation is 4.9 ± 0.1 . It is reported that oxygen is detrimental to the ductility through producing interstitial solid solution with Ti at high temperature [17, 18]. Better oxygen control during build-up is good for improving the elongation property (up to 13%) [19]. Besides, the elongation to failure is strongly dependent on the present microstructure, therefore, another effective way is reforming the microstructure by heat treatment (up to 14%) [12] because the α' martensite microstructure itself shows a low ductility.

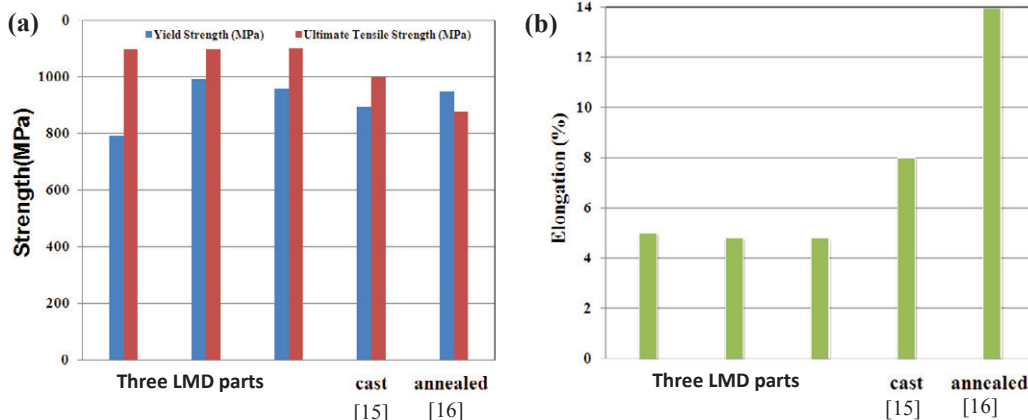


Fig. 6. Tensile test results of the Ti6Al4V specimens (a) Yield and Ultimate tensile strengths (b) Elongation

Heat accumulation is inevitable during LMD process and will get increased layer by layer, which can lead to an increasing pool spreading behavior [20], a high oxidation level and a big heat distortion [21] producing bad deposition shape or accuracy of the built parts. It can also lead to the coarsening of the microstructure due to the increasing temperature and the decreasing cooling rate of melt pool. In order to decrease the accumulated heat compared with the use of a constant heat input, the monitoring and control system was introduced into our process. This system developed for laser cladding consists of two parts, E-MAqS and LompocPro. The E-MAqS monitors the melt pool area as soon as LMD process is started. Then the obtained pool area data are transferred to the Lompocpro and compared with the pool area setpoint. The laser power is controlled if these data can't correspond well to the pool area setpoint. The laser power will be decreased if these data are bigger than the pool area setpoint. On the contrary, it will be increased.

Figure 7(a) shows the pool area variations during multi-layer LMD process with water cooled substrate marked in blue and without water cooled substrate marked in red. The pool area during multi-layer LMD was measured on-line. It is increased more than 20% after 3000 seconds without water cooling of the substrate and has not reached a steady state yet. The heat accumulation effect is less when the substrate is cooled. The enlargement of the pool area can also be observed by comparing the images at the beginning (see Fig. 7(b)) and near the end (see Fig. 7(c)) of the process.

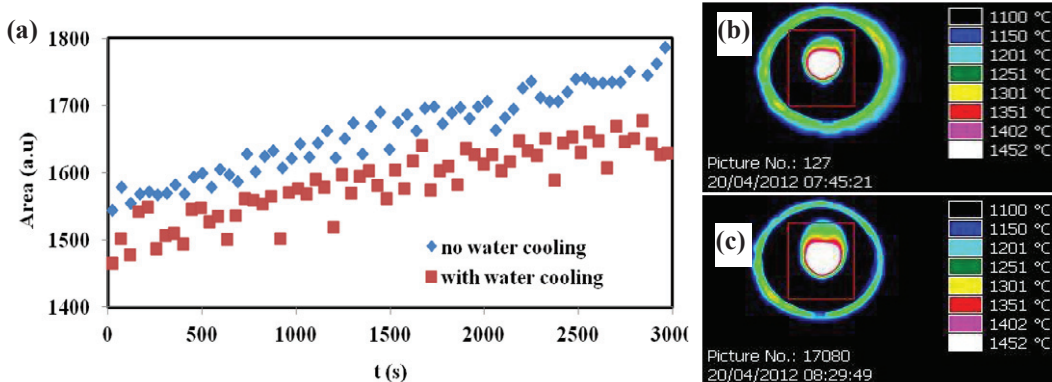


Fig. 7. Area variations during multi-layer LMD process using monitoring and control system ; (a) data analysis; (b) image at the beginning of the process; (c) image near the end of the process

In order to increase the deposition efficiency, a high scan speed is accepted as sets 4 and 5 in Table 1 wherein the other parameters are correspondingly changed to get a 0.5mm layer thickness. The interior qualities of the fabricated parts using both parameter sets wherein $P=520\text{W}$ and $P=570\text{W}$, respectively, are good by further analyzing their cross sections (see Fig. 8(a)), which only have a few micro pores. The pool area was monitored and it kept increasing at the higher scan speed (Fig. 8(a)). The pool area has an increase of more or less 20% when using laser power 570W than using laser power 520W. This is much more than the increase of the laser power (~10%). Figure 8(b) shows the variations of the controlled laser power, changing according to the comparisons of the monitored pool area and the pool area setpoint. The current area setpoint, which is equal to 1950 and is provided according to the area level of using 570W laser power, was followed by the real pool area during the whole process by changing the laser power, even though the laser power dropped to a little lower than 500W due to the heat accumulation effect. The decreased heat inputs reduced the heat effect compared with the use of a constant 570W laser power during multi-layer deposition process. The interior quality of the fabricated part with controlled laser power is also good after checking its cross section, as shown in Fig. 8(b).

Macroscopic banding on the cross section of LMD Ti6Al4V parts, which has already been noted in several literatures [6, 12], is caused by the reheating of previously deposited material that occurred during the subsequent deposition process. This leads to microstructural changes like microstructural coarseness. Figure 9(a) shows this banding phenomenon clearly. The α' phase gets coarse and its aspect ratio is increased in region 1 compared to one in region 2 (see Figs. 9(1) and (2)). However, with control the overall cross section is more or less the same due to the decreased pool temperature and heat accumulation (see Fig. 9(b)). Besides, the total depth of the dilution and heat-affected zone of the substrate is decreased from 0.5mm to 0.35mm with the use of monitoring and control system, as illustrated in Figs. 9(a) and (b).

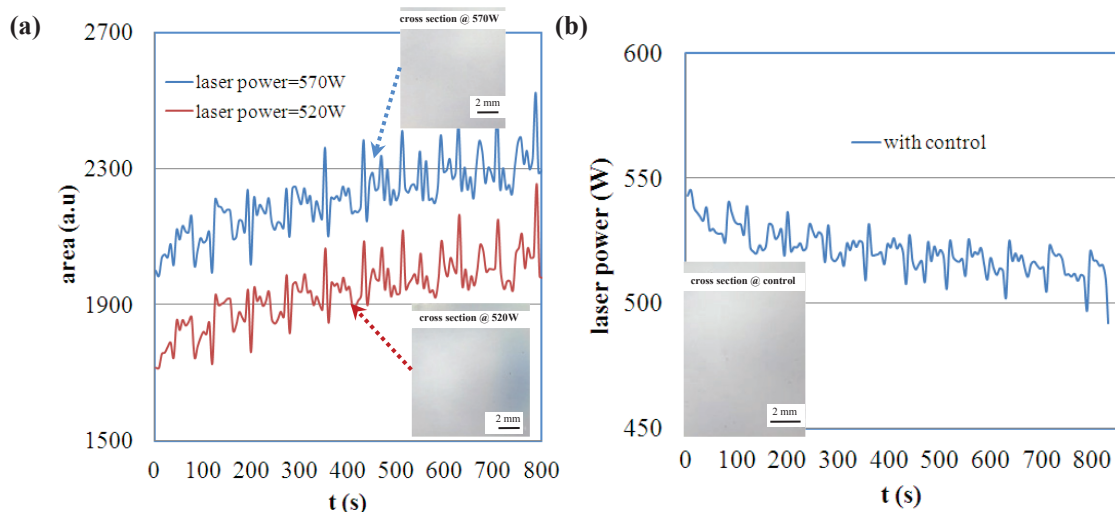


Fig. 8. Monitoring and control for LMD process using monitoring and control system; (a) area variations using parameter sets 4 and 5 in Table 1 with high scan speed; (b) variations of the controlled laser power with high scan speed ($V=1500\text{mm/min}$)

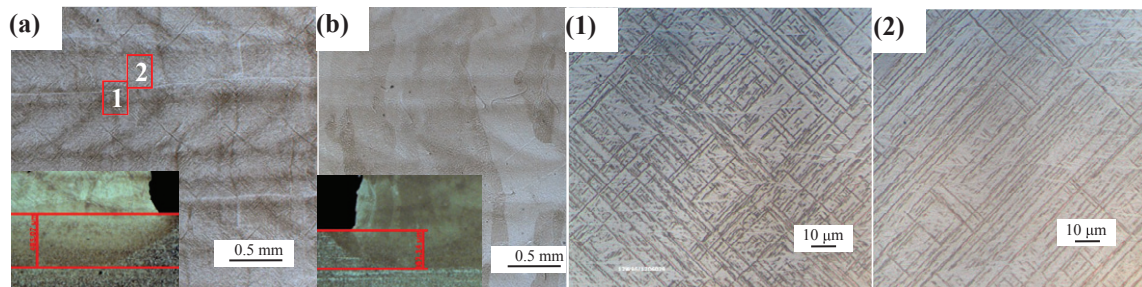


Fig. 9. Microstructures for specimens built without (a) and with (b) monitoring and control system (1) big magnification of region 1 (2) big magnification of region 2 in Fig. 9(a)

Conclusions

Based on the application requirements of laser metal deposition Ti6Al4V parts, the microstructure and mechanical properties of the fabricated parts were investigated. The microstructure shows typical acicular α' -martensite phase due to the rapid cooling of the melt pool. The hardness of the LMD parts is 360 ± 10 HV and higher than the forging plate. The yield and ultimate tensile strengths are 976 ± 24 MPa and 1099 ± 2 MPa, respectively, which are superior to the cast and annealed wrought material. The elongation is lower (4.9 ± 0.1). These results depend on the formed microstructure and the minor elements content in the fabricated parts. The tested oxygen content was 0.13 wt% and can be decreased by the use of an inert gas chamber. Heat accumulation has much effect on the fabricated parts, like the microstructure, oxygen level, pool spreading behavior and heat distortion. The monitoring and control system was applied during LMD process to decrease the heat accumulation effect, by monitoring the pool area and controlling the laser power real-time. As a result, the microstructure is more or less consistent between layers and tracks and the total depth of the dilution and heat-affected zone is lowered as well.

References

- [1] Arcella, F.; Abbott, D. H.; House, M. A.: Titanium Alloy Structures for Airframe Application by the Laser Forming Process. Alexandria: 2000: 1465-2000.
- [2] Banerjee, R.; Collins, P. C.; Genc, A.: Direct Laser Deposition of in Situ Ti-6Al-4V-Tib Composites. Materials Science and Engineering A. 2003, 358: 343-349.
- [3] Banerjee, R.; Nag, S.; Fraser, H. L.; A Novel Combinatorial Approach to the Development of Beta Titanium Alloys for Orthopaedic Implants. Materials Science and Engineering C. 2005, 25(3): 282-289.
- [4] Rombouts, M.; Maes, G.; Persoons, R.: Material study of laser cladded Inconel 625. Material study of laser cladded Inconel 625. Innovative Developments in Virtual and Physical Prototyping. Proceedings of the 5th International Conference on Advanced Research in Virtual and Rapid Prototyping, Leiria, Portugal, 28 September - 1 October, 2011: 333-337.
- [5] Thijss, L.; Verhaeghe, F.; Craeghs, T.; et al.: A study of the microstructural evolution during selective laser melting of Ti-6Al-4V. Acta Materialia 2010, 58: 3303-3312.
- [6] Boyer, R.W.; Collings, G.E.W.: Materials properties handbook: titanium alloys. Materials Park (OH): ASM International; 1994.
- [7] Murr, L.E.; Gaytan, S.M.; Medina, F.; et al.: Characterization of Ti-6Al-4V open cellular foams fabricated by additive manufacturing using electron beam melting. Mater. Sci. Eng. A 2010, 527, 1861-1868.
- [8] Murr, L.E.; Esquivel, E.V.; Quinones, S.A.; et al.: Microstructures and mechanical properties of electron beam-rapid manufactured Ti-6Al-4V biomedical prototypes compared to wrought Ti-6Al-4V. Mater. Charact., 2009, 60: 96-105.
- [9] Murr, L.E.; Quinones, S.A.; Gaytan, S.M.; et al.: Microstructure and mechanical behavior of Ti-6Al-4V produced by rapid-layer manufacturing, for biomedical applications. J. Mech. Behavior Biomed. Mater., 2009, 2: 20-32.
- [10] Koike, M.; Greer, P.; Owen, K.; et al.: Evaluation of titanium alloys fabricated using rapid prototyping technologies-electron beam melting and laser beam melting. Materials 2011, 4: 1776-1792.
- [11] G. Lütjering. Influence of processing on microstructure and mechanical properties of ($\alpha+\beta$) titanium alloys. Materials Science and Engineering A. 1998, 243: 32-45.
- [12] Zhang, S. Y.: Research on the heat treated microstructures and properties of laser solid forming. Ph.D thesis of Northwest Polytechnical University. 2009.
- [13] Kobryn, P.A.; Moore, E.H.; Semiatin, S.L.: The influence of laser power and traverse speed on microstructure, porosity, and build height in laser-deposited Ti-6Al-4V. Scripta mater. 43, 2000: 299-305.
- [14] Fujii, H.: Nippon steel technical report, No. 62, July, 1994: 74-79.
- [15] Eylon, D.; Newman, J. R.; Thorne, J. K.: Titanium and titanium alloy casting. ASM Handbook, Volume 2, Properties and selection: nonferrous alloys and special-purpose materials, ASM International, 1990, in ASM Handbook on DVD, ASM International and The Dialog Corporation, 1999.2.
- [16] Lampman, S.: Wrought titanium and titanium alloy. ASM Handbook, Volume 2, Properties and selection: nonferrous alloys and special-purpose materials, ASM International, 1990, in ASM Handbook on DVD, ASM International and The Dialog Corporation, 1999.2.
- [17] Zhou, Y. B.: Introduction to Titanium Alloy Casting. Beijing: Aviation Industry Press, 2000: 76-101.
- [18] TAN S.S.: Non-ferrous metal materials. Beijing: Metallurgical Industry Press, 1993: 76-121.
- [19] Tan, H; Chen, J; Zhang, F. Y; Lin, X.; Huang W. D.: Microstructure and Mechanical Properties of Laser Solid Formed Ti-6Al-4V from Blended Elemental Powders. Rare metal materials and engineering, 2009, 38(4):0574-0578.
- [20] Yu, J.; Lin, X.; Wang J.J.; et al.: Mechanics and energy analysis on melt pool spreading during laser solid forming. Applied Surface Science 2010, 256: 4612-4620.
- [21] Huang, W.D.; Lin, X.; Chen, J.: Laser solid forming. Northwestern Polytechnical University Press. 1th Ed. Xi'an: 2007.4.

Heat-treated microstructure and mechanical properties of laser solid forming Ti-6Al-4V alloy

ZHANG Shuangyin, LIN Xin, CHEN Jing, and HUANG Weidong

School of Materials Science and Engineering, State Key Laboratory of Solidification Processing, Northwestern Polytechnical University, Xi'an 710072, China

Received 24 December 2008; received in revised form 26 March 2009; accepted 28 March 2009

Abstract

The effects of heat treatment on the microstructure and mechanical properties of laser solid forming (LSF) Ti-6Al-4V alloy were investigated. The influences of the temperature and time of solution treatment and aging treatment were analyzed. The results show that the microstructure of LSFed samples consists of Widmanstätten α laths and a little acicular in columnar prior β grains with an average grain width of 300 μm , which grow epitaxially from the substrate along the deposition direction (Z). Solution treatment had an important effect on the width, aspect ratio, and volume fraction of primary and secondary α laths, and aging treatment mainly affects the aspect ratio and volume fraction of primary α laths and the width and volume fraction of secondary α laths. Globular α phase was first observed in LSFed samples when the samples were heat treated with solution treatment (950°C, 8 h/air cooling (AC)) or with solution treatment (950°C, 1 h/AC) and aging treatment (550°C, above 8 h/AC), respectively. The coarsening and globularization mechanisms of α phase in LSFed Ti-6Al-4V alloy during heat treatment were presented. To obtain good integrated mechanical properties for LSFed Ti-6Al-4V alloys, an optimized heat treatment regimen was suggested.

Keywords: metal material; Ti-6Al-4V alloy; laser solid forming; microstructure; mechanical properties; heat treatment

1. Introduction

Ti-6Al-4V alloys, as α/β titanium alloys with excellent comprehensive mechanical properties, have a large number of applications in the aerospace industry. They can be used for making engine blowers, compressor disks, vanes, and some important aircraft force-bearing structures such as girders, junctions, and bulkheads. These key parts are generally composed of integral ribbed structures with complex shape, which are mainly fabricated by numerical control machining after forging. However, these previous methods present a lower material utilization, a longer lead time, and a higher manufacturing cost. Especially, large-scale frame and girder structural parts are generally made by means of bolting or welding of several smaller parts being separately manufactured, which will not only increase the weight of parts but also reduce the entire mechanical properties.

In recent years, laser solid forming (LSF) of bulk near-net-shape metallic components using the solid freeform fabrication route has been shown to be a viable and promising manufacturing technology. To develop LSF of titanium alloy parts is in favor of solving the previous processing handicap mentioned above. In fact, LSF can form directly the parts which have complex inner caves and outer shape,

and is especially suitable for fabricating parts with integral rib reinforcement structures. A number of researches have been carried out on the LSF of titanium alloys [1-8]. Most of the investigations [1-4] concentrated on the relationship between laser processing parameters and microstructure formation. Wu *et al.* [3-4] have investigated the effect of processing conditions, such as laser power, scan speed, and powder feed rate, on the microstructure of direct laser-fabricated Ti-6Al-4V and burn-resistant Ti alloys. Lin *et al.* [5-6] have investigated microstructure and phase evolution in laser solid forming of a functionally graded Ti-Rene88DT alloy and Ti-6Al-4V-Rene88DT alloy. Banerjee *et al.* [7-8] have investigated microstructural evolution and phase precipitation in a laser-deposited compositionally graded Ti-V and Ti-8Al-V alloy. Moreover, the transformation mechanisms and models by which lamellar microstructures coarsen or transform to a globular morphology after forging and heat treatment have been studied [9-13]. Stefansson *et al.* [12] have shown that the mechanisms controlling static globularization of Ti-6Al-4V after deformation and annealing include boundary splitting and lamellar termination migration. Zhou *et al.* [13] found that a trimodal microstructure, consisting of about 15% equiaxed α , 50%-60% lamellar α , and transformed β matrix, can be

obtained through the near- β forging process of titanium alloys, and materials with trimodal microstructure show high room-temperature and high-temperature mechanical properties. It should be indicated that, compared to casting and forging microstructure, there should be many differences not only in microscopic structure and dimension but also in the residual stress distribution of LSFed microstructure due to rapid solidification and rapid annealing repeatedly during laser forming. However, the microstructure transformation after heat treatment of LSFed Ti-6Al-4V alloys was scarcely investigated. This means that our understanding on the microstructural evolution and mechanical properties of titanium alloys formed by LSF is still far from complete. In particular, there is a lack of clear comprehension on the evolution of phases and microstructures during heat treatment of LSFed Ti-6Al-4V alloys, which has an important influence on the final mechanical properties of LSFed Ti-6Al-4V alloys.

The aim of this work is to investigate the influence of heat treatment regimens, including solution temperature, solution time and aging temperature, aging time, on the microstructure and phase evolution of LSFed Ti-6Al-4V alloys.

2. Experimental

The samples were fabricated using a laser solid forming system, which consists of a 5 kW continuous wave CO₂ laser, a four-axis numerical control working table, and a powder feeder with a lateral nozzle. The experiments were conducted inside a controlled atmosphere box, which was filled with argon gas, in which the oxygen content is controlled to be less than 150 ppm in order to prevent the melt pool from oxidizing and oxide contamination from occurring during processing, and argon gas was also used to deliver the Ti-6Al-4V powders. Gas atomized Ti-6Al-4V powders with the size of about -100 to +150 mesh were used. In order to eliminate the moisture that may be trapped in the powders, the powders were dried in a vacuum oven for 24 h. Pure titanium plates with the thickness of 6 mm were used as a substrate. The substrate surface was polished with sandpaper and then cleaned thoroughly with acetone prior to LSF. The processing parameters are as follows: laser power 2400-2700 W, laser spot diameters 3-5 mm, scanning velocity 4-6 mm/s, powder feeding rate 1.0-2.0 g/min, and flux of shielding gas 100-200 L/h. The dimensions of LSFed samples were approximately 90 mm × 18 mm × 10 mm (Fig. 1).

After LSF, the samples were machined by linear cutting to prepare for further heat treatment. The dimensions of the heat treatment samples were 10 mm in length (along the laser scanning direction (X direction)), 12 mm in width (verti-

cal to the laser scanning direction (Y direction)), and 8 mm in height (along Z direction). According to the heat treatment regimen of Ti-6Al-4V wrought reported in literature [14], four groups of heat treatment parameters were selected, as listed in Table 1. The microstructures of the samples were characterized by VEGA LMH scanning electronic microscope. An Olympus analysis data system was used to quantitatively analyze the size and aspect ratio of α and β phases. The tensile tests were carried out in an Instron 1196 materials testing machine.

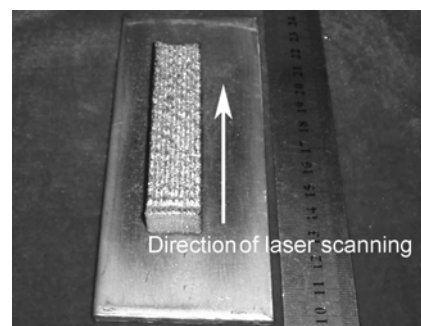


Fig. 1. LSFed sample of Ti-6Al-4V alloy.

3. Results

3.1. As-deposited microstructures

Fig. 2 shows the typical macrostructure and microstructure of as-deposited Ti-6Al-4V alloys. It can be seen that there exhibits a continuously epitaxial columnar β cellular growth across several deposit layers, the growth direction of which is along the deposition direction and inclines towards the scanning direction in some sort. The average cellular spacing is about 300 μm . The as-deposited macrostructure presents the characteristic of light and shade strips due to different crystallography orientations in them, as also shown in Fig. 2(a). During LSF, temperature gradient at the bottom of the molten pool is very high and its direction is vertical to the laser scanning direction. Meantime, solidification first initiates the bottom of the molten pool. For the small freezing range (about 5 K) of Ti-6Al-4V alloy, the transition of columnar to equiaxed grains is not prone to occur in most of the regions in the molten pool. Thus, β -Ti columnar grains will grow epitaxially along the deposition direction. The microstructures in prior β -Ti grains consist mainly of fine Widmanstätten α -Ti laths (SEM microstructures insert in Fig. 2). It also can be seen that there are several layer bands between the deposited layers, which result from the coarsening of α -Ti laths in the heat-affected zone of different deposited layers due to the reheating during the deposition of subsequent layers.

Table 1. Sample grouping and corresponding heat treatment regimens

Group	Solution treatment		Aging treatment		Numeration
	Temperature / °C	Time / h	Temperature / °C	Time / h	
A	850	1	—	—	A-1
	900	1	—	—	A-2
	950	1	—	—	A-3
	975	1	—	—	A-4
	1000	1	—	—	A-5
B	950	1	—	—	B-1
	950	2	—	—	B-2
	950	4	—	—	B-3
	950	8	—	—	B-4
C	950	1	450	4	C-1
	950	1	500	4	C-2
	950	1	550	4	C-3
	950	1	600	4	C-4
D	950	1	550	2	D-1
	950	1	550	4	D-2
	950	1	550	8	D-3
	950	1	550	16	D-4

Note: Using air cooling after solution treatment and aging treatment.

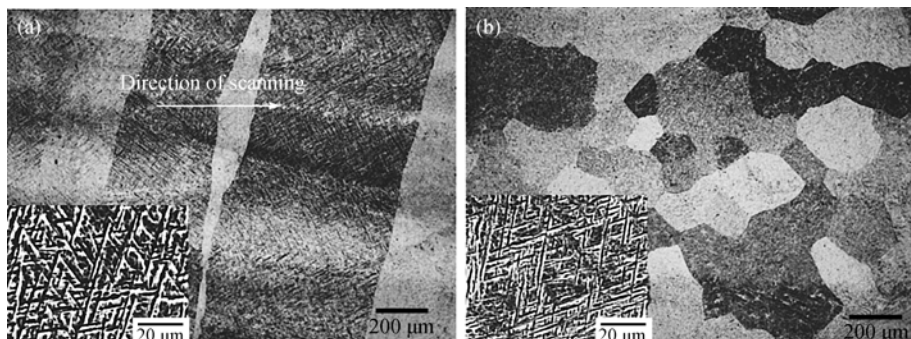


Fig. 2. Optical microscopic structures of the as-deposited Ti-6Al-4V alloy (the bottom left insert is the SEM microstructure): (a) parallel to the direction of laser scanning; (b) normal to the direction of laser scanning.

3.2. Heat-treated microstructure

3.2.1. Influence of solution temperature

Fig. 3 shows the typical microstructures at different solution temperatures for LSFed samples.

It can be seen that after solution treatment the microstructure consists of basket-weave microstructure with intricately mixed multiple variants of α -Ti laths; the prior β grain boundaries are no longer continuous as the result of precipitation of α phases at grain boundaries (Fig. 3(d)). With increasing solution temperature from 850°C to 1000°C, the average aspect ratio of α -Ti laths decreases from 15 (Fig. 3(a)) to 2.5 (Fig. 3(f)). Meantime, the average width of α laths is found to be increased from 1 μm with solution temperature of 850°C to 4–5 μm with solution temperature of 1000°C. It is also found that the recrystallization of β -Ti

grains happen when solution temperature is higher than 950°C. Fig. 3(e) shows the recrystallization microstructure of β -Ti grains with solution temperature of 975°C, and the macrostructure changes from as-deposited columnar prior β grain to equiaxed morphology through solution treatment (the optical microscope macrostructure insert in Fig. 3(e)).

3.2.2. Influence of solution time

Fig. 4 shows the influence of solution time on the microstructures of LSFed Ti-6Al-4V alloys. With increasing solution time, the primary α laths coarsened gradually. Comparing the microstructure of solution treated for 2 h (Fig. 4(a)) with 4 h (Fig. 4(b)), the width of primary α laths increases from 2 μm to 4 μm . More and more refined secondary α laths are precipitated from the matrix when solution time is above 2 h (Fig. 4(b)). As the solution time increases beyond 8 h, it is found that some primary α change from coarsening

α laths to globular α phases (Fig. 4(c)).

3.2.3. Influence of aging temperature

It can be seen from Fig. 5 that, with increasing aging temperature, there are no obvious changes on the width of primary α laths, but their aspect ratios decrease from 12.5 to 2.5. The volume fraction of primary α laths is also reduced from 42.5% to 27.7%. At the same time, the secondary α

laths coarsen continuously with the increase of aging temperature. From Figs. 5(a) and 5(b), it can be found that the width of secondary α laths increases from 1 μm to 2-3 μm . When the sample is aging treated at a temperature of 600°C, the whole microstructure is refined obviously and becomes uniform, although there are some short and coarse primary α laths (Fig. 5(c)).

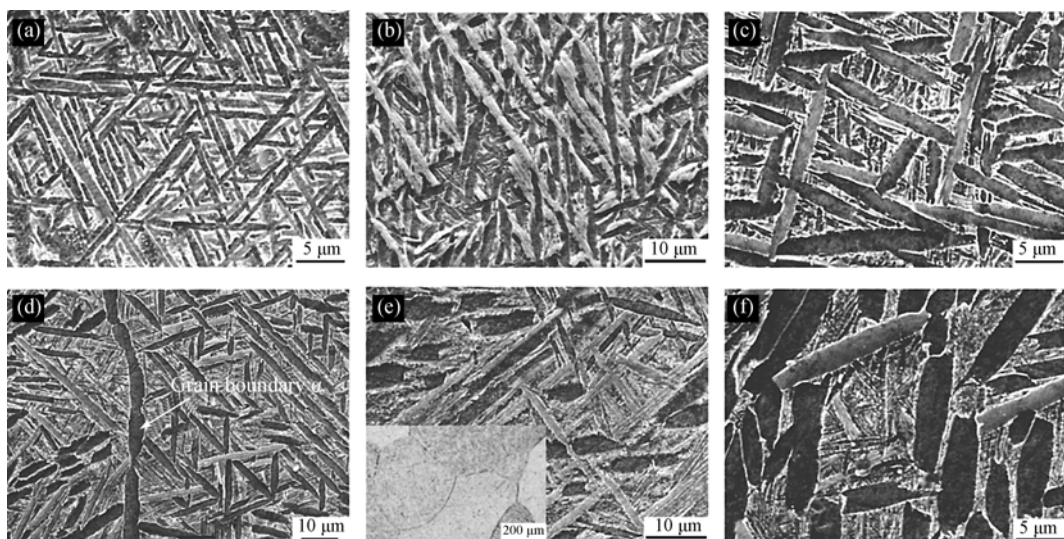


Fig. 3. Typical microstructures at different solution temperatures: (a) 850°C, (b) 900°C, (c) and (d) 950°C, (e) 975°C, and (f) 1000°C for 1 h followed by air cooling.

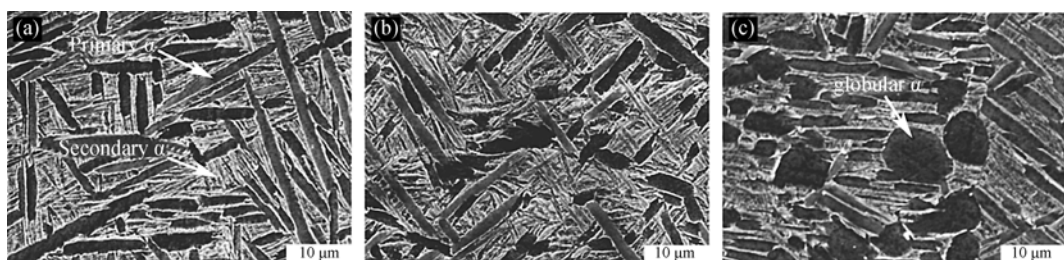


Fig. 4. Typical microstructures showing the influence of solution time: solution treated at 950°C for (a) 2 h, (b) 4 h, and (c) 8 h followed by air cooling.



Fig. 5. Typical microstructures showing the influence of aging temperature: solution treated at 950°C for 1 h followed by air cooling and aging treated at (a) 450°C, (b) 500°C, and (c) 600°C for 4 h followed by air cooling.

3.2.4. Influence of aging time

Fig. 6 shows the typical microstructures of samples LSFed for different aging times. With increasing aging time, it seems that the width of primary α laths has the tendency

to decrease, and the volume fraction of secondary α increases from 29.2% to 35.3%. When the aging time at 550°C reaches 8 h, local globularization of α phases takes place (Fig. 6(b)). It is interesting to note that a further in-

crease in aging time results in the obvious decrease of the volume fraction of primary α laths (from 63.8% to 21.4%) and the increase of the volume fraction of spheroidal α phase (about 15%). It also can be found that the spheroidal α phase presents local aggregation (Fig. 6(c)).

3.3. Mechanical properties

The room-temperature tensile properties of LSFed Ti-6Al-4V alloy are shown in Figs. 7 and 8. It can be seen that the LSFed alloys have a higher tensile strength and a lower ductility. In comparison with the as-deposited samples, samples by solution aging treatment have a higher ductility. The tensile strength is strongly influenced by heat treatment parameters.

3.3.1. Solution temperature and time

Fig. 7 shows the influence of solution temperature and time on the mechanical properties. Samples are aging treated (550°C, 4 h/AC) after solution treatment. It can be seen that samples heat treated with solution (850°C, 1 h/AC) and aging (550°C, 4 h/AC) treatment show the similar tensile properties with those of the as-deposited samples. In fact, there are also little differences of microstructures for the as-deposited sample and the solution-aging treated sample in

comparing Fig. 2(b) with Fig. 3(a), except that the microstructure of the solution-aging treated sample is coarsened slightly. With increasing solution temperature, the tensile strength of the heat-treated sample decreases but the ductility increases until the solution temperature reaches 950°C. Microstructure observation shows that, with increasing solution temperature, the average aspect ratio of α -Ti laths decreases and the width of α laths increases, which cause the higher ductility of the samples. The discontinuous prior β grain boundaries (Fig. 3(b)) also make the function of boundary hindrance weakened. All of the above result in the decrease of tensile strength meantime. It can be also found that LSFed samples solution treated at 975°C have a higher tensile strength and a lower ductility, which is attributed to the prior columnar β grains transforming to equiaxed grains consisting of uniform basket-weave α -Ti laths (Fig. 3(d)) by recrystallization. The microstructure has a tendency to coarsen obviously at 1000°C (Fig. 3(e)), thus resulting in the reduction of tensile strength and ductility. Therefore, solutions at a temperature of 20–50°C below the β transus could make samples have a good combination of tensile strength and ductility.

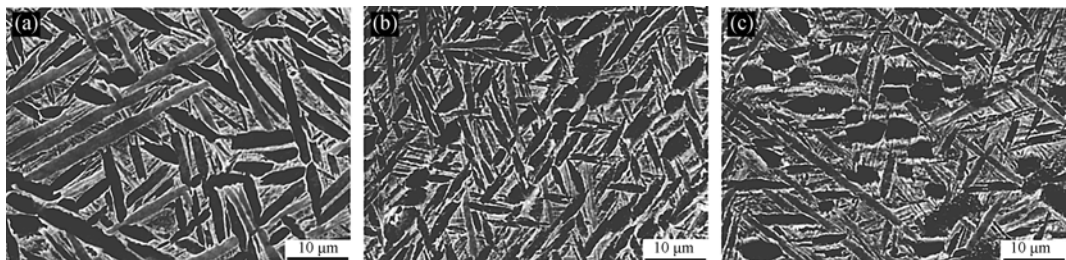


Fig. 6. Typical microstructures showing the influence of aging time: solution treated at 950°C for 1 h followed by air cooling and aging treated at 550°C for (a) 2 h, (b) 8 h, and (c) 16 h followed by air cooling.

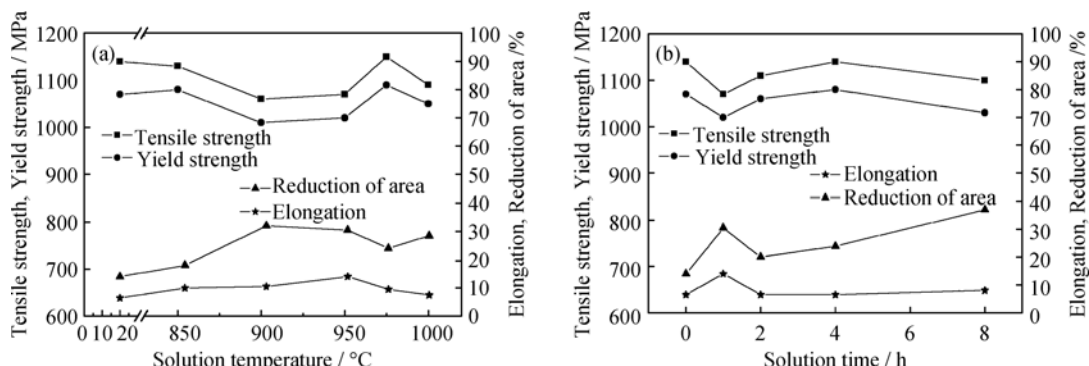


Fig. 7. Room-temperature tensile properties of LSFed Ti-6Al-4V alloys at different solution parameters but the same aging treatment (550°C, 4 h/AC): (a) solution temperature increasing from 850°C to 1000°C with the solution time of 1 h (20°C on X axis refers to as-deposited samples); (b) solution time increasing from 1 h to 8 h with the solution temperature of 950°C (0 in X axis refers to as-deposited samples).

From Fig. 7(b), it can be seen that the sample heat treated with solution (950°C, 1 h/AC) and aging (550°C, 4 h/AC)

treatment presents a lower tensile strength and a higher ductility than the as-deposited samples, which results from the

formation of coarsening primary α laths (Fig. 3(c)). A further increase in solution time results in the increase of tensile strength and the decrease of ductility of heat-treated samples. It is due to the fact that the volume fraction of coarsening primary α laths is decreased and the volume fraction of fine secondary α laths is increased (Fig. 4(a)). When the solution time reaches 4 h, both primary and secondary α laths are coarsened obviously (Fig. 4(b)), which leads to the increase of the ductility of heat-treated samples again. As the solution time increases to 8 h, a quantity of globular α phases appear in β grains and grain boundaries and the microstructure becomes more uniform (Fig. 4(c)), which exhibits better integrated mechanical properties for the heat-treated samples, that is, the reduction of area is higher and the tensile strength only declines a little.

3.3.2. Aging temperature and time

Fig. 8 shows the influence of aging temperature and time on the mechanical properties. It can be seen that the samples heat treated by solution (950°C , 1 h/AC) and aging (450°C , 4 h/AC or 550°C , 2 h/AC) treatment present a lower tensile strength and a higher ductility than the as-deposited samples, which also results from the coarsening of α laths through solution-aging treatment (Figs. 5(a) and 6(a)). From Fig.

8(a), it can be seen that both the tensile strength and ductility of the heat-treated sample increase with increasing aging temperature, except that there exists a drop in the reduction of area for the sample heat treated by solution (950°C , 1 h/AC) and aging (500°C , 4 h/AC) treatment. It is due to the fact that the aspect ratio and the volume fraction of primary α laths decrease and the volume fraction of refined secondary α laths increase. Moreover, the secondary α laths are coarsened gradually with increasing aging temperature (Figs. 5(a-c)). The origin of the drop of reduction of area at the aging temperature of 500°C is currently not understood. From Fig. 8(b), it can be found that both the tensile strength and ductility of the heat-treated sample increase slightly with increasing aging temperature. However, there is no obvious variation in tensile strength and elongation when the aging time is above 4 h. This is due to the fact that the microstructures have already become more uniform at the prolonged aging time. At the same time, with further increasing aging time, although the volume fraction of refining α laths increases, the volume fraction of globular α phase also increases gradually as the volume fraction of coarsening α laths decreases. In addition, the secondary α laths are also coarsened slightly (Figs. 6(b and c)).

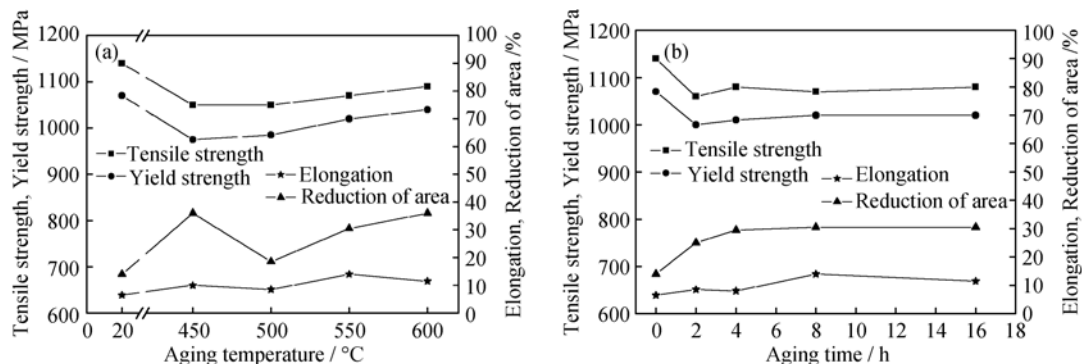


Fig. 8. Room-temperature tensile properties of LSFed Ti-6Al-4V alloy heat treated at different aging parameters after the same solution treatment (950°C , 1 h/AC): (a) aging temperature increasing from 450°C to 600°C with the aging time of 4 h (group C in Table 1; 20°C in X axis refers to as-deposited samples); (b) aging time increasing from 2 h to 16 h with aging temperature of 550°C (group D in Table 1; 0 in X axis refers to as-deposited samples).

4. Discussion

4.1. Microstructure transformation

Fig. 9 shows the calculated Ti-6Al-4V phase diagram using the Thermo-Calc software with the aim of the TTT Ti alloys database. The abscissa NP denotes the molar fraction of phases. The solution and aging temperature ranges are shown in the shadow region. From Fig. 9, it can be seen that if the solid solution temperature is below the β transus, α phase will not transform to β phase completely, and partial α phase will be retained and coarsened. During aging treatment, secondary α phase can further precipitate in β phase again. Based on the heat treatment regimen in the present work, if Ti-6Al-4V alloy is heated up to $850\text{-}950^{\circ}\text{C}$, the

equilibrium microstructure should consist of $\alpha+\beta$ phases

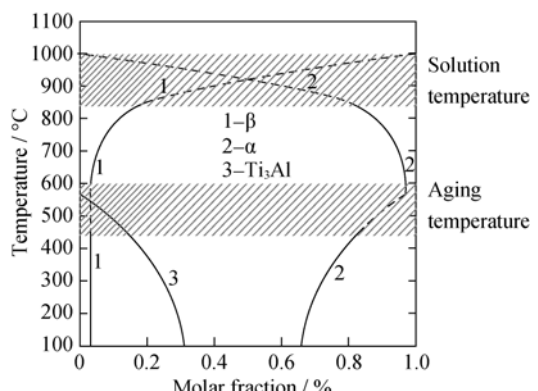


Fig. 9. Ti-6Al-4V phase diagram

because the β transus temperature is about 1000°C. Then, with air cooling, the prior β phase will decompose further, which will lead to the precipitation of secondary α laths in β matrix. Meantime, some primary α and β phases will be reserved. Subsequently, the metastable β phase will further decompose into $\alpha + \beta$ phases by diffusion during aging treatment.

4.2. Coarsening and globularization mechanism of α precipitate

The LSF theory described that, for diffusion-controlled particle coarsening, the precipitates grow at an almost constant volume fraction [15]. In light of this, Voorhees and Glicksman [16] use a new statistical mean field theory that accurately reproduces the simulation data of the multiparticle diffusion problem and gives the following equation:

$$d^3 - d_0^3 = \frac{8\sigma C_e V_m^2 D}{9R_g T(1 - f_v^{1/3})} t \quad (1)$$

where d_0 and d are the average particle diameters of the precipitation phase at the onset of the coarsening process and at the time t after the onset, σ is the matrix-precipitated phase interface-specific free energy, C_e is the matrix concentration of precipitating elements in equilibrium with a flat surface, V_m is the precipitate molar volume, D is an effective diffusion coefficient that mainly depends on the diffusion coefficients of the precipitating elements in the matrix, R_g is the gas constant, T is the absolute temperature, and f_v is the volume fraction of the precipitated phase.

It is apparent that the size of the precipitate depends not only on coarsening time but also on volume fraction and processing temperature. From Eq. (1), it can be seen that the heat treatment temperature T is one of the important parameters that directly influence the particle coarsening process. On the other hand, the parameters D and f_v also both depend on treatment temperature. Fig. 3 shows that, with increasing temperature, the volume fraction f_v of α phase decreases, which increases the denominator of the right side of Eq. (1). Thus, the α laths coarsen obviously at a higher treatment temperature, which results in that the selections of solution and aging temperature have important influences on the coarsening of primary and secondary α phases.

As for the coarsening and globularization of α phase after heat treatment, many researchers have studied possible mechanisms by which lamellar microstructures coarsen or transform to equiaxed morphology [12-13]. As a result, a number of mechanistic models have been proposed to describe the process, including boundary splitting, lamellar termination migration, and various capillarity-induced instabilities based on the Rayleigh perturbation theory. Recently, Stefansson *et al.* [12] established the mechanism controlling

static globularization of Ti-6Al-4V after deformation and annealing at 900°C and 955°C. The mechanism of lamellar microstructures coarsening and transforming to equiaxial cluster α consists of two stages: segmentation of the lamellae via boundary splitting and microstructural coarsening. Based on Stefansson *et al.*'s analysis, the globularization depends on the formation and evolution of dislocation substructure. The globularized percent is a function of local effective strain and increases at a constant rate with increasing local strain, which suggests an important effect of pre-strain on globularization behavior.

According to the traditional thermal mechanical theory and the existing literatures on titanium alloys, it is difficult to transform lamellar α to globular α only by heat treatment. So far, in order to achieve this purpose, alloys should be deformed at the two-phase region and then heat treated [12-14], that is, pre-strain is one of the necessary factors to cause α phase globularization. As for the LSFed samples, a strong residual stress will be reserved from rapid heating and cooling during LSF. It is possible that the interaction between residual stress and heat treatment results in the globularization of α phase in partial β grains, because there are no external forces that make samples deform during heat treatment.

5. Summary

The microstructure evolution during heat treatment of laser solid forming Ti-6Al-4V alloy was investigated. The effects of the temperature and time of solution treatment and aging treatment on the microstructure and mechanical properties were analyzed.

(1) The microstructure of LSFed samples consists of the columnar prior β grains with an average grain width of 300 μm , which grow epitaxially from the substrate along the deposition direction (Z). There are mainly Widmanstätten α laths and a little acicular α in prior β grains.

(2) With increasing solution temperature, the width of primary α laths increases and the aspect ratio and volume fraction of α laths decrease, which make the tensile strength of the heat-treated sample decrease and its ductility increase. Recrystallization of the prior columnar β grain results in the increase of tensile strength and the decrease of ductility occurring in the heat-treated sample when the solution temperature reaches 975°C. However, the obvious coarsening of α laths results in the reduction of tensile strength and ductility again when the solution temperature reaches 1000°C.

(3) With increasing solution time, the volume fraction of refined secondary α laths increases and both primary and secondary α laths are coarsened slowly; especially, the globularization of α phase occurs when the solution time is

beyond 8 h. This phenomenon of microstructural evolution makes the tensile strength of the heat-treated sample first increase to a maximum and then decrease and its ductility first decrease to a minimum and then increase with the increasing of the solution time.

(4) With increasing aging temperature, there are no obvious changes in the width of primary α laths, but their aspect ratio and the volume fraction of primary α laths decrease; in addition, the volume fraction of refined secondary α laths increases. Meantime, the secondary α laths are coarsened continuously, which results in the increase of tensile strength and ductility of the heat-treated sample. With increasing aging time, the width of primary α laths decreases slightly, the volume fraction of secondary α laths increases and the coarsening of secondary α laths also occurs at the same time, which makes both the tensile strength and ductility of the heat-treated sample increase slightly. There are no obvious variation on the tensile strength and elongation when the aging time is above 4 h because the microstructures have already become more uniform at the prolonged aging time.

(5) The globular α phase is first observed in LSFed samples when the samples are heat treated with solution (950°C, 8 h/AC) or with solution (950°C, 1 h/AC) and aging (550°C, above 8 h/AC) treatment, respectively. It is most possible that the interaction between the residual stress from LSF process and heat treatment results in the globularization of α phase in partial β grains, because there are no any external forces that make the samples deform during heat treatment.

(6) To obtain good integrated mechanical properties for LSFed Ti-6Al-4V alloys, it is suggested that solution treatment is performed at the temperature of 20-50°C below the β transus and the time of 4-8 h and aging treatment is performed at the temperature of 550-600°C and the time of 4-8 h.

Acknowledgments

This work was financially supported by the Program for New Century Excellent Talents in Universities of China (No. NCET-06-0879), the National Natural Science Foundation of China (No. 50331010), the Northwestern Polytechnical University Foundation of Fundamental Research (No. NPU-FFR-JC200808), the National Basic Research Program of China (No. 2007CB613800), and the Program of Introducing Talents of Discipline to Universities, China (No. 08040).

References

- [1] Kobryn P.A., Moore E.H., and Semiatin S.L., The effect of laser power and traverse speed on microstructure, porosity, and build height in laser-deposited Ti-6Al-4V, *Scripta Mater.*, 2000, **43** (4): 299.
- [2] Kelly S.M. and Kampe S.L., Microstructural evolution in laser-deposited multilayer Ti-6Al-4V builds: Part I. Microstructural characterization, *Metall. Mater. Trans. A*, 2004, **35** (6): 1861.
- [3] Wu X., Sharman R., Mei J., and Voice W., Microstructure and properties of a laser fabricated burn-resistant Ti alloy, *Mater. Des.*, 2004, **25**: 103.
- [4] Wu X.H., Liang J., Mei J.F., Mitchell C., Goodwin P.S., and Voice W., Microstructures of laser-deposited Ti-6Al-4V, *Mater. Des.*, 2004, **25**: 137.
- [5] Lin X., Yue T.M., Yang H.O., and Huang W.D., Microstructure and phase evolution in laser rapid forming of a functionally graded Ti-Rene88DT alloy, *Acta Mater.*, 2006, **54**: 1901.
- [6] Lin X., Yue T.M., Yang H.O., and Huang W.D., Solidification behavior and the evolution of phase in laser rapid forming of graded Ti6Al4V-Rene88DT alloy, *Metall. Mater. Trans. A*, 2007, **38** (1): 127.
- [7] Banerjee R., Collins P.C., Bhattacharyya D., Banerjee S., and Fraser H.L., Microstructural evolution in laser deposited compositionally graded α/β titanium-vanadium alloys, *Acta Mater.*, 2003, **51**: 3277.
- [8] Banerjee R., Bhattacharyya D., Collins P.C., Viswanathan G.B., and Fraser H.L., Precipitation of grain boundary α in a laser deposited compositionally graded Ti-8Al-xV alloy—an orientation microscopy study, *Acta Mater.*, 2004, **52**: 377.
- [9] Zeng L. and Bieler T.R., Effects of working, heat treatment, and aging on microstructural evolution and crystallographic texture of α , α' , α'' and β phases in Ti-6Al-4V wire, *Mater. Sci. Eng. A*, 2005, **392**: 403.
- [10] Lütjering G., Influence of processing on microstructure and mechanical properties of ($\alpha + \beta$) titanium alloys, *Mater. Sci. Eng. A*, 1998, **243**: 32.
- [11] Semiatin S.L., Seetharaman V., and Weiss I., Flow behavior and globularization kinetics during hot working of Ti-6Al-4V with a colony alpha microstructure, *Mater. Sci. Eng. A*, 1999, **263**: 257.
- [12] Stefansson N., Semiatin S.L., and Eylon D., Mechanisms of globularization of Ti-6Al-4V during static heat treatment, *Metall. Mater. Trans. A*, 2003, **34** (3): 691.
- [13] Zhou Y.G., Zeng W.D., and Yu H.Q., An investigation of a new near-beta forging process for titanium alloys and its application in aviation components, *Mater. Sci. Eng. A*, 2005, **393**: 204.
- [14] Ma J.M., Wang Q.R., and Wei S.Y., *Engineering Material Application Manual* (in Chinese), edited by Yan M.G., and Liu B.C., Chinese Standard Publishing Company, Beijing, 2001: 104-105.
- [15] Lifshitz I.M. and Slyozov V.V., The kinetics of precipitation from supersaturated solid solutions, *J. Phys. Chem. Solids*, 1961, **19** (1-2): 35.
- [16] Voorhees P.W. and Glicksman M.E., Solution to the multi-particle diffusion problem with applications to Oswald ripening—I. Theory, *Acta Metall.*, 1984, **32** (11): 2001.